The effect of co-doping of nitrogen and electric field on the magnetism of (Zn,Fe)Te

INDRAJIT SAHA

February 2020

The effect of co-doping of nitrogen and electric field on the magnetism of (Zn,Fe)Te

INDRAJIT SAHA

Doctoral Program in Nano-Science and Nano-Technology

Submitted to the Graduate School of

Pure and Applied Sciences

in Partial Fulfillment of the Requirements

for the Degree of Doctor of Philosophy in

Engineering

at the

University of Tsukuba

Dedicated to my Parents and Family

with Love and Gratitude

Table of Contents

Chapter 3: Experimental Methods

Chapter 4: Experimental results and discussions – I

Chapter 5: Experimental results and discussions – II

Abstract

The noteworthy mentioning point about most Diluted Magnetic Semiconductors (DMSs) is that the charge state of the magnetic ions and hence, the corresponding interaction energy between them depends on the position of the Fermi level with respect to the band edges of the host semiconductor compound. This property opens an unprecedented opportunity to modify the magnetic properties of DMSs in which the magnetic impurity levels resides within the bandgap of the host semiconductors, by engineering the Fermi level position using co-doping, electric fields or light.

The binding energy of nitrogen acceptor in ZnTe is about 50 meV and can be doped easily, a maximum doping concentration of the order of 10^{20} cm^{-3} can be achievable. On the other hand, the $Fe^{2+/3+}$ donor level is located at 150 meV above the top of the valence band of ZnTe. In addition, the pure dilute phase of zinc-blende structure is obtained for $Zn_{1-x}Fe_xTe$ thin films with Fe composition, $x \leq 0.02$ and the isoelectronic Fe^{2+} state on the substitutional site of II-VI compounds is found to produce only field-induced magnetic moments, typical van-Vleck type paramagnetic behavior. As the substitutional Fe forms the deep donor $Fe^{2+/3+}$ levels within the bandgap of the host ZnTe, the trap of carriers introduced by additional charge doping or application of external gate voltage is expected to deviate the Fe charge state from Fe^{2+}, resulting in a possible modification of magnetic properties. In this study, we have co-doped nitrogen (N) acceptor impurity and applied external electric field in $Zn_{1-x}Fe_xTe$ thin films with $x \leq 0.02$ to change the valence state of Fe and hence to observe the possible modification of its magnetic properties. The summary of the experimental works is represented under the following headlines:

Structural and magnetic properties of N-doped $Zn_{1-x}Fe_xTe$ thin films with $x \leq 0.02$

N-doped $Zn_{1-x}Fe_xTe$ thin films were grown by molecular beam epitaxy (MBE) in the ultra-high vacuum condition of 10^{-10} Torr. We have used elemental solid sources of Zn, Te and Fe and nitrogen plasma source with N_2 gas excited by rf-plasma. We have grown $Zn_{1-x}Fe_xTe$: N thin films under different growth conditions by keeping Fe composition fixed and varying the N concentrations by changing only the size of holes in the shutter of the plasma source. However, the other N concentration controlling parameters such as, the operating power of the rf-plasma source, the distance between the plasma source and the substrate and the N_2 flow rate have been remained same for a series of samples.

(*i*) Te-rich growth condition (Te to Zn flux ratio, $\frac{Te}{Zn}$ ~ 2.40):

We have investigated the effect of co-doping of nitrogen (N) acceptor impurity on the structural and magnetic properties of $Zn_{1-x}Fe_xTe$. We grew $Zn_{1-x}Fe_xTe$: N thin films by MBE with a fixed Fe composition, x = 1.5% and varied N concentrations in the range of [N] = $8 \times 10^{17} - 4 \times 10^{19}$ cm^{-3}. Structural analyses by using x-ray absorption fine structure (XAFS) reveals that N-doped films with intermediate N concentrations [N] = 8×10^{17}- 7×10^{18} cm^{-3} are mainly composed of pure diluted phase with substitutional Fe atoms in the valence state deviated from Fe^{2+} as determined from the shifting of the Fe-K pre-edge peak position towards higher energy in the XANES spectra, while Fe is predominantly incorporated in forming an Fe-N compound at the highest N concentration ,[N] = 4×10^{19} cm^{-3}. According to the previous research on Fe-K pre-edge peak by several research groups, the pre-edge peak energy position of the XANES spectra is very sensitive to Fe redox states and shifts towards higher energy with increasing oxidation state. The separation between the average pre-edge positions for Fe^{2+} and Fe^{3+} states is 1.4 ± 0.1 eV. These results are in agreement with the transmission electron microscopy (TEM) observation where the crystal structure of N-doped film with intermediate N concentration, [N] = 7×10^{18} cm^{-3} are found to compose of zinc blende structure; while in the N-doped film with highest N concentration, [N] = 4×10^{19} cm^{-3}, translational Moire fringes are observed to form at the surface region and consequently, some additional diffraction spots are detected in the corresponding fast Fourier transform (FFT) pattern. Accordingly, the magnetization measurement

using SQUID confirms a drastic change of magnetic properties; a linear dependence of magnetization on magnetic field (*M-H*), typical of van-Vleck paramagnetism in the film without N-doping changes into ferromagnetic behaviors with hysteretic *M-H* curves at the intermediate N concentrations and comes back to a linear *M-H* dependence at the highest N concentration. The ferromagnetism in the intermediate [N] range may reflect a deviation of the valence state of the substitutional Fe from Fe^{2+}, while the linear *M-H* at the highest [N] would be attributed to precipitates of an Fe-N compound.

(*ii*) Zn-rich growth condition (Te to Zn flux ratio, $\frac{Te}{Zn}$ ~ 0.70):

We have also investigated the structural and magnetic properties of nitrogen (N) acceptor impurity co-doped $Zn_{1-x}Fe_xTe$ thin films grown under Zn-rich condition with Fe composition fixed at x = 1.4% and N concentrations varied in the range of [N] = $1.8 \times 10^{18} - 5.1 \times 10^{19}$ cm^{-3}. Structural analysis by X-ray diffraction (XRD) detects some additional extrinsic diffraction peaks alongside with the intrinsic diffraction peaks from GaAs substrate and ZnTe buffer layer in the N-doped film with the highest N concentration, [N] = 5.1×10^{19} cm^{-3} only, which may possibly originate from Fe-N compounds,. This finding is, in agreement with the result of XAFS analysis which shows the shifting of Fe atoms from the substitutional position for N-doped films with higher N concentrations, [N] = $1.8 \times 10^{19} - 5.1 \times 10^{19}$ cm^{-3} ; Whereas, N-doped films with lower N concentrations [N] = $1.8 \times 10^{18} - 4.3 \times 10^{18}$ cm^{-3} are composed of pure diluted phase with substitutional Fe atoms in the valence state deviated from Fe^{2+} as determined from the shifting of the Fe-K pre-edge peak position towards higher energy in the XANES spectra. However, the pre-edge peak position is found to be higher as compared to those of Te-rich samples even for the same N concentration. This indicates that the change of valence state from Fe^{2+} to Fe^{3+} due to N-doping is more significant in Zn-rich samples. Consequently, more pronounced change of magnetic properties are observed in the magnetization measurement using SQUID; typical of van-Vleck paramagnetism in the film without N-doping changes into room temperature ferromagnetic behaviors with hysteretic *M-H* curves for all N-doped films in the N concentrations range of [N] = $1.8 \times 10^{18} - 5.1 \times 10^{19}$ cm^{-3}. However, the weak room temperature ferromagnetic behavior observed in the N-doped films with lower N concentrations, [N] = $1.8 \times 10^{18} - 4.3 \times 10^{19}$ cm^{-3} may reflect the deviation of valence state of substitutional Fe from Fe^{2+} to $Fe^{2+/3+}$ mixed states. On the other hand, the robust room temperature ferromagnetic behavior observed in the N-doped films with higher N concentrations, [N] = 1.8×10^{19} - 5.1×10^{19} cm^{-3} would be attributed to precipitates of Fe-N compounds in which Fe is in $Fe^{2+/3+}$ or in other valence state.

The major difference in modification of magnetic properties due to N-doping among Te-rich and Zn-rich growth conditions is observed for N-doped films with N concentration of the order of [N] ≈ 10^{18} cm^{-3}. In the Te-rich case, the van-Vleck type paramagnetic behavior of the undoped film changes into low temperature ferromagnetic behavior in the N-doped film with [N] ≈ 10^{18} cm^{-3}, while in the Zn-rich case, it changes into room temperature ferromagnetic behavior even for the same N-doping concentration. This difference in magnetic modification can be explained by the observed difference in pre-edge peak position of the N-doped films with same N-doping concentration for these two different growth conditions. The higher energy position of the Fe-K pre-edge peak in the Zn-rich case indicates that the larger deviation of valence state of substitutional Fe from Fe^{2+} to Fe^{3+}due to N-doping. This large deviation of valence state of substitutional Fe can produce robust finite magnetic moment even at zero external magnetic field and modify the exchange interaction between magnetic moments. Thus, we get room temperature ferromagnetic behavior in the N-doped films with [N] ≈ 10^{18} cm^{-3} grown under Zn-rich condition.

Structural and magnetic properties of modulation-doped $Zn_{1-x}Fe_xTe$ thin films with $x \leq 0.02$

We have studied the structural and magnetic properties of $Zn_{1-x}Fe_xTe$ thin films with Fe composition x = 1.3% grown on N-doped ZnTe buffer layer with a particular intension to investigate whether the impact of interfacial holes can inducing any exchange interactions and hence alter the magnetic properties of $Zn_{1-x}Fe_xTe$ thin films. The

N concentrations of the p-ZnTe layer are of the order of 10^{19} cm^{-3}. Structural analysis by XRD confirms the absence of extrinsic precipitate compounds. Diffraction peaks from the ZnTe buffer and GaAs substrate have only been identified. However, the ZnTe peaks for the (400) and (600) diffractions are found to be separated due to N acceptor doping. In the magnetization measurements by SQUID, we have observed different magnetic properties other than the van-Vleck paramagnetic behavior as observed for $Zn_{1-x}Fe_xTe$ thin films grown on the undoped ZnTe buffer layer. The magnetization result has shown (ordinary) paramagnetic behavior with S-like *M-H* curve for $Zn_{1-x}Fe_xTe$ thin films grown on the p-ZnTe buffer layer. This difference of magnetic behavior might reflect the impact of interfacial holes on the magnetic properties of $Zn_{1-x}Fe_xTe$.

Effect of external electric field on the magnetism of $Zn_{1-x}Fe_xTe$ thin films with $x \leq 0.02$

We have also constructed field effect transistor and electric double layer transistor device structure by using Al_2O_3 film and liquid electrolyte respectively as gate insulator and Pt foil as gate electrode to module the magnetic properties of $Zn_{1-x}Fe_xTe$ thin films of Fe composition, x = 1.3%.We have measured the magnetization of the $Zn_{1-x}Fe_xTe$ thin films after the application of external gate voltages across the device structures by using SQUID. In both cases, we have followed the measurement sequence 0V → +V → -V → 0V(Re). The magnetic modulation by external gate voltages across the field control device using ionic liquid is found irreversible. The saturation magnetization decreased from the initial value at V_G = 0V after the application of positive gate voltage, V_G = +1.5V, but after that there is apparently no change of magnetization with the change of external gate voltages of the order of V_G = -2.5V and finally V_G = 0V (Re). So, it is believed that the modulation of magnetization may not originate from the change of intrinsic magnetic properties of $Zn_{1-x}Fe_xTe$. One possibility of this irreversible behavior may be the anion and cation in the ionic liquid used for the insulating layer did not move when the gate voltage is switched from positive to negative and even, if returned to 0V. Another reason may be any chemical reaction between ionic liquid and $Zn_{1-x}Fe_xTe$ layer or interface. Unfortunately, we have also not seen any modulation of magnetic properties after the application of external gate voltages, V_G = ± 10V and ± 20V across the channel layer of $Zn_{1-x}Fe_xTe$ using the existing field control device consisting of solid Al_2O_3 insulating layer. The thin $Zn_{1-x}Fe_xTe$ layer with the thick diamagnetic GaAs substrate may make it difficult to measure the electrical manipulation of magnetization of the $Zn_{1-x}Fe_xTe$ layer. The magnetization dependent Hall effect may be helpful to extract the small change in the electrical field controlled magnetic properties of the $Zn_{1-x}Fe_xTe$ layer directly.

The ability to externally control the properties of magnetic materials would be highly desirable from fundamental and technological viewpoints, particularly in view of recent developments in magneto electronics and spintronics. In this study, we have modulated the magnetic properties of dilute phase of zinc-blende structured $Zn_{1-x}Fe_xTe$ thin films by co-doping with nitrogen acceptor impurity, from van-Vleck type paramagnetic without N-doping to room temperature ferromagnetic with N-doping. We have also performed several trials to modulate the magnetic properties of (Zn,Fe)Te thin films by applying gate voltages, but yet not succeed to find the magnetic modulation in a reversible way.

Chapter 1: Introduction

1.1 Research background

1.1.1 Spintronics

In this rapidly growing world, the developments in the fields of electronics and information technologies depends greatly on the efficient synchronization of the physical properties exhibited by charge and spin of electrons. The newly branch of physics "Spintronics" which deals with both the charge and spin of electrons has blessed the modern technology with new functionalities that even not believed before. For example, the invention of switching the magnetic phase of a ferromagnetic semiconductor reversibly using electric fields which is never observed in the case of a ferromagnet or a semiconductor separately. This is one of the examples of Spintronics devices in the semiconductor fields which is steadily growing now. But there are more mature examples available in the field of magnetic metal multilayers such as, reading heads of high-density hard disks (HDD), magnetic random-access memories (MRAM), etc. The operational principles of these devices can be explained on the basis of giant magnetoresistance (GMR, spin-dependent scattering) and tunnel magnetoresistance (TMR, spin-dependent tunneling). The major advantages of these Spintronics devices are the capability of simultaneous mass storage and processing of information efficiently by exploiting "flipping" spin of electrons instead of shutting electrons around as in modern electronics devices. Thus, we can get the combined attributes of non-volatility, high density, high-speed operation and unlimited read and write endurance, low-power consumption in information processing and storage by using Spintronics devices.

1.1.2 Diluted Magnetic Semiconductors (DMSs)

Diluted Magnetic Semiconductors (DMSs) are semiconductor compounds in which a substantial portion of semiconductor atoms are substituted by transition metal or rare earth elements (lanthanides) that produce localized magnetic moments in the semiconductor matrix. Usually, magnetic moments originate from the unfilled 3d or 4f shells of transition metals or rare earths (lanthanides) respectively. For example, transition metal elements like Cr, Mn, Fe, Ni, Co etc. which have net spin can be used in III-V, II-VI, II-IV based semiconductor compounds like GaAs, GaN, ZnO and ZnTe etc. to exhibit the dual characteristics of both semiconductor and magnetic materials. The *sp-d* interactions between the s, p band carries of host semiconductor and localized d states of the transition metals is responsible for the outstanding properties of this new functional materials. In particular, the mixing between the d electrons of the cation substituted transition metals and *p* orbitals of the host anions around the transition metals are crucial for this type of interaction. The interaction can be ferromagnetic or antiferromagnetic depending on the impact of the cation-substituted transition metal ions on the number of spin-up and/or spin-down states in the valence band of the host semiconductor.

At the beginning of the DMS study, purified Mn was used to fabricate Mn-doped II-VI bulk alloys by various modifications of the Bridgman method. It was observed that II-VI DMSs show less defect concentrations and can be doped easily with shallow impurities. In addition, it was become possible to explore several novel spin related phenomena by the available magneto-optical and magneto transport techniques. However, several difficulties such as the disorder spin orientations in the absence of applied magnetic field even at very low temperatures due to the random distributions of magnetic ions has been observed. So, the interactions between the magnetic ions was predominantly antiferromagnetic in nature. However, due to the developments of the crystal growth methods far from thermal equilibrium such as, molecular beam epitaxy (MBE), laser ablation, it has now become possible to dope magnetic ions beyond the previously thermal-equilibrium solubility limits. In addition, the electrical activity of the shallow impurities can be enhanced by using the MBE growth process. Accordingly, the efforts of making

the II-VI wide band-gap semiconductors based optical devices such as, light emitting diodes (LEDs) and diode lasers emitting in the blue-green region were not possible due to the self-compensation effect during doping. This means that they can be doped by either donor (n-type) or acceptor (p-type) impurity. For example, ZnSe can be doped by shallow donor (n-type) impurity only. Due to the invention of the non-equilibrium MBE technique and the availability of radio-frequency plasma, it has now become possible to dope ZnSe with acceptor (p-type) impurity [1, 2]. In the case of III-V semiconductor compounds based DMSs such as, (Ga,Mn)As in which Mn^{2+} ions provide both magnetic moments and carriers, the use of low-temperature MBE provides thin films with Mn composition up to 7% and the hole concentration over 10^{20} cm^{-3} [3]. The discovery of carrier-induced ferromagnetism in (Ga,Mn)As and p-type doped (Zn,Mn)Te thin films has allowed to explore the physics and possible applications of previously unavailable combinations of quantum structures and ferromagnetism in semiconductors [4, 5]. Efforts are directed intensively to develop new room temperature ferromagnetic DMSs and describe their properties theoretically.

It has been long appreciated that the physics of particular DMSs can be explained by the position of the levels derived from the open d or f shells with respect to the band-edges as well as by the degree of mixing between the local and band levels [6]. The Vonsovskii model for II-VI compound semiconductors has been represented in Fig. 1.1 (a) to explain the position of 3d localized levels of different transition metals [7]. Transition-metal impurity can provide electrons if the corresponding donor levels lie above the bottom of the conduction band and holes if the acceptor levels reside below the top of the valence band. In such cases, carrier-mediated interaction between magnetic ions have been observed. For example, carrier-induced ferromagnetism is studied in details on (Ga,Mn)As due to the peculiar position of Mn *d* levels relative to the valence band of GaAs as shown in Fig. 1.1(b). The Mn atoms provide both the spins and holes that tailor the ferromagnetic coupling between the localized spins. Similar mechanism has also been noticed in the case of (Zn,Mn)Te co-doped with nitrogen acceptor impurity. The $Mn^{2+/3+}$ donor levels locate in the valence band of ZnTe and the isoelectronic Mn^{2+} will not provide any carriers in the valence band of the host semiconductor matrix. On the framework of carrier-mediated interaction, the free carriers play an important role for ferromagnetic ordering. So, extrinsic nitrogen acceptor co-doping is required to generate carrier-induced Mn^{2+} spin-spin interactions in (Zn,Mn)Te. However, it is observed that in most of the studied DMSs, the impurity band reside in the band gap region of the host semiconductor. In such DMSs, the doping of transition metals will provide only localize magnetic moment, but no additional carrier in the host semiconductor matrix. For example, in the case of (Zn,Cr)Te, the substitutional Cr on the Zn-site forms the deep donor $Cr^{2+/3+}$ and acceptor $Cr^{1+/2+}$ levels reside within the bandgap of the host ZnTe semiconductor compounds. The superexchange or the double exchange has been regarded as the origin of the ferromagnetic interaction in (Zn,Cr)Te [8, 9].

It is now generally believed that the Zener's *p-d* exchange and double exchange interactions are the two important mechanism to describe ferromagnetic interactions in semiconductors [10]. According to the theory of ferromagnetic semiconductors, most of the DMSs such as II-VI and III-N semiconductor compound based DMSs belong to the impurity band system, where the Zener's double exchange is the dominate ferromagnetic exchange mechanism. On the other hand, the Zener's p-d exchange mechanism can apply only for limited DMSs such as, (Ga,Mn)As, (Ga,Mn)Sb with very shallow impurity levels in the band gap and deep 3*d* states in the valence band [11]. The schematic electronic structure of a transition metal (TM) impurity at the tetrahedral substitutional site in zinc blende structure for the above two ferromagnetic exchange mechanism is shown in Fig. 1.2 (a) Zener's double exchange case (b) Zener's p-d exchange case.

In general, the fivefold degenerate d-states of TM impurity are split into threefold degenerate dε states (*xy*, *yz*, *zx*) and twofold degenerate dγ states (x^2-y^2, $3z^2$-r^2).The wavefunction of the dε states hybridize strongly with the p-state of anion which make the host valence band, resulting in the bonding states, t^b in the valence band and the counterpart, antibonding states, t^a in the band gap as shown in Fig, 1.2 (a). On the other hand, the hybridization of the dγ states with the host valence states are very weak, leading to the non-bonding states, e in the band gap. For

finite concentrations, due to the anti-bonding nature of the t^a states, rather broader impurity band (that is, delocalized) is formed in the band gap. While the impurity band formed by e states are relatively narrow (that is, localized) reflecting their non-bonding character. In the right-side panel of Fig. 1.2 (a), the spin polarized density

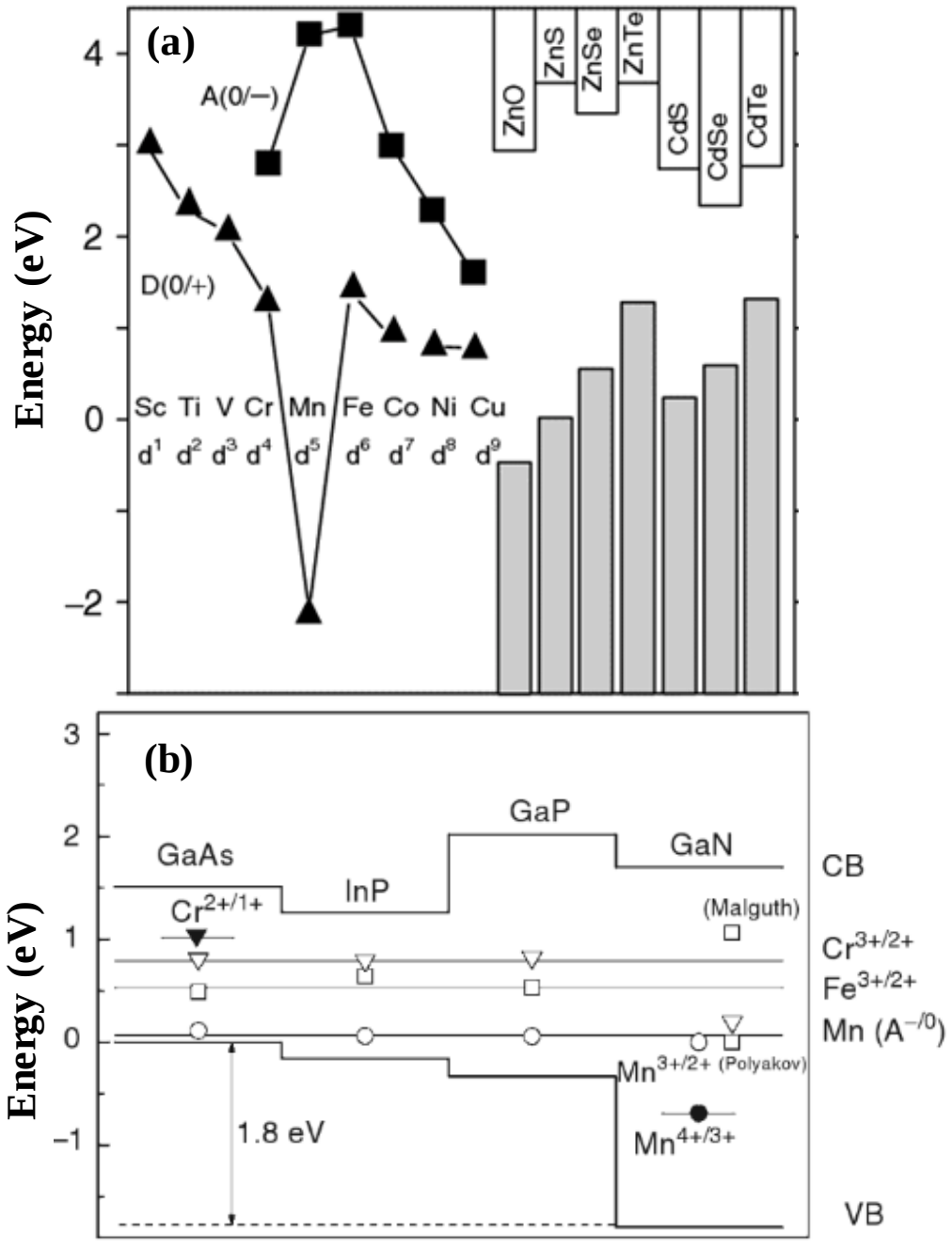

Figure 1.1: (a) Approximate positions of levels derived from d shells of transition metals relative to the conduction and valence band-edges of II-VI semiconductor compounds. Donor (triangles) and acceptor (squares) states are represented [2] **(b)** Location of Mn (circles), Fe (squares) and Cr (triangles) acceptor or donor states within the band structure of a series of III-V semiconductor compounds [7, 12].

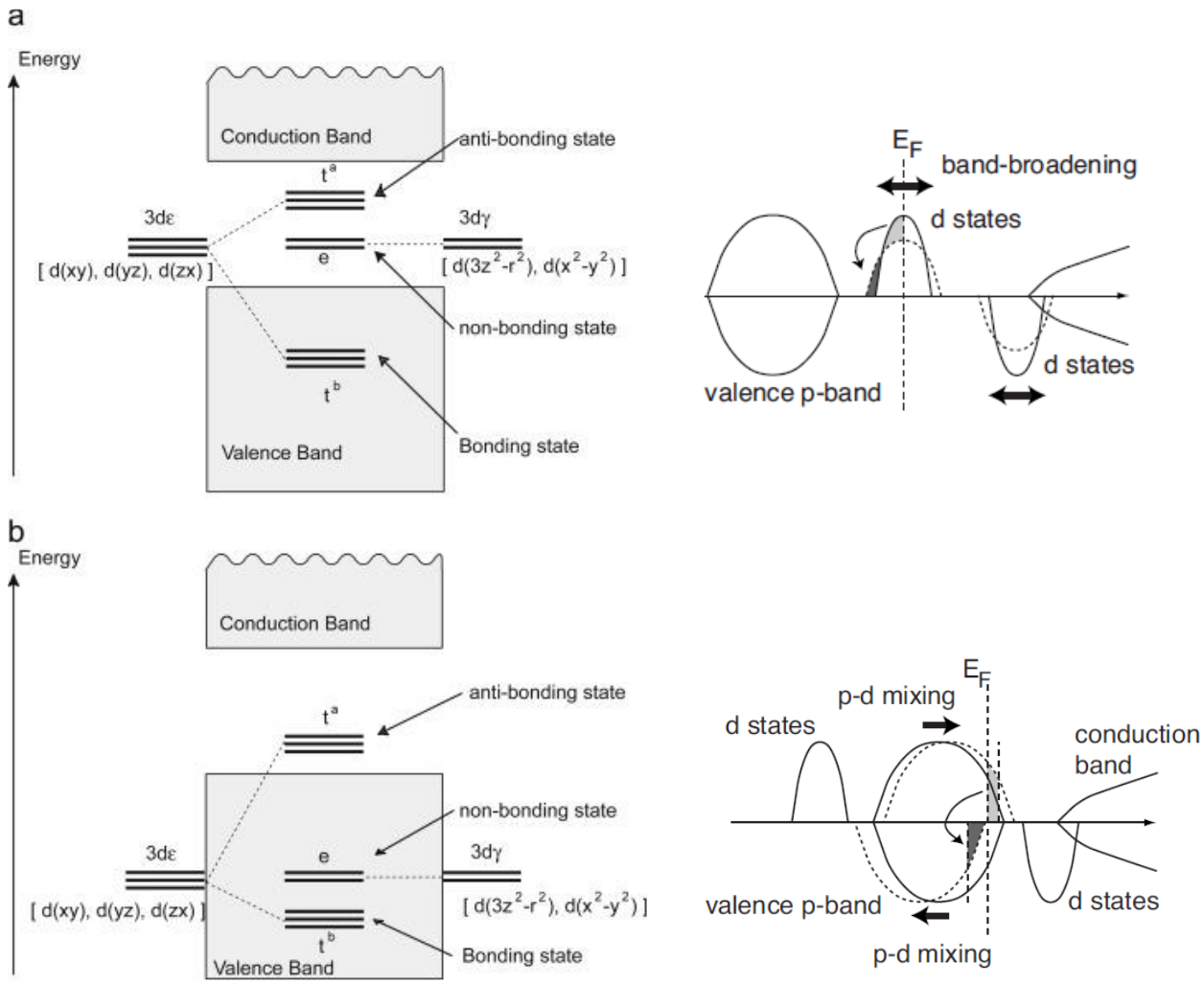

Figure 1.2: Schematic electronic structure of a transition metal impurity at the tetrahedral substitutional site in zinc blende structure. (a) When the d-states of TM impurity are above the host valence band, the anti-bonding t^a states mainly consist of transition metal d-states (Zener's double exchange mechanism). (b) When the d-states of TM impurity are below the host valence band, t^a states mainly consist of the valence p-states (Zener's p-d exchange mechanism) [10, 13].

of states (DOS) of a TM impurity in a wide-gap semiconductor is presented schematically. The stabilization of the ferromagnetic interaction depends on the width of the impurity band. The Fermi level will lie in the middle of the impurity band, only when the bonding states are occupied, and the antibonding states are vacant. In this case, the energy gain which is represented bands in the right panel of Fig. 1.2 (a) by the shaded area between the smaller concentrations (solid lines) and larger concentrations (dash lines) of spin-up and spin-down impurity is maximum. On the other hand, no energy is gained for ferromagnetically coupled impurities when the impurity band is completely filled (both bonding and antibonding states are occupied) or completely empty. The double exchange interaction is strong but of short-range character due to the exponential decay of the impurity wave function in the gap. The 3*d* electrons in the partially filled 3*d*-orbitals of TM can hop with 3*d*-orbitals of neighboring TM having

parallel magnetic moments. In this way, the *d*-electrons lowers its kinetic energy by hopping in the ferromagnetic state.

Fig 1.2 (b) represents the mechanism of the Zener's p-d exchange interaction. This interaction is basically observed in narrow-gap semiconductor based DMSs such as (Ga,Mn)Sb or (In,Mn)Sb etc. In such cases, the Mn d majority level resides below or at the lower portion of the Sb *p* band, While the minority *d* levels reside above the Fermi level. Thus, the Mn magnetic moments are well localized and the isoelectronic state of Mn^{2+} will provide a hole in the valence band to keep charge neutrality. This situation is explained by the solid line curve in the right panel of Fig. 1.2 (b) where ½ electron per Mn impurity is missing in both spin-up and spin-down valence bands. Since the main part of Mn-3d states which appears as t^b impurity bands in the valence band hybridize strongly with anion p-states, the majority-spin p band is moved to higher energies, while the minority p band is moved to lower energies due to the hybridization with the higher-lying minority-spin d state as indicated by the dash lined curves shown in the right panel of Fig. 1.2 (b). For sufficiently strong hybridization, the minority p band becomes completely occupied, while one electron per Mn atom is missing in the majority p band, resulting to a half-metallic density of states. As a result, the valence bands are polarized. This polarization in turn produces effective magnetic field to align Mn magnetic moments and stabilize the ferromagnetic state. The most notable point is that the p-d exchange interaction is comparatively weak due to the extended p-state wavefunctions giving rise of the hole state. As a result, it is not influenced by the percolation limit in the diluted state.

Another mechanism which is dominantly used to explain the ion-ion spin interactions in DMSs is the superexchange interaction [14, 15]. Due to the exchange interaction between the *sp*-electrons of the valence band with the localized d electrons of the magnetic ions, the valence band electrons are either attracted or repulsed by the adjacent magnetic ions depending on their mutual spin orientations. This leads to a spatial rearrangement of spin-up and spin-down valence band electrons. The total energy of the system becomes minimum for the antiparallel alignment of the neighboring localized spins of magnetic ions. This indirect form of exchange interaction between *d*-electrons of adjacent TM ions via p-d hybridization of entirely occupied anion p-states is known as superexchange interaction. Unlike the double exchange and *p-d* exchange interaction, it does not require a finite density of sates at the Fermi level and mostly observed in insulating magnets. The reason behind this is the hybridization between two localized states located at the opposite side of the Fermi energy level. Fig. 1.3 explains the density of states of two impurity systems with equal concentration but with antiparallel alignment of magnetic moments $\boldsymbol{s}_\mathbf{a}$ and $\boldsymbol{s}_\mathbf{b}$. The solid lines represent the local density of states without hybridization between the antiparallel spin alignment of the impurity systems, while the dotted lines represent those after hybridization. Since the electronic states with the same spin direction hybridize with each other, the lower, filled energy peaks are moved further towards lower energies and the higher, vacant energy peaks are moved further towards higher energies as mentioned by the dotted bands in Fig. 1.3. Due to the lowering in energy position of the lower, filled level, band energy is gained and stabilize the antiferromagnetic coupling. The superexchange interaction will remain independent on Fermi energy level when it resides in between the two impurity bands. However, for Fermi energy level residing in the band, there will be a competition between superexchange and double exchange.

However, for the viewpoint of practical applications in Spintronics, DMSs exhibiting room temperature ferromagnetic behavior are considered to be prominent materials. Theoretical studies showed that transition metal doped (TM) doped wide band gap semiconductors are promising candidates for room temperature ferromagnetism (RTFM) [16]. Therefore, research on DMSs consisting of various combinations of host semiconductors and magnetic elements are therefore ongoing to identify new candidate of high-temperature ferromagnetic DMSs [17, 18]. For examples, (Ga,Mn)As [T_C ~ 190K], (Ga,Mn)N [T_C ~ 900K], (Zn,Co)O [T_C ~ 300K], (Zn,Cr)Te [T_C ~ 300K], etc. But except for Mn in GaAs, in most of the cases, the origin of magnetism is not clear; controversial experimental results have been reported even for the same material. The key observation behind these, is the limited solubility of magnetic ions in the host semiconductor matrix [19].

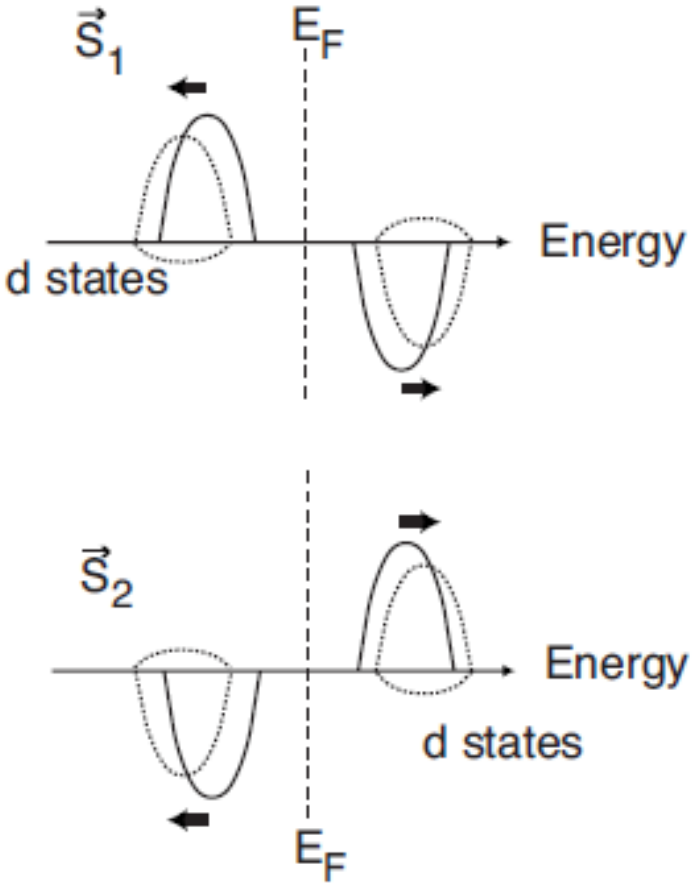

Figure 1.3: Schematic diagram of the density of states (DOSs) for two impurity systems with antiparallel spin alignment to explain the superexchange mechanism [13].

1.1.3 Externally charge co-doped DMSs

It is generally believed that ferromagnetic interactions can be obtained in TM doped III-V, II-VI and group IV semiconductor based DMSs if there are sufficient number of valence band holes present (Zener's p-d exchange mechanism) or if the TM ions of different valence states co-exist in the band gap of the host semiconductor (Zener's double exchange mechanism). In fact, the double exchange is the appropriate mechanism to explain ferromagnetic interactions in most of the cases. The worthy noting point about majority of DMSs is that the charge state of the magnetic ions and hence, the corresponding interaction energy between them depends on the position of Fermi level with respect to the band edges. Based on the above discussions, the study of co-doping with shallow donors or acceptors has proven to be an efficient method to alter the magnetic properties of DMSs. For example, in the case of (Zn,Mn)Te, Mn assumes the isoelectronic Mn^{2+} valence state. The spin-dependent hybridization between anion *p*-states and Mn-3*d* states leads to superexchange interaction; a short-range antiferromagnetic coupling between the Mn moments. However, when (Zn,Mn)Te is co-doped with nitrogen acceptor impurity, the additional holes in the valence band mediates ferromagnetic interactions between the Mn^{2+} ions [20].

However, the effect of co-doping is found to be even more pronounced in the case of DMSs in which the TM ions reside within the bandgap of the host semiconductor. In such cases, it is proposed that the additional charge carriers provided by the co-doping of donors or acceptors are trapped by these 3*d*-levels of TM impurities. This trapping will change the valence state of magnetic ions and hence, modifies chemical and spin-dependent interactions between them [21, 22]. Accordingly, co-doping of DMSs with shallow donors or acceptors, during growth or post-growth processing can modify the lattice position that is, interstitial versus substitutional and the distribution of magnetic impurities over cation sites. For examples, we can consider the II-VI magnetic semiconductor (Zn,Cr)Te and III-V magnetic semiconductor (Ga,Fe)N. In both cases, a close relation between the co-doping with shallow impurities, magnetic properties and magnetic ions distribution has been observed.

In the case of (Zn,Cr)Te, the apparent Curie temperature, $T_C^{(app)}$ and the aggregation of Cr-rich nanocrystals have changed drastically with the concentration of nitrogen (N) acceptor impurity. When the concentration of N has become comparable with that of Cr, the ferromagnetic interaction has suppressed completely. In other words, when the concentration of N acceptor and Cr impurity become equal, all the Cr atoms become charged and their Coulomb repulsion impedes the formation of nanocrystals as identified in the EDS mapping of Cr shown in Fig. 1.4 (a). However, in the case of (Zn,Cr)Te co-doped with the iodine donor impurity, both the apparent Curie temperature $T_C^{(app)}$ and the inhomogeneity of the Cr distributions have found to be enhanced in the Cr EDS mapping shown in Fig. 1.4(b).

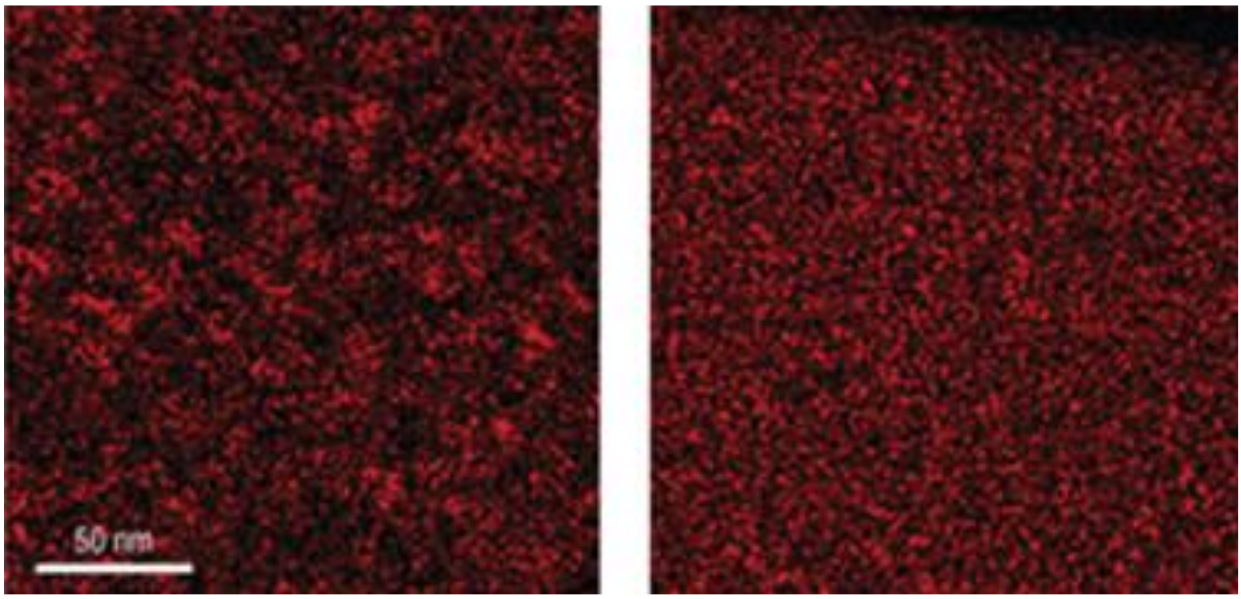

Figure 1.4: Effect of (a) donor impurity (Iodine) and (b) acceptor impurity (Nitrogen) on the spinodal decomposition of Cr ions in (Zn,Cr)Te are shown in the left and right panel respectively [9].

In the case of (Ga,Fe)N, the Fermi level engineering by co-doping with shallow acceptors (Mg) or donors (Si) is instrumental for controlling magnetic ions aggregation [23, 24]. According to the experimental observations by synchrotron XRD, TEM and SQUID magnetometry, it is confirmed that Fe is incorporated in three different ways in (GA,Fe)N such as (*i*) substitutional Fe^{3+} diluted ions on the Ga-site has accounted for the paramagnetic response, (*ii*) Fe-rich wurtzite regions of spinodal decomposition commensurate with stabilized by the GaN host lattice and (*iii*) Hexagonal ε-Fe_3N secondary phases. The last two factors are responsible for the observed room temperature

ferromagnetic behavior in (Ga,Fe)N. However, the co-doping of Si and Mg has impeded the formation of nanocrystals and the spinodal decomposition of Fe ions to provide experimental evidence for theoretical suggestions.

1.1.4 Study of externally applied electric field on DMSs

In recent time, one of the most exciting issues that drawing attention of the scientific community is either to control magnetic properties through electric field /charge configurations or to enhance the effect of magnetic field on transport. Nowadays, most of the Spintronics devices especially, magnetic tunnel junctions (MTJs) and domain wall motion devices are using spin-transfer torque (STT) to control magnetism. Despite the significant improvement in the field information technology by using spin-polarized current to manipulate magnetism, there is growing interest to reduce the switching power by using alternating means [25, 26]. In order to reduce this energy consumption, using electric field instead of current is the best alternative. In addition, STT devices produce unnecessary Joule heating while controls the magnetization though spin-polarized current. On the other hand, to control magnetism by using electric field, one has to supply sufficient amount of charge in order to charge or discharge a capacitor which consumes very little energy as compared to STT driven devices. Thus, we can get more versatile transistors with added non-volatile functionality and can tune the magnetic properties without the application of external magnetic field. The electric field control of magnetism study is of keen interest not only for technological developments but also it can make a way to discover new properties of magnetic materials that is not yet known.

The experimental demonstration of the electric field control of magnetism has remained undiscovered for long time. At the beginning, it was difficult to choose materials on which the application of an electric field can produce an observable change in its magnetic properties. In the case of ferromagnetic metals, it is not possible to change the bulk properties of ferromagnets by applying electric field. This is because very large electric field is needed to to observe any observable change without inducing the electric breakdown of the gate insulator. However, as the electrical conductivity of semiconductors are usually 3 to 6 orders of magnitude smaller than those of ferromagnetic metals, application of electric field across the semiconductor can change the carrier concentration in the interface region with the insulator. In case of ferromagnetic semiconductors, the carrier concentrations are still low but sufficient enough to mediate ferromagnetic interactions. This property makes the ferromagnetic semiconductors thin films, dominant contender for the activity of electric field control of magnetism.

Electrical manipulation of magnetic properties was first investigated in thin films of (In,Mn)As ferromagnetic semiconductor used as channel material in the field effect transistor (FET) structure [27]. The anomalous Hall effect (AHE) has been employed to extract the magnetic modulation of the material after the application of electric field. Fig. 1.5 represents the carrier dependent spin orientations of Mn ions at different applied external gate voltages. However, direct magnetometry of magnetization modulation by external applied gate voltages was first observed in (Ga,Mn)As thin films [28]. In these materials, the Mn^{2+} ions not only provide local magnetic moment but also an itinerant hole acceptor. Ferromagnetic interaction between the localized magnetic moments is mediated by the valence band holes in the framework of Zener's p-d exchange mechanism. Following these breakthroughs, researchers started intensive work to find such type impact on metals. The first success was observed in the case of FePt and FePd thin layers by using an electric double layer transistor (EDLT) structure [29]. The large electric field generated in the EDLT structure induced surface charges that control the coercivity at room temperature. This work has changed the concept that electric field control is not possible due to the short screening length. Later, theoretical works explained that the electric field effect on surface magnetization and surface magneto crystalline anisotropy can be sufficient enough for ferromagnetic metals such as, Fe, Ni and Co due to the spin-dependent screening of the electric field. These works inspired to observe electric field effects on different materials systems

including Fe (Co)/Mg system where the modulation of interface anisotropy has identified as the origin. The electric field induced room temperature ferromagnetism was reported for the magnetic oxide semiconductor, $(Ti,Co)O_2$.

From the prospective of fundamental and technological aspects, controlling magnetic properties by external means without changing temperature is of high demand. The observation of electric controlled magnetic properties of magnetic semiconductors and of magnetic metals has widen the way for the emergence of electric field controlled Spintronics devices, whose operation scheme is compatible with existing semiconductor technology.

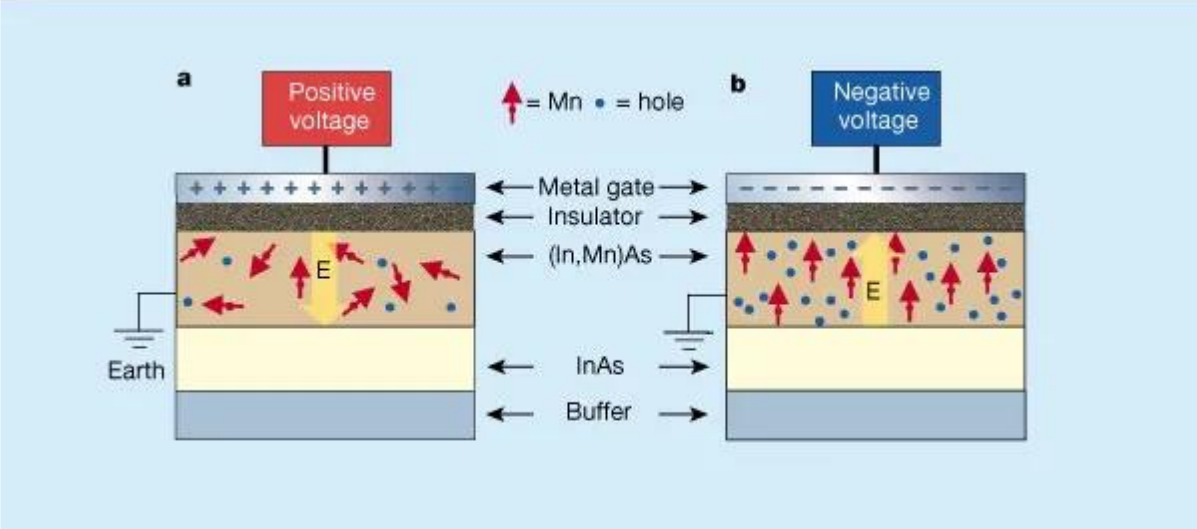

Figure 1.5: An electrically controlled magnetic switch device structure consisting of the (In,Mn)As thin film as channel layer in the field effect transistor (FET) structure. (a) Effect of positive gate voltage (b) negative gate voltage on the magnetic properties of (In,Mn)As thin film [27].

1.1.5 Purpose of the present study

In this research study, we want to investigate the effect of nitrogen acceptor co-doping and electric field on the magnetism of (Zn,Fe)Te thin films. Among various II-VI DMSs, Fe-doped selenides or tellurides have been known to produce van-Vleck type paramagnetism [30, 31]. The magnetic properties of Fe based DMS are originated from the nonzero orbital momentum of Fe^{2+} ions having $3d^6$ configuration (S = 2 and L = 2). The tetrahedral crystal field and the spin-orbit interaction induce a magnetically inactive singlet ground state, separated from higher lying excited states with energies in the range of 10-30 K, showing van-Vleck paramagnetism at low temperatures (the susceptibility is constant). However, in the presence of external magnetic field, the singlet ground state is mixed with other excited states, inducing a nonzero magnetic moment which is termed as magnetic field induced paramagnetism. This was also confirmed in the previous experimental works on $Zn_{1-x}Fe_xTe$ thin films grown under different growth conditions in our laboratory; the pure dilute phase of magnetism was observed for Fe composition, $x \leq 0.02$ and the isoelectronic Fe^{2+} state on the substitutional site of II-VI compounds produced only field-induced magnetic moments [32, 33].

In the case of II-VI DMSs, the exchange interaction between the delocalized electrons (s-like) and localized electrons (*d* or *f*) is found to be independent of the host lattice or the magnetic ion. On the other hand, the exchange interaction between the delocalized holes (*p*-like) and the localized electrons (*d* or *f*) for all DMSs with Mn, Fe and Co is antiferromagnetic and that for Cr-based DMSs is found to be ferromagnetic. The *p-d* exchange is strongly based on the energy separation between the p and d states and on the degree of hybridization between the *p* and *d* wavefunctions.

However, it is suggested that the charge state and resulting spin of Fe are crucial in calculating the potential ferromagnetic coupling. The valence state change of Fe requires a d-electron to move from the Fe impurity band to one of the bands of the host semiconductor matrix or vice versa. The energy needed in this charge transfer process can be identified with the presence of donor or acceptor levels in the band gap of the host semiconductor. According to the previous research of Fe on ZnTe, the $Fe^{2+/3+}$ donor level is observed to be located at 150 meV above the top of the valence band of ZnTe known from electron paramagnetic resonance (EPR) and photoconductivity measurements [34, 35]. Fig. 1.6 (a) has shown the different charge transfer levels in II-VI based semiconductor compounds and Fig. 1.6 (b) has shown the specific energetic value of donor and acceptor levels of Fe in ZnTe.

The key noting point about most DMSs is that the charge state of the magnetic ions and hence the corresponding interaction energy depends on the position of the Fermi level with respect to the band edges of the host semiconductor. Therefore, for DMSs in which the 3d impurity levels of TMs reside in the band gap, the Fermi level engineering by external charge co-doping, electric field or light are the most efficient approach to modify the magnetic properties. In the case of co-doping by external impurities, the 3d impurity levels in the band gap region can trap the carriers introduced by donor or acceptor impurities and hence, alter the charge state of magnetic ions. This deviation in valence state in turns, can modify the chemical and spin-dependent interaction between the magnetic ions. As typical examples, we can consider (Zn,Cr)Te and (Ga,Fe)N thin films, in which remarkable changes in ferromagnetic properties on co-doping with shallow impurities were reported [9, 24].

In this study, we have used nitrogen as acceptor impurity. The binding energy of N at infinite dilution deduced from Hall measurements and photoluminescence spectra is 53.4 ± 1 meV [36]. It is also known that, the maximum doping concentration of N, $p \approx 10^{20}$ cm^{-3} was achieved for ZnTe. Thus, it is clear that the donor levels of Fe are situated just above the acceptor levels of N in the ZnTe matrix. However, the trap of carriers introduced by additional charge doping is expected to deviate the Fe charge state from Fe^{2+}, resulting in a possible modification of magnetic properties. Therefore, we are motivated to investigate how the co-doping of acceptor impurity N affects the magnetic properties of Fe-doped ZnTe, which has not yet been experimentally studied. The schematic diagram for the (Zn,Fe)Te: N study is shown in Fig. 1.7.

We have also prepared field effect transistor device structures consisting of the (Zn,Fe)Te channel layer and Al_2O_3 thin films / liquid electrolyte as insulating layer to modulate the magnetic properties of (Zn,Fe)Te thin films which exhibit van-Vleck type paramagnetic behavior. In this case, our intension is that the effect of external electric field may change the valence state of Fe from Fe^{2+} and hence, can impact on its magnetic properties.

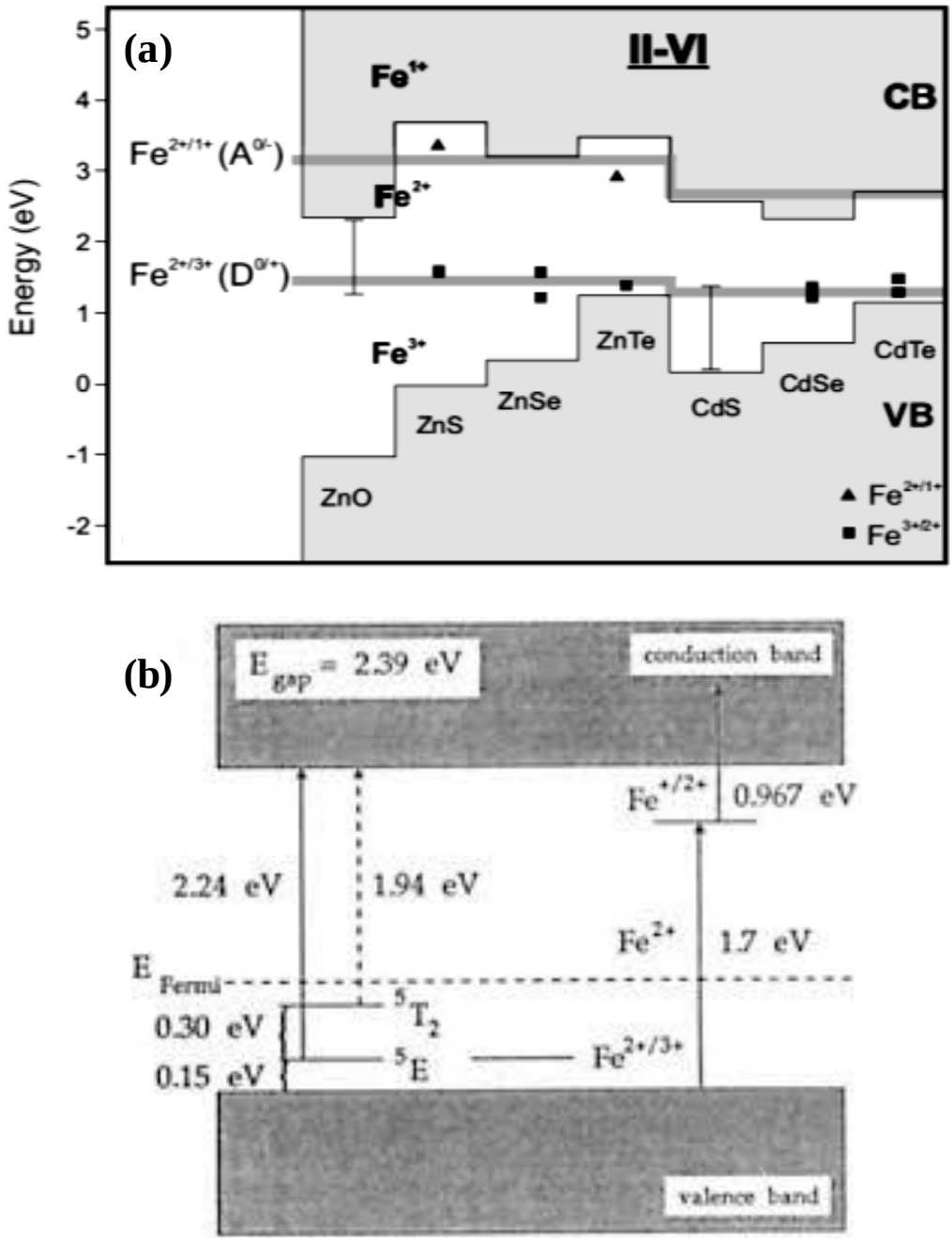

Figure 1.6: (a) Charge transfer levels $Fe^{2+/1+}$, $Fe^{3+/2+}$ and $Fe^{3+/4+}$ in II-VI semiconductor compounds. **(b)** Energetic positions of the donor level $Fe^{3+/2+}$ and acceptor level $Fe^{2+/1+}$ of Fe in ZnTe [35, 37].

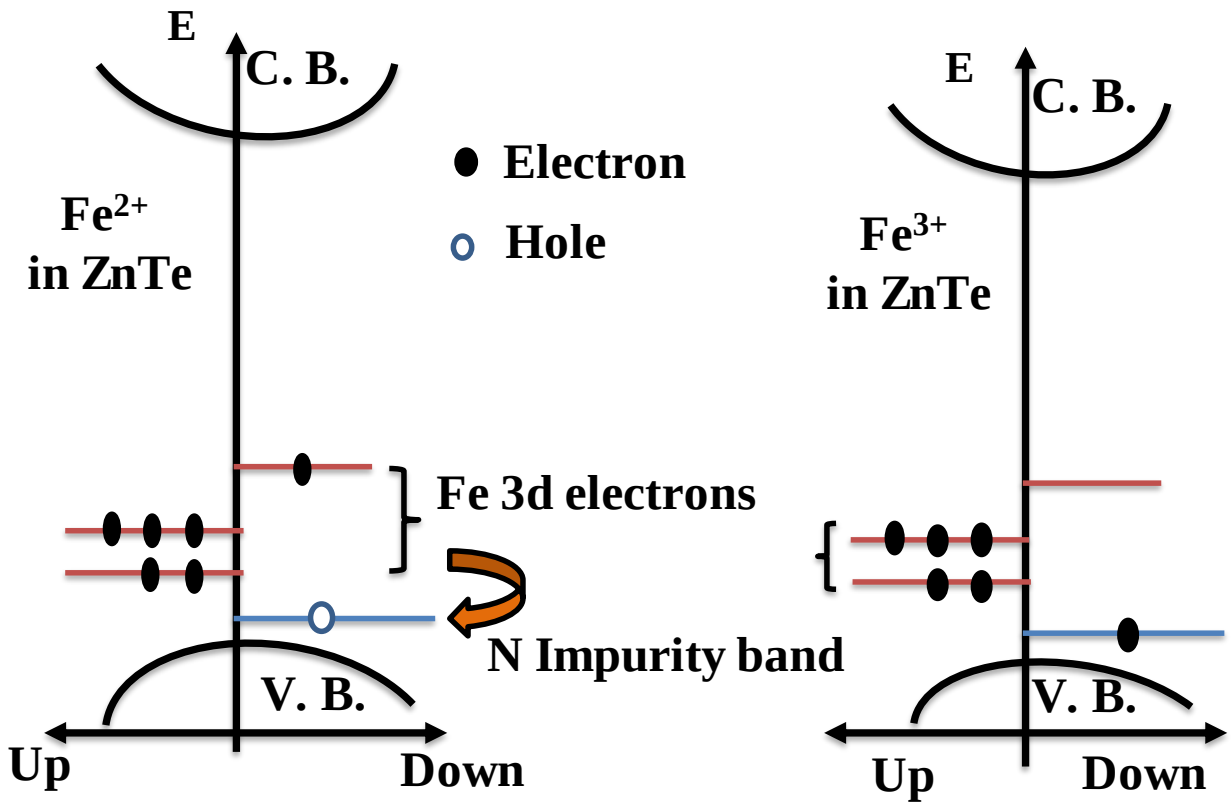

Figure 1.7: Schematic view of the N acceptor co-doped (Zn,Fe)Te research

Chapter 2: Basic physical properties and previous research

2.1 The physical properties of II-VI semiconductor compound: ZnTe

Group II-VI family semiconductor compounds consist of group II B elements such as, zinc Zn, cadmium Cd, mercury Hg and group VI B family elements such as, sulphur S, selenium Se, tellurium, Te) in the atomic ratio of 1:1. Due to their excellent material properties such as optical and electrical properties, these wide band gap materials are widely used in photovoltaic conversion and optoelectronic applications. Among them, ZnTe has a direct band gap of 2.26 eV at room temperature [38]. This band gap energy belongs to the category of green region in the electromagnetic spectra. Therefore, ZnTe is a promising material for the construction of green light emitting diodes. It also finds application in THz emitters, detectors and photodetectors [39]. In fact, one of the prominent applications of ZnTe includes the photo detection in the visible region. In the present study, we will deal with II-VI semiconductor compound, ZnTe having a cubic (zinc blende: ZB) crystal structure.

2.1.1 Energy band structure

Figure 2.1 shows the energy band diagram of ZnTe. From the energy band diagram, it is observed that the conduction band minimum (CBM) and valence band maximum (VBM) has occurred at the same point (Γ- point) in k-space. This is a characteristics of a direct band gap semiconductor. In such case, the electric dipole transition from VBM to CBM is allowed and the electron-hole pairs can combine radiatively with a high probability. This is why, ZnTe is a potential candidate for lasers, light emitting diodes (LEDs) and other photonic devices. Basically, ZnTe has anion p-type character with minor contribution from Zn [40].

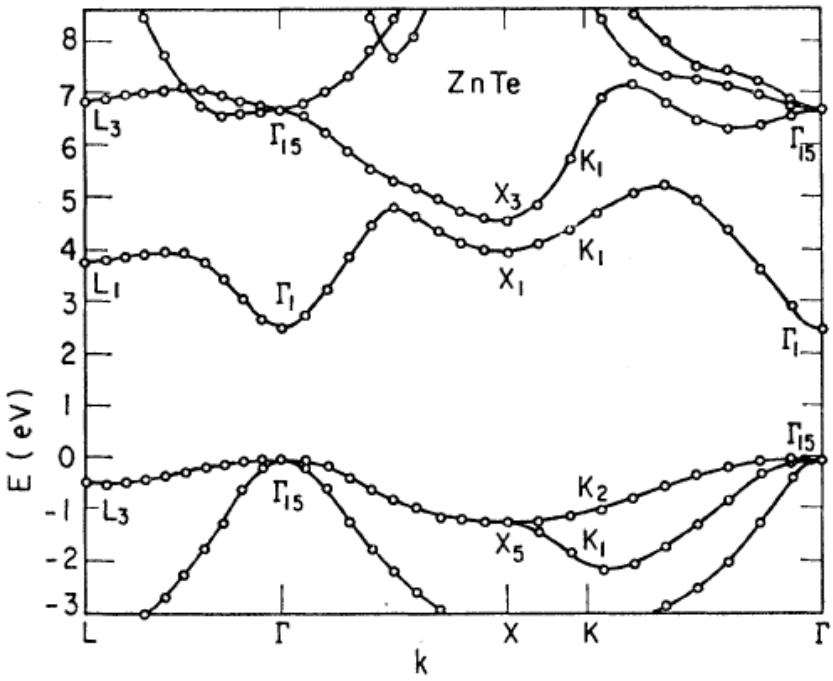

Figure 2.1.1: Band structure of ZnTe [41]

2.1.2 Crystal structure of ZnTe

Each element of group II-VI semiconductor compounds has four valence electrons per atom and is in tetrahedral co-ordination. This tetrahedral geometry can be either of zinc-blende (ZB) or of wurtzite crystal structure depending on the arrangement of the neighbouring atoms. Several II-VI semiconductor compounds including ZnTe used in this study has zinc-blende crystal structure. Fig. 2.1.2 shows the crystal structure of ZnTe. It has face centred cubic structure along [111] direction. The Zn atom is located at the origin and the Te atom is located at (¼, ¼, ¼). Each Zn atom is surrounded by four Te atoms and in turn each Te atom is surrounded by zinc atoms which are also disposed towards the corner of a regular tetrahedron. We may say that the cations and anions are in equivalent position and the co-ordination of ZB structure is described as 4:4. The space group is $F\bar{4}\,3m$. The volume of the unit cell id directly related to lattice constant, a. The nearest-neighbour atomic distance is ($\sqrt{3}$ /4) a and the lattice constant is 6.1037Å. In Fig. 2.1.2, Zn atoms are represented by blue circles and Te atoms by red circles.

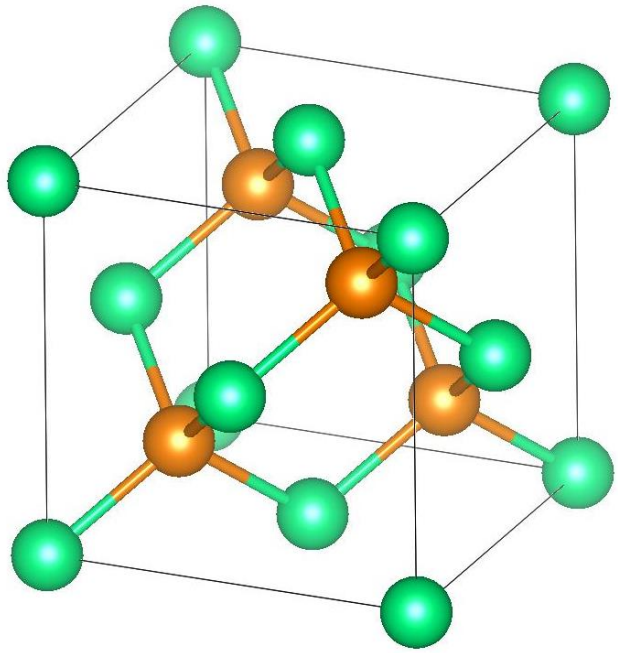

Figure 2.1.2: Crystal structure of ZnTe (Zinc-blende structure)

2.1.3 Previous research on nitrogen (N) acceptor doped ZnTe

The *ab* initio electronic band structure calculations for ZnO, ZnS and ZnTe crystals depending on the local-density approximation (LDA) treatment of electronic exchange and correlations and on the augmented spherical wave (ASW) for the solution of effective single-particle equations are shown in Fig. 2.1.3 [42]. For a hole to reside in the unfilled orbital of an atom, the reduction of energy due to the ionic and electronic polarization is given by

$$\Delta E = -\frac{e^2}{8\pi r \varepsilon_0\left(1-\frac{1}{\varepsilon_S}\right)} \tag{2.1.1}$$

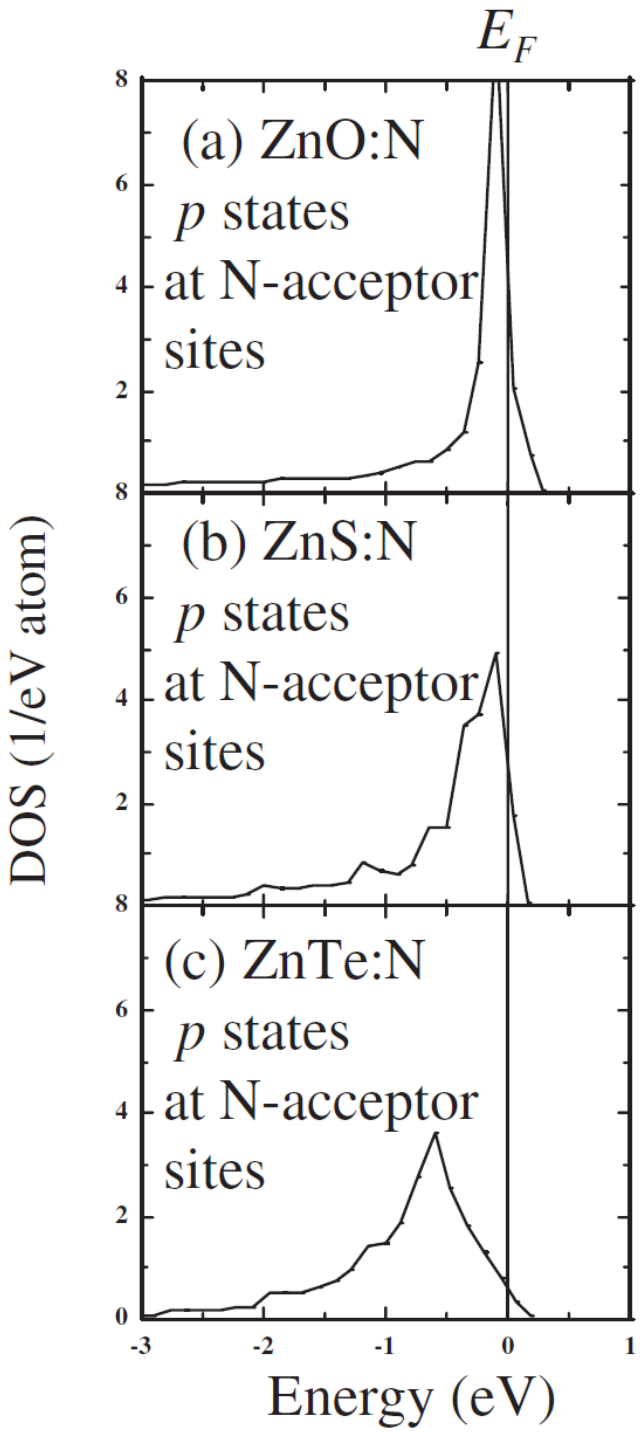

Figure 2.1.3: N-site decomposed density of states (DOSs) for (a) ZnO:N (b) ZnS:N and (c) ZnTe:N [42]

Where *r* stands for the bond length, ε_s represents the static dielectric constant o the solid.

By considering ε_s include contributions from both the ionic and electronic effects, the lowering energy associated with ionic polarization is given by,

$$\Delta E_{ion} = -\frac{e^2}{8\pi r \varepsilon_0\left(\frac{1}{\varepsilon_{opt}}-\frac{1}{\varepsilon_s}\right)} \tag{2.1.2}$$

Equation (2.1.2) suggests that localization of holes is determined by a large difference between ε_s and ε_{opt}. It should be mentioned that equation (2.1.2) provides an estimation of the ionic relaxation energy.

By taking the difference in electronegativity between the Zn atoms and the group VI elements into account, ΔE_{ion} is found as, ZnO (0.49 eV), ZnS (0.30 eV) and ZnTe (0.15 eV). This shows that ZnO has fair degree of of ionic character.

At high doping levels, the impurity band is formed due to the overlapping of the acceptor orbitals which will enhance the delocalization of holes by decreasing the bandwidth of the impurity band, W to half. So, the condition for the delocalization of holes can be written as,

$$\frac{W}{2} = |\Delta E_{ion}| \tag{2.1.3}$$

From Fig, 2.1.3, the sharp DOS peaks which stands for the bonding states between the *p*-states at the N-site and *p*-states at the neighbouring Zn-sites, it is observed that the sharp DOS peak for ZnO and ZnS are position at around -0.1 eV from the Fermi energy level position because of strong repulsive potentials, while that for the ZnTe is situated at about -0.6 eV from the Fermi energy level due to the weak repulsive potentials. For ZnTe:N, the calculated N-impurity band width, W is found around 1.7 eV which is larger than twice the energy for the ionic-polarization. Thus, we can ascertain that the *p*-type doping of N in ZnTe will delocalize holes at higher doping concentrations.

However, for the application point of view, the N-acceptor doped ZnTe epitaxial layer showing low resistivity is needed to be grown by molecular beam epitaxy (MBE). At the beginning, it was not possible to get the physical incorporation of the dopant species because of the low sticking co-efficient. After the extensive works for more than a decade, it has now become possible to dope N in ZnTe by using both radio frequency (rf) plasma source and direct current (DC) glow plasma source [43, 44]. It is now known that hole density as high as 10^{20} cm^{-3} is achievable by N-doping on ZnTe. The large incorporation of N atoms ($\approx 10^{19}$ cm^{-3}) in the Te-site in ZnTe crystal can induce a significant change in the lattice parameter as shown in Fig. 2.1.4 [45]. The relative change of the lattice parameter for an epitaxial layer with $[N_{Te}] = 10^{19}$ cm^{-3} is given by:

$$\left(\frac{\Delta a}{a}\right)_{ZnTe:N} = \frac{\delta d}{d_{Zn-Te}} \frac{[N_{Te}]}{[Te]_{ZnTe}} \quad (2.1.4)$$

Where, $d_{Zn\text{-}Te}$ = 2.62 Å, is the bond length between Zn and Te in ZnTe, $[Te]_{ZnTe}$ represents the concentration of Te atoms.

If we consider one N atom (ionic radius = 0.7 Å) substitutes on Te atom (ionic radius = 1.32 Å) in ZnTe, then the difference in local bond length, δd = -0.62 Å and the change lattice parameter calculated from equation (4) will be -1.3×10^{-4}.

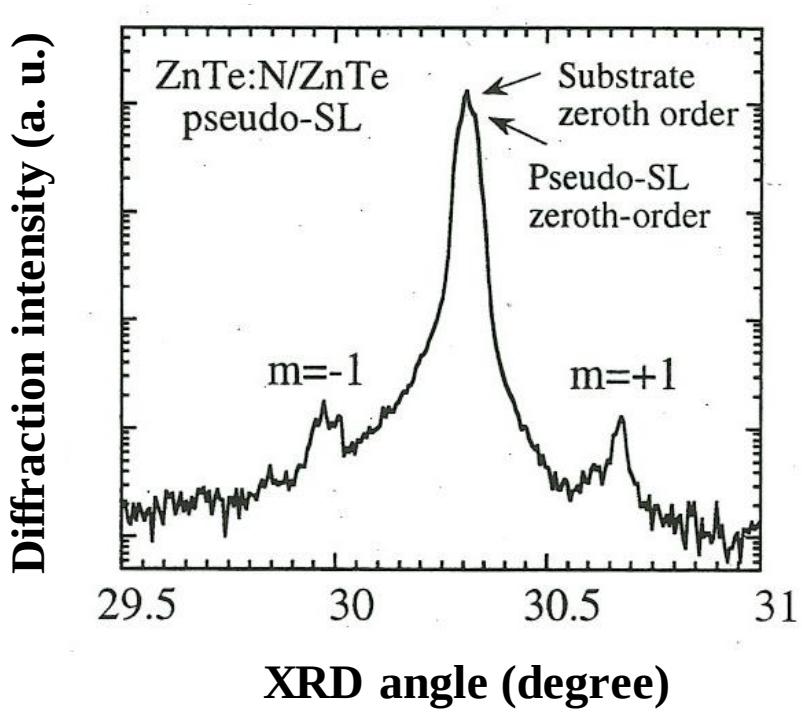

Figure 2.1.4: XRD rocking curves showing the Bragg angle (004) for a 59 period ZnTe:N/ZnTe pseudo-superlattice (SL). The two satellite peaks indicate the periodic structure of the pseudo-SL [45].

The XRD pattern of the superlattice (SL) for the (004) reflection is found to be sensitive to the lattice parameter changes as seen from the Fig. 2.2.4. A 59 period pseudo-SL where each period includes 25ML from both undoped ZnTe and ZnTe:N was grown on ZnTe (001) substrate. The zeroth order lines from the substrate and the pseudo-SL are clearly discernible. The main distinguishable feature that confirmed the presence of two epitaxial layers with different lattice parameters is two satellite peaks (m = ± 1).

Fig. 2.1.5 shows the optical spectroscopy of ZnTe:N layer at low temperature which is an essential tool to characterize dopants in the epitaxially grown layer by MBE. The Pl spectra of Undoped Zn Te layer has the dominant *A °X* line (exciton bound to a residual neutral acceptor), While that of the N-doped ZnTe contains the *D °A °* (neutral donor-acceptor pair recombination) or the *e A °* (conduction band electron-neutral acceptor recombination) emissions. Depending on the excitation power and the sample temperature, these *D °A °* and *e A °*

bands provides the ionization energy of the acceptor. In this study, the binding energy of N for the ZnTe:N layer was found to be 53.7 ± 0.7 meV. The reflectivity measurements of the ZnTe:N (≈ 3000 Å) layer grown by homoepitaxy on ZnTe (001) substrate for N concentrations of 2×10^{18} cm^{-3} clearly show the splitting of the light and heavy hole exciton lines. These are represented by E_{1h} (light exciton) and E_{hh} (heavy exciton) in the reflectivity spectra of ZnTe:N as shown in Fig. 2.2.5. These splitting suggests the presence of compressive strain in the layer. The ZnTe (001) substrate spectra is inverted after the growing of ZnTe:N layer.

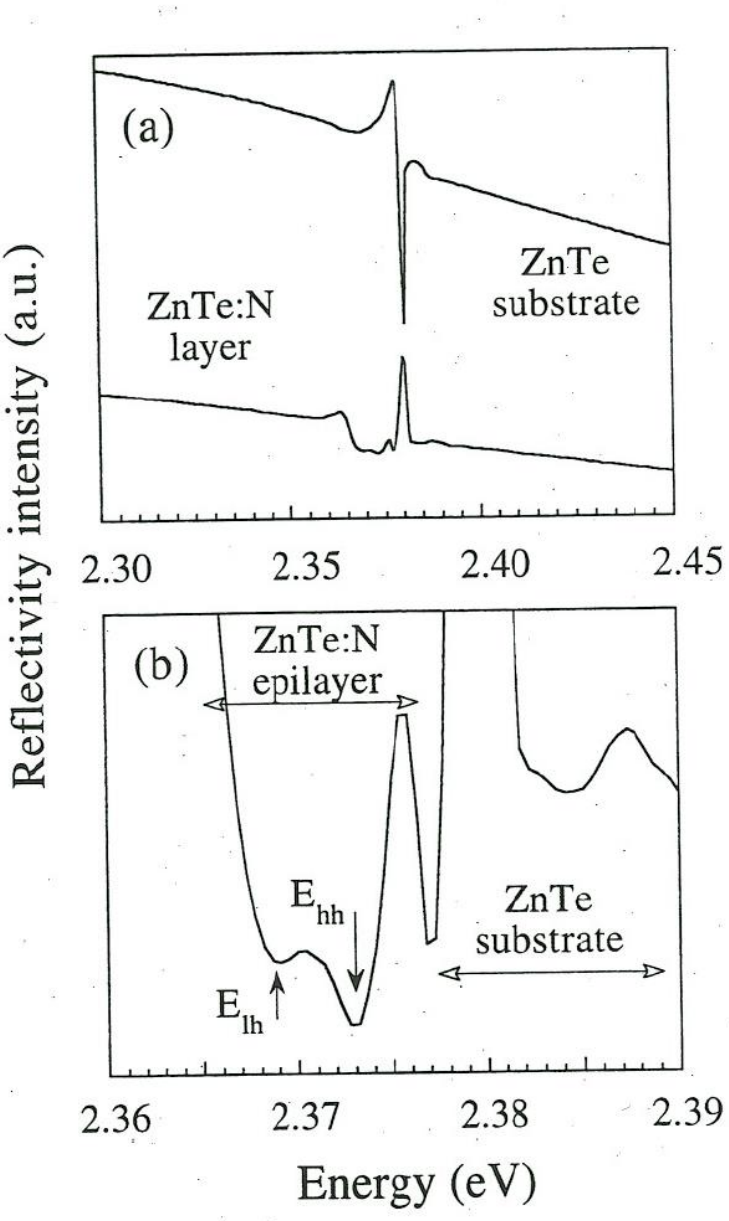

Figure 2.1.5: (a) Reflectivity spectra of ZnTe (001) substrate and ZnTe:N homoepitaxial grown layer at 1.8 K. **(b)** Clear indication of the presence of light exciton (E_{1h}) and heavy exciton (E_{hh}) in the ZnTe:N homoepitaxial grown layer [45].

The electrical properties of a N-doped ZnTe layer grown at substrate temperature of 275°C as a function of temperature is shown in Fig. 2.2.6. It is observed that the hole concentration and mobility has influenced very little with the variation of temperature. This gives the clue that the transport is accomplished by the formation of impurity band due to the overlapping of impurity wavefunctions. For N concentration of the order of 10^{19} cm^{-3}, the atomic spacing between impurity atoms becomes of the order of Bohr radius for hydrogenic acceptor.

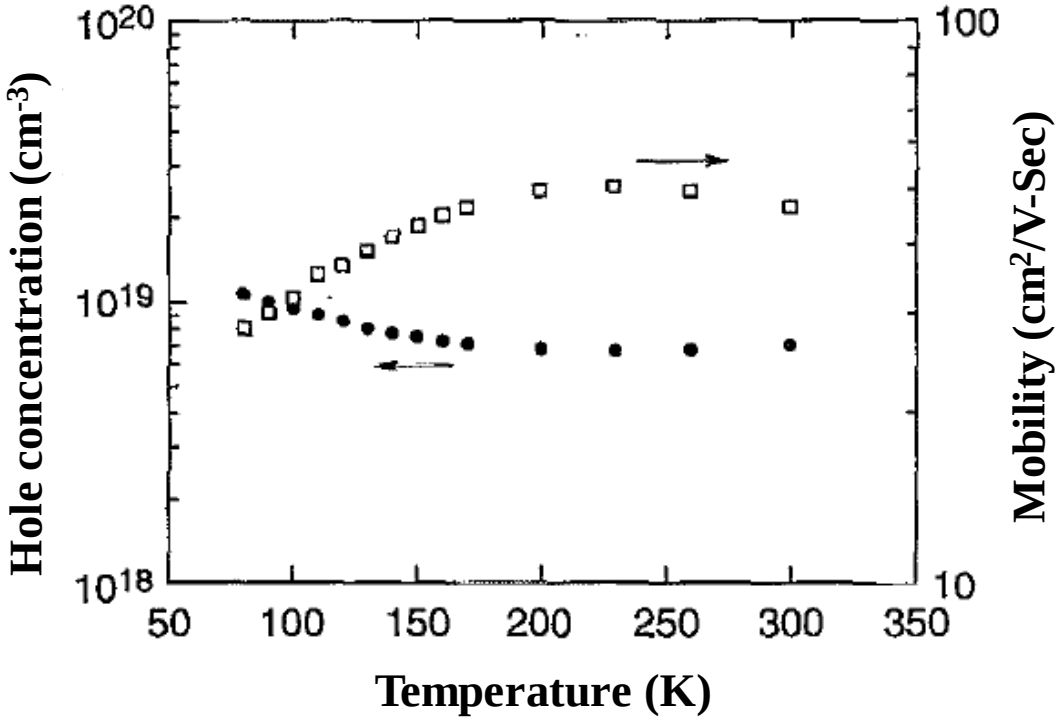

Figure 2.2.6: The hole concentration and mobility as a function of Temperature [46]

2.2 The physical properties of $Zn_{1-x}Fe_xTe$ DMS

2.2.1 Theoretical study for the electronic structure of Fe^{2+} in $Zn_{1-x}Fe_xTe$

The tetrahedrally coordinated transition metal (TM) doped II-VI DMSs has been the field of extensive research to the scientific community due to their excellent magnetic and magneto-optical properties [47]. The *sp-d* exchange interaction between the 3*d* electrons of TM impurity and the *sp* electrons of the host semiconductor has been the key factor in explaining various exciting phenomena in DMSs such as, large excitonic Zeeman effect, the associated Faraday and Voigt effects and the spin-flip Raman shifts of donor bound electrons [48, 49]. The thermal average of the magnetic moments of the TM impurities is maintained by macroscopic mechanisms such as crystal-

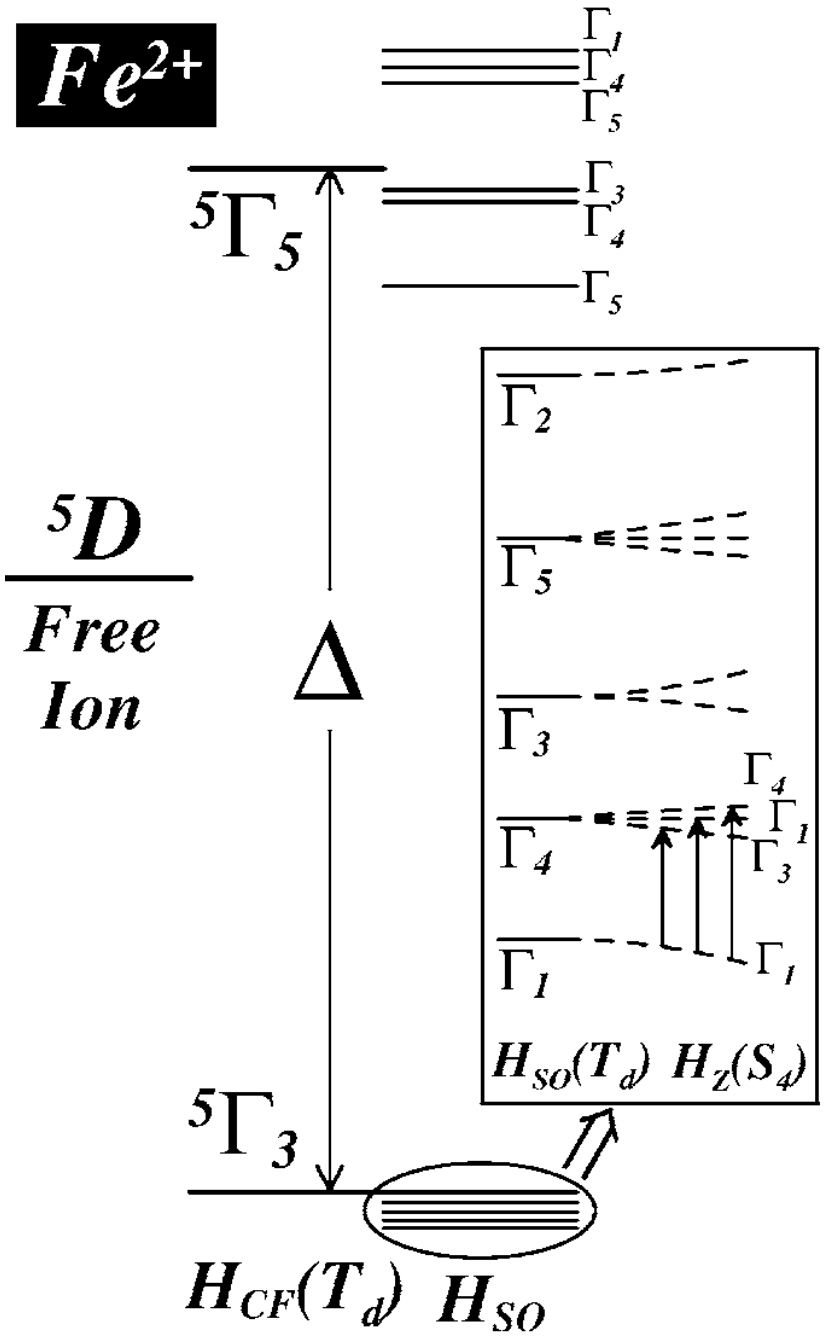

Figure 2.2.1: Energy levels of Fe^{2+} ion in tetrahedral crystal field, H_{CF} (T_d) under the effects of spin-orbit interaction (H_{SO}) and Zeeman (H_Z) splitting. The energy values for the Fe^{2+} were determined by numerical calculations [50].

field effect, spin-orbit interaction, static and dynamic Jahn-Teller effects, etc. Based on these mechanisms, various magnetic behavior has been proposed for different transition metal doped DMSs. For example, Mn^{2+} DMSs do not affect by the crystal field splitting and exhibit "atomic like" ground state, ${}^6S_{5/2}$ having effective spin of (5/2) $\hbar$. The associated magnetization shows $B_{5/2}$ Brillouin function behavior. On the other hand, Co^{2+} in CdTe

semiconductor compounds has a ground state of effective spin 3/2 due to the crystal field and spin-orbit effects. The case of Fe^{2+} is comparatively different from the above-mentioned cases. Fig. 2.2.1 explains the energy level splitting of Fe^{2+} ion in the presence of crystal field, spin-orbit interaction and external magnetic field. For Fe^{2+} ion, the ^5D (orbital angular momentum, L = 2, spin angular momentum, S = 2) ground states undergoes splitting into orbital doublet, $^5\Gamma_3$ and an orbital triplet, $^5\Gamma_5$ under the influence of the tetrahedral crystal field, H_{CF} (T_d). These two terms are separated by an energy gap, $\Delta = 4000$K. Spin-orbit interaction, $\mathcal{H}_{SO} = \lambda\, \mathbf{L}.\mathbf{S}$ gives the structure consisting of nonmagnetic singlet ground state, Γ_1 and several higher lying magnetic excites states which are separated by energy gap of the order of 20K from the ground state. At low temperatures, only the nonmagnetic ground state is occupied, providing no net magnetic moment. However, in the presence of external magnetic field **H,** the Zeeman interaction, $\mathcal{H}_Z = \mu_B \mathbf{B}.(\mathbf{L} + 2\mathbf{S})$ mixes the ground state, Γ_1 with the higher lying excited states to induce a magnetic moment in the direction of the externally applied magnetic field, **H**. This is known as van-Vleck paramagnetic behavior [50].

2.2.2 Theoretical study for the stability of ferromagnetic state and chemical trend in $Zn_{1-x}Fe_xTe$

In DMSs, it is well known that the TM ions are usually randomly substituted on the cation-site. Fig. 2.2.2 shows the theoretically calculated stabilized state for TM (V, Cr, Mn, Fe, Co and Ni) doped ZnTe semiconductor compound based DMSs [10]. In the Korringa-Kohn- Rostoker coherent potential approximation (KKR-CPA) method, the concept of disordered local moment (DLM) is normally used to describe paramagnetic state at finite temperature. On the basis of KKR-CPA method, the total energy difference between the between the DLM state and the ferromagnetic state is used to identify the stable magnetic states in these magnetic semiconductors. The positive energy difference reflects the stable state as ferromagnetic, While the negative value indicates the stable state as paramagnetic. As observed, for Mn-doped ZnTe, the spin-glass state (paramagnetic) is more stable, while for Cr and V doped ZnTe, the ferromagnetic state is more stable than the paramagnetic state. Lastly, for Fe, Co and Ni doped ZnTe, the ferromagnetic state becomes stable as the atomic number of the TM increases, but the paramagnetic state is still found to be stable in these cases.

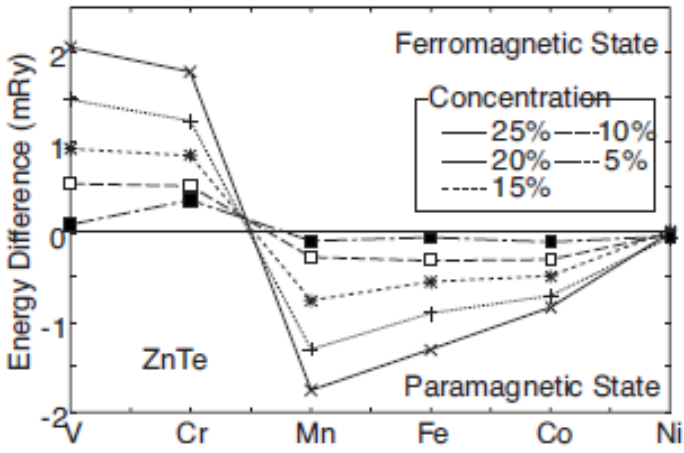

Figure 2.2.2: Calculated total energy difference between the spin-glass (paramagnetic) states and the ferromagnetic states for DMSs in ZnTe. Positive value means ferromagnetic state is stable [10].

In order to explain the magnetic structures in DMSs, the calculation of total spin polarized electron density of states (EDOS) is an important tool. Fig. 2.2.3 shows the EDOS for the model samples of TM doped ZnTe semiconductor compound based DMSs for TM composition of 3.125% [51]. This shows significant difference in the calculated EDOS for different TM doped ZnTe DMSs. Remarkable spin polarized EDOS for one spin channel and zero EDOS for other spin channel has observed for V, Cr, Fe and Ni-doped ZnTe. However, for V and Cr, the Fermi level resides on the majority spin states, While for Fe and Ni, the Fermi level reside on the minority spin

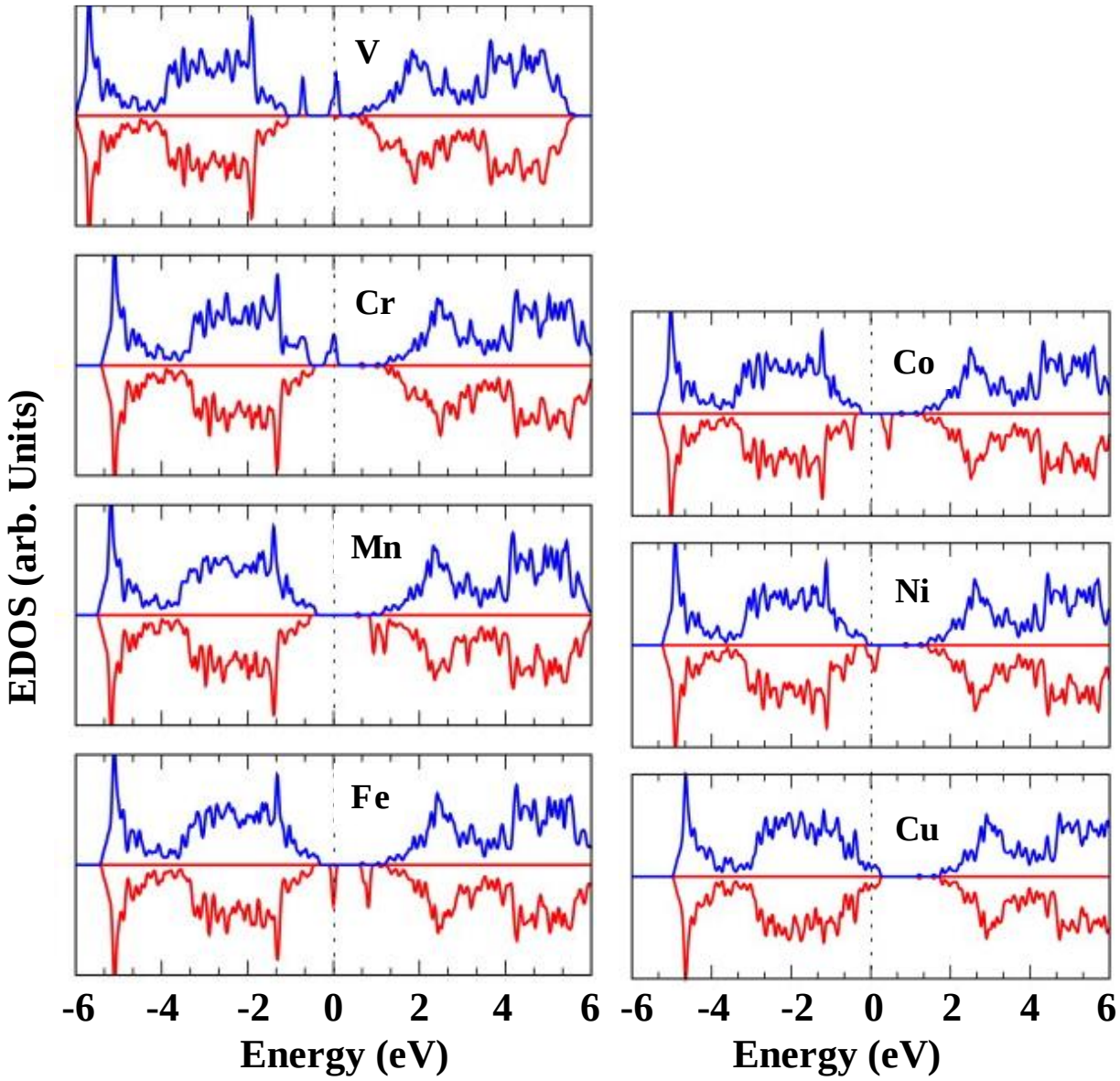

Figure 2.2.3: The electron density of states (EDOS) near the Fermi energy level of the model samples of ZnTe doped with different 3*d* TM impurities at cation sites. E = 0 eV corresponds to the Fermi energy level. Blue curves indicate spin-up EDOS and red curves indicate spin-down EDOS [51].

states. These mentioned TM doped ZnTe DMSs exhibit half metallic behavior with 100% spin polarization and are good candidates for Spintronics applications. On the other hand, Mn doped and Co doped ZnTe belong to the class of magnetic insulators as there is no spin polarized EDOS at the Fermi level and usually not a good candidate for Spintronics applications. However, Co doped ZnTe has spin polarized EDOS in the energy gap region of the host ZnTe matrix.

In the case of substitutional Mn^{2+} (having d^5 electronic configuration) on the Zn-site in ZnTe, it is suggested that the anti-ferromagnetic super-exchange interaction between the Mn^{2+} ions stabilize the spin-glass state. However, in the case of other substitutional TM impurities on the Zn-site in ZnTe such as, V^{2+}, Cr^{2+}, Fe^{2+}, Co^{2+} and Ni^{2+} having electronic configurations of d^3, d^4, d^6, d^7 and d^8 respectively, there are the spin polarized EDOS either in the Fermi energy level or in the energy gap region. That is, in such cases, the 3*d* impurity band up-spin or down-spin sates are not fully filled. These partially filled 3*d*-orbitals of the TM is allowed to hop to the 3*d*-orbitals of the neighboring TM, if the neighboring TM ions have parallel magnetic moments. As a consequence, the *d*-electrons lower its kinetic energy by hopping in the ferromagnetic state. This exchange mechanism is known as double exchange. This type of energy gain is not possible if the neighboring TMs have anti-parallel magnetic moments [10].

2.2.3 Experimental report on Fe doped II-VI DMSs

In this section, we have presented the experimental result about the magnetic properties of (Zn,Fe)Se bulk crystal prepared by modified Bridgman method under pressure of a neutral gas. The cubic crystalline structure for (Zn,Fe)Se was confirmed by X-ray diffraction analysis [52]. The Magnetization results of (Zn,Fe)Se with Fe composition of 13% measure at temperatures in the range 2-50 K has exhibited van-Vleck paramagnetic behaviour as shown in Fig. 2.3.1. As we have mentioned in section 2.2.1, the ground state of Fe^{2+} ion having spectroscopic notation, ^5D (L = 2, S = 2) is split by tetrahedral crystal field into two levels, orbital doublet and orbital triplet. These states are further split by spin-orbit interaction to yield a magnetically inactive singlet ground state. At lower temperature, only the ground state is occupied, so there is no net magnetic associated with Fe^{2+} ion. In the presence of external magnetic field, the ground state mixes with the higher lying excited energy states to induce magnetic moments in the direction of the applied magnetic field which is generally termed as van-Vleck paramagnetic behaviour.

The magnetization of (Zn,Fe)Se crystal was basically independent of temperature until 6K, but after that decreased monotonically with temperature. Similar behaviour was also observed in Eu^{3+} compounds. The magnetic element Eu^{3+} has six 4*f* electrons. The total orbital angular momentum, L = 3 and total spin angular momentum, S = 3. Hence, the total angular momentum, $J = |L - S| = 0$. For Eu^{3+} compounds, the energy difference between the ground state and the first excited state is not so large as compared to the thermal energy, so the unique temperature-independent susceptibility, typical of van-Vleck paramagnetic behaviour was observed at low temperatures. So, the observed independency of (Zn,Fe)Se magnetization on temperature at lower temperature region up to 6K was discussed on the same principle.

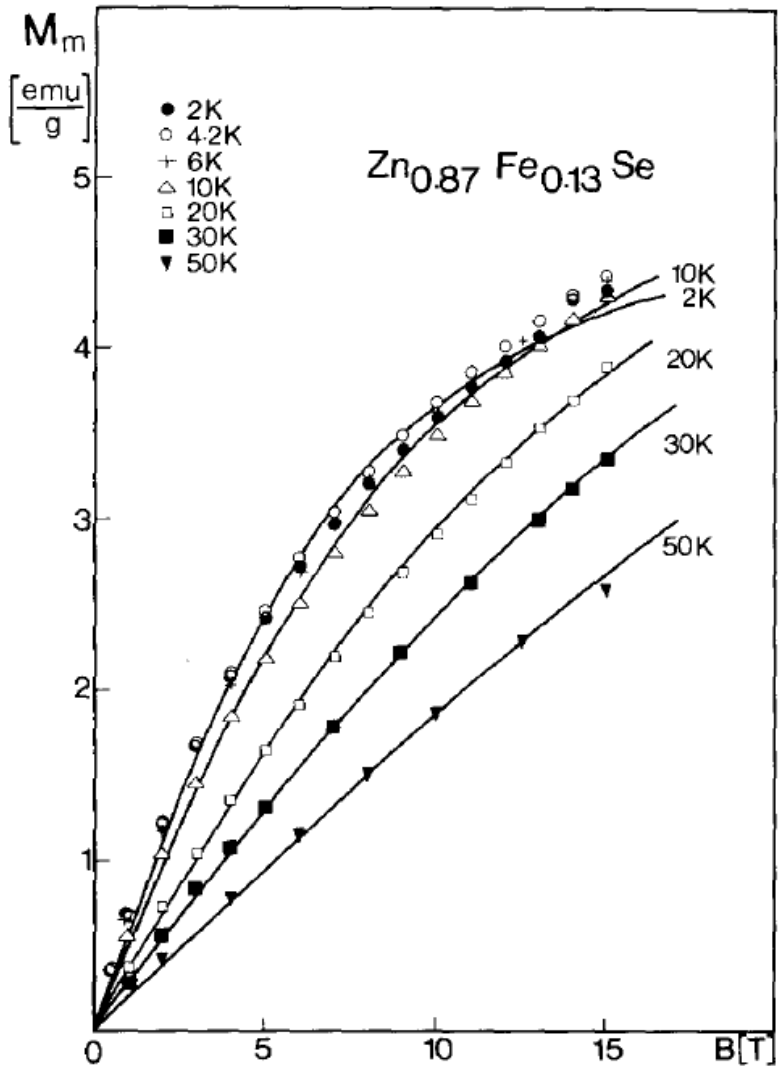

Figure 2.2.4: Magnetization characteristic of the $Zn_{0.87}Fe_{0.13}Se$ bulk crystal [52]

2.2.4 Experimental report on $Zn_{1-x}Fe_xTe$ bulk crystal

Figure 2.2.5 shows the magnetization curves for (Zn,Fe)Te bulk crystals prepared by modified Bridgman method with Fe contents of 0.875 and 1.16% [53] . The open and close circles have represented the experimental values of magnetization for Fe composition of 0.875 and 1.16 %. The magnetization was measured at 1.8 K by using SQUID magnetometer. The dash lines have indicated the calculated values of magnetization for the respective Fe compositions determined by X-ray fluorescence, while the solid lines have shown the best fitting with the experimental measured values. Thus, these results have confirmed that the magnetization of (Zn,Fe)Te bulk crystal with very low Fe composition is Paramagnetic.

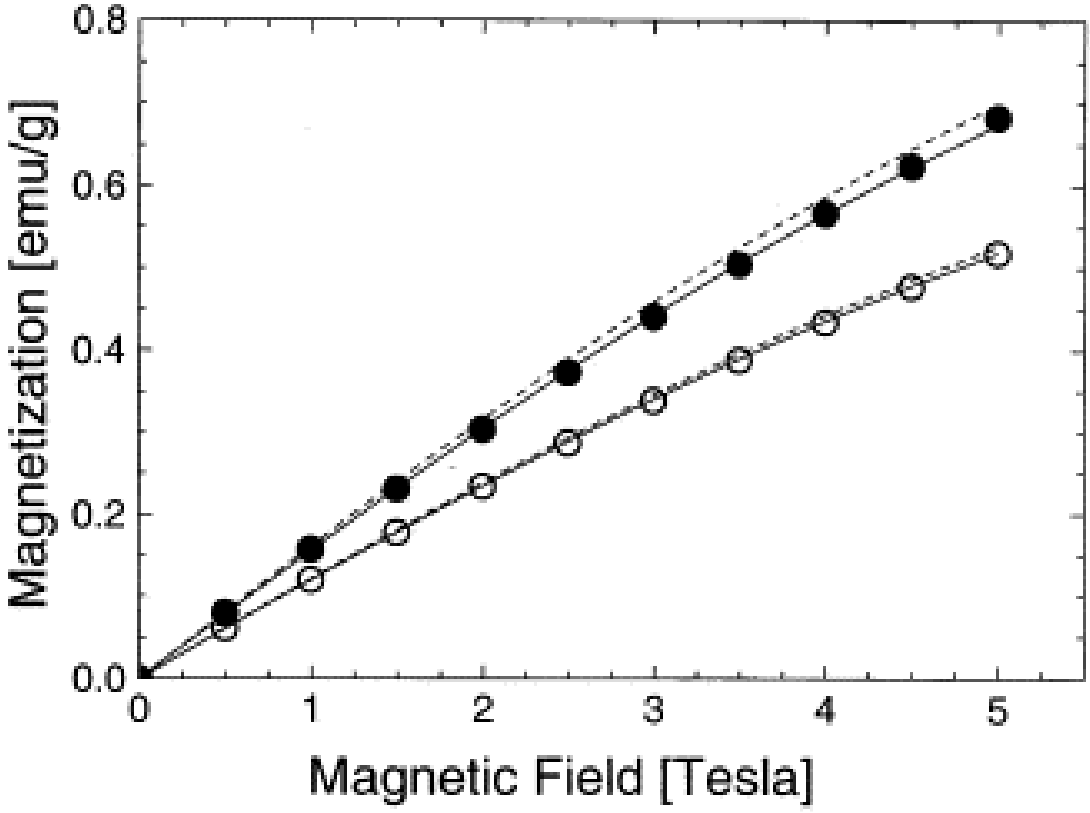

Figure 2.2.5: Magnetization curves (Zn,Fe)Te bulk crystals with Fe compositions 0.875% (open circle) and 1.21% (close circle) measured by SQUID at 1.8 K. Dashed lines: Calculated magnetization for the mentioned Fe compositions using X-ray fluorescence. Solid lines: Best fitting to the experimental results [53].

2.2.5 Previous research on $Zn_{1-x}Fe_xTe$ thin films grown by molecular beam epitaxy (MBE)

$Zn_{1-x}Fe_xTe$ thin films grown under Te-rich condition

The structural and magnetic properties of $Zn_{1-x}Fe_xTe$ thin films with Fe composition in the range, $0 < x \leq 20\%$ has been studied by previous members of our laboratory [32]. In this section, we have presented the experimental results based on the structural and magnetic properties of $Zn_{1-x}Fe_xTe$ thin films grown in excess of Te flux over Zn flux. The $Zn_{1-x}Fe_xTe$ films with thickness ~ 300 nm were grown on thick buffer layer of thickness (~600 nm) which in turn, was grown over GaAs (001) substrate. The structural analysis by X-ray diffraction (XRD) analysis has revealed that film with Fe composition, $x < 2\%$ was composed of pure diluted phase of zinc-blende structure with diffraction peaks observed from ZnTe buffer layers and GaAs substrate as shown in Fig. 2.2.6. However, films with Fe composition, $x > 2\%$ have included diffraction peaks from extrinsic precipitates such as, FeTe and $FeTe_2$ compounds of different phases. Theses extrinsic phases were confirmed from the available XRD data of these compounds in the inorganic database of (National Institute for Materials Science). With the increase of Fe composition, the diffraction peaks of the precipitated phases became more intense and some new phases appeared.

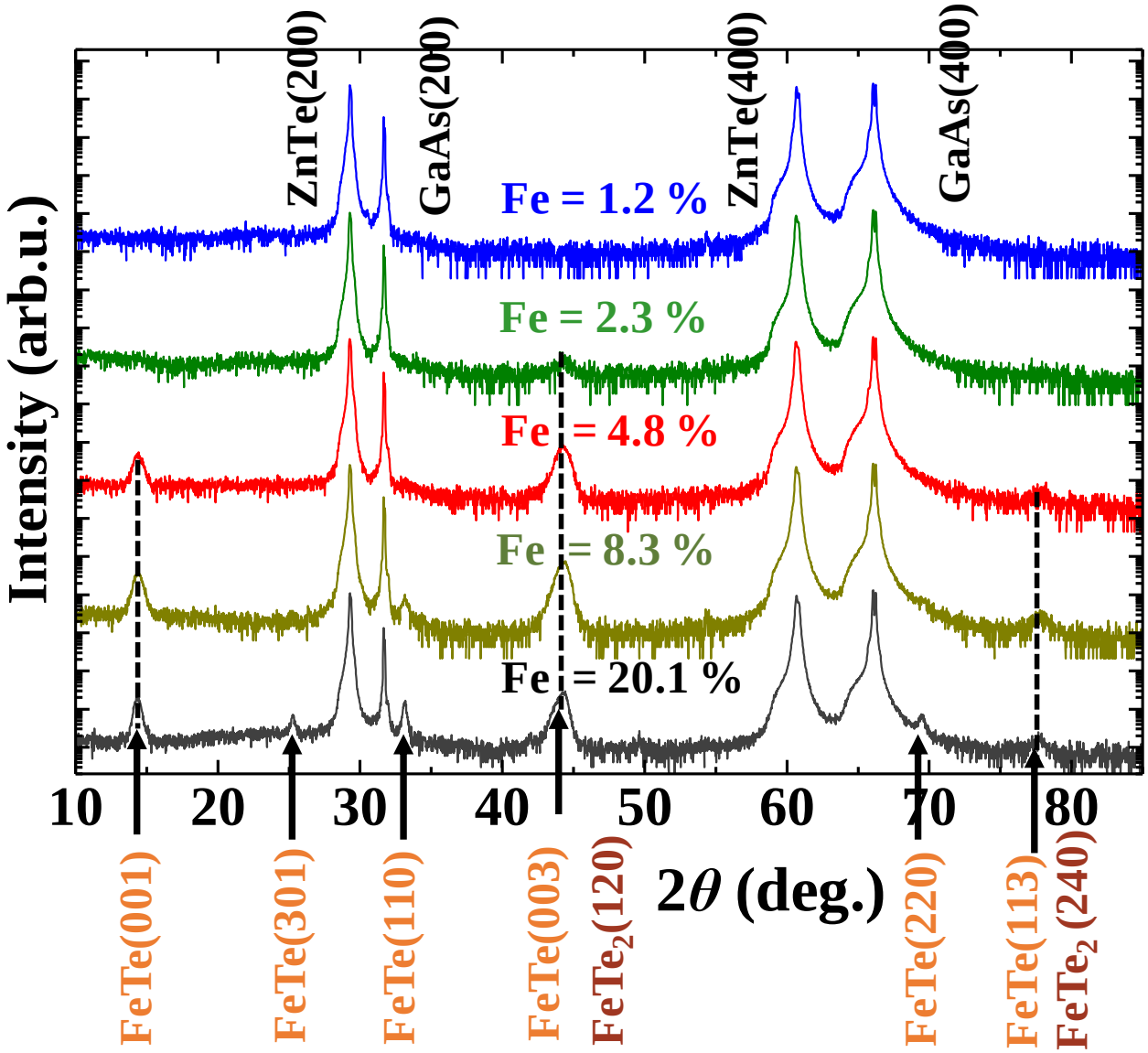

Figure 2.2.6: Results of XRD measurement for $Zn_{1-x}Fe_xTe$ thin films with different Fe compositions grown under Te-rich condition. Positions of extrinsic precipitates were identified by the arrows [32].

In order to identify the structural properties of the grown films on the atomic scale, X-ray absorption fine structure (XAFS) analysis was performed for the Fe-K absorption edge. Figure 2.2.7 shows the X-ray absorption near edge structure (XANES) spectra for the grown sample films. The XANES spectra for all the films consisted of the pre-edge peak (1*s* to 3*d* like transition), the shoulder peak and the main absorption peak (1*s* to 4*p* like transition). In the case of $Zn_{1-x}Fe_xTe$ thin films with Fe composition, x = (1-2) %, the pre-edge peak, shoulder peak and the main peak were clearly discerned at positions of 7.109 keV, 7.116 keV and 7.122 keV respectively. On the other hand, for higher composition films, the shape and positions of the absorption peaks were different. This discrepancy in the XANES spectra clarified the distinction between low Fe composition pure dilute phase films

from the externally precipitated films with high Fe composition. The Fourier transforms of the extended X-ray absorption fine structure (EXAFS) oscillations weighted by k^3 were also plotted to investigate the local environment around Fe atom. Similar to the XANES spectra, clear difference in the first nearest neighbour (1st NN) position of Fe between the films with lower and higher Fe composition was observed. In $Zn_{1-x}Fe_xTe$ thin films with Fe composition, x = (1-2) %, the 1st NN position was found at around 2.5 Å belonging to the bond with Te atoms, while in the higher Fe composition films, the position was different suggesting the incorporation of Fe in different sites or in some extrinsic phases.

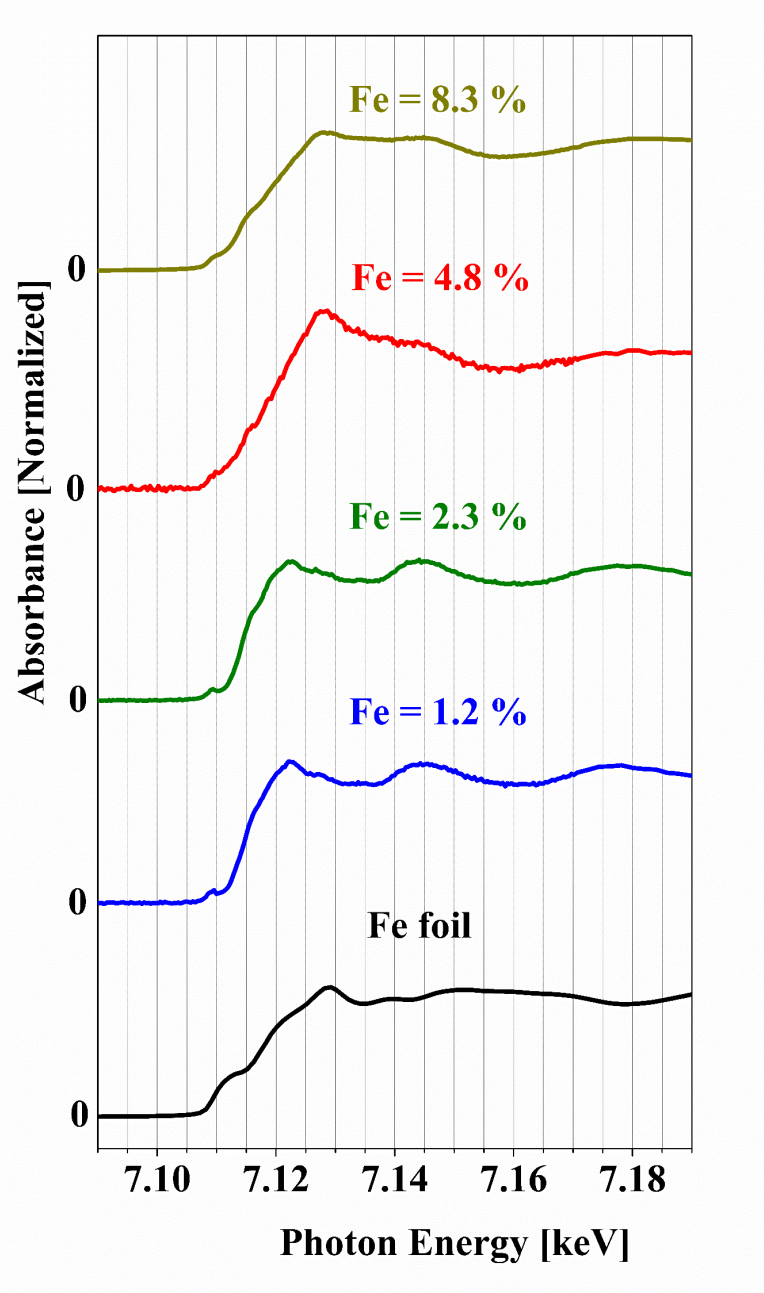

Figure 2.2.7: XANES spectra of $Zn_{1-x}Fe_xTe$ thin films with different Fe composition grown under Te-rich condition [32]

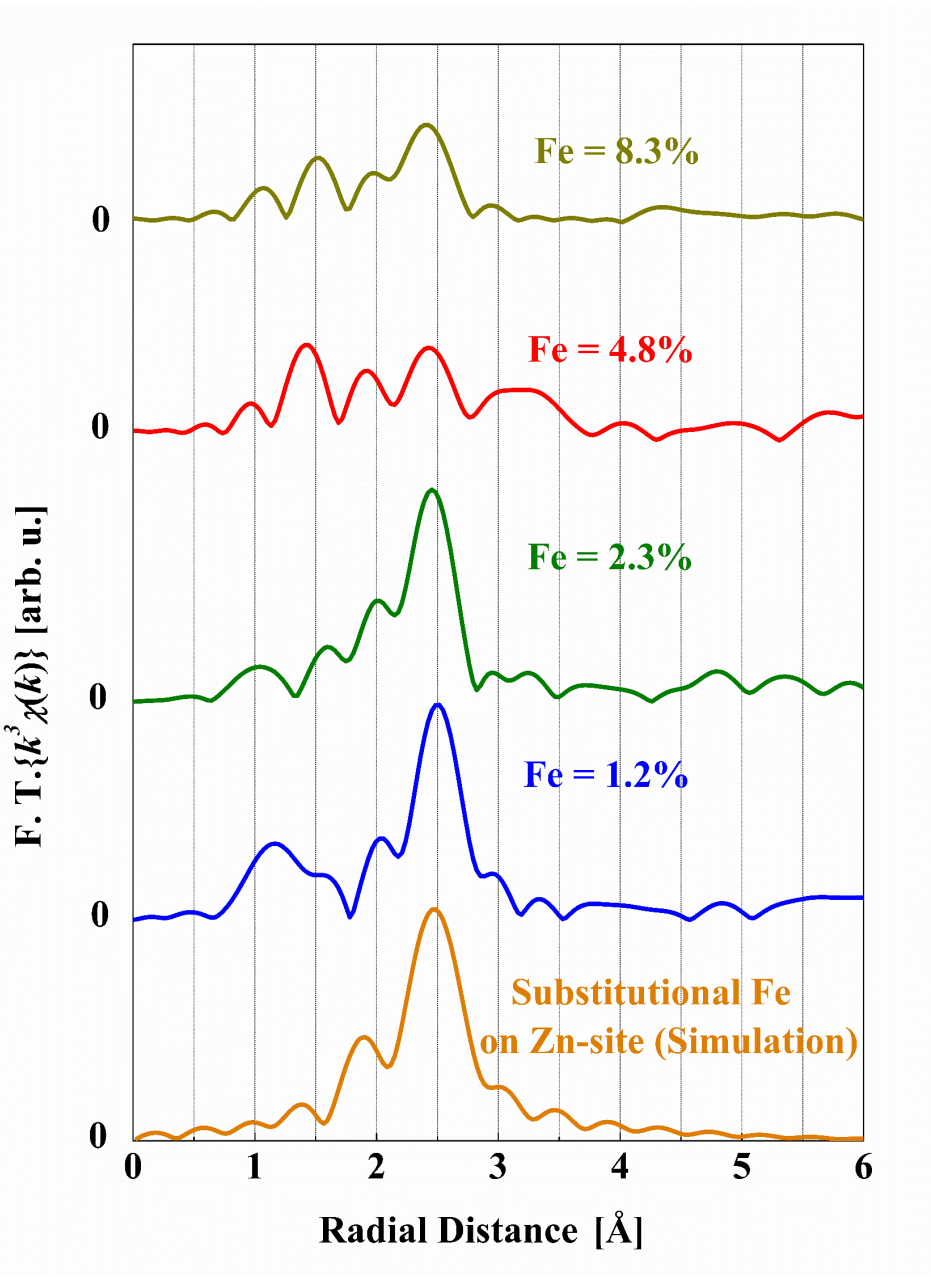

Figure 2.2.8: Radial distribution function (RDF) spectra of $Zn_{1-x}Fe_xTe$ thin films with different Fe composition grown under Te-rich condition [32]

In order to detect the precipitate that formed in the $Zn_{1-x}Fe_xTe$ thin films with Fe composition, x = 8.3%, transmission electron microscope (TEM) observation has been performed. Figure 2.2.9 shows the typical cross-sectional TEM images and the corresponding Fe mapping as obtained from the electron energy loss spectroscopy (EELS) data. In the cross-sectional TEM image, translational Moiré fringes extending in the growth direction of the film were observed. Accordingly, the distribution of Fe was also different in the regions where translational

Moiré fringes were formed. These observations suggested the formation of extrinsic precipitates of Fe-rich compounds having crystal structure different from the zinc-blende structure in the studied film.

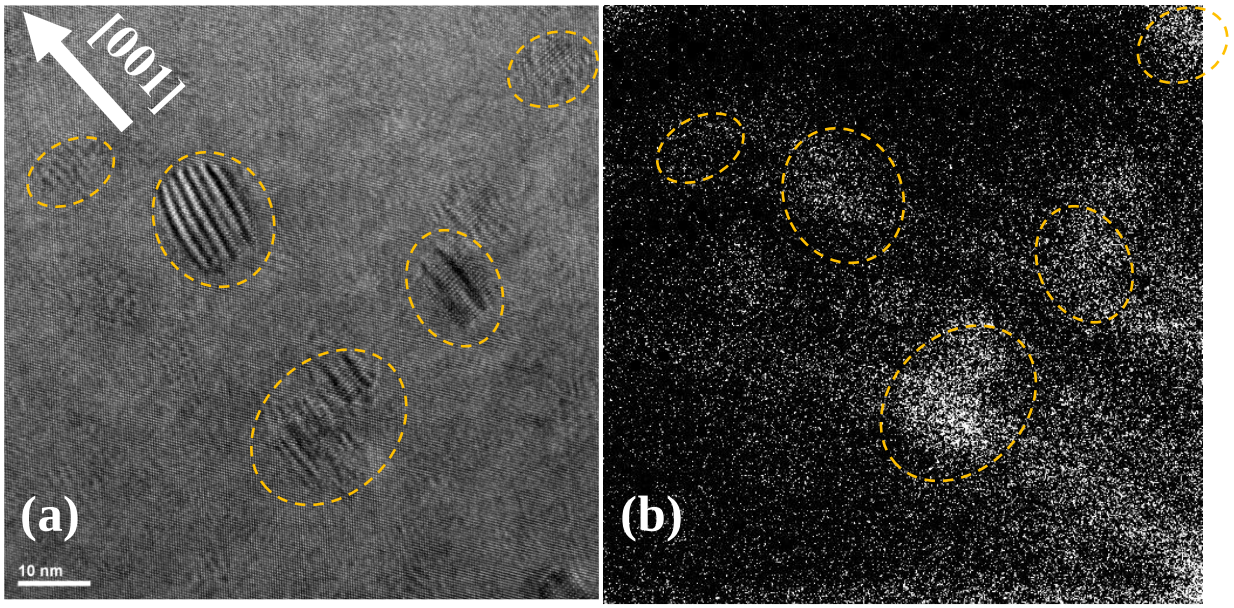

Figure 2.2.9: (**a)** Cross-sectional TEM image and **(b)** the corresponding Fe-mapping derived the EELS data for $Zn_{1-x}Fe_xTe$ thin film with Fe composition, x = 8.3%, grown under Te-rich condition [32]

Figure 2.2.10 shows the *M-H* curves for the grown $Zn_{1-x}Fe_xTe$ thin films measured at 2K by using superconducting quantum interference device (SQUID). The measurement was performed by applying external magnetic field perpendicular to the film plane. For Fe composition, $x \leq 8.3\%$, the $Zn_{1-x}Fe_xTe$ films exhibited van-Vleck type paramagnetic behaviour. But, the magnetic moment per Fe atom decreased sharply with the increase of Fe composition from 2.3% to 8.3%. The origin of this decrease in magnetization was due to the presence of FeTe and $FeTe_2$ extrinsic precipitates having crystal structures of tetragonal and orthorhombic phases respectively which were already detected by the XRD analysis. The bulk crystal of these precipitates has antiferromagnetic behaviour. However, ferromagnetic hysteresis curve was observed for the film with Fe composition, x = 20.1 % which was mentioned to be originated from other ferromagnetic precipitate compounds. The possible precipitate may be α-Fe, but the presence of such diffraction peak was not detected from the XRD measurement.

From these experimental results, it has been concluded that $Zn_{1-x}Fe_xTe$ thin films with Fe composition, $x \leq 2\%$, are composed of pure dilute phase of zinc-blende structure and the intrinsic magnetism is van-Vleck type paramagnetic. However, $Zn_{1-x}Fe_xTe$ thin films with Fe composition $x \geq 2\%$, Fe deviates from the substitutional site on the Zn-site and incorporates at different site or in the formation of antiferromagnetic FeTe, $FeTe_2$ or other ferromagnetic extrinsic precipitates [32].

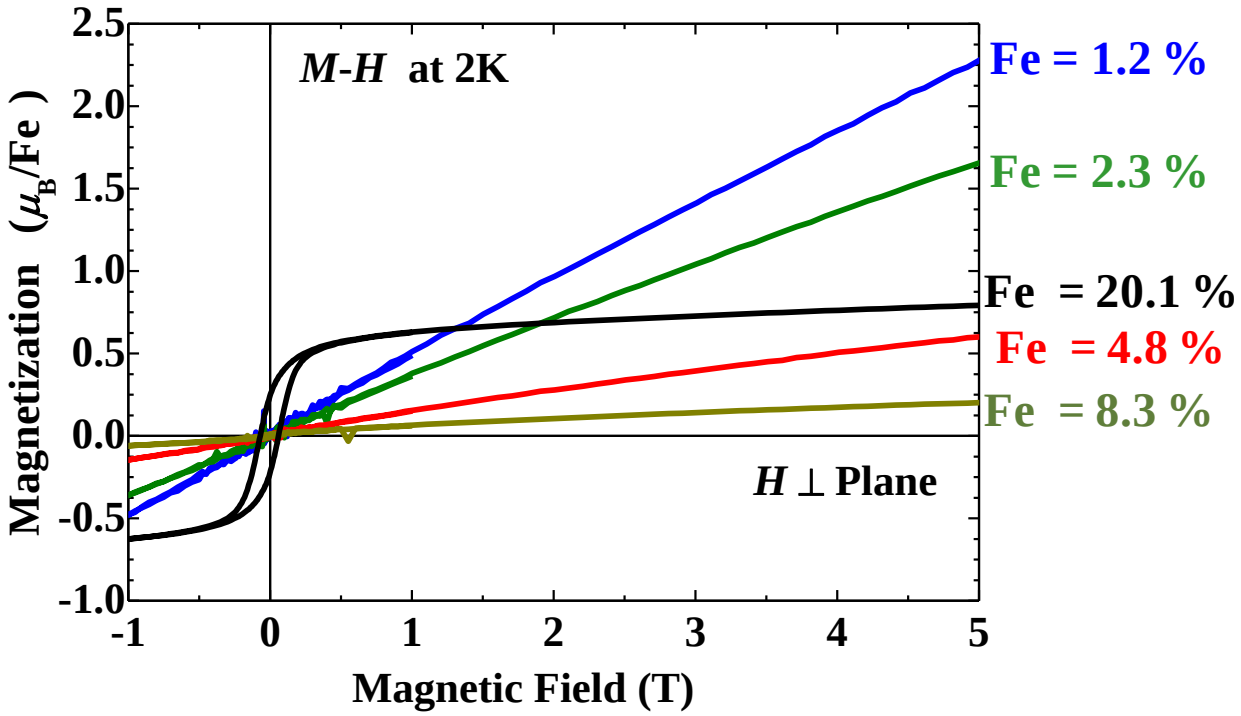

Figure 2.2.10: *M-H* curves for $Zn_{1-x}Fe_xTe$ thin films with different Fe composition grown under Te-rich condition [32]

$Zn_{1-x}Fe_xTe$ thin films grown under Zn-rich condition

In this section, the structural and magnetic characterizations of $Zn_{1-x}Fe_xTe$ thin films grown under Zn-rich flux condition has been explained [33]. The Fe composition of the films was varied in the range $0 < x \leq 25\%$. $Zn_{1-x}Fe_xTe$ layer was grown on the GaAs wafer (001) by depositing a thick ZnTe buffer layer in between the magnetic layer and the wafer to reduce the lattice mismatch. The structural analysis of the grown films was accomplished by XRD analysis. Figure 2.2.11 has shown the results of XRD measurements for the films with different Fe compositions. The XRD results have confirmed the absence of extrinsic precipitates in the studied films; diffraction peaks were detected only from the ZnTe buffer layer and the GaAs substrate.

In order to further analyze the structural properties on the atomic scale, X-ray absorption fine structure (XAFS) analysis at the Fe-K absorption edge was performed for the $Zn_{1-x}Fe_xTe$ thin films with different Fe compositions. Figure 2.2.12 has presented the X-ray absorption near edge structure (XANES) spectra of the films along with that of the elemental Fe foil as reference. For Fe composition, $x = 1.5\%$ film, the pre-edge peak, shoulder peak and the main absorption peak of the XANES spectrum was found at positions 7.109 keV, 7.116 keV and 7.123 keV respectively. However, with the increase of the Fe composition, the shape of the pre-edge and position of the main absorption peak changed. In the case of $Zn_{1-x}Fe_xTe$ thin film with Fe composition, $x = 2.9\%$, the positions of the three absorption peaks remained same. But with further increase of Fe composition, the change in the position of

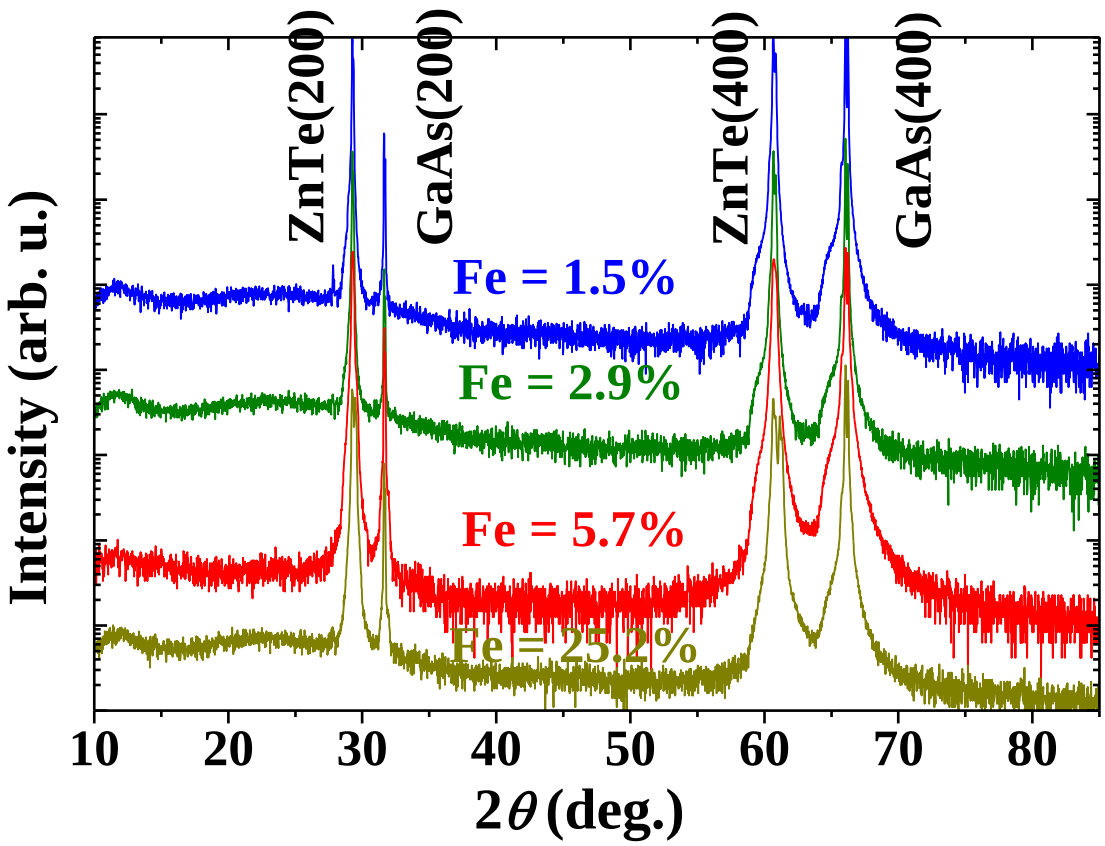

Figure 2.2.11: Results of XRD measurement for $Zn_{1-x}Fe_xTe$ thin films with different Fe compositions grown under Zn-rich condition [33].

the main absorption was significant. This change in the position of the main absorption peak in the higher Fe composition films has been regarded as the change in the atomic configuration and /or the electronic configuration of Fe. In order to investigate the local environment around the Fe atoms, the radial distribution function (RDF) derived from the Fourier transforms of the extended X-ray absorption fine structure (XANES) spectra weighted by k^3 were also shown for the studied films in Fig. 2.2.13. In addition, the simulation data foe Fe on the substitutional position on the Zn-site was also included in the plotting. In the simulation, it was considered that only one Fe atom substituting the Zn-site without bringing any change in the lattice constant of the host ZnTe host semiconductor compound and only single scattering path was taken into account. The RDF spectrum for the film with Fe composition, x = 1.5% resembled the simulation curve for the substitutional Fe on Zn-site showing the 1st nearest neighbour (1st NN) peak at around 2.5Å which is the bond length with Te atoms. However, with the increase of Fe composition, the 1st NN position shifted towards the shorter distance, suggesting the incorporation of Fe at different site or in the formation of extrinsic precipitates compounds.

Figure 2.2.14 shows the cross-sectional transmission electron micrograph (TEM) and the corresponding Fe mapping based on the electron energy loss spectroscopy (EELS) for the $Zn_{1-x}Fe_xTe$ thin film with Fe composition, x = 25.2%. In the cross-sectional TEM image, some small ring-shaped structural disorder regions were identified near the interface between the $Zn_{1-x}Fe_xTe$ layer and the ZnTe buffer layer shown in Fig. 2.2.14 (a). The corresponding Fourier fast transforms (FFT) pattern shown in the inset of Fig. 2.2.14 (a) confirmed the presence of superimposing zinc-blende hexagonal patterns with different orientations in these marked regions. Similarly,

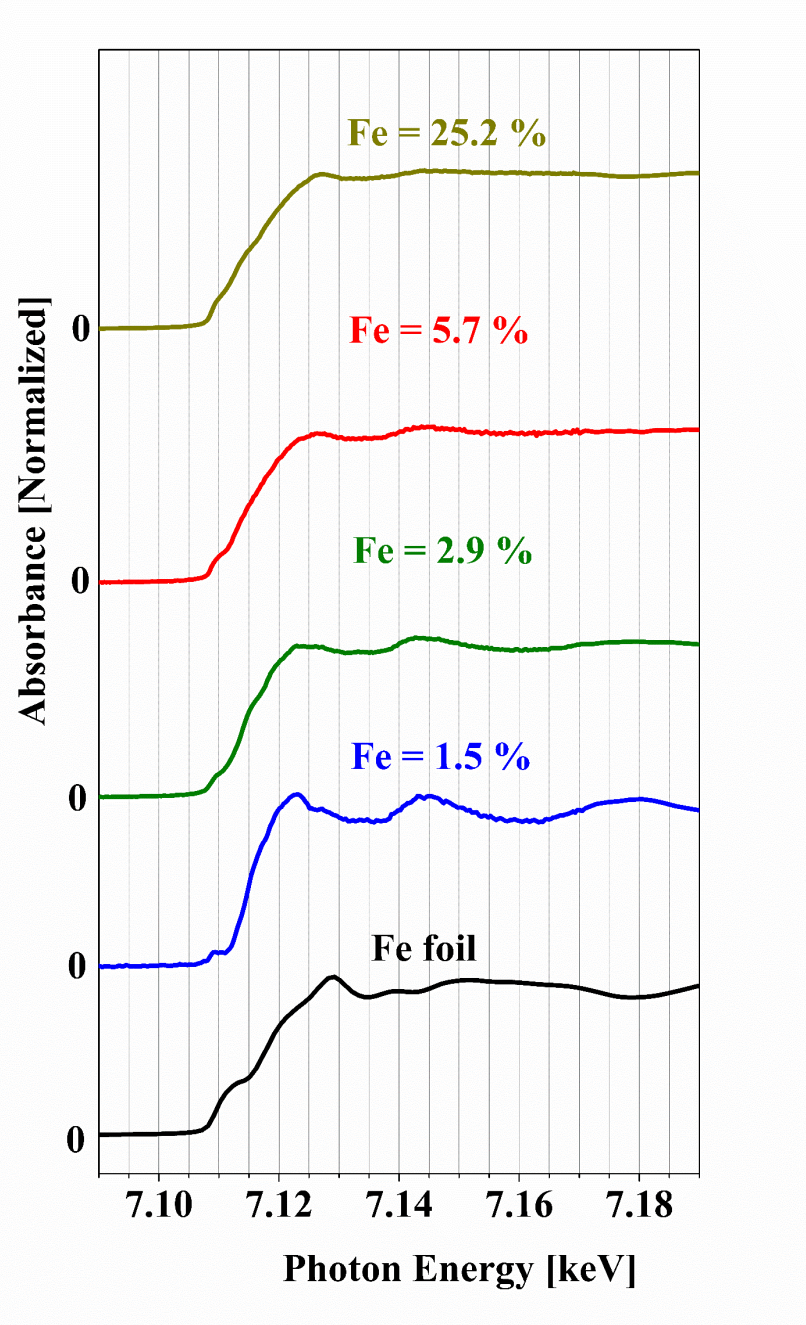

Figure 2.2.12: XANES spectra of $Zn_{1-x}Fe_xTe$ thin films with different Fe composition grown under Zn-rich condition [33]

the Fe-mapping of these respective regions as obtained from the EELS data showed the formation of ring-shaped Fe aggregation region as shown by the marked circular regions in Fig. 2.2.14 (b). From these observations, it has been concluded that, the Fe-rich regions having zinc-blende crystal structure have formed $Zn_{1-x}Fe_xTe$ thin film at high Fe composition.

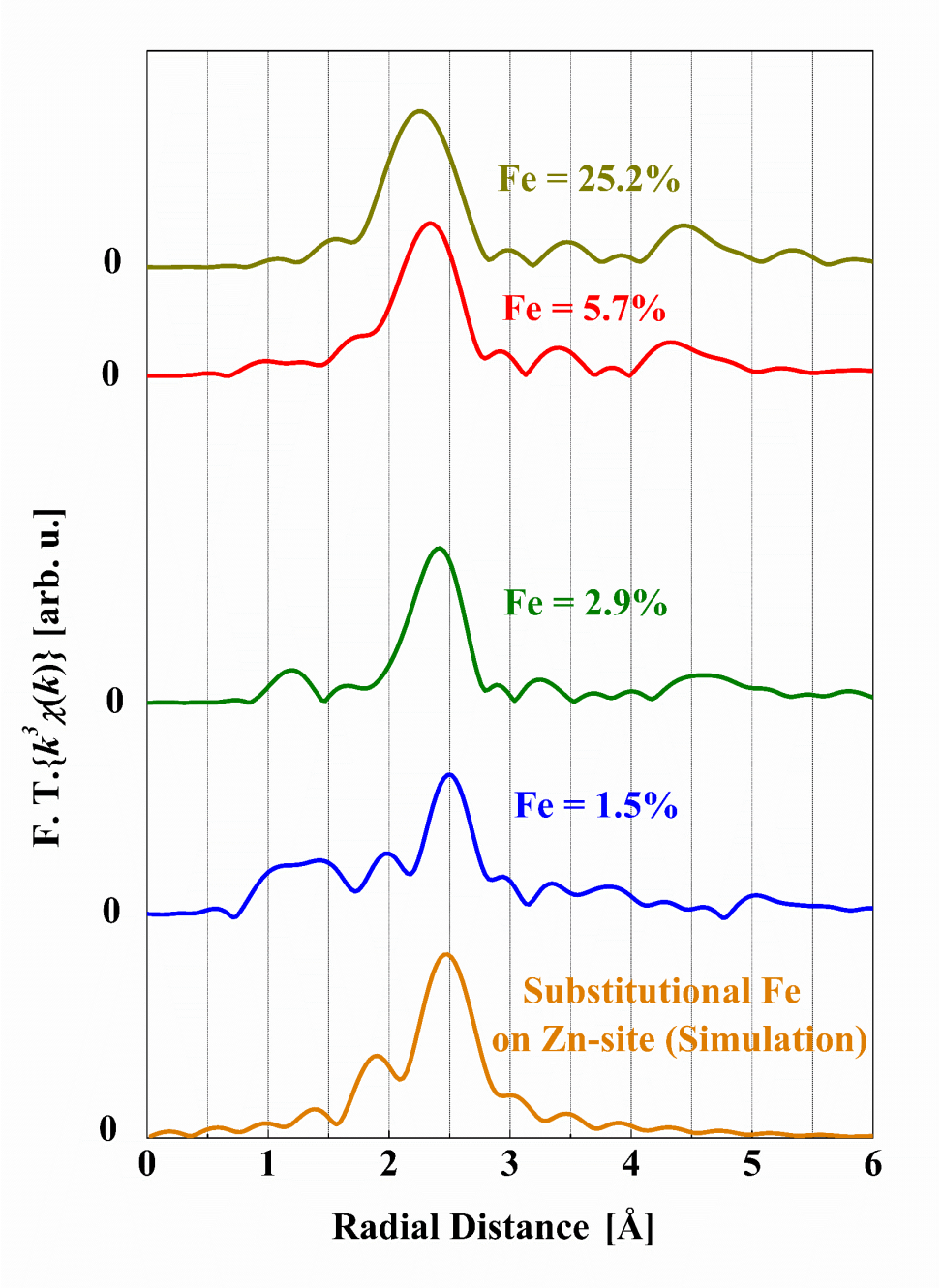

Figure 2.2.13: Radial distribution function (RDF) spectra of $Zn_{1-x}Fe_xTe$ thin films with different Fe composition grown under Zn-rich condition [33]

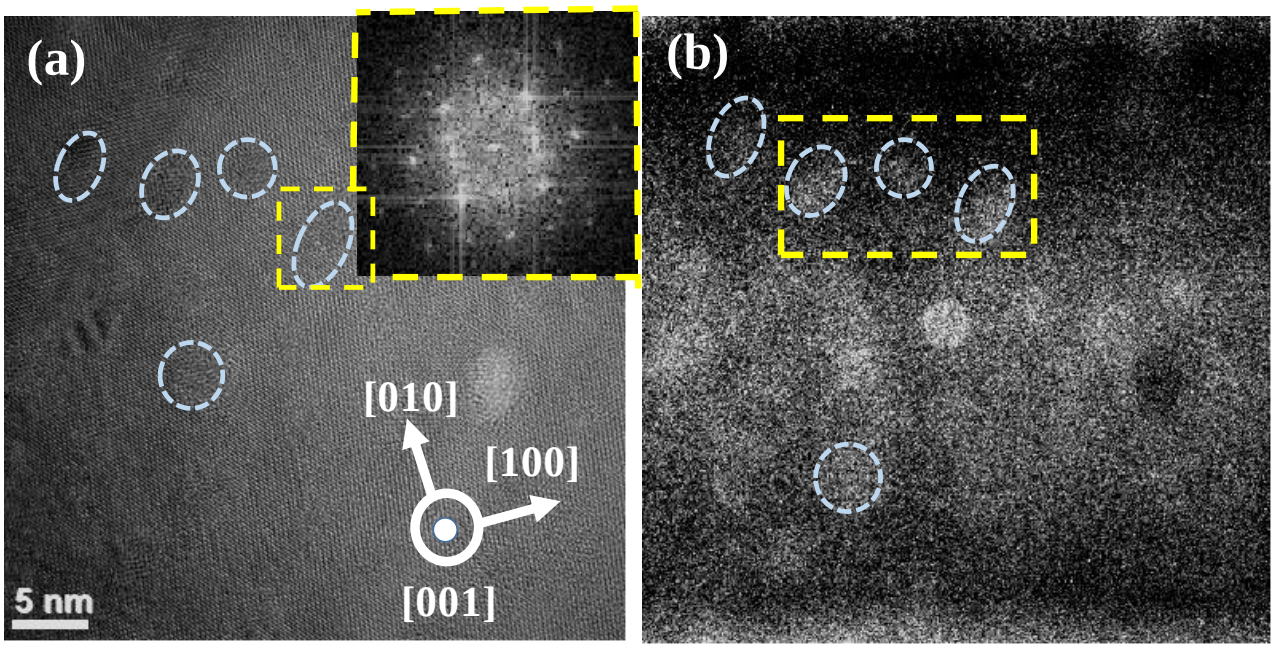

Figure 2.2.14: (**a)** Cross-sectional TEM image and **(b)** the corresponding Fe-mapping derived from the EELS data for $Zn_{1-x}Fe_xTe$ thin film with Fe composition, x = 25.2%, grown under Zn-rich condition [33].

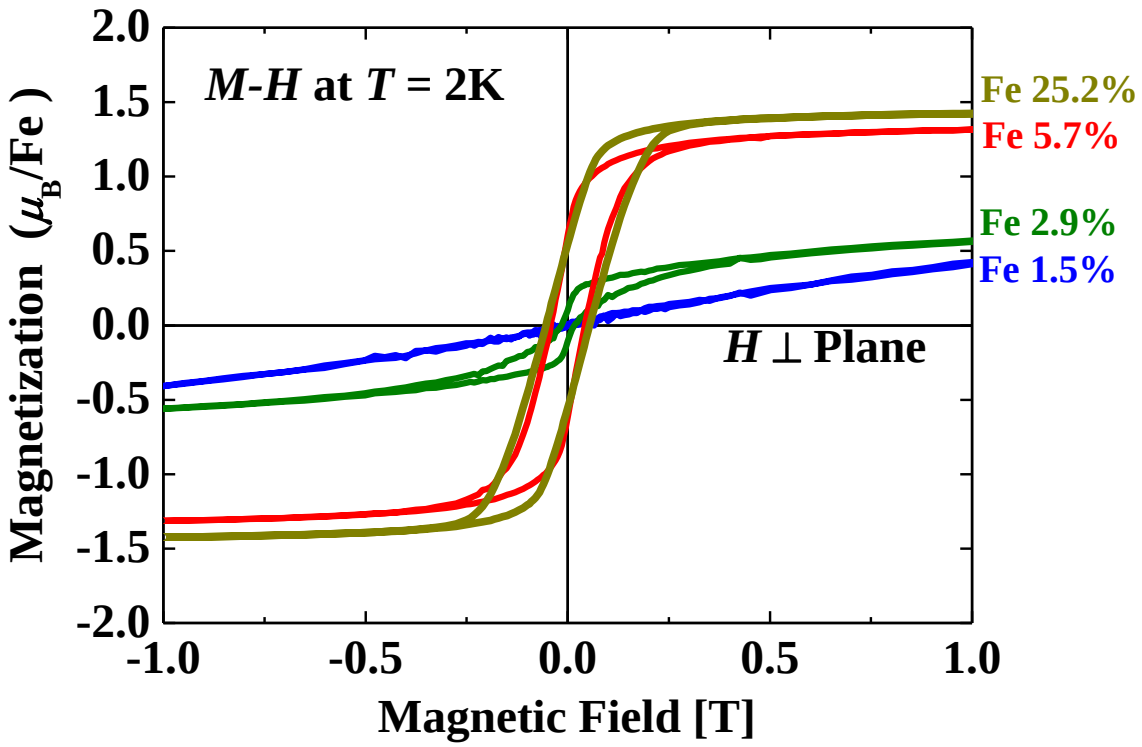

Figure 2.2.15: *M-H* curves for $Zn_{1-x}Fe_xTe$ thin films with different Fe composition grown under Zn-rich condition [33].

Figure 2.2.15 shows the *M-H* curves for the $Zn_{1-x}Fe_xTe$ thin films with different Fe compositions grown under Zn-rich condition. The magnetization was measured at 2K by applying external magnetic field perpendicular to the film plane. The $Zn_{1-x}Fe_xTe$ thin film with Fe composition, x = 1.5% has shown linear dependence of the magnetization on magnetic field, van-Vleck type paramagnetic behaviour. However, with the increase of Fe composition, the *M-H* curves have exhibited ferromagnetic behaviour with enlarged coercivity of the hysteresis curve and saturation magnetization. The magnetization dependence on temperature curves for the grown films are also demonstrated in Fig. 2.2.16. The magnetization under zero field cooled (ZFC) and field cooled (FC) processes have shown monotonic increase with the decrease of temperature in the case of the $Zn_{1-x}Fe_xTe$ thin film with Fe composition, x = 1.5%. On the other hand, for higher Fe composition films, the cusp-like behaviour of the ZFC curve explaining blocking phenomena has been observed. This blocking phenomena, characteristic of superparamagnetic behaviour usually originates from the formation of Fe clusters not responding to the overall magnetization at low temperature due to magnetic anisotropy. It was mentioned that the ferromagnetic behaviours observed in the films with Fe composition could be associated with the same blocking phenomena.

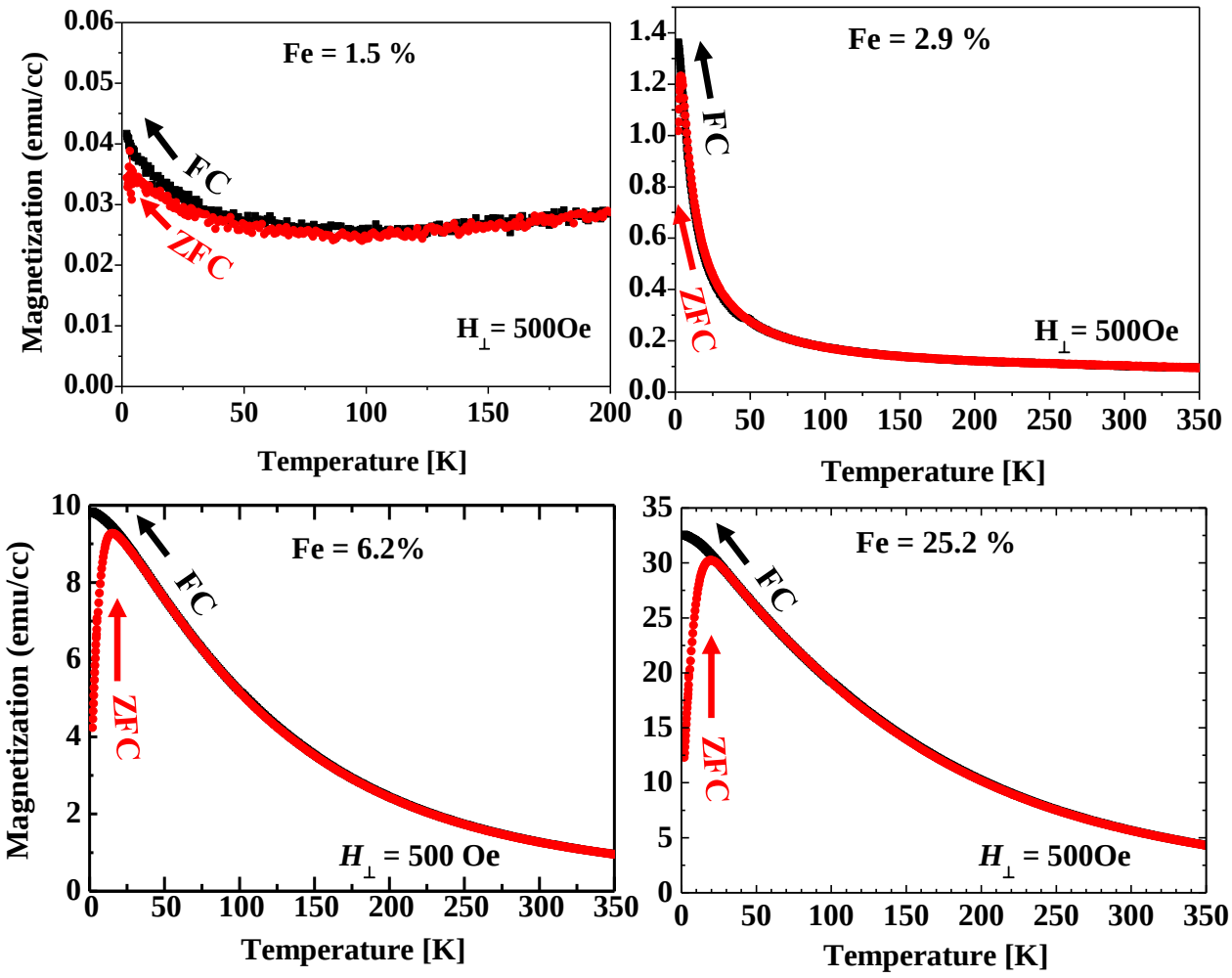

Figure 2.2.16: *M-T* curves for $Zn_{1-x}Fe_xTe$ thin films with different Fe composition grown under Zn-rich condition [33].

From these results, it can be concluded that $Zn_{1-x}Fe_xTe$ thin film with Fe composition, x = 1.5% has been composed of pure dilute phase of zinc-blende structure and exhibited van-Vleck paramagnetic behaviour. However, for higher Fe composition films, depending on the present experimental observations, it can be said that the observed hysteresis *M-H* curves and the blocking phenomena of *M-T* curves attributed to the supermagnetic behaviours have originated from the aggregation of Fe ions or the formation of extrinsic precipitate compounds.

2.3 Theoretical study for co-doping of donor/acceptor impurities in DMSs

In semiconductors, the chemical potential of an electron can be changed from the valence band maximum (VBM) to conduction band minimum (CBM) by acceptor or donor doping [54, 55]. So, it is expected to observe DMSs consisting of TM impurity with multiple charge change by co-doping with additional external charge doping. The microscopic origin of the multiple charge states in DMSs is the strong intra-atomic Coulomb repulsion (*U*) of the 3*d* -TM impurity and the strong *p-d* hybridization between the 3*d* electrons of TM impurity atoms with the *sp* valence electrons of the host semiconductor as explained by the Haldane and Anderson using the Anderson model. Later, the *ab*-initio calculations performed by Katayama-Yoshida and Zunger and others have confirmed the presence of multiple charge states. The Coulomb interaction for an isolated TM impurity atom can be calculated as:

$$U_0 = E\,(N+1) + E\,(N-1) - 2E\,(N) \qquad (1)$$

Where, *E* (N) is the total energy of the *N*-electron system. This Coulomb interaction is usually of 20 eV in magnitude.

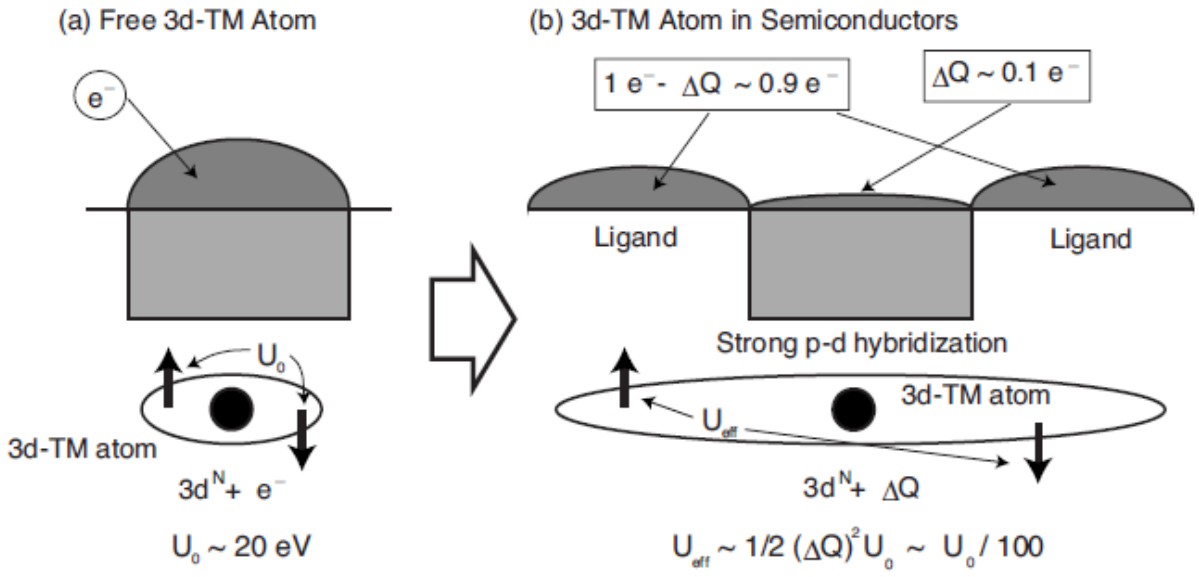

Figure 2.3.1: Schematic representation of the microscopic reduction mechanism of the intra-atomic Coulomb repulsion energy of 3*d* TM impurity atom (a) in isolated condition and (b) in semiconductors [13].

However, when TM impurity atoms are in a semiconductor compound, the effective intra-atomic Coulomb repulsion (U_{eff}) is observed to be reduced. It is calculated as 0.2 ~ 0.5 eV in magnitude. The schematic representation of this scenario is presented in Fig 2.3.1. According to the Haldane and Anderson mechanism, it may happen that majority (~ 90%) of the charge added to the deep impurity states by external doping is delocalized in the crystal due to the Coulomb repulsive interaction and the strong *p-d* hybridization and the minority portion (~ 10%) is localized in the 3*d*-TM impurity atomic site. On the perspective of applications, this mechanism of reduction in effective intra-atomic Coulomb repulsion is important to change the charge and spin states by controlling the chemical potential by co-doping or an applied electric field by a gate voltage.

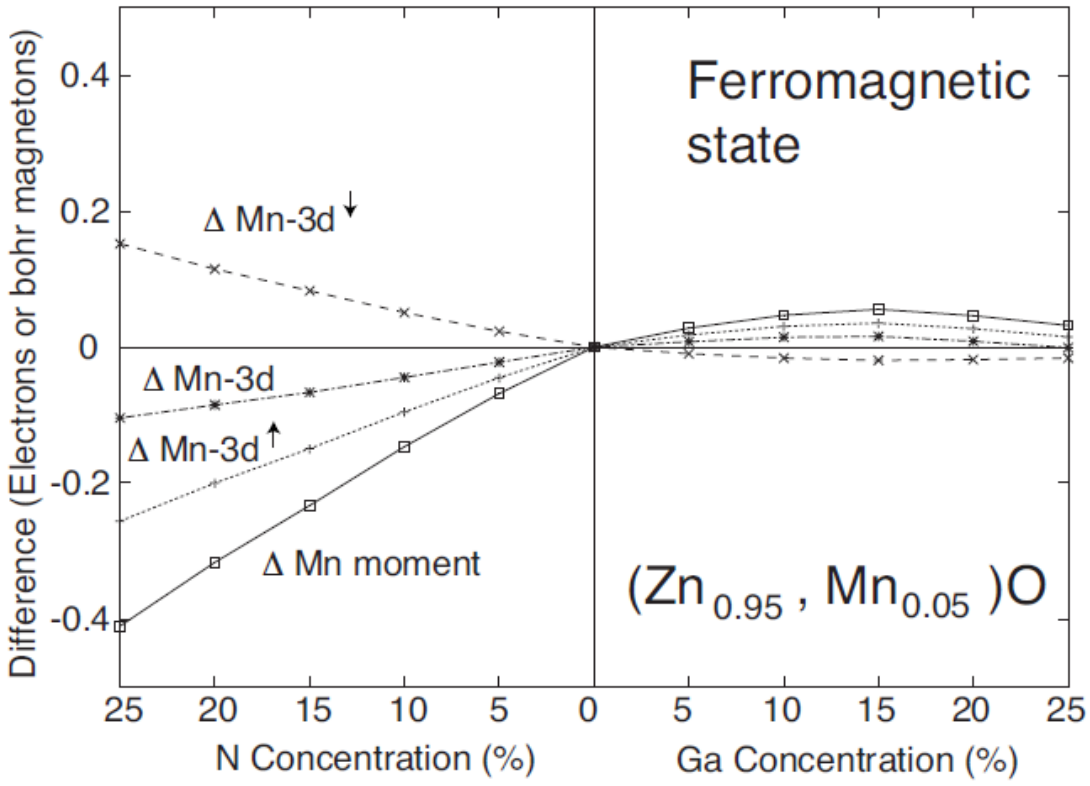

Figure 2.3.2: The impact of external acceptor (N) and donor (Ga) doping on the magnetic moment (ΔM) and no of 3*d* electrons with different spin orientations [13].

It is well known that TM impurities possess both charge and spin DMSs. The charge-charge interaction is a long ranged direct Coulomb interaction which is protected by long-wavelength electrons (monopole screening), While the spin-spin interaction is a short-ranged exchange-correlation interaction which is protected by short-wavelength electrons (multiple screening) in semiconductors with large dielectric constant. Thus, the charge and spin of the TM impurity is screened differently in semiconductors. For example, we can consider ZnO system co-

doped with N acceptor or Ga donor impurities as shown in Fig 2.3.2. The change in magnetic moment and no of 3*d* electrons with different spin orientations with the N-doping concentration is shown in the left panel, while those for Ga-doping is shown in the right panel. With the increase of N-acceptor doping, the number of 3*d* electrons with up spin reduces and 3*d* electrons with down spin increases. The change in the magnetic moment related to the change in the number of up and down spin orientation of 3*d* electrons is large enough to stabilize ferromagnetic interaction in (Zn,Mn)O:N [56]. The reason for this drastic change is that the exchange-correlation interaction is not well protected by multiple screening of electrons. On the other hand, the co-doping of Ga-donor impurity on (Zn,Mn)O DMS has not shown any change in the magnetic moment of Mn. This is because the introduced electrons have predominantly occupied the conduction band.

2.4. Research on (Zn,Cr)Te DMS:

The exceptional magnetic and magnetooptical properties of (Zn,Cr)Te have been attracting attention to the scientific community for long time. In this case, either the *p-d* double exchange or the ferromagnetic superexchange mechanism has been theoretically proposed to explain the short-ranged ferromagnetic interaction between Cr ions. Experimentally, the ferromagnetic behavior was noticed for Cr composition of few percent and room temperature ferromagnetism was achieved for Cr composition of 20%. Figure 2.4.1 represents the theoretical calculation based on the mean field approximation (MFA) and Monte Carlo simulation together with the experimentally obtained results of $Zn_{1-x}Cr_xTe$ thin films to show the dependence of Curie temperature, T_C with Cr contents [9, 57].

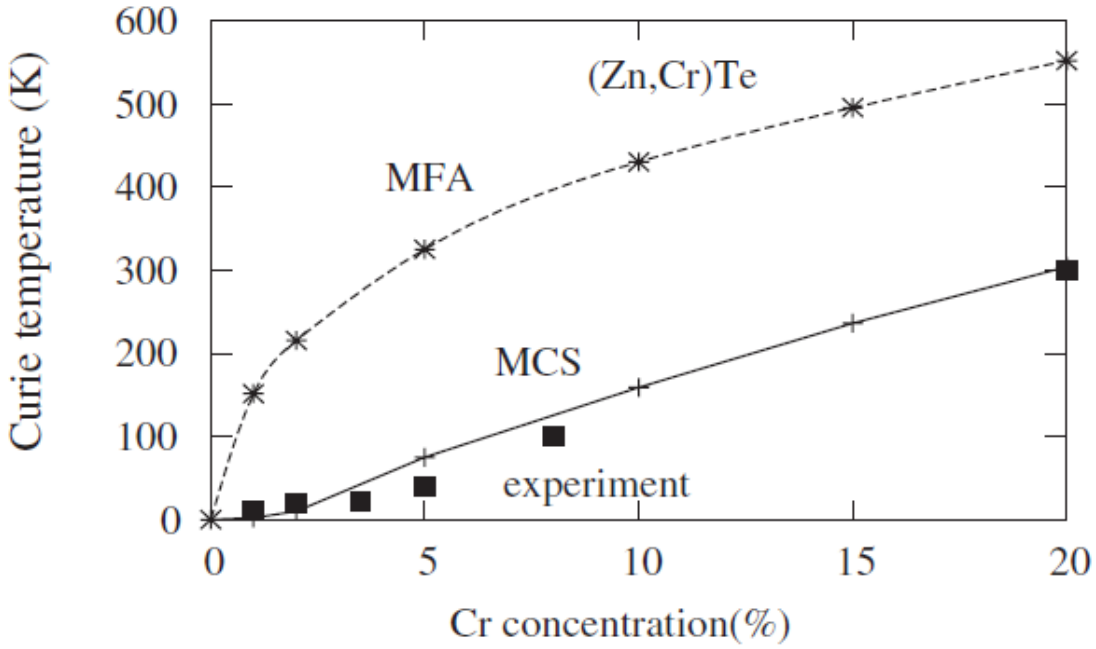

Figure 2.4.1: Curie temperatures of (Zn,Cr)Te calculated by the mean field approximation , Monte Carlo simulation and experimentally observed results as a function of Cr concentration. The black squares represent the experimental data [9, 57].

However, chemical and crystallographic phase separation has been observed in $Zn_{1-x}Cr_xTe$ thin films depending on the growth conditions and amount of Cr contents. Figure 2.4.2 (a) and (b) shows the energy dispersive spectra (EDS) for the Cr mapping in the $Zn_{1-x}Cr_xTe$ thin films with Cr composition, x = 5% grown under Te -rich and Zn-rich conditions. The EDS mapping for the $Zn_{1-x}Cr_xTe$ thin films with different Cr compositions, x = 5% and x = 20% grown under Te-rich condition are also demonstrated in Fig. 2.4.3 (a) and (b) respectively to observe the Cr distribution.

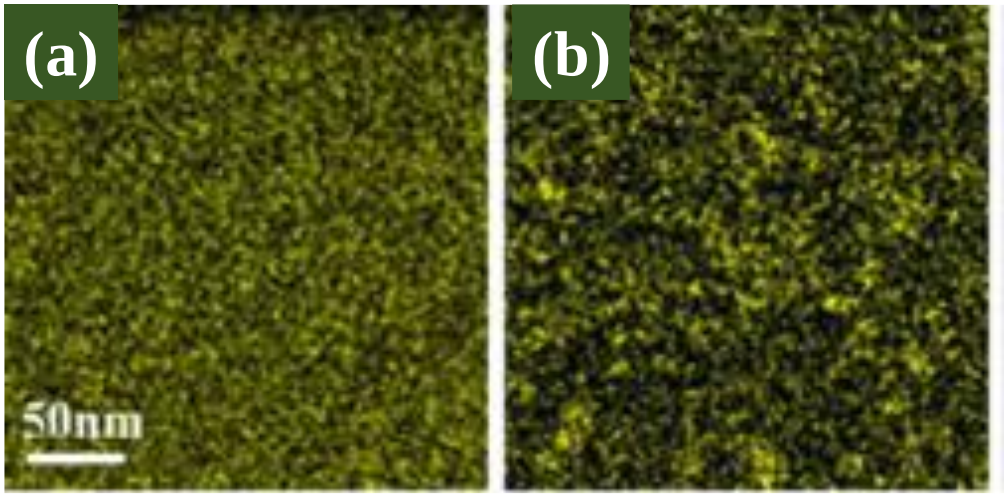

Figure 2.4.2: EDS mapping showing Cr distribution in $Zn_{1-x}Cr_xTe$ thin films with Cr composition, x = 5% grown under (a) Te-rich growth condition (b) Zn-rich growth condition [9].

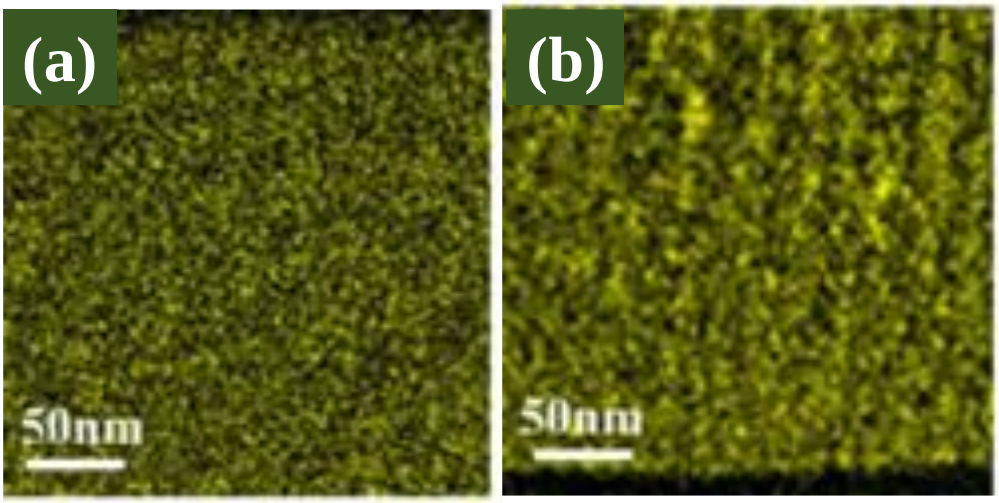

Figure 2.4.3: EDS mapping showing Cr distribution in $Zn_{1-x}Cr_xTe$ thin films grown under Te-rich growth condition with Cr compositions, (a) x = 5% and (b) x = 20% [9].

As observed from the EDS mapping images in Fig. 2.4.2 for the $Zn_{1-x}Cr_xTe$ thin films with Cr composition, x = 5%, the Cr distribution is uniform in Te-rich grown film within the spatial resolution of 2-3 nm and non-uniform under Zn-rich growth condition. Similarly, it is observed that the Cr distribution becomes non-uniform with the increase of Cr composition for the $Zn_{1-x}Cr_xTe$ thin films grown in the same growth condition as shown in Fig. 2.4.3. The Cr distributions are found to be very non-uniform in the case of $Zn_{1-x}Cr_xTe$ thin films with Cr composition, x = 20%.

In addition, the magnetic properties are also found to change accordingly with the change in growth condition and Cr composition. Figure 2.4.3 shows the dependence of paramagnetic Curie-Weiss temperature, θ_P, the magnitude of blocking temperature, T_B and the Curie temperature, T_C as a function of Te/Zn beam flux ratio and Cr compositions. The data for the Cr compositions, x = 5% and x = 20% are demonstrated by close and open symbols respectively.

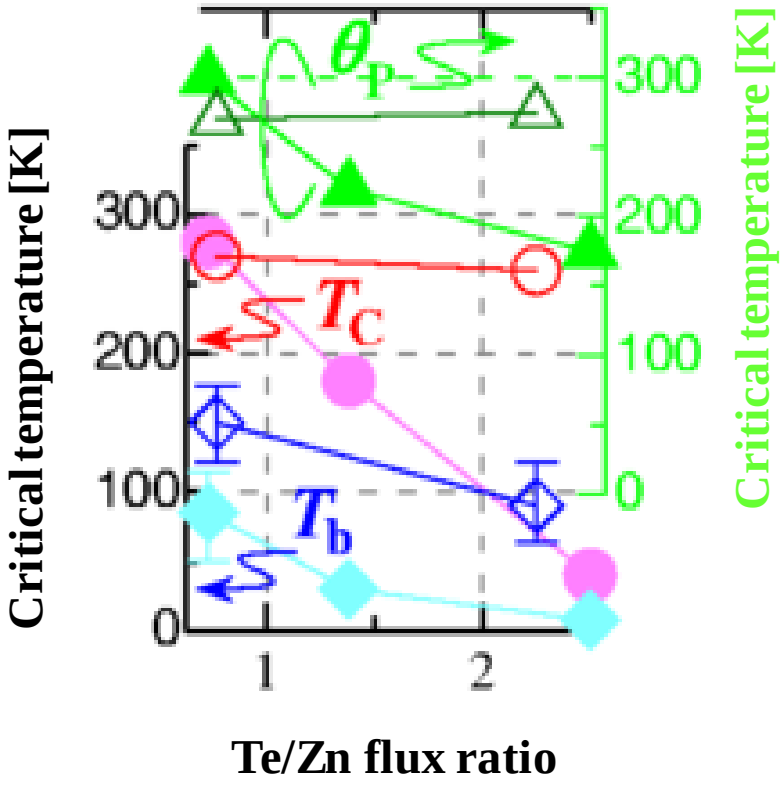

Figure 2.4.4: Three characteristics temperatures: the apparent Curie temperature, $T_C^{(app)}$ (circles), the paramagnetic Curie-Weiss temperature, θ_P (triangles) and the blocking temperature, T_B (diamonds) for $Zn_{1-x}Cr_xTe$ thin films have been shown as a function of Te/Zn flux ratio and Cr compositions. The close and open symbols represent the data for Cr compositions, (a) x = 5% and (b) x = 20% respectively [9].

These experimental observations have provided evidences for the correlation of magnetic properties of $Zn_{1-x}Cr_xTe$ thin films with the uniformity of Cr distributions. Especially, the characteristics temperatures have changed significantly with the change in growth conditions and hence, the Cr distributions for $Zn_{1-x}Cr_xTe$ thin films with Cr composition, x = 5% as shown by the closed symbols in Fig. 2.4.4. However, when the Cr composition has reached the percolation limit, x ~ 20%, the long-ranged ferromagnetic order is observed, and the characteristics temperatures are found to vary very little with the growth condition. In order to observe the relationship between the Cr-concentration and the ferromagnetism in $Zn_{1-x}Cr_xTe$ thin films, the Cr 2p XMCD spectra and the magnetization, M for the Cr compositions, x = 3% and 15% are demonstrated in Fig. 2.4.5.

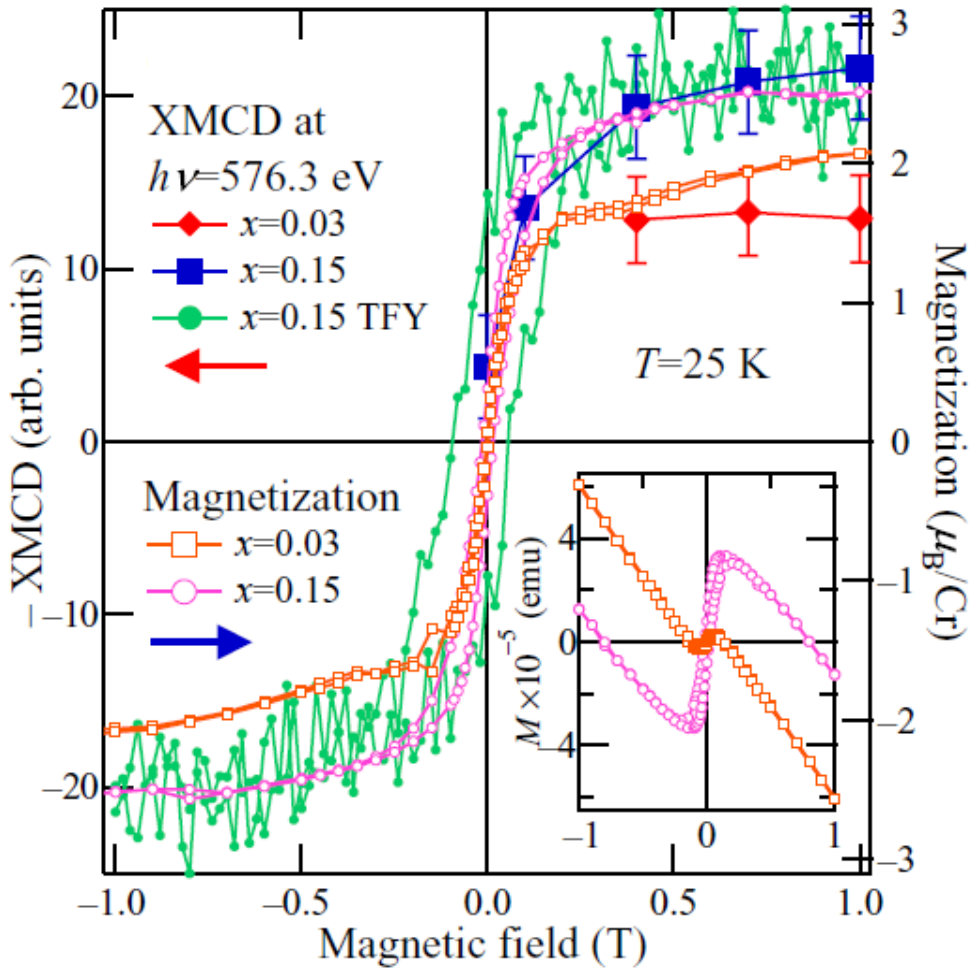

Figure 2.4.5: Magnetic-field dependence of the Cr 2p XMCD spectra and the magnetization curves for $Zn_{1-x}Cr_xTe$ thin films with Cr compositions, x = 3% and 15%. The subtracted diamagnetic component from the raw data of magnetization curves are also shown in the inset. The XMCD hysteresis loop has been measured by using the total -electron-yield (TFY) mode [58].

The near coincidence of the ratios of the XMCD intensity and the magnetization, *M* in the high magnetic field regions has indicated the bulk magnetic properties of $Zn_{1-x}Cr_xTe$ thin films. It is known that the XMCD is very sensitive to local electronic states, the enhancement of the magnetization per Cr ion with the rise in Cr concentrations has reflected the impact of the distance between Cr ions on the magnetism of $Zn_{1-x}Cr_xTe$. It has also given clue in favor of the participation of the majority Cr ions in the interaction with each other. For all the above observations, it can be concluded that the ununiform distributions of Cr ions mainly govern the ferromagnetic properties in $Zn_{1-x}Cr_xTe$ [58].

2.4.1 Experimental studies on nitrogen (N) acceptor co-doped (Zn,Cr)Te:

In the previous section, we have mentioned about the occurrence of crystallographic or chemical phase separation in $Zn_{1-x}Cr_xTe$ if the Cr composition exceeds the solid solubility limit in ZnTe semiconductor compound which is rather low. The driving force which enhances this crystallographic or chemical phase separation is the attractive interaction between the magnetic ions. In the case intrinsic ZnTe, it is normally assumed that Cr ions stay in the isoelectronic Cr^{2+} state. According the previous experimental results on magnetic resonance and optical studies, the $Cr^{2+/3+}$ donor level is resided above 0.2 eV above the host valence band as shown in Fig. 2.4.6(a) [59, 60]. The position of nitrogen acceptor level is located just in between the $Cr^{2+/3+}$ donor level and the valence band. On the other hand, the $Cr^{2+/1+}$ acceptor level is situated at 1.1eV below from the bottom of the host conduction band and 1.08 eV below the iodine donor level as shown in Fig. 2.4.6 (a). In this level diagram, Cr is considered to substitute the Zn cation site and stay in the isoelectronic Cr^{2+} state. In such DMSs, in which the 3*d* TM impurity level reside in the band gap region of the host semiconductor, the co-doping with shallow impurities is proposed to be the efficient method to change the charge states of the magnetic ions by trapping the additional carriers and hence make an impact on their chemical and spin dependent interactions.

By taking the *ab* initio all-electron DFT calculations into account, the calculated energy for bringing two Cr atoms to the nearest-neighbor position in the cationic site in the zinc-blende crystal structure is shown in Fig. 2.5.1 (b) [59, 60]. The pairing energy, E_d is minimum in ZnTe for the two Cr cations in the 2+ charge state. However, altering Cr valence state by co-doping with shallow impurities produces Coulomb repulsion between the Cr ions which increases the value of E_d as shown in Fig. 2.4.6 (b). If additional coulomb repulsive energy together with the entropy term exceeds the energy required for the bonding of two TM impurities, it is proposed to impede the spinodal decomposition of magnetic ions and stabilizes the uniform epitaxy.

In the case of ZnTe, it is known that the cation vacancies can be formed very easily [40]. Due to the formation of Zn vacancies, the as-grown ZnTe has p-type conductivity, typical concentration of native acceptors is of the order of 10^{18} cm^{-3} [59, 60]. Therefore, in $Zn_{1-x}Cr_xTe$ thin films grown under Te-rich condition, a portion of the isoelectronic Cr^{2+} ions assume the Cr^{2+} charges due to the presence of native Zn vacancies and exhibit ferromagnetism. Concerning the origin of ferromagnetism, the ferromagnetic superexchange and the double exchange has been widely discussed by several research groups [8, 61]. According to the first principle calculations, Cr 3*d* electrons generate nonbonding '*e'* state and antibonding 't_a' state in the band gap region of ZnTe. The Fermi level is situated in the middle of the upper 't_a' state, the ferromagnetic interaction between the Cr ions is mediated by the band broadening through the electron hopping (double exchange mechanism) [8]. The schematic representation of this mechanism has already discussed in section 1.1.2. The virtual hopping mechanism between the neighboring 3*d* orbitals of TM impurities having parallel magnetic moments is schematically shown in Fig. 2.4.7.

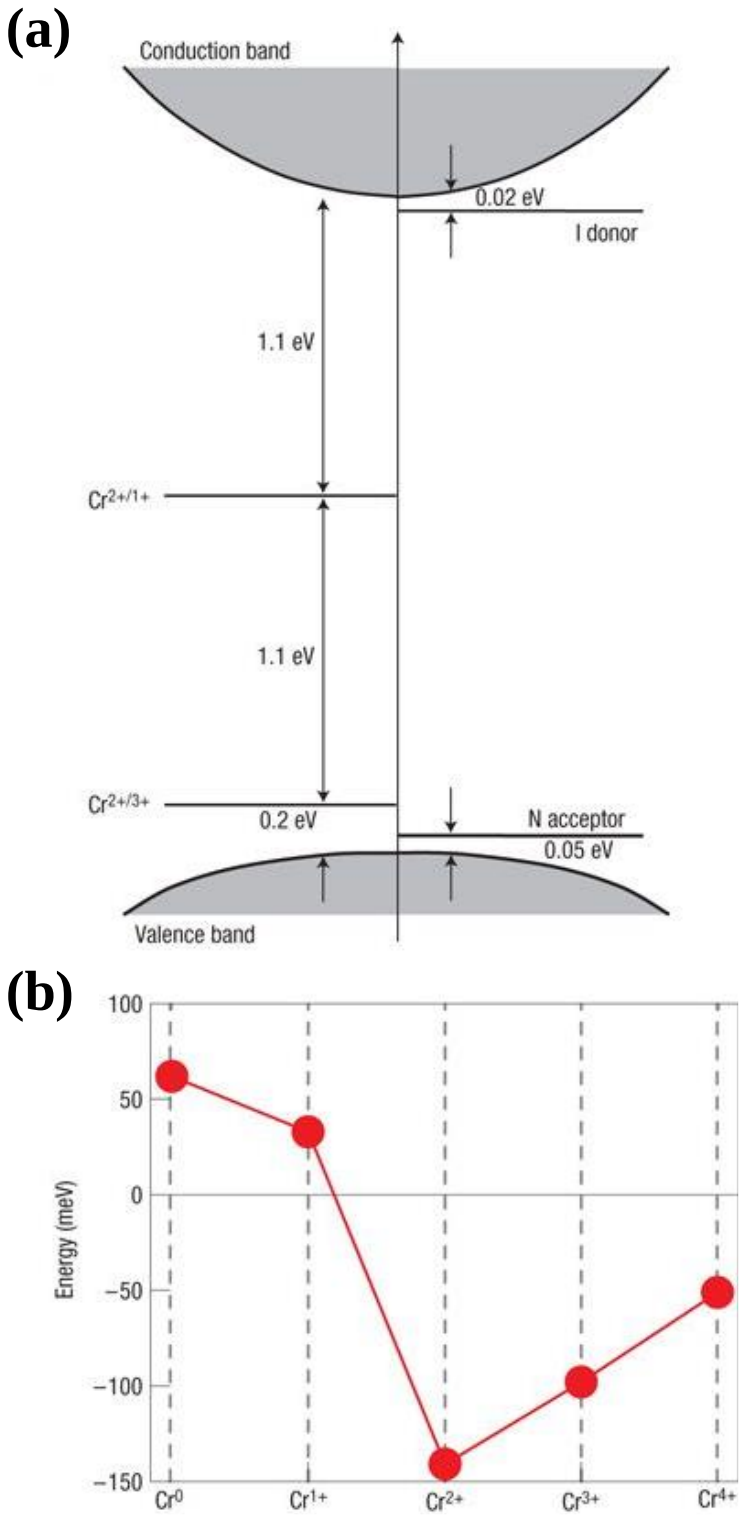

Figure 2.4.6: (a) Schematic positions of different charge states of Cr in ZnTe and **(b)** *ab* initio calculation results for the formation energy of Cr pairs in the nearest-neighbor positions on the cation -site in zinc-blende ZnTe crystal [59, 60].

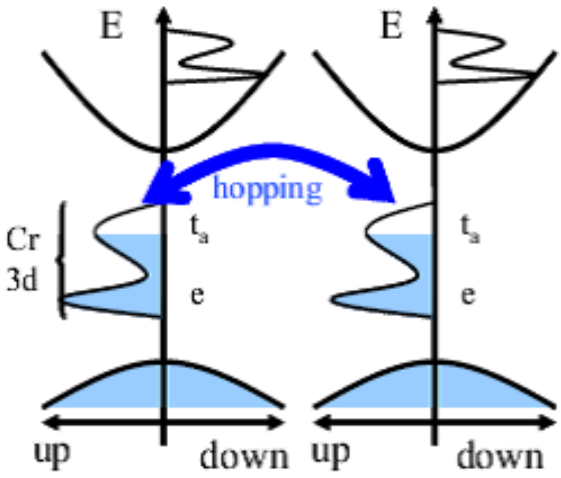

Figure 2.4.7: Schematic diagram of double exchange interaction in (Zn,Cr)Te [8]

In order to understand the mechanism for the origin of observed ferromagnetism in undoped $Zn_{1-x}Cr_xTe$, the structural and magnetic properties of nitrogen (N) acceptor co-doped and iodine (I) donor co-doped (Zn,Cr)Te have also been studied [61, 62]. Remarkable changes in the structural and magnetic properties due to additional charge co-doping has been observed. The undoped thin films of $Zn_{1-x}Cr_xTe$ grown under Te-rich condition, exhibit insulating properties with high resistivities. Figure 2.4.8 represents the temperature dependence resistivity of $Zn_{1-x}Cr_xTe$: N thin films with different Cr compositions but almost the same N-doping concentration of 10^{20} cm^{-3}. The Hall concentrations are observed to decrease from 4.7×10^{20} cm^{-3} with the lowest Cr composition, $x = 0.4\%$ to 3.4×10^{17} cm^{-3} with the highest Cr composition, x = 5%. Accordingly, the result of *R-T* measurements shows different behavior depending on the Cr composition. For example, $Zn_{1-x}Cr_xTe$ thin film with the lowest Cr composition, $x = 0.4\%$, exhibits metallic behavior, while film with the highest studied Cr composition, $x = 5\%$ exhibits insulating behavior. This variation of the electrical properties from metallic to insulating with the increase of Cr composition could be due to the variation in the density of trapping of N acceptor provided holes by the deep Cr 3*d*-TM impurity levels.

The magnetic properties of $Zn_{1-x}Cr_xTe$ film grown under Te-rich condition has changed drastically due to the co-doping of N acceptor impurity. The ferromagnetic behavior of undoped $Zn_{1-x}Cr_xTe$ has been suppressed and the linear *M-H* dependence has been observed with N-doping concentration of the order of 10^{20} cm^{-3} for films containing Cr composition, $x \leq 9\%$ [63]. Figure 2.4.9 and 2.4.10 have presented the *M-H* curves and the characteristic temperatures of magnetic properties for undoped and N-doped $Zn_{1-x}Cr_xTe$ thin films with Cr composition, $x = 5\%$ and N concentration of the order of 10^{20} cm^{-3} respectively. The paramagnetic Curie-Weiss temperature, θ_P, the magnitude of blocking temperature, T_B and the Curie temperature, T_C which were observed to have some finite value in the case of undoped film are reduced to zero by the co-doping N acceptor impurity. The EDS mapping for the undoped and the N-doped $Zn_{1-x}Cr_xTe$ films with Cr composition, $x = 5\%$ has shown almost uniform Cr distribution as presented in Fig. 2.4.11. By comparing the EDS mapping and the results of magnetic studies for the films, it has been concluded that apparent Curie temperature, $T_C^{(app)}$ is low and even vanishes when the Cr distribution is homogeneous [9].

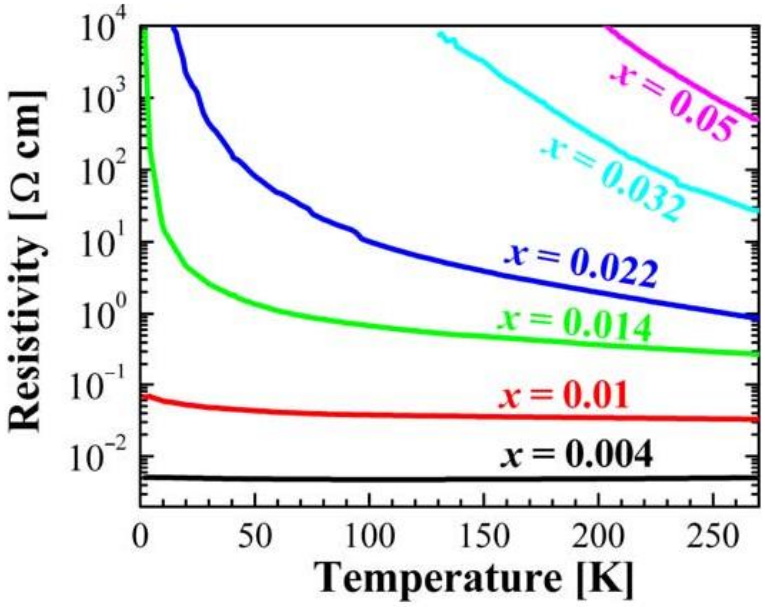

Figure 2.4.8: Electrical resistivity versus temperature graph for $Zn_{1-x}Cr_xTe$: N thin films with different Cr compositions but with same N concentrations of the order of 10^{20} cm^{-3} [63].

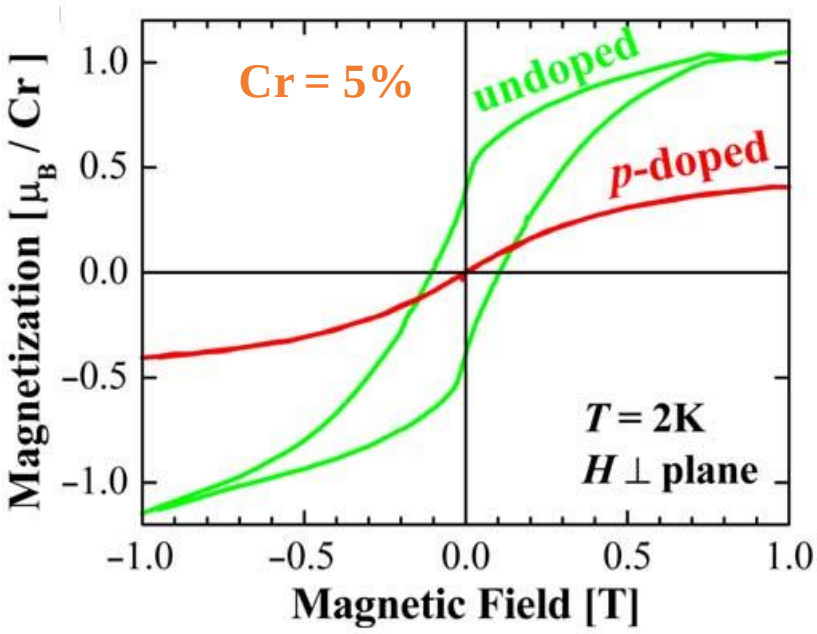

Figure 2.4.9: *M-H* curves for the undoped and N-doped $Zn_{1-x}Cr_xTe$ thin films with Cr composition, x = 5%. The N concentration of the N-doped film was of the order of 10^{20} cm^{-3}. The measurements were accomplished by applying external magnetic field perpendicular to the film plane [63].

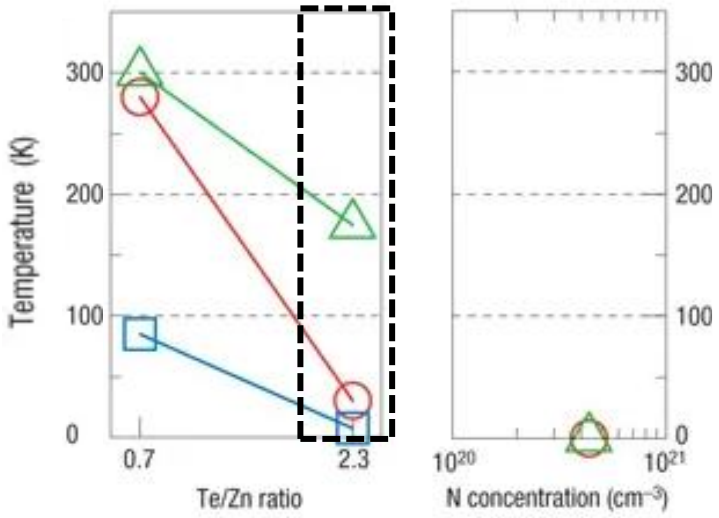

Figure 2.4.10: Three characteristics temperatures: the apparent Curie temperature, $T_C^{(app)}$ (circles), the paramagnetic Curie-Weiss temperature, θ_P (triangles) and the blocking temperature, T_B (diamonds) for undoped (data marked by the shaded area in the left panel) and N-doped (right panel) $Zn_{1-x}Cr_xTe$ thin films with Cr composition, x = 5% [9].

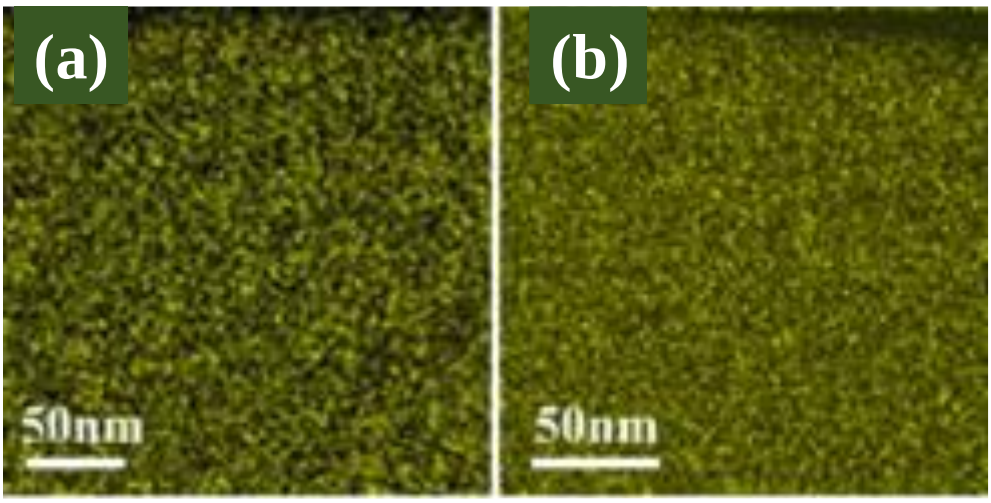

Figure 2.4.11: EDS mapping showing Cr distribution in **(a)** undoped and **(b)** N-doped $Zn_{1-x}Cr_xTe$ thin films grown under Te-rich growth condition with Cr composition, x = 5% [9].

Based on the previously explained double exchange mechanism, the suppression of ferromagnetism in N-doped $Zn_{1-x}Cr_xTe$ films has qualitatively explained [62]. The Femi level which was resided in the middle of the upper 't_a' state in the undoped film has moved downwards for the reduced density states of unpaired 3*d* electrons due to the trapping of carriers provided by N acceptor impurity. This in turn, has decreased the ferromagnetic interaction between Cr ions and the paramagnetic behavior appears when the concentrations of N acceptor and Cr becomes comparable, At this situation, majority of the Cr^{2+} ions have acquired the Cr^{3+} charge state and the double exchange mechanism explain ferromagnetism disappear. Figure 2.4.12 has shown the schematic mechanism of the N acceptor co-doped $Zn_{1-x}Cr_xTe$ study.

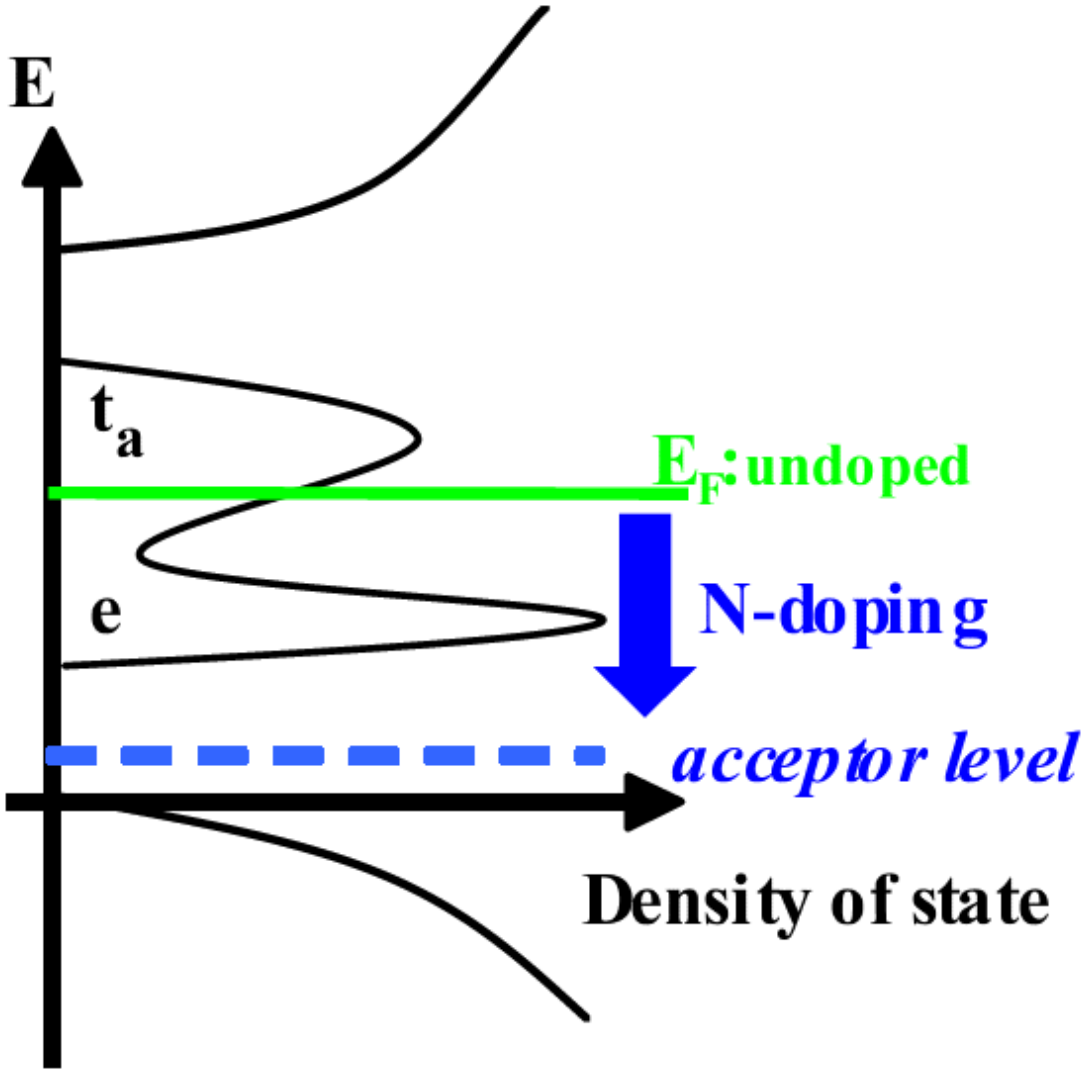

Figure 2.4.12: The mechanism in the framework of double exchange to explain the suppressing of ferromagnetism in $Zn_{1-x}Cr_xTe$: N thin films grown under Te-rich condition [62].

2.4.2 Experimental studies on iodine (I) donor co-doped (Zn,Cr)Te:

In this section, we have presented the structural and magnetic properties of iodine (I) donor co-doped $Zn_{1-x}Cr_xTe$ thin films grown under Zn-rich condition with fixed Cr composition, x = 5% and varied I concentrations in the range of 10^{17} – 10^{19} cm^{-3} [9, 61]. In contrast to the N concertation dependence electrical behaviors of $Zn_{1-x}Cr_xTe$: N thin films, $Zn_{1-x}Cr_xTe$: I thin films pursue the insulating properties even with the I-doping concentrations of the order of 10^{19} cm^{-3}. Figure 2.4.13 demonstrates the cross-sectional high-resolution transmission electron microscope (HRTEM) image and selected-area electron diffraction (SAED) of $Zn_{1-x}Cr_xTe$: I thin film with Cr composition, x = 5% and I concentration, [I] = 2×10^{18} cm^{-3}. The TEM micrograph shows predominantly single crystalline Zinc-blende structure, except the occurrence of stacking faults along the {111} plane in some restricted regions. In the SAED, along with the intense fundamental spots of the hexagonal zinc-blende structure, additional weak spots at one-third positions of the line connecting the fundamental spots are observed. These weak spots are considered to be associated with the triplet periodicity of the staking sequence along the {111} plane in the stacking faults areas. Despite these stacking faults areas, no other precipitates have been detected though these observations.

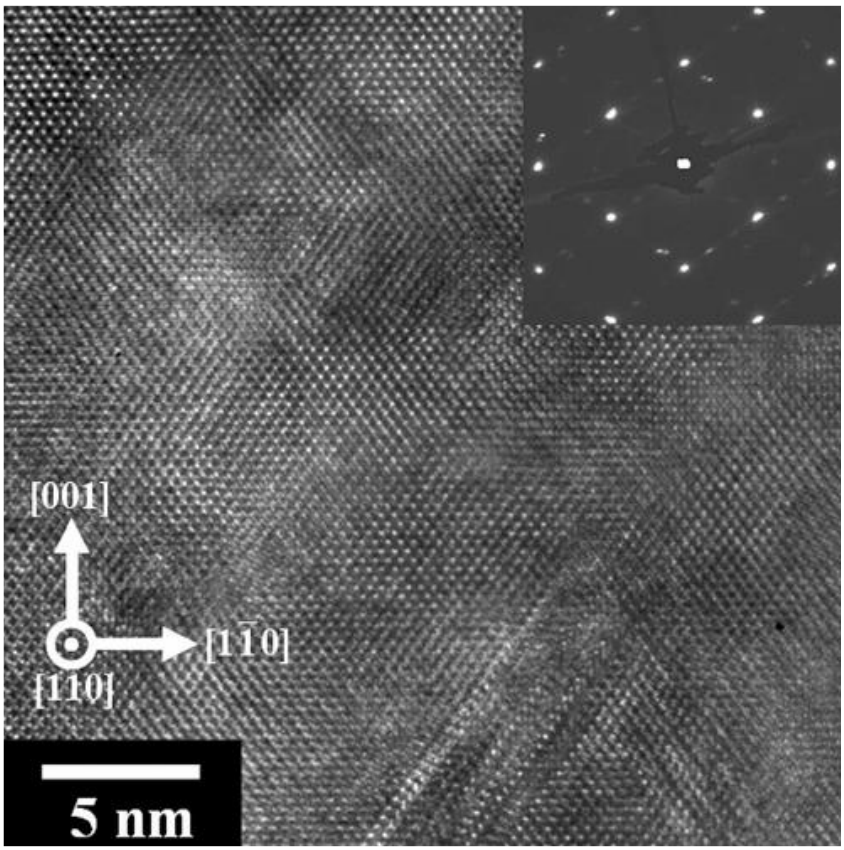

Figure 2.4.13: Cross-sectional image of high-resolution transmission electron microscope (HRTEM) of $Zn_{1-x}Cr_xTe$: I thin film with Cr composition, x = 5% and I concentration, [I] = 2×10^{18} cm^{-3}. The selected area electron diffraction (SAED) has been shown in the inset [9].

The *M-H* curves for the undoped, I-doped and N-doped $Zn_{1-x}Cr_xTe$ thin films with Cr composition, x = 5% and I concentration, [I] = 2×10^{18} cm^{-3} and N concentration, [N] = 5×10^{20} cm^{-3} have been demonstrated in Fig. 2.4.14 [61]. It is seen that the ferromagnetic properties of $Zn_{1-x}Cr_xTe$ thin film is remarkably enhanced due to the co-doping of I donor and in fact, room temperature ferromagnetism has been observed in $Zn_{1-x}Cr_xTe$: I thin film. The suppression of ferromagnetic properties of $Zn_{1-x}Cr_xTe$ thin film with N acceptor co-doping has already been discussed in the previous section.

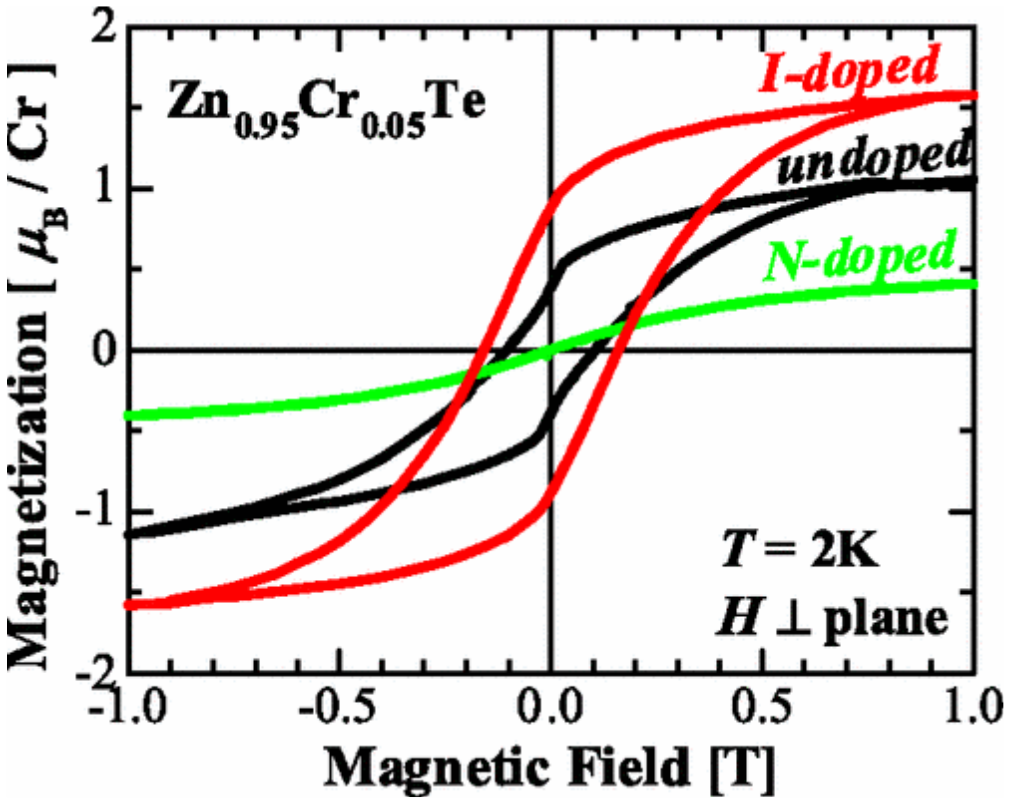

Figure 2.4.14: *M-H* curve of the undoped, I-doped and N-doped $Zn_{1-x}Cr_xTe$ thin films with Cr composition, x = 5% and I concentration, [I] = 2×10^{18} cm^{-3} and N concentration, [N] = 5×10^{20} cm^{-3}. The magnetization was measured at 2K with the application external magnetic field perpendicular to the film plane [61].

In order to investigate the origin of ferromagnetism is either intrinsic or extrinsic, the magnetic circular dichroism (MCD) measurement has been performed for the $Zn_{1-x}Cr_xTe$: I thin film with Cr composition, x = 7 % and I concentration of the order of 10^{18} cm^{-3}as shown in Fig. 2.4.15 (a) [61]. In case of ZnTe , a sharp peak corresponding to the intrinsic Zeeman splitting at the Γ point has been observed at energy value of 2.38 eV, while in case of $Zn_{1-x}Cr_xTe$: I, a broad negative band has been noticed at the lower energy side of the sharp peak at 2.38 eV. Similar result has been observed for undoped $Zn_{1-x}Cr_xTe$ thin films with the same Cr composition grown under Te-rich condition [63]. As the possible reasons of the broad band, the lattice relaxation during the optical transitions from the valence band to the Cr 3*d* levels in the band gap region [64] and the impact of Cr-rich regions by magnetization dependent boundary conditions for light propagation (the Kerr effect) have been mentioned.

However, the plotting MCD intensity at photon energy of 2.2 eV against the magnetic field and the magnetization data measured by superconducting quantum interference (SQUID) magnetometer has observed to be in sufficient agreement as shown in Fig. 2.4.15 (b). These finding has concluded that the origin of ferromagnetism is intrinsic and is originated from the exchange interaction between the Cr 3*d* electrons with *sp*-electrons of the host at the critical point of the energy band.

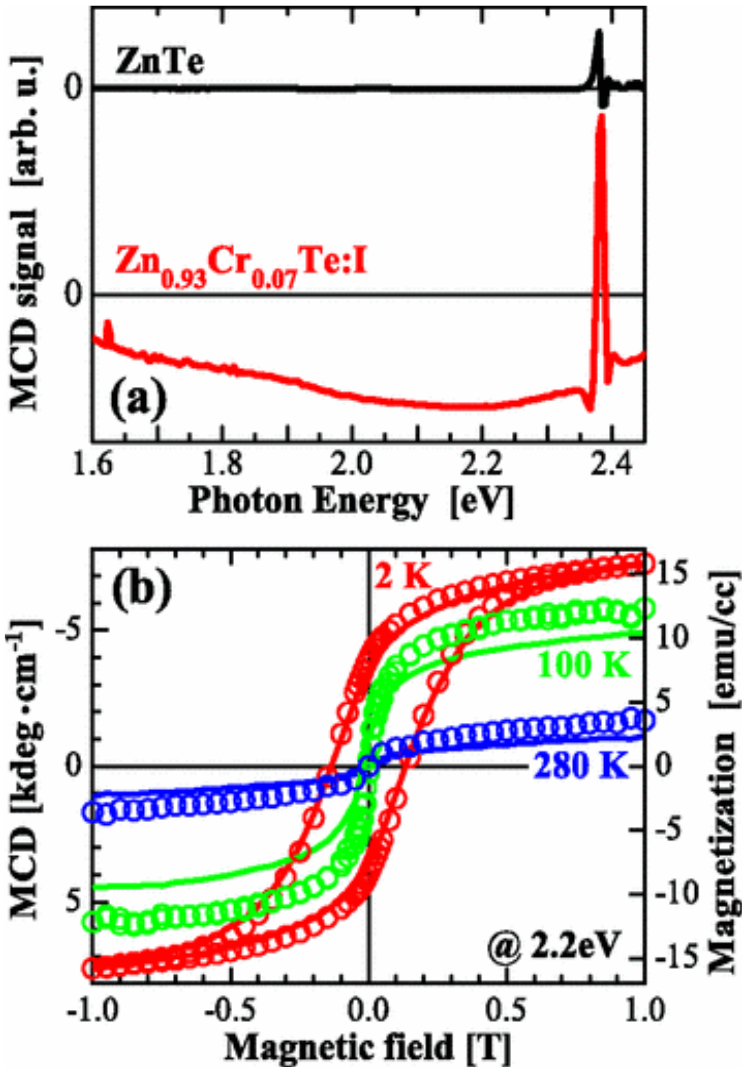

Figure 2.4.15: (a) The MCD spectra of ZnTe and I-doped $Zn_{1-x}Cr_xTe$ thin films with Cr composition, *x* = 7% and I concentration, [I] ~ 10^{18} cm^{-3} measured at 2K. The measurement was done in the transmission mode with the application external magnetic field perpendicular to the film plane and **(b)** the comparison of the magnetic field dependence of the MCD intensity at photon energy of 2.2 eV and the magnetization data obtained from SQUID [61].

The dependence of the ferromagnetic properties on I concentration and corresponding structural characterization have also been performed for a series of $Zn_{1-x}Cr_xTe$ thin films grown under Zn-rich condition with fixed Cr composition, x = 5% and varied I concentrations in the range of 10^{17} – 10^{19} cm^{-3} [61]. Figure 2.4.16 shows

the characteristic temperatures namely, the Curie temperature, T_C and the paramagnetic Curie-Weiss temperature, θ_P, for the $Zn_{1-x}Cr_xTe$ thin films with fixed Cr composition, x = 5% and varied I concentrations. Accordingly, Fig. 2.4.17 represents the EDS mapping to observe Cr distributions in $Zn_{1-x}Cr_xTe$ thin films with fixed Cr in different I concentrations.

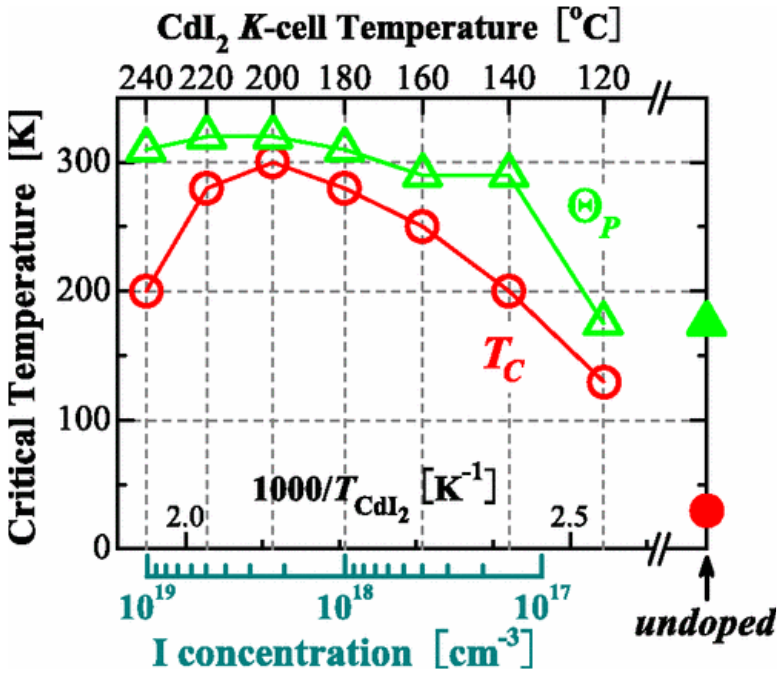

Figure 2.4.16: Two characteristic temperatures: The Curie temperature, T_C (circles) and the paramagnetic Curie-Weiss temperature, θ_P (triangles) for $Zn_{1-x}Cr_xTe$ thin films with Cr composition, x = 5% as a function of I concentrations [61].

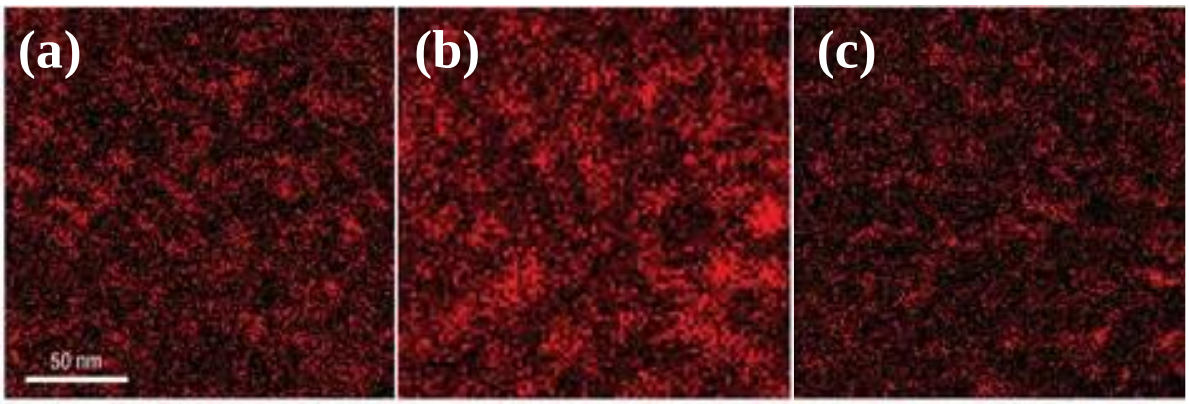

Figure 2.4.17: Comparison of Cr distributions in $Zn_{1-x}Cr_xTe$ thin films with Cr composition, x = 5% and different I concentrations **(a)** [I] = 1×10^{19} cm^{-3} **(b)** [I] = 2×10^{18} cm^{-3} and **(c)** [I] < 1×10^{17} cm^{-3} [9].

In Fig.2.4.16, we have observed the increase of both ferromagnetic transition temperature, T_C and the paramagnetic Curie-Weiss temperature, θ_P with the increase of I concentration up to [I] = 2×10^{18} cm^{-3} but after that both characteristic temperatures decrease with further increase in I concentration. Similarly, in the $Zn_{1-x}Cr_xTe$: I thin films grown under Zn-rich conditions; we have observed the non-uniform distributions of Cr in all the three cases. However, the size of the Cr-rich nanocrystals is observed to be larger in the case of $Zn_{1-x}Cr_xTe$: I thin film with [I] = 2×10^{18} cm^{-3} as shown in Fig. 2.4.17 (b). As we have mentioned before, in $Zn_{1-x}Cr_xTe$ grown under Te-rich growth condition, due to the availability of native cation vacancies, a portion of the isoelectronic Cr^{2+} ions assume the Cr^{3+} charge state. Accordingly, due to the growth of the $Zn_{1-x}Cr_xTe$ thin films under Zn-rich condition or co-doping with I donor, all the Cr ions stay in the isoelectronic Cr^{2+} state for which the Fermi level lies in the mid band gap region. In addition, the theoretical calculations shown in Fig. 2.4.6 (b) have already mentioned the pairing energy for two neighboring Cr atoms is minimum when both stay in the isoelectronic Cr^{2+} state. So, naturally the $Zn_{1-x}Cr_xTe$ thin films grown under such situations exhibit semi-insulating behavior. In such cases, neither the double exchange nor the carrier mediated spin-spin interactions can describe the room temperature ferromagnetism. So the decrease in size of the Cr-rich nanocrystals for I concentration, [I] = 1×10^{19} cm^{-3} as shown in Fig. 2.4.17 (c) signifies the appearance of Cr^{1+} ions in $Zn_{1-x}Cr_xTe$: I thin film which can create additional Coulomb repulsion between Cr ions and raise the pairing energy, E_d.

2.5 Experimental studies on silicon (Si) donor co-doped (Ga,Fe)N:

Substitutional Fe on the Ga-site of (Ga,Fe)N has been drawing attention due to the short bond length and strong *p-d* exchange interaction [65]. According to the density functional theory (DFT) calculations, the spin-spin exchange interaction between magnetic ions is antiferromagnetic in (Ga,Fe)N. However, ferrimagnetic interaction between magnetic ions in the presence of holes by additional charge doping has been recently reported; thus reviving the attention to focus on the nature of magnetic interaction in (Ga,Fe)N [66].

In the case of (Ga,Fe)N, it is generally observed that with the increase of growth temperature, T_g, aggregation magnetic ions has occurred in the host semiconductor matrix. The key worth mentioning point is that a change of growth temperature, T_g of 5°C, new Fe_xN compounds have become stabilize and promotion of spinodal decomposition resulting in Fe-rich nanocrystals (coherent chemical phase separation) have formed in the host semiconductor compound. As e result, the enhancement of ferromagnetic properties in (Ga,Fe)N has been observed. Figure 2.5.1 shows the metal organic vapour phase epitaxy (MOVPE)of (Ga,Fe)N material system as a function of growth temperature, T_g in the range from 800 to 950°C and Fe compositions in the range of (1 - 4) × 10^{20} cm^{-3}. The experimentally observed solid solubility limit of Fe in GaN is o.4% according to the MOVPE technique [23]. Based on the available experimental observations by synchrotron based XRD (SXRD), EXAFS, XANES, HRTEM and SQUID magnetometry, the formation of various Fe_xN compounds have noticed at various growth temperature, T_g as shown in Fig. 2.5.1 [23].

In this section, the effect of co-doping of Si donor doping on the structural and magnetic properties of (Ga,Fe)N DMS grown by metal organic vapour phase epitaxy (MOVPE) has been discussed [24]. It has been observed that at growth temperature, T_g = 850°C, the dominant extrinsic precipitate contributing in the structural and magnetic properties of (Ga,Fe)N is ε-Fe_3N having wurtzite crystal structure [23]. Figure 2.5.2 represents the SXRD analysis of the undoped (Ga,Fe)N and Si-doped (Ga,Fe)N layer grown at 850°C. In the SXRD of undoped sample, two main diffraction peaks of ε-Fe_3N associated with the (002) and the (111) reflexes have identified, while in the SXRD of Si-doped (Ga,Fe)N sample, the diffraction peaks from the ε-Fe_3N precipitates have disappeared, thus reflecting the effect of co-doping of shallow impurity to impede the formation of extrinsic precipitate [24].

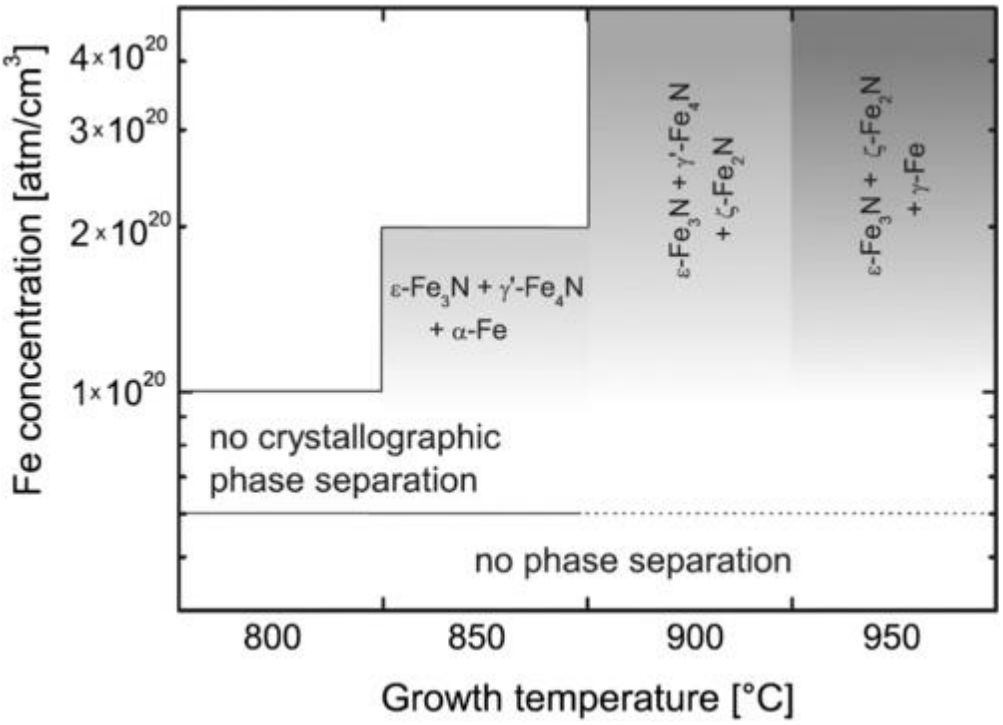

Figure 2.5.1: A phase diagram for (Ga,Fe)N layers grown in the MOVPE technique under different growth temperatures [23].

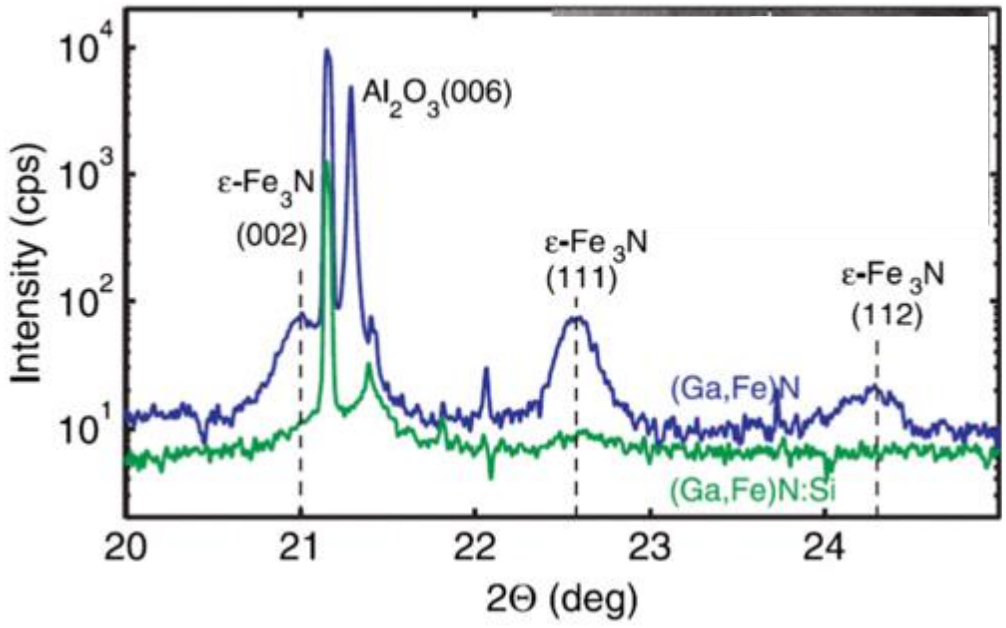

Figure 2.5.2: Synchrotron based XRD results for (Ga,Fe)N and (Ga,Fe)N: Si layer grown in the MOVPE technique with Fe composition above the solid solubility limit in GaN matrix [24].

Figure 2.5.3 represents the high-resolution transmission electron microscope (HRTEM) images of the (Ga,Fe)N and Si-doped (Ga,Fe)N layers. In the micrographs (a) and (c), (Ga,Fe)N include the ε-Fe_3N extrinsic precipitates as indicated by the translational Moire fringes and Fe aggregation respectively. In the micrographs (b) and (d), the impact of Si-doping on hampering the formation of the ε-Fe_3N extrinsic precipitate by the removal of translational Moire fringes and converting the Fe aggregation region into uniform epitaxy has been demonstrated respectively.

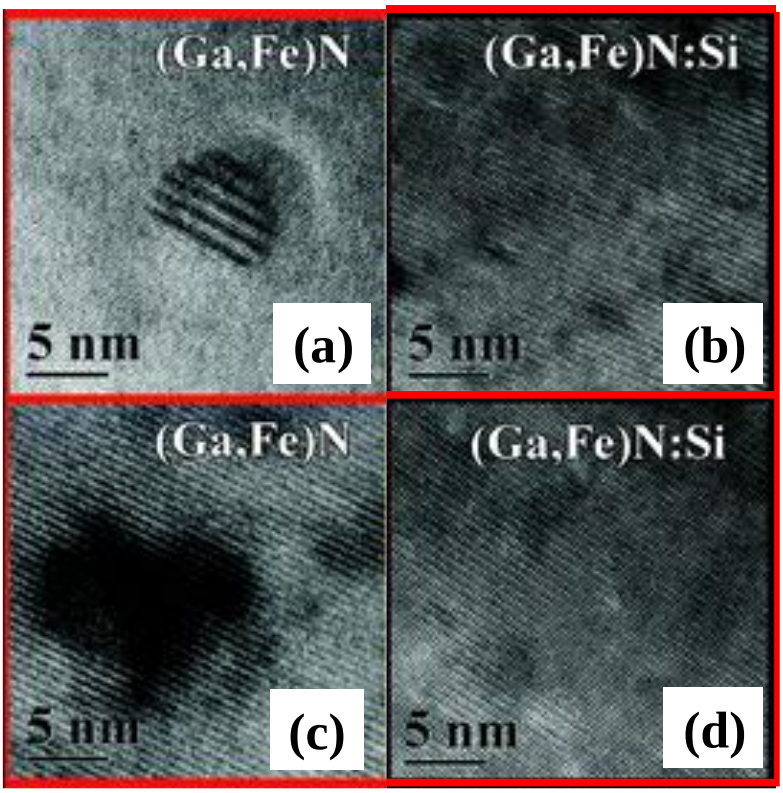

Figure 2.5.3: HRTEM images of (Ga,Fe)N revealing **(a)** the presence of ε-Fe_3N secondary phases **(c)** regions of spinodal decomposition. The effect of co-coping of Si donor impurity on hampering the formation of Fe-rich regions **(b)** and **(d)** [24].

The above experimental findings can be discussed on the basis of the theoretical proposal which states that DMSs with the 3*d* -TM impurity levels residing in the band gap region of the host semiconductor can trap the additional carriers supplied by shallow impurities [21, 66]. Due to this trapping the charge state of the magnetic ions can alter which modifies the Coulomb repulsion between the magnetic ions. In addition, in the previous section, we have observed the theoretical calculations for valence state dependence variation of pairing energy between Cr ions in ZnTe matrix [59, 60] and the experimental findings about the impact of I donor on hampering Cr-rich nanocrystals by changing the charge state of a portion of Cr ions from Cr^{2+} to Cr^{1+} for [I] = 1×10^{19} cm^{-3}

[9]. Since the $Fe^{3+/2+}$ acceptor levels reside in the mid gap level of GaN semiconductor compound, the trapping of electrons provided by the donor impurity can change the valence state of Fe ions. In order to investigate the valence state of Fe in the samples, the near-edge region of the absorption spectra (XANES) has been studied. The position of the pre-edge peaks due to the partially forbidden $1s \rightarrow 3d$ transitions has widely used in previous studies to determine the valence state of Fe in Fe compounds [67, 68]. The position of the pre-edge peak for Fe^{2+} has been observed at about 7112 eV and that of Fe^{3+} at about 7114 eV. Figure 2.5.4 represents the normalized XANES spectra for (Ga,Fe)N and (Ga,Fe)N: Si.

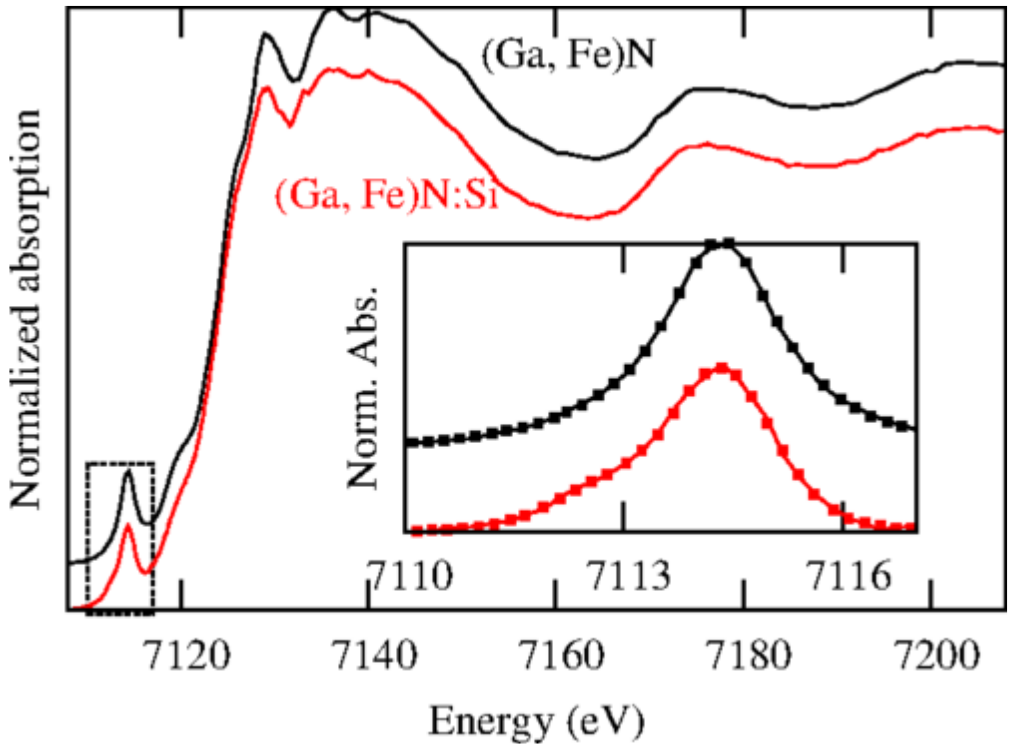

Figure 2.5.4: XANES spectra of (Ga,Fe)N and (Ga,Fe)N: Si. The inset shows the pre-edge peak positions for the studied samples which are determined by comparing the fitting curves (solid lines) with the background subtracted experimental data (symbols) [24].

As observed in Fig. 2.5.4, the undoped sample show a single peak at the position of 7113.9 ± 0.1 eV, while the Si-doped sample exhibit the same peak at 7113.9 ± 0.1 eV and an additional peak at energy position of 7112.8 ± 0.1 eV. These data signifies the existence of Fe^{3+} in the (Ga,Fe)N and the coexistence of Fe^{3+} and Fe^{2+} ions in the (Ga,Fe)N: Si. Thus, the co-doping Si donor impurity has partially reduced the magnetic ions ($Fe^{3+} \rightarrow Fe^{2+}$).

In addition, the effect of co-doping of Mg acceptor on hampering the formation of nanocrystal assembling and the onset of spinodal decomposition has also been reported [23]. However, the $Fe^{3+/4+}$ donor levels are expected to locate in the valence band of GaN [37]. But it has been proposed that the potential introduced by TM impurity is sufficiently deep to trap a hole [69]. Based on this explanation, Mg cooping can also impede Fe aggregation.

2.6 Experimental studies on electrical field controlled magnetic properties of (In,Mn)As:

The ability to control the magnetic properties of DMSs by external gate voltages is highly demandable on the perspective of the technological viewpoints. In this section, electric field controlled magnetic properties of (In,Mn)As ferromagnetic semiconductor has been explained [27]. In (In,Mn)As, the ferromagnetic interaction between Mn ions is observed to be mediated by hole carriers; the Mn ions on the substitutional position of In has provided the magnetic moment and the hole due to its acceptor behaviour [70-72]. As the ferromagnetic interaction between Mn ions depend on the presence of holes, so the variation of holes by applying electric field is highly desirable. Figure 2.6.1 shows the cross-sectional view of the field-effect transistor (FET) structure consisting the (In,Mn)As as the magnetic channel layer with Mn composition of 3%.

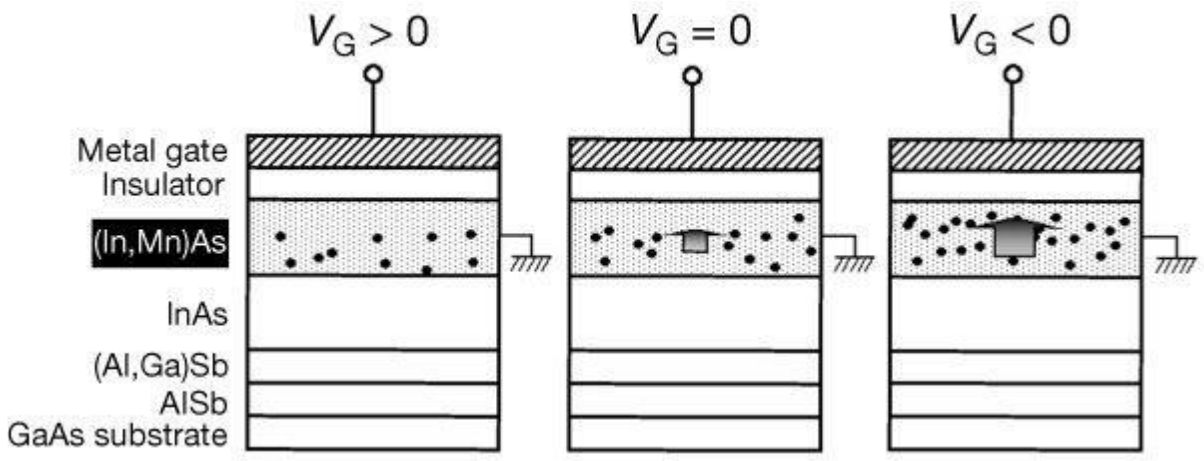

Figure 2.6.1: Field-effect transistor structure for controlling the magnetic properties of (In,Mn)As by applying external gate voltages. The hole concentrations in the magnetic layer and the corresponding magnetization values are represented by the filled circles and size of arrow respectively [27].

In the structure, all the layers have been grown by MBE. The InAs/(Al,Ga)Sb/AlSb heterostructures have been grown before growing the (In,Mn)As layer in order to reduce the lattice mismatch. A thick polyimide layer having dielectric constant of 3.3 has been used as the insulating layer and Au gate electrode has been used to apply external gate voltages across the FET structure. In order to reduce the difficulty in measuring directly the magnetization of the (In,Mn)As thin magnetic layer (≈ 5 nm) grown over the thick GaAs (001) diamagnetic substrate, a Hall bar geometry mesa has been utilized in this research. The gate leakage currents have been determined as less than 5 $nAcm^{-2}$ in all devices. The magnetization dependent Hall effect has been used to extract the magnetization of the (In,Mn)As channel layer. The sheet Hall resistivity, R_{Hall} is given by

$$R_{Hall} = \frac{R_0}{d} B + \frac{R_S}{d} M \qquad 2.6.1$$

Where, R_0, R_S represent the ordinary and anomalous Hall coefficient respectively and B, M and d represents the magnetic field, magnetization and thickness of the channel layer respectively.

Figure 2.6.2 demonstrates the Hall resistivity, R_{Hall} Vs magnetic field, B curves for different values of applied gate voltages, V_G at 22.5 K. The external gate voltages, V_G are applied in the sequence of 0 V → +125 V → -125 V → 0 V. The R_{Hall} -B curve at V_G = 0 V indicates ferromagnetic hysteresis curve at 22.5 K. The application of positive gate voltage, V_G = + 125 V, has turned the magnetic properties into paramagnetic feature having no hysteresis and reduced susceptibility and has indicated the direction of depletion of holes. On the other hand, application of negative gate voltage, V_G = - 125 V has increased the number of hole carriers and hence, enhanced the ferromagnetic properties with square hysteresis shown in the R_{Hall} -B curve. More importantly, the application of V_G = 0 V again, the channel layer has resembled the moderate hysteresis in the initial condition. From the gate capacitance, the variation of sheet hole concentration of the order of 3×10^{12} cm^{-2} has been anticipated by the application of gate voltage, V_G = ± 125 V. Thus, the magnetism of (In,Mn)As has been controlled isothermally in a reversible way by externally applied gate voltages.

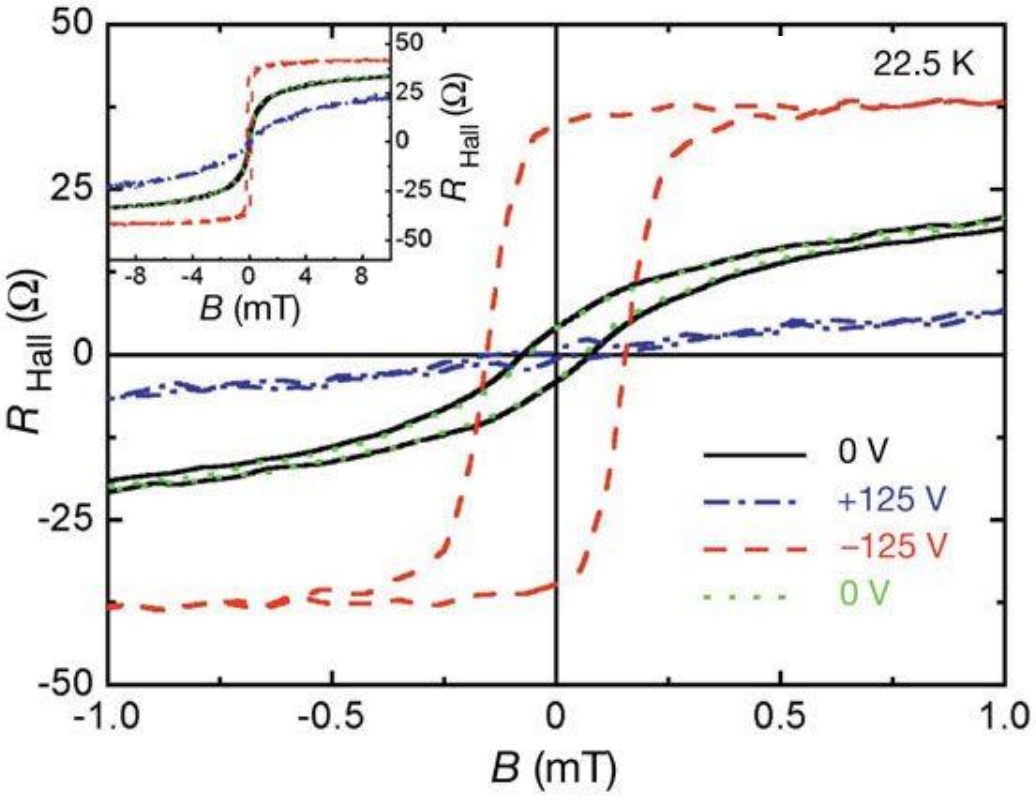

Figure 2.6.2: Hall resistivity, R_{Hall} versus magnetic field, B curves for three gate voltages, V_G = 0 V, +125 V and -125 V measured at 22.5 K. The inset represents the same R_{Hall} -B curves at higher magnetic fields [27].

2.7 Experimental studies on electrical field controlled magnetic properties of $(Ti,Co)O_2$:

In this section, the electrical control of magnetic properties of $(Ti,Co)O_2$ thin films (≈ 33 nm) grown by pulsed laser deposition method with Co composition of 10% at room temperature has been demonstrated [73]. In order to observe the electric field-controlled ferromagnetism at room temperature, the origin of magnetism should be based on carrier mediated mechanism [74, 75]. In case of electric field effect transistor structure to accumulate charge density larger than 10^{14} cm^{-2} for transforming various electronic and magnetic phases, a gate insulator with sufficiently high dielectric constant is of prime importance. In this study, liquid electrolyte has been used as gate insulator which forms electric double layer transistors (EDLTs) structure with the magnetic channel layer. With the application of the gate voltage, the anions and cations of the liquid electrolyte move towards the magnetic channel layer and gate electrode depending on the polarity of the applied voltage to form nano-meter thick electric double layers which generate high electric field of the order of 10 MV cm^{-1}. Figure 2.7.1 represents the EDLT structure in which a drop of liquid electrolyte is used to connect the $(Ti,Co)O_2$ layer with the Pt planar gate electrode.

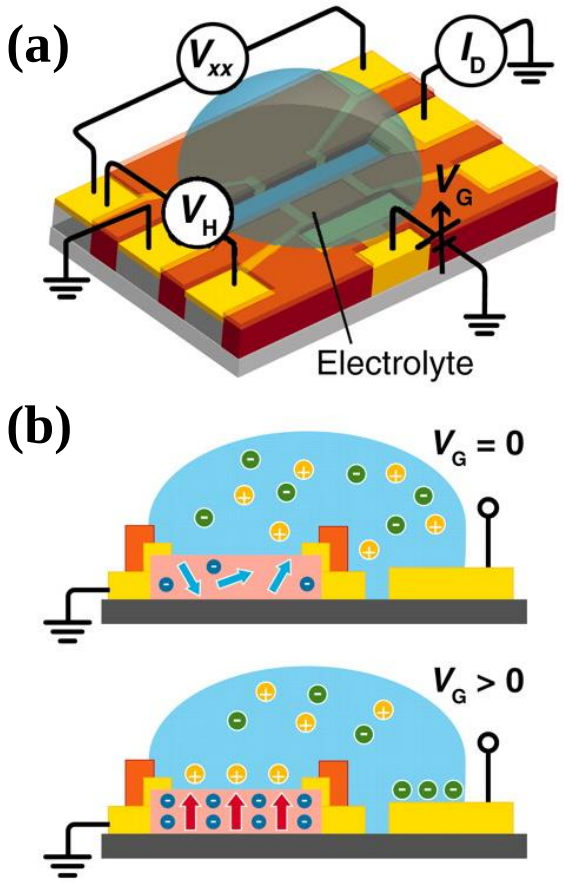

Figure 2.7.1: (a) Formation of electric double layer transistor (EDLT) structure at the interface of the $(Ti,Co)O_2$ magnetic channel layer with the liquid insulating layer **(b)** Explanation of electrically induced change in the magnetic properties due to the accumulation of electron carriers with finite gate voltage [73].

In the case of $(Ti,Co)O_2$ thin film with Co composition of 10% substituting on the Ti-site, the Co^{2+} ions and associated spins are localized and the random spin alignment between the Co^{2+} ions provide paramagnetic behavior. On the other hand, with the application of positive gate voltage, the cations and anions of the liquid electrolyte accelerates towards the $(Ti,Co)O_2$ channel layer and the electrode respectively and accumulate electron carriers in the channel layer by forming the EDLT structure. This charge accumulation has changed the electrical properties of the $(Ti,Co)O_2$ channel layer from insulative to metallic as shown in Fig. 2.7.2. These mobile electrons convey information for parallel spin alignment between Co^{2+} ions and hence, exhibit ferromagnetic behavior.

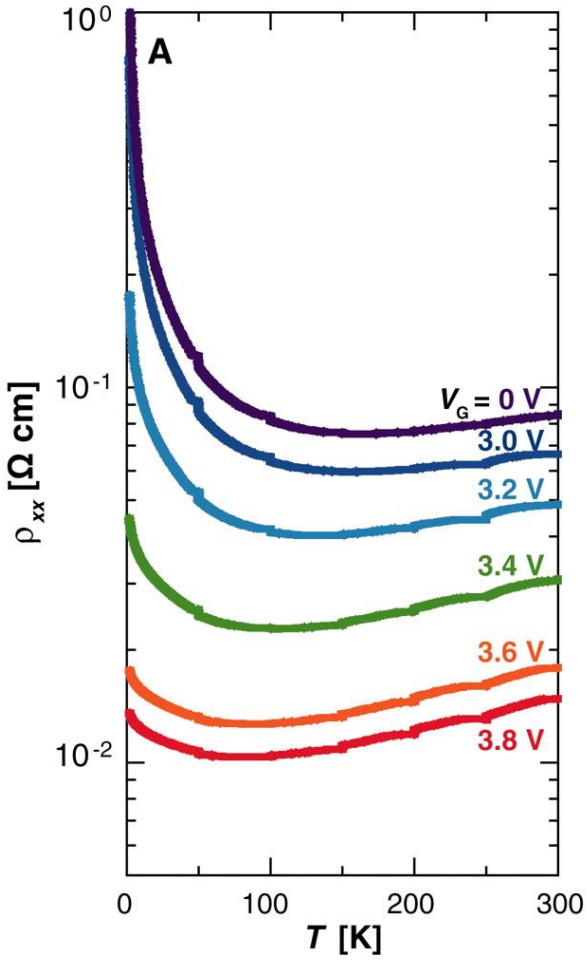

Figure 2.7.2: The resistivity, ρ_{xx} of $(Ti,Co)O_2$ thin films with Co composition of 10% under different gate voltages, V_G as a function of temperature [73].

In order to ensure the ferromagnetic properties originated from the accumulation of electrons, the Hall measurements has been performed. Figure 2.7.3 shows the anomalous Hall conductivity, σ_{AH} – magnetic field, H curves for the films with different positive values of applied gate voltage measured at room temperature. In the case of imbalance in electron's spin populations, the anomalous Hall effect which originates from the spin-orbital

coupling produces asymmetry scattering. That is, carriers with up and down spin are deflected in the opposite directions, both perpendicular to the charge current. At V_G = 0 V, the anomalous Hall conductivity, σ_{AH} of $(Ti,Co)O_2$ layer is very small and reflecting its paramagnetic behavior. But, with the application of positive gate voltages, σ_{AH} become more significant and the carrier induced ferromagnetic interaction has appeared. The relationship between the anomalous Hall conductivity, σ_{AH} and electron density at room temperature has also been observed for two device structures namely, Device 1 which uses DEME-TFSI (ionic liquid) as gate insulator and Device 2 which uses $CsClO_4$ (electrolyte salts) and PEO (polyethylene) as gate insulator. In addition, the experimental data for $(Ti,Co)O_2$ layers grown under different oxygen vacancies which act as electron donor are also presented. From the comparison of all the experimental evidences it has been concluded that the enhancement of anomalous Hall conductivity and hence, the appearance of ferromagnetism occur as soon as the electron density exceeds the limit of 1×10^{19} cm^{-3}.

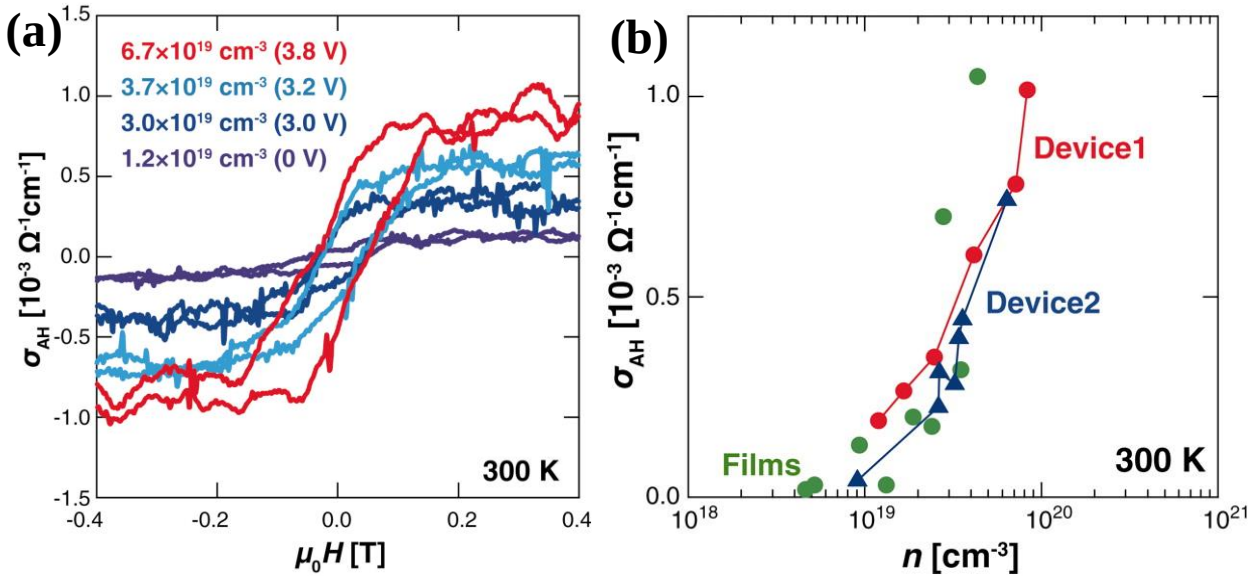

Figure 2.7.3: (a) The anomalous Hall conductivity, σ_{AH} versus magnetic field, H curves for $(Ti,Co)O_2$ layers with Co composition of 10% measures at room temperature for different values of positive gate voltages. **(b)** Dependence of anomalous Hall conductivity, σ_{AH} on electron density for different device structures (device 1 and device 2) and $(Ti,Co)O_2$ layers with Co composition of 10% grown under different oxygen vacancies [73].

Chapter 3: Experimental methods

3.1 Samples preparation by molecular beam epitaxy (MBE):

3.1.1 Molecular Beam Epitaxy (MBE) equipment

In this study, molecular beam epitaxy (MBE) has been used for the crystal growth of the thin film sample. It has been developed as a widely used growth technique far from the thermodynamic equilibrium due to the precise control of the compositional profiles. The word "epitaxy" comes from the Greek roots "epi" and "taxis" which mean to arrange upon. That is, arranging one or more thermal particles on the top a heated substate and maintaining the crystal structure is the explanation of the word "epitaxy".

The epitaxial growth of the thin films is performed on single crystalline substrate materials such as Si and GaAs. The crystal growth of the thin film sample is performed by evaporating the constituent elements to supply a molecular beam. An important feature of the MBE method is the presence of ultra-high vacuum ($\sim 10^{-10}$ Torr) inside the growth chamber. As a result of this high vacuum condition, the mean free path of molecules is longer than the distance between the evaporating source and the substrate surface and we can obtain a highly directional molecular beam of the elemental species striking the substrate surface. The reduction of residual gases is advantageous to suppress the adsorption of impurities on the substrate surface. Since the substrate and the evaporation source can be heated separately, it is possible to adjust the molecular dose at the heating temperature of the cell and to control the growth rate and thickness of the layers.

Figures 3.1.1, 3.1.2 and 3.1.3 represent the schematic views of the MBE system used for this study. Each of the raw materials are placed in separate cells. This makes it possible to vary independently the temperature of each raw material and hence their desired compositions in the thin films of the grown compounds. MBE apparatus EV500 manufactured by Eiko Engineering Co. Ltd. Has been used. There are two vacuum chambers namely, the growth chamber and the preparation chamber, separated by a gate valve. Due to the availability of the preparation chamber, the ultra-high vacuum condition of the growth chamber is not affected by the outside air during transferring the samples. Evacuation of the chambers has been maintained by operating the turbo-molecular pump in fabrication MBE and the oil rotary pump. Liquid nitrogen is supplied during the whole process for cooling the walls of the growth chamber and adsorbing the residual gases to ensure a higher degree of vacuum available in the growth chamber.

In this study, a molybdenum holder has been used to attach the GaAs substrate. The substrate holder is then set to the substrate manipulator positioned at the center of the growth chamber for heating. The substrate manipulator is equipped with a thermocouple capable of controlling the position and a heater for controlling the temperature of the substrate holder. The thermocouple is connected of the substrate holder; the distance was controlled so that it remains unchanged during the growth. The manipulator attaching the substrate holder is kept rotating during the growth process to observe the in-situ of the layer at different orientations by reflected high energy electron diffraction and hence, ensure uniformity of the grown epitaxial layer.

In an effusion cell, high purity (99.999%) raw material is kept on a crucible which is subsequently heated by a tantalum filament. A thermocouple is used to measure the temperature of the cell. In this study, two types of cells are utilized. The Knudsen cells containing crucible made of pyrolytic boron nitride (PBN) are used for elements such as Fe, Mn etc. for which high temperature is required to get the desired molecular beam flux. On the other

hand, crystal cells in which the crucible are made of quartz glass, have been used for raw materials such as, Zn, Te etc. This is because sufficient beam flux can be obtained for these materials at relatively low temperature. Depending on the difference between the temperature reading and the temperature set point the heating power of the tantalum filament is set by a feedback loop. This will help to maintain constant temperature in the effusion cell. A shutter is connected in each cell to keep the raw material free from outside impurity and to measure the BEP of each element precisely. The equation explaining the relationship between the flux and the cell temperature is represented by [76]:

$$F = \frac{P(T)}{\pi L^2} \frac{a}{\sqrt{2\pi T k_B}} \qquad 3.1.1$$

Where P (T) represents the equilibrium vapor pressure, a indicates the area of the cell aperture, L is the distance between the effusion cell and the substrate surface, m is the mass of the elemental species, K_B is the Boltzmann constant and T represents the effusion cell temperature.

In this study, the flux of the molecular beam supplied from the cell is measured by using an ion gauge as a flux monitor. The position of the flux monitor can be changed. To measure the flux for the molecular beam of an element, the flux monitor is set just under the heated substrate. Then the shutter of the heated cell containing the material is opened and the flux monitor measures the pressure of the corresponding amount of molecular beam supplied that is, the beam equivalent pressure (BEP). By changing the temperature of the cell, the BEP and hence, the supply of the molecular beam amount can be controlled for each raw material. In this way, the atomic composition ratio of the constituent elements has been controlled.

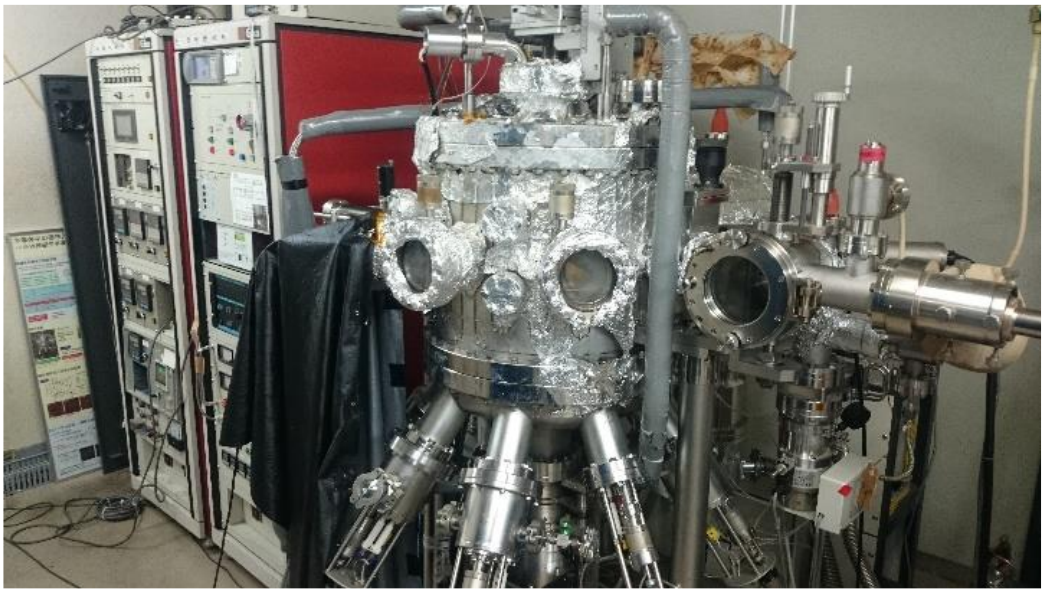

Figure 3.1.1: MBE system EV500 (EIKO)

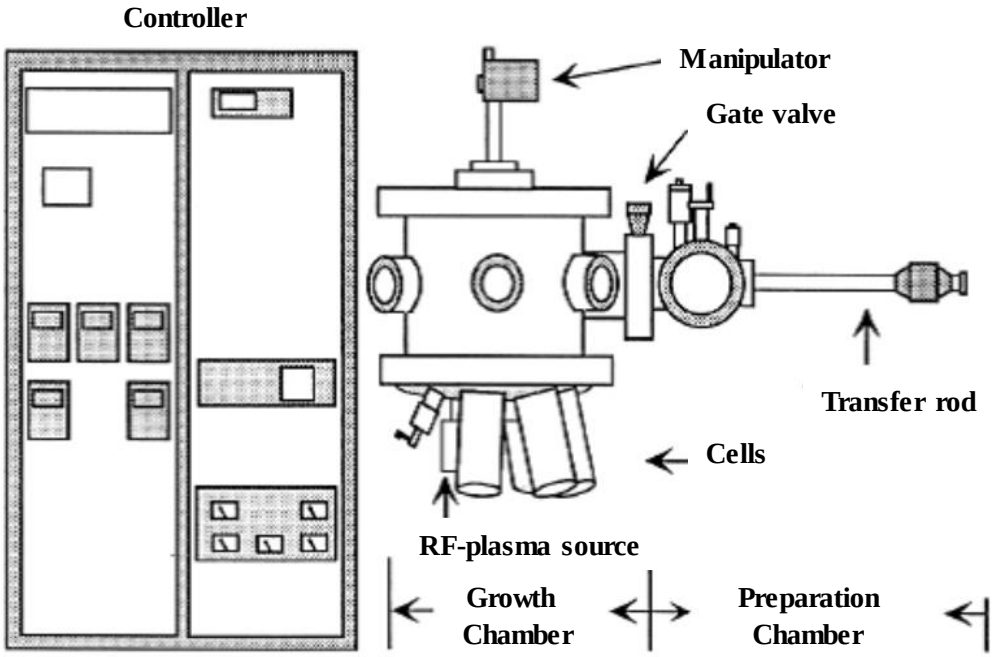

Figure 3.1.2: Simplified view of the MBE system

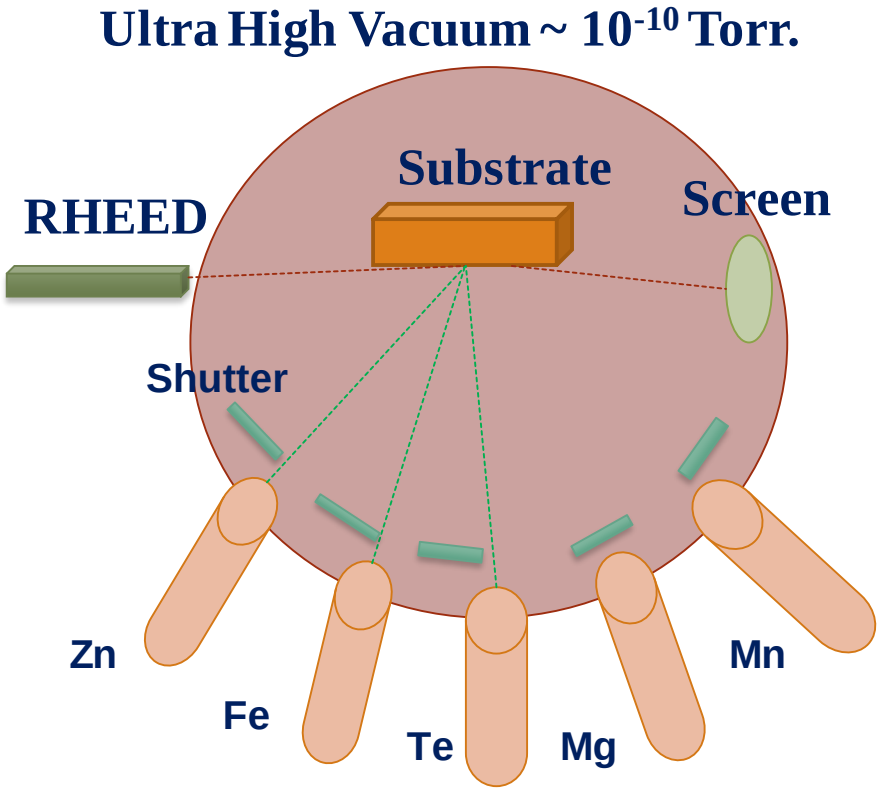

Figure 3.1.3: Inside view of the MBE system

3.1.2 Sample preparation

In this research study, we have prepared both undoped and N-doped $Zn_{1-x}Fe_xTe$ thin films on thick ZnTe buffer layer which is grow over GaAs (001) substrate to reduce the lattice mismatch. The lattice constant for GaAs and ZnTe has been measured as 5.6533 Å and 6.1037 Å respectively which means there exists a lattice mismatch of around 7% between them. If $Zn_{1-x}Fe_xTe$ thin film is grown on GaAs (001) substrate directly, some dislocations might form and disturb the crystal structure and flatness of the film.

Before sample preparation, we usually clean the GaAs substrate to remove oxidized layers and other contaminated substances by performing ultrasonic cleaning. The steps of the substate cleaning are mentioned bellow:

1. At first, the ultrasonic cleaning is performed by submerging the substate in a container carrying sufficient amount of acetone for 5 minutes at 43 Hz frequency. After that, we put the substrate in a container carrying ethanol for 5 minutes with the same frequency of 43 Hz. Finally, we clean the substrate by distilled water two times by using ultrasonic frequency of 43 HZ and 23 Hz respectively for a total time of 10 minutes.

2. Then, we collect the cleaned substrate and set to the molybdenum substrate holder and keep in the preparation chamber of the MBE machine. By opening the gate valve between the growth chamber and the preparation chamber, we install the substrate holder in the manipulator and start raising the temperature of the substrate up to 400°C to perform hydrogen cleaning. During the hydrogen cleaning process, hydrogen radicals ($H\cdot$) are generated by radiofrequency (rf) plasma. These hydrogen radicals ($H\cdot$) covert the Ga_2O_3 species which is one of the oxides that form at the substrate surface, into the volatile Ga_2O like oxide. It should be mentioned here that the valence state of Ga in Ga_2O_3 is +3, while in the case of Ga_2O it is +1. At substrate temperature higher than the desorption temperature, Ga_2O rapidly disappears and bring another new species of Ga_2O_3 to interact with the hydrogen radicals and in turn, generates the Ga_2O species. This cyclic process will provide Ga_2O_3 free surface within a very short time.

Figure 3.1.4 represents the hydrogen spectrum obtained by exciting rf -plasma in this study. The peaks are associated with the transitions of electron from shells with principal quantum number, $n \geq 3$ to $n = 2$ in hydrogen atom according to the Balmer series. The transition from state, $n = 3$ to $n = 2$ refers to as H_α and transition from $n = 4$ to $n = 2$ is termed as H_β. Figure 3.1.5 has provided the evidence of the removal of oxide layers from the GaAs substrate as observed from the RHEED pattern of the substrate. Before the hydrogen cleaning, the RHEED pattern is not clear as shown in Fig. 3.1.5 (a), while after the hydrogen cleaning the streak RHEED pattern has been observed suggesting flat surface as shown in Fig. 3.15 (b).

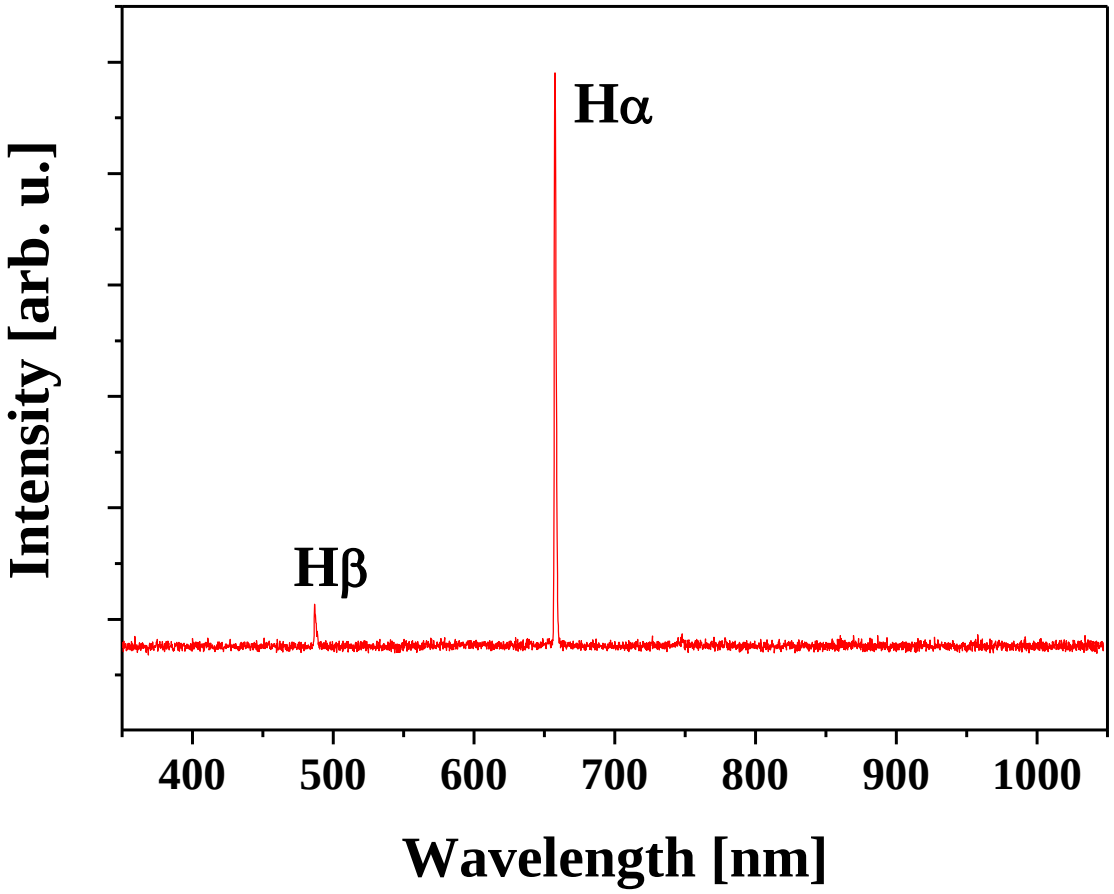

Figure 3.1.4: Hydrogen emission spectra observing the Balmer lines H_α and H_β

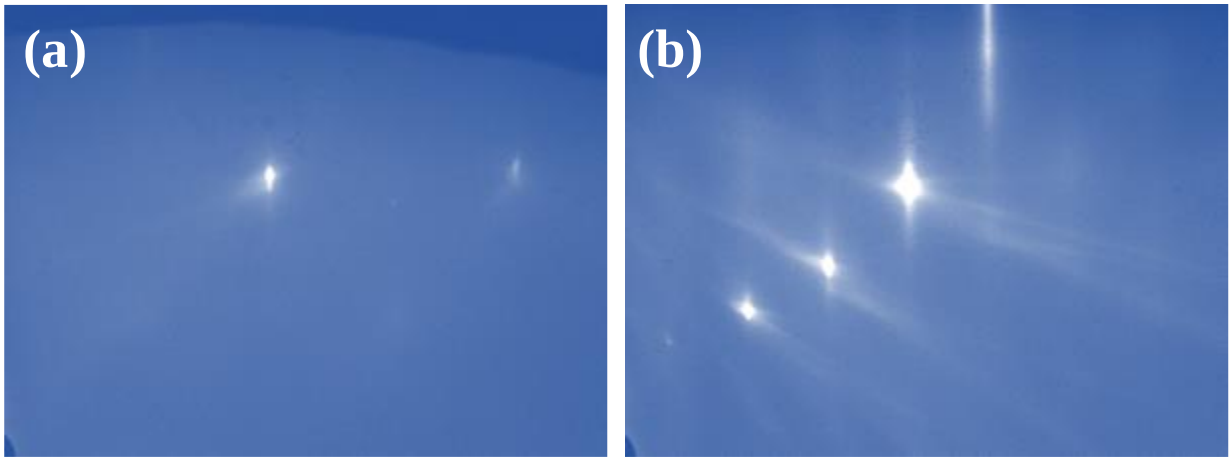

Figure 3.1.5: Reflection high energy electron diffraction (RHEED) pattern **(a)** before and **(b)** after hydrogen cleaning

3.1.3 Reflection high-energy electron diffraction (RHEED) method

In the present study, reflection high-energy electron diffraction (RHEED) method has been utilized to the in-situ monitor of the growth processes of the thin films and analyse the crystal structures of the surface at atomic levels. In RHEED method, a finally collimated electron beam having energy of around 10-50 KeV has been irradiated to the same surface at an angle of incidence lower than 3° onto a fluorescent screen. Figure 3.1.6 represents schematically the geometrical arrangement in RHEED method where an incident beam is incident at an angle, $\theta < 3°$ and reflected to the screen at a distance, L from the point of incidence. The spacing between the diffraction spots have been represented by W. We consider the incident electrons have wave vector, **k** and the diffracted electrons have wave vector, **k**'. On the basis of the Laue diffraction, the maximum intensity of the diffracted beams can only be obtained if the difference between the wave vectors of the incident and diffracted beams (**k - k**') intercept the reciprocal lattice rod as shown in Fig. 3.1.7. This will explain the Ewald sphere of radius, **k.** Diffracted beams with wave vector, **k**' can create some spots on the screen and are identified by the intersection between the Ewald sphere and the reciprocal lattice rod.

When the sample has an atomically flat surface and a perfect single crystalline structure, its reciprocal rods are very sharp without intensity modification along the rods under an assumption that the RHEED detects the topmost atomic layer only. Then the diffraction pattern is a reflection type in which all diffraction spots are on the Laue zones and have the same intensity. In reality, however, the electron beam penetrates into several atomic layers below the surface. Then the intensity is modulated along the reciprocal rods, resulting in that some diffraction spots are stronger, and others are weaker. This is due to interference among waves scattered from different atomic layers. As shown in Fig. 3.1.8, the RHEED pattern is streak for the completely flat sample surface. On the other hand, for rough sample surface with three dimensional islands, the electron beam transmits through the protrude parts of islands, the diffraction pattern becomes spotty.

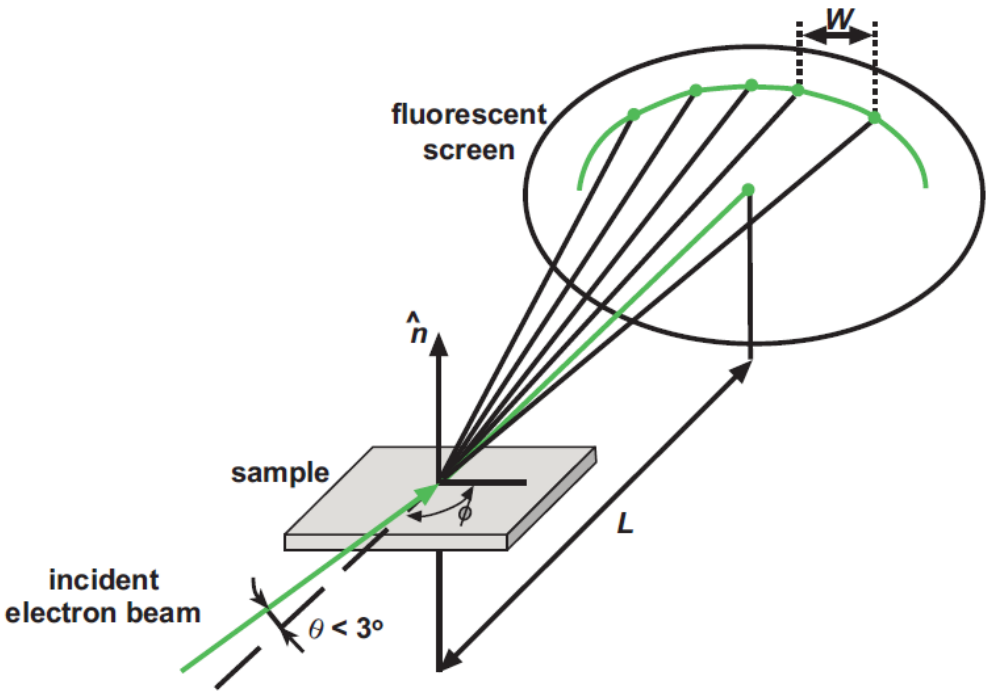

Figure 3.1.6: Schematic diagram of RHEED geometry [77]

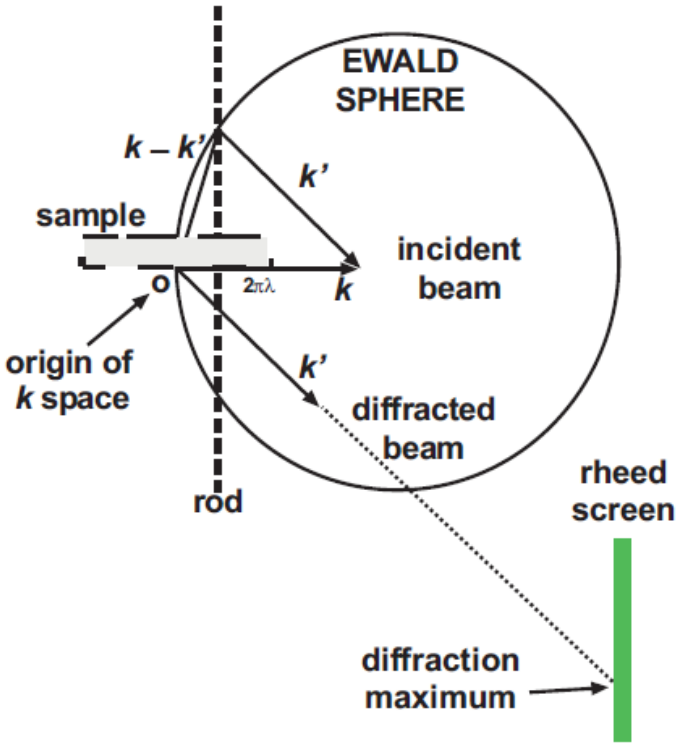

Figure 3.1.7: Diffracted beams with wave vector, **k**' generating diffraction peak on the screen as the Ewald sphere of radius, **k** and the reciprocal lattice rod intersect with each other (satisfying Laue diffraction condition) [77].

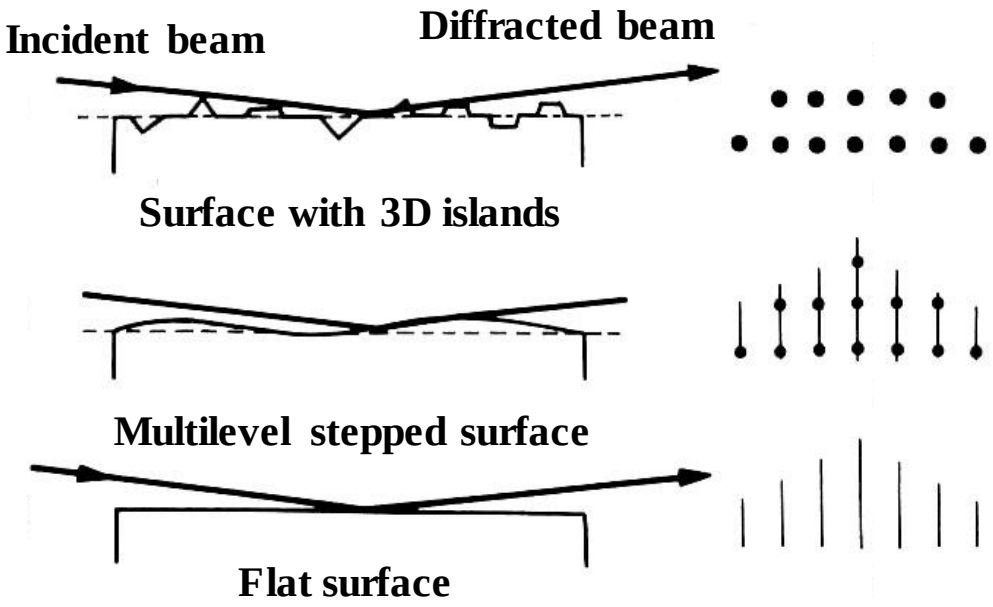

Figure 3.1.8: RHEED Diffraction pattern from sample surface having different morphology

3.1.4 Radiofrequency (rf) plasma source

In this study, the nitrogen (N) doping has been performed by irradiating the substrate with nitrogen gas. An ER-1000 rf-plasma source from EIKO has been used. This device can active species of neutral atomic nitrogen at high frequency discharge of 13.56 MHz and irradiate the substrate surface. The rf-power supply can output up to 300 W of plasma power and the high frequency coil inside the main body discharges. The advantages of the ER-1000 type rf- plasma source are described below:

1. Since the discharge chamber is sufficiently large and has no electrode, even if plasma discharge is continued for long time, it is possible to supply stable nitrogen plasma without any contamination.

2. It is possible to monitor the intensity of plasma emission during the discharge by an optical fiber scope and to adjust the amount of beam.

3. Growth can be performed without damaging the substrate by trapping active ions using parallel plate electrodes near the jet nozzle.

However, in this study, the ion trapper cannot be used because it was broken. So, not only the neutral active species but also the ionized species has been irradiated to the substrate. Figure 3.1.9 represents the N-spectra observed in this research. The mass flow control unit PAC-D2 manufactured by STEC corporation, has been used to adjust the gas flow rate. In this apparatus, the flow rate can be controlled in the range 0 ~ 1000 by a digital scale. In the case of N-doping the flow rate has been maintained at 0.3 cc/min. In fact, in MBE, since the chamber is an ultra-high vacuum; this value may not be essentially accurate.

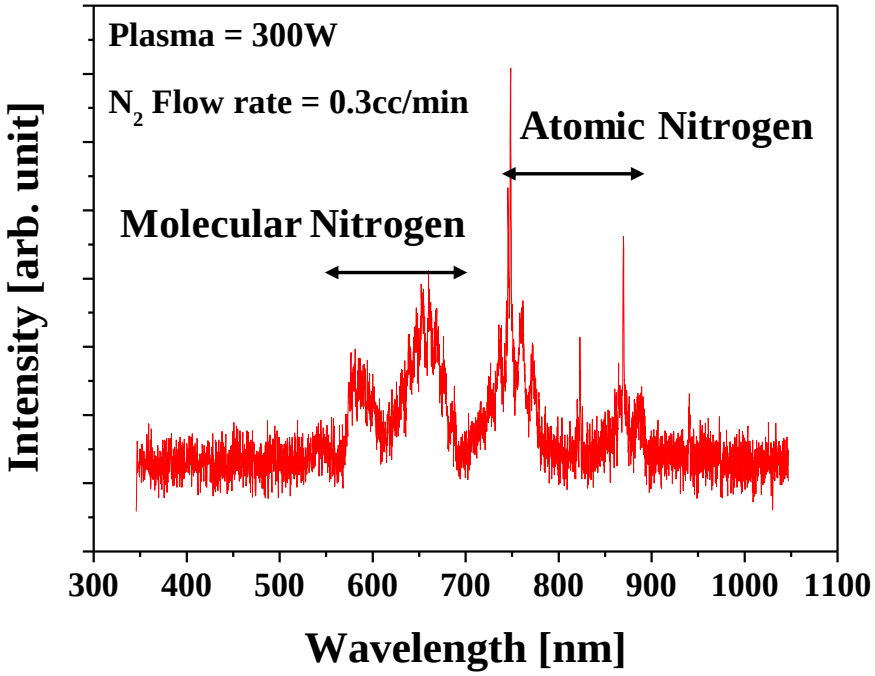

Figure 3.1.9: Nitrogen spectra showing active species of nitrogen generated by radiofrequency plasma

Figure 3.1.10 represents the schematic diagram of the plasma source. The amount of active nitrogen emitted by the plasma source to the substrate is varied by changing the distance between the exit and the substrate. The amount of N-doping concentration is higher if the position of the plasma source is closed to the substrate and N-doping concentration is lowest for the farthest position of the plasma source. The N-doping amount can also be changed by using the size of the holes in the plasma shutter by keeping the position of plasma source same. In this process, we can vary the N-doping amount under three status namely, small shutter open (diameter of the hole ≈ 0.3 mm), large shutter open (diameter of the hole ≈ 1.0 mm) and fully shutter open. Another option to change the N-doping amount is to the operating power of the plasma source and also by changing the flow rate of the N_2 gas. In our study, we have prepared the N-doped samples by changing the size of the holes in the plasma shutter, the plasma power and also the distance between the plasma source and the substrate.

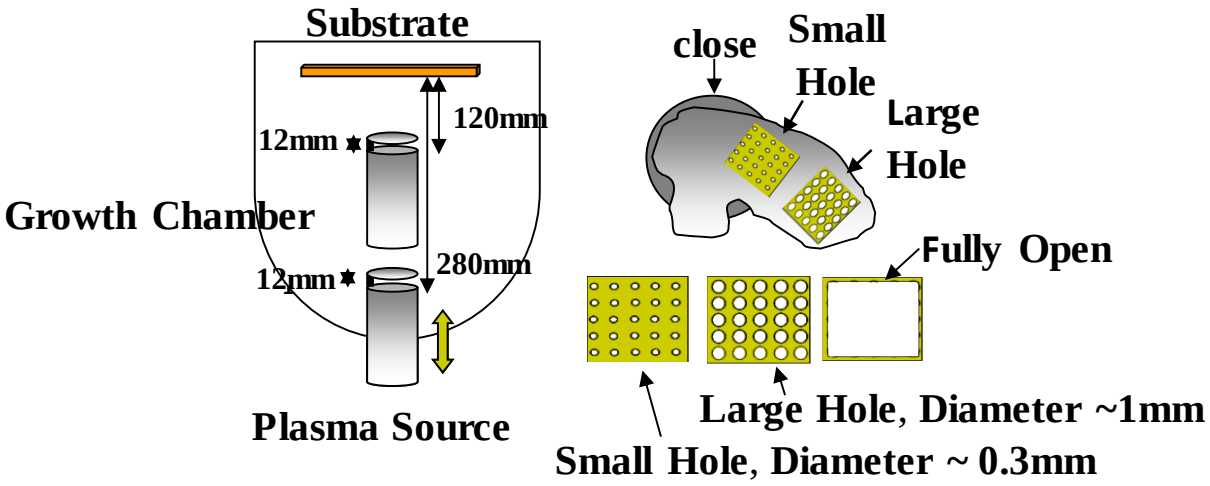

Figure 3.1.10: Schematic view of the variation of N-doping amount in samples

3.2 Samples characterization: Compositional analysis of elemental species

3.2.1 Electron probe micro-analyzer (EPMA) measurement

In this study, we have used the electron probe micro-analyzer (EPMA) to measure the Fe composition in the undoped and N-doped (Zn,Fe)Te thin films. Figure 3.2.1 represents the EPMA system EPMA (JEOL JXA - 8100) used in this study. The system is usually functioned by four major components such as, electron gun, several electromagnetic lens, a sample chamber with adjustable sample stage (X-Y-Z) and several set of electron detectors. The functional details of the EPMA system has been presented in Fig. 3.2.2. The electron gun works as an electron source. The electromagnetic lenses are positioned to condense and focus the electron beam. These electron optics-based lenses work in a similar way as light optics. The electron detectors usually collect the X-rays and secondary electrons emitted from the sample surface. The key noting point about EPMA is that it can precisely measure the quantitative elemental analysis at very small sizes (~ 1-2 microns) by using wavelength-dispersive spectroscopy (WDS). The operational principle of EPMA has been schematically shown in Fig. 3.2.3. When an electron beam of sufficiently high energy is incident on the sample, the bombardment between the electron and the sample yield

Figure 3.2.1: The EPMA system (JEOL JXA - 8100) used in this study

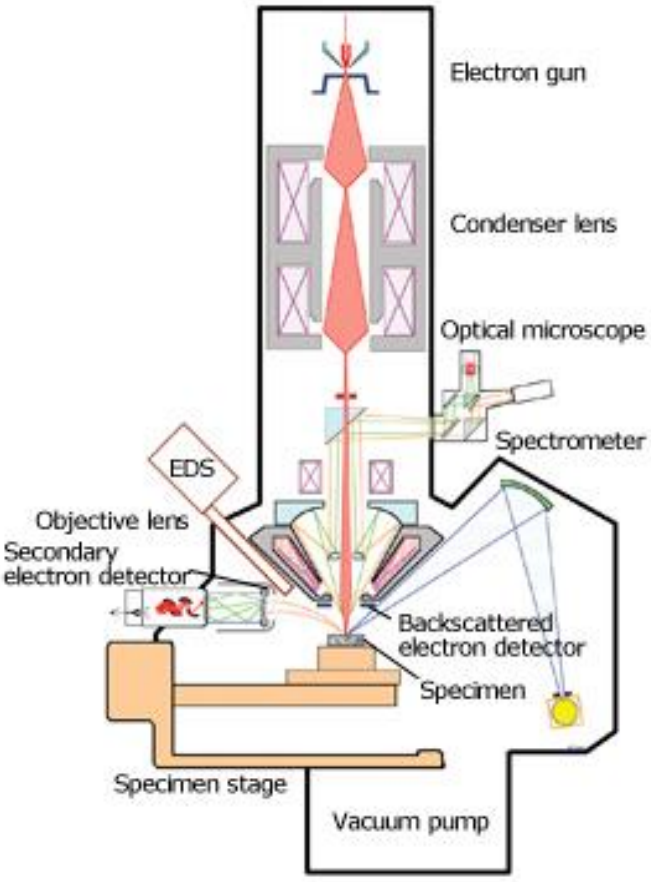

Figure 3.2.2: Functional components of an EPMA system [78]

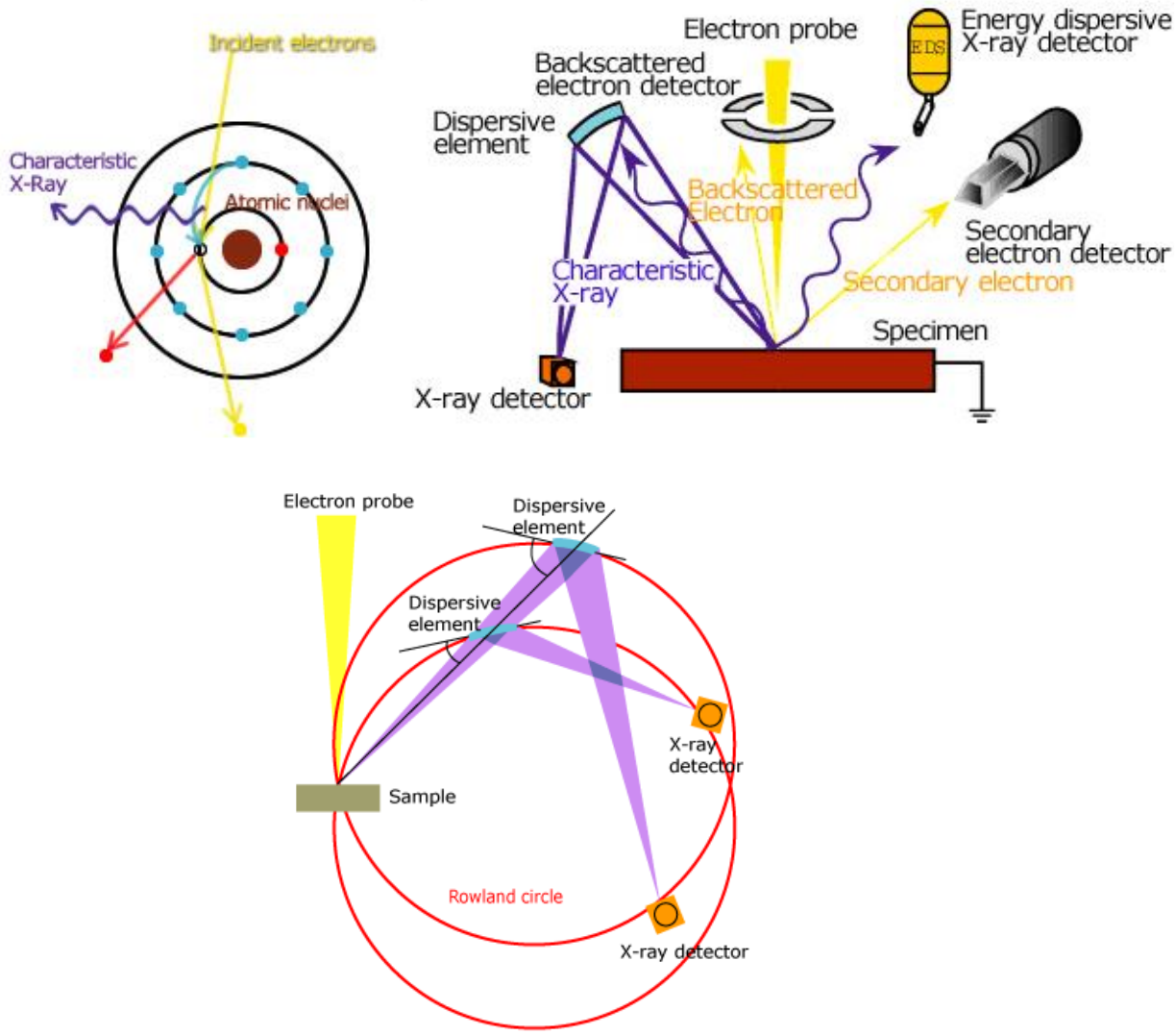

Figure 3.2.3: Operational principle of the EPMA system [78]

Characteristic X-rays and derivative electrons such as secondary, backscattered and auger ete. These X-rays are categorized by using analytical crystals with specific lattice spacings. The sample and analytical crystal are involved in such a geometrical orientation that X-rays facing the analytical crystal at a particular angle will satisfy the Bragg's condition are reflected and a single wavelength is travelled to the detector. The sample, analytical crystal and the detector must stay on the Rowland circle to focus X-rays efficiently as shown in Fig. 3.2.3. Detectors in wavelength-dispersive spectrometers are generally gas proportional counter types. Once, the X-ray intensities of all the element of interest are measured, they are compared with standard samples containing known values of the respective elements. The penetration depth of the incident X-ray beam in the sample depends on the accelerating voltage. In our research, the thickness of the undoped and N-doped (Zn,Fe)Te thin films are around 700 nm and we have used accelerating voltage and current of 7 keV. In our measurements, we take data for 10 positions of each samples with the probe diameter of around 10 μm, accelerating voltage, 7 keV and current, 1×10^{-7} A and take the average to determine the Fe composition.

3.2.2 Secondary ion mass spectroscopy (SIMS) measurement

In SIMS measurements, a primary beam of either positive (for example, Cs) or negative (for example, O) is accelerated and focussed on a sample surface to generate secondary ions which are then shifted to a mass spectrometer under a high electrostatic potential. The interaction between the primary beam and the sample under high vacuum condition can yield sufficient energy to ionize more elements. However, the amount of ionized species depends on the mode of SIMS measurement. In the static SIMS, the amount of ionized species is of the order of 1×10^{12} ions/cm^2 and is generally used for analysis of elemental species in the atomic monolayers of material surfaces. On the other hand, in the dynamic mode which is generally used for bulk analysis of the elements require more ionized secondary ions to provide precise information. In the static SIMS measurement, which is used in this study, a pulsed ion beam of Cs+ is utilized to liberate secondary ions from the topmost atomic layer of the thin film sample. The schematic view of the operation principle of SIMS measurement process is demonstrated in Fig. 3.2.4. These secondary ions are then speed up into a flight path on the way to the detector and their mass can be determined based on the "time-of-flight" principle. Since the "time-of-flight" from the time of impact to the detector on the scale of nanoseconds, a mass resolution as fine as 0.00N atomic mass units (one part in a thousand of the mass of a proton) can be achievable.

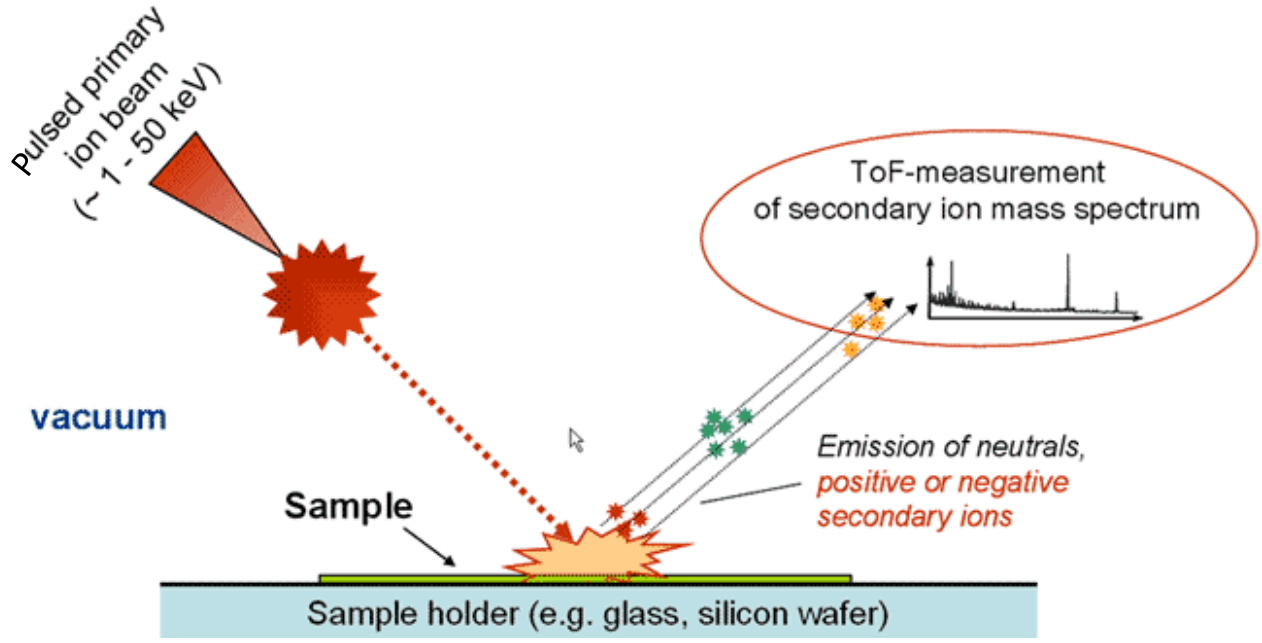

Figure 3.2.4: The operation principle of "time-of-flight" secondary ion mass spectroscopy [79]

Since secondary ions are mainly released from the surface region of several tens of angstroms, SIMS are regarded as promising tool for analyzing the elemental species in the thin film sample. Quantitative chemical analysis in the depth direction of the sample can be performed by mass analysis of secondary ions liberated from the uniformly sputtered the surface. In this study, SIMS measurement has been performed based on this principle to measure the N doping amount of (Zn,Fe) Te: N thin films. We have used primary ion beam of $^{133}Cs^+$ accelerated at 3keV and quantified the N concentration by measuring a N-implanted ZnTe thin film as reference. We confirmed an almost flat depth profile of N concentration across the entire region of the N-doped film.

3.3 Structural characterization of samples:

3.3.1 X-ray diffraction (XRD) measurement

In this study, XRD measurement has been performed with an attention to investigate the crystal structure and hence, the lattice constant of the sample. In a crystalline solid, the atoms behave like a periodic array of coherent scatterers and can diffract light. Diffraction from different planes of atoms produces a diffraction pattern which provides information about the atomic arrangement in the crystal. Figure 3.3.1 represents the basic configuration of a diffractometer. The detector moves in a circle around the samples. The incident angle of the X-ray beam is represented by ω and the diffraction angle between the incident beam and the detector is reparented by 2θ. In the θ: 2θ instrument (Rigaku) used in this study, the tube is fixed, the sample rotates at θ°/min and the detector rotates at 2θ°/min. Detector records the number of X-rays observed at each angle 2θ. In this study the X-ray intensity has measured by 2θ in the range of 10° - 120° and the X-ray source used is Cu Kα. Two x-rays Kα1 and Kα2 has been irradiated simultaneously. The wavelength of the respective X-rays is: λ (Kα1) = 1.540562 Å and λ (Kα2) = 1.544390 Å.

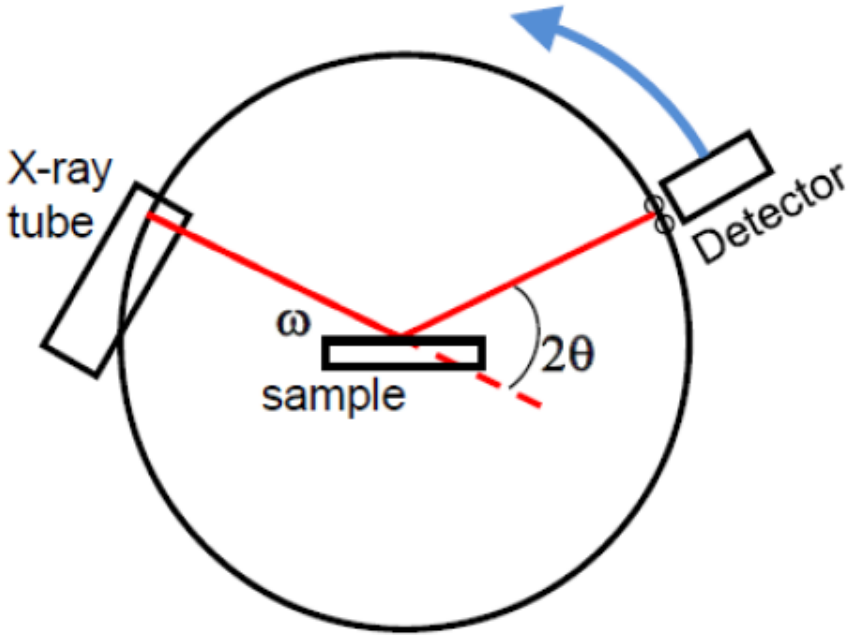

Figure 3.3.1: The basic configuration of an X-ray diffractometer [80].

Figure 3.3.2 represents the operational principle of an X-ray tube to generate characteristic X-rays. The cathode is irradiated by a heating source to generate an electron beam. The electron beam is then accelerated towards the metal target (usually tungsten) by applying high voltage source. X-rays are generally created when the electrons are suddenly decelerated upon collision with the metal target. If the collide electrons have sufficient energy to

liberate an inner shell electron from the metallic target, then an enteron form higher energy shell will fill the vacancy produced in the inner shell and in turns, emit X-ray photons (characteristic X-rays).The target heated material is always kept water cooled to avoid energy dissipation and the target and the filament must be contained in a vacuum condition. The characteristic X-rays represented in Fig. 3.3.3 illustrating two peaks will occur if the vacancies are generated in the n = 1 or *K*-shell. The X-rays associated with the transition from the n = 2 (*L*-shell) to n = 1 (*K*-shell) levels are known as *K*α X-rays. Similarly, that associated with the transition from the n = 3 (M-shell) to n = 1 (*K*-shell) levels are known as *Kβ* X-rays. Since the (*L*-shell) consists of three sub-energy levels (*L*I, *L*II, *L*III), the transition from *L*III sub-shell to the *K*-shell is referred to as *K*α1 and from *L*II sub-shell to the *K*-shell is referred to as *K*α2.

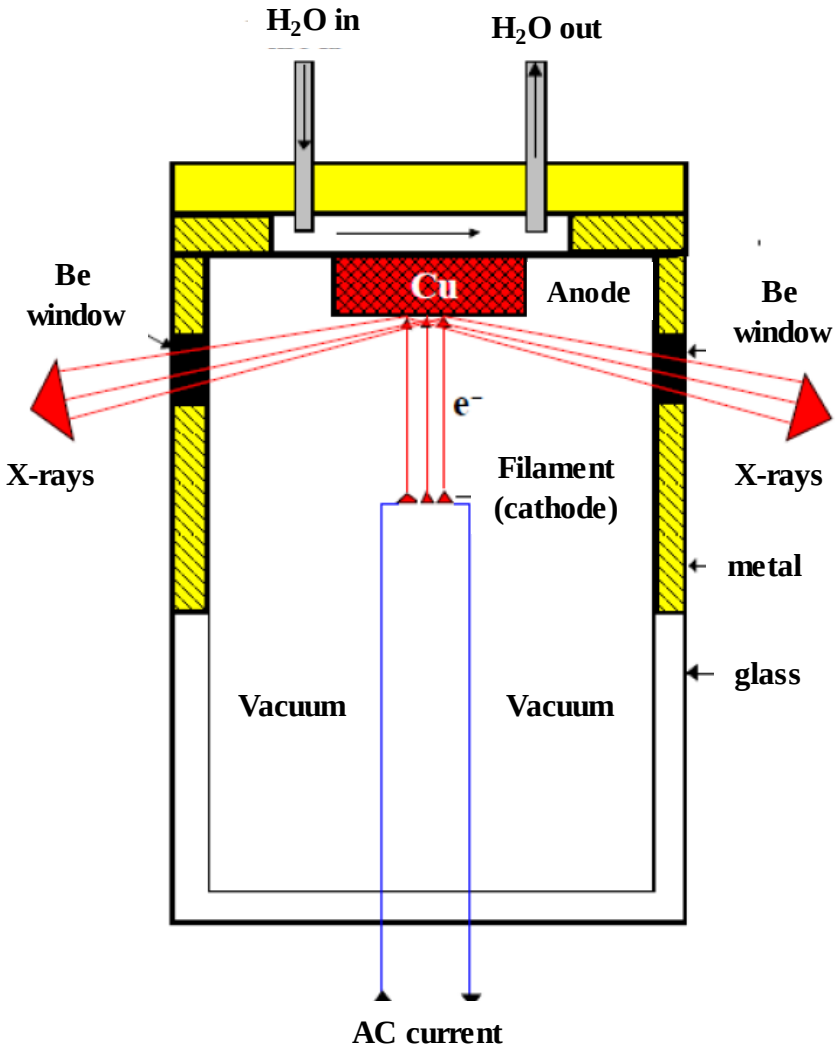

Figure 3.3.2: Schematic view of the construction details of an X-ray tube [80]

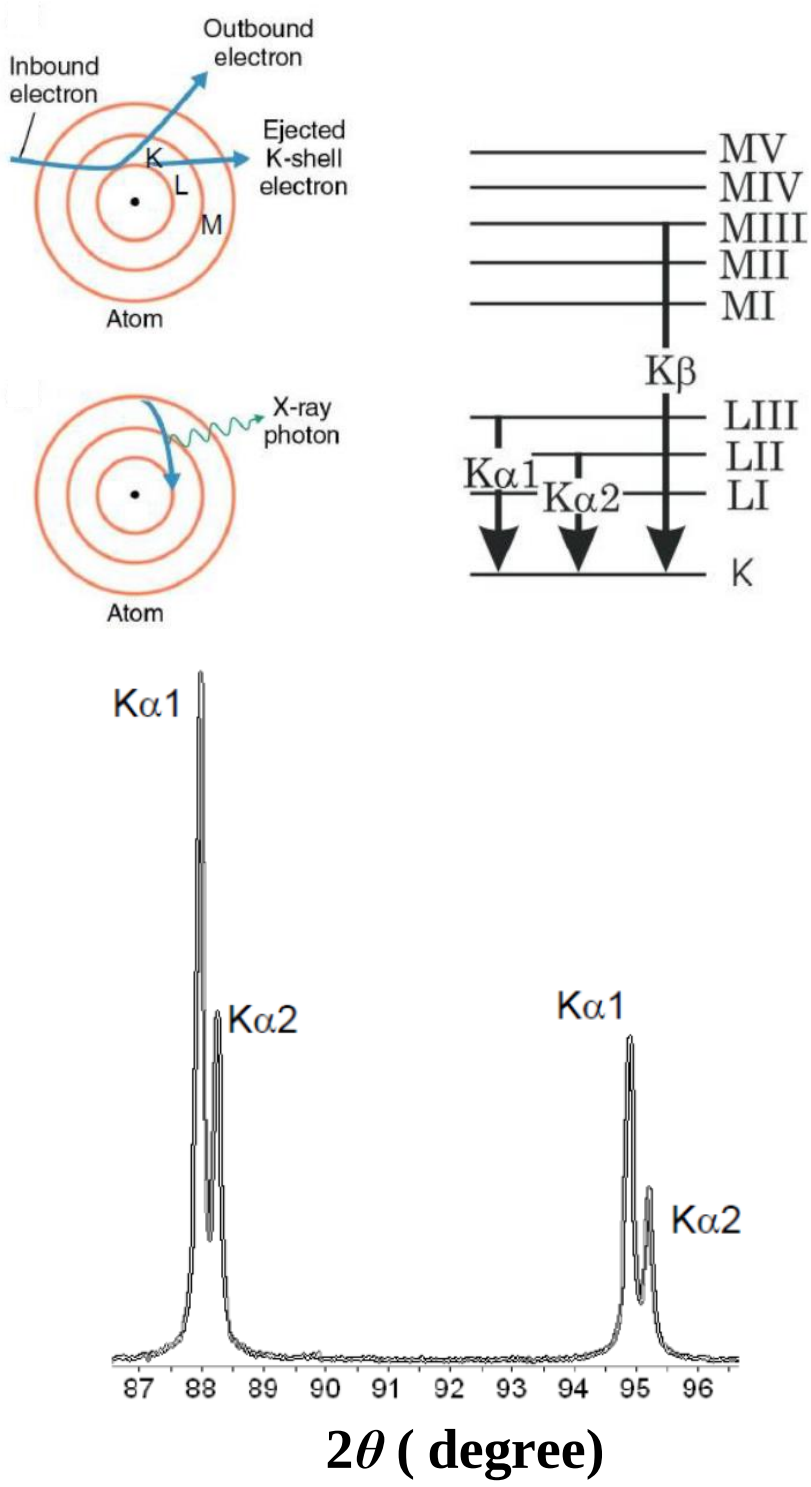

Figure 3.3.3: The operation principle of an X-ray tube generating characteristic X-rays (*K*α1 and *K*α2) from Cu *K*α X-ray source. The *K*α1 and *K*α2 doublet are always present as shown in the diffraction pattern.

Here, we have presented the method used in this study to calculate the lattice constant, a by using the 2θ values of the diffraction peak detected by the XRD measurement. In this case, we have mentioned the lattice constant, a measured by using the Bragg's law for the ZnTe (400) diffraction,

$$2dsin\theta = \lambda \quad 3.3.1$$

Where, d represents the interplanar distance and the λ is the wavelength of the X-ray used. Since ZnTe has cubic zinc-blende crystal structure, we can write $d = a/4$ for the ZnTe (400) diffraction peak which yields the relation:

$$\text{Lattice constant, } a = \frac{2 \times 1.540562}{Sin\theta} \quad 3.3.2$$

In this study, we have used the above equation to calculate the lattice constant of undoped and N-doped $Zn_{1-x}Fe_xTe$ thin films. The diffraction peaks have also provided us the information about the presence or absence of extrinsic precipitates.

3.3.2 X-ray absorption fine structure (XAFS) spectroscopy

In this study, we have used the X-ray absorption fine structure (XAFS) analysis to investigate the electronic state and local environment of Fe in undoped and N-doped $Zn_{1-x}Fe_xTe$ thin films. In the XAFs spectroscopy, the broadband X-ray spectrum from a synchrotron provides rapid, highly accurate absorption measurements. We have used the XAFS set up in the beamline of BL9A and 12C of the high energy accelerator research organization (KEK). In case of X-ray diffraction, we get information about the average structure of the coherent portions of the solid. However, XAFS spectroscopy is a short-ranged technique which provides insight into the average structure surrounding each absorption sight. For example, we can measure the distances between the absorber and the nearest neighbour atoms, the number and typed of absorber atoms and the oxidation sate of the absorbing element. By choosing the energy of the X-ray, we can get information for any element in the sample. That is, XAFS spectroscopy is an element specific technique. Figure 3.3.4 represents the typical set up for XAFS measurement. The full spectrum of X-rays radiated from the synchrotron travel though an entrance slit to the double crystal monochromator in which two parallel silico crystals are positioned making an angle, θ with the incoming beam. This X-ray beam is then allowed to pass through an ion chamber and the intensity is measured as I_0. Here, a part (50 – 90%) of the intensity of the beam is absorbed and the reduced intense beam, I is incident on the sample. The relationship between I_0 and I is expressed as:

$$I = I_0 e^{-\mu(E)L} \quad 3.3.3$$

Where μ (E) represents the energy-dependent absorption coefficient of the sample, L is the sample thickness and E is the energy of the incident x-ray.

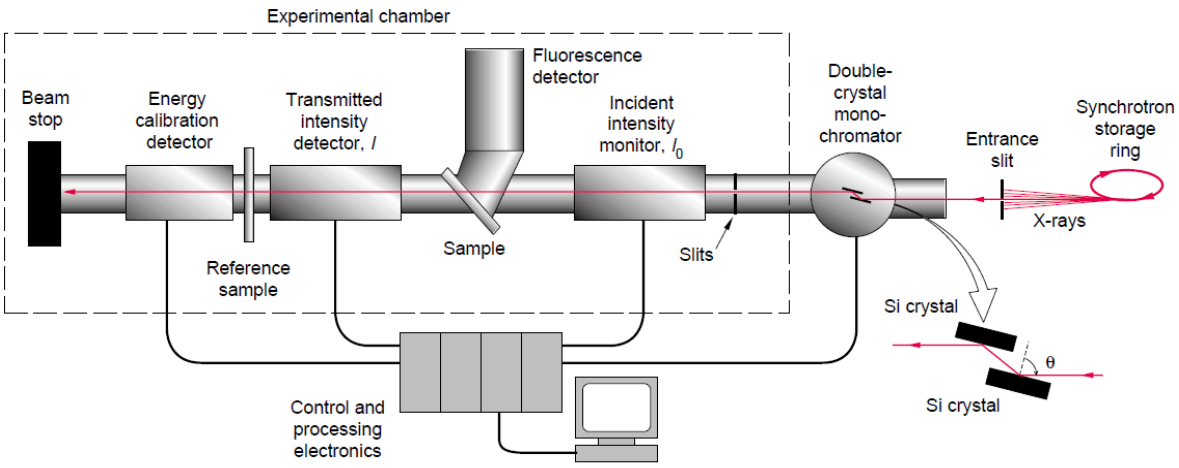

Figure 3.3.4: The typical experimental set up for X-ray absorption fine structure (XAFS) analysis [81]

The X-ray absorption spectrum exhibits a tendency of decreasing intensity with increasing energy as shown in Fig. 3.3.5. When the energy of the incoming photons is sufficient to liberate an electron from the inner core level to a n excited state or to the continuum, a sharp rise in the absorption intensity is seen. This is referred to as the absorption edge or threshold energy. For any energy above this, the photoelectron possesses kinetic energy which is expressed as:

$$E_k = h\vartheta - E_{binding} \qquad 3.3.4$$

Since the synchrotron can provide energy in excess of 10 keV, the ejection of electron from the inner orbitals such as, 1*s*, 2*s*, $2p_{1/2}$, $2p_{3/2}$ has been observed. The absorption edge associated with the excitation of electron from 1*s*, 2*s*, $2p_{1/2}$ and $2p_{3/2}$ shells are generally termed as *K*, L_1, L_2 and L_3- edge respectively. Figure 3.3.6 represents the normalized XAFS spectra of a typical Fe foil. The narrow region of about 30 eV starting from just before the absorption edge is termed as X-ray absorption near edge structure (XANES). This region carries information about the oxidation state of the observed atom. The oscillatory part the begins there after and persists up another 100 eV is termed as extended X-ray absorption fine structure (EXAFS). This region carries the most important information about the local environment around the absorbed atom such as, the distance between the absorber and its nearest neighbours, the number and type of neighbouring atoms.

According to Quantum mechanics, the outgoing photoelectron can be represented as spherical wave having wavelength, λ given by the equation:

$$\lambda = \frac{2\pi}{k} \qquad 3.3.5$$

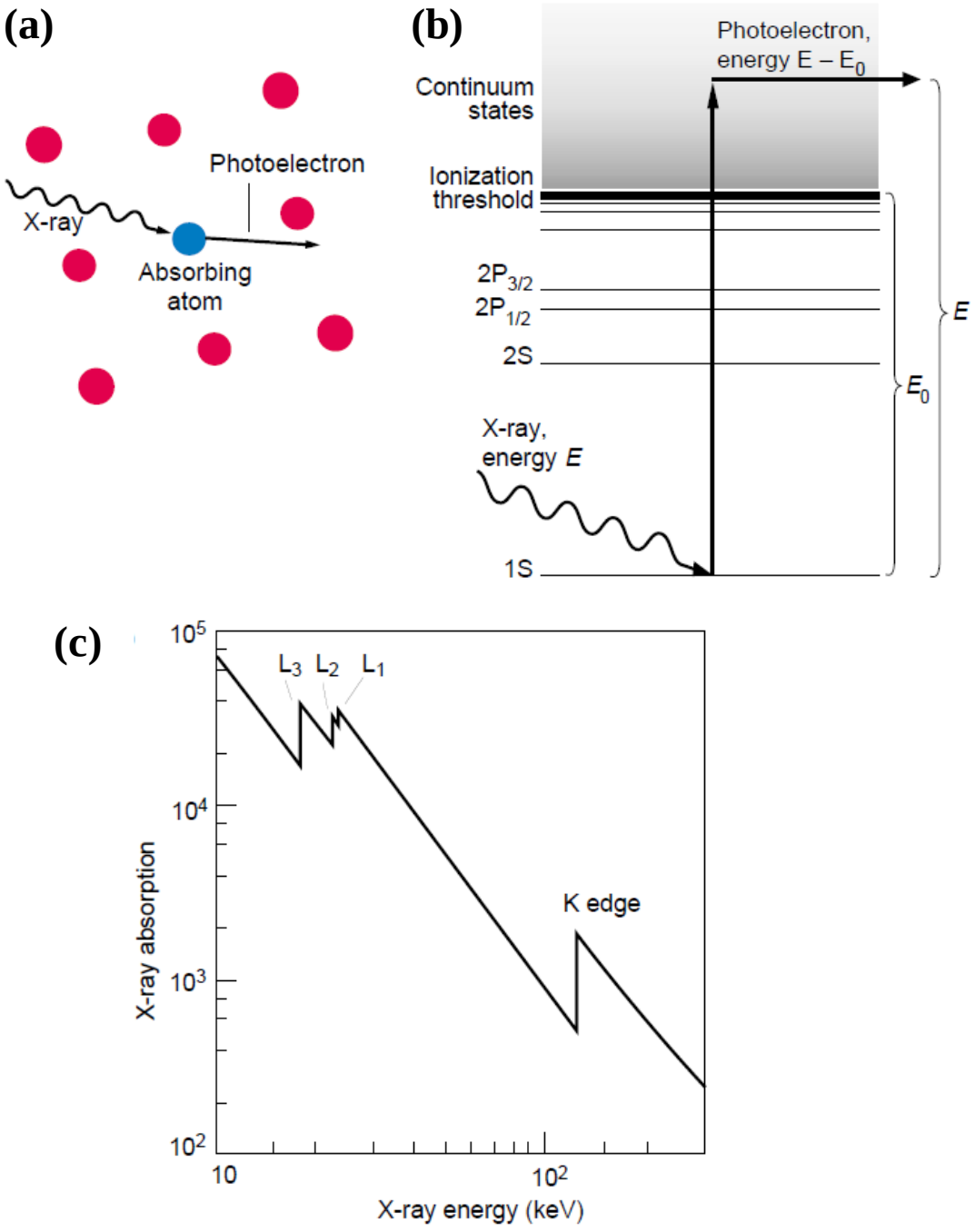

Figure 3.3.5: The mechanism of absorption of X-ray photon in the XAFS spectroscopy. **(a)** An atom (blue) is surrounding by its neighbours (red) **(b)** The schematic energy level diagram of the absorbed atom and the energy level position of the photoelectron **(c)** The schematic diagram representing the absorption edges corresponding to different core inner levels. [81]

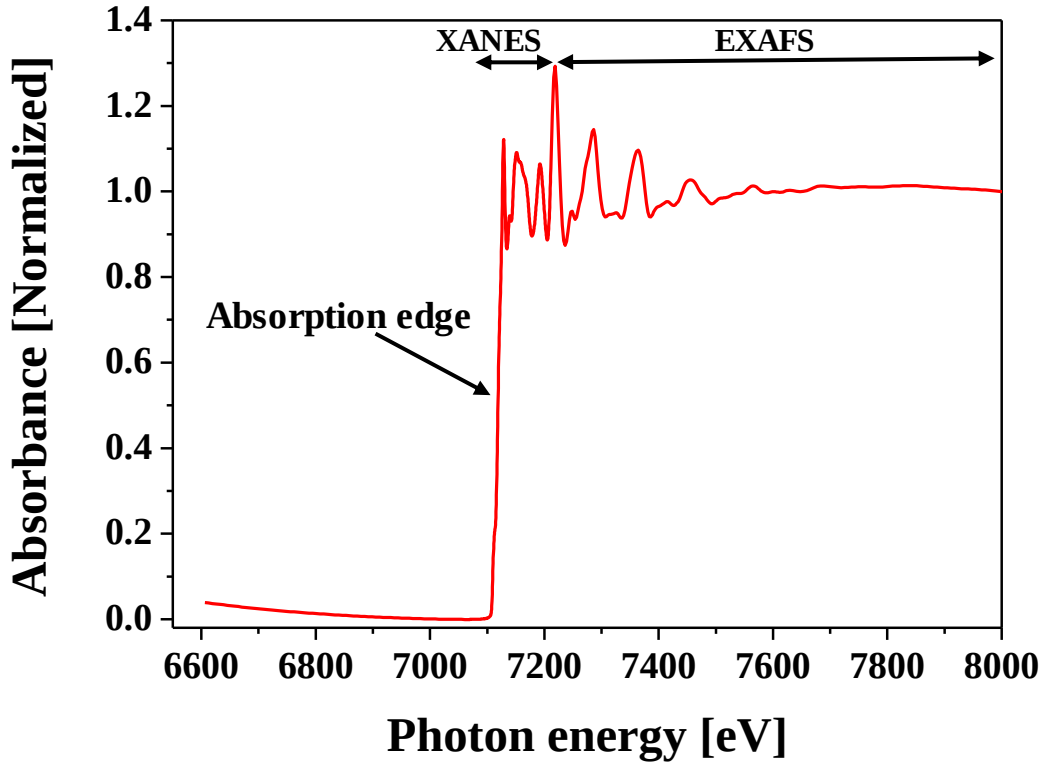

Figure 3.3.6: The normalized XAFS spectrum for an elemental Fe foil

$$\text{and } k = \sqrt{\frac{8\pi^2 m(h\vartheta + E_0 - E_{edge})}{h^2}} \qquad 3.3.6$$

In the EXAFS region due to the large kinetic energies of the photoelectron, the scattering of the photoelectron from the nearest neighbours is usually explained on the basis of single-scattering approximation. The absorption above the absorption edge can be expressed as

$$\mu_{total} = \mu_0 [1 + \chi_{Ex}] \qquad 3.3.7$$

Where μ_0 represents the linear absorption coefficient in the case of an isolated atom and χ_{EX} explains the oscillatory portion of the scattering of the outgoing photoelectron with the neighbouring atoms. The final electron state is described as the superposition of the outgoing and scattered waves as shown in Fig. 3.3.7. The experimentally observed EXAFS oscillations of e Fe foil as a function of the wave vector, *k* is schematically shown in Fig. 3.3.8.

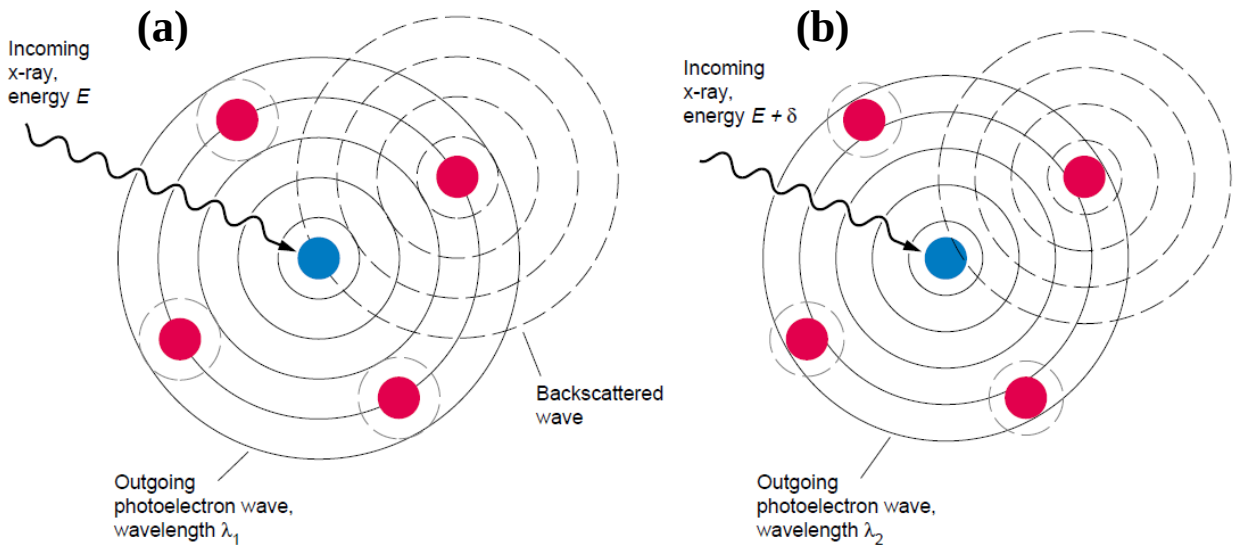

Figure 3.3.7: The interference pattern between the outgoing photoelectron wave and the backscattering wave form the nearest neighbours **(a)** the constructive interference condition and **(b)** the destructive interference condition [81].

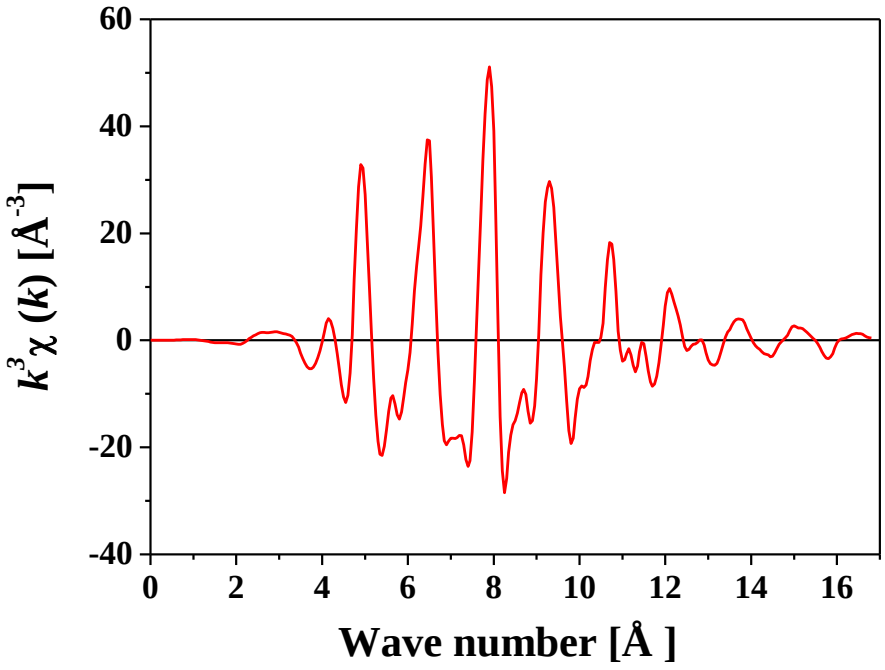

Figure 3.3.8: The EXAFS oscillations of an elemental Fe foil measured by XAFS spectroscopy.

In the single scattering plane wave approximation, the EXAFS formula as function of wave vector, *k* can be written as:

$$\chi\,(k) = \sum_{i=1}^{shells} A_i\,(k)\ \sin \emptyset_i\ (k) \qquad 3.3.8$$

The backscattering is resonant in nature, the amplitude of the backscattering wave is enhanced at energy values of the photoelectron that are equal to the orbital energies in the backscattering atoms. Since each atom has its unique electronic configuration, the backscattering pattern as a function of wave vector, *k* is also unique. The amplitude A_i (*k*) of the EXAFS equation provides information about the coordination number around the absorbed atom and the argument of the sine function,$\emptyset_i$ (*k*) gives the information of the interatomic distance between the absorber and the nearest neighbours atoms. The Fourier transformation of $\chi\,(k)$ represents the radial distribution function (RDF) [82]. The Fourier transformation is defined as

$$FT\,(k) = \frac{1}{\sqrt{2\pi}} \int_{k_{min}}^{k_{max}} k^n\ \chi\,(k) e^{i2kR}\,dk \qquad 3.3.9$$

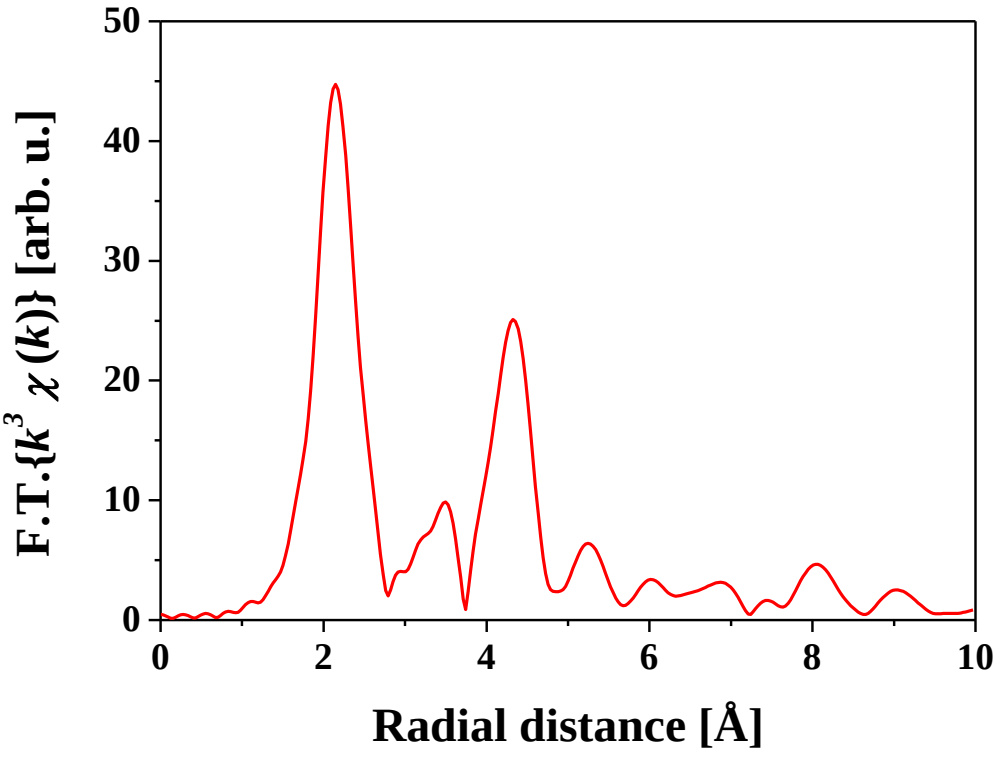

Figure 3.3.9 The radial distribution function derived from the Fourier transformation and weighted by k^3 of the EXAFS oscillations for an elemental Fe foil measured by XAFS spectroscopy.

In the Fig. 3.3.9, the radial distribution function for the Fe foil has been presented. In order to avoid contributions from low atomic number element in the EXAFS oscillations, it is multiplied by k^3. At higher values of *k*, the scattering power of high atomic number elements is larger. The low atomic number elements may come from the support and other absorbates present in the sample surface.

3.3.3 Transmission electron microscope (TEM) observation:

The transmission electron microscopy is an instrument built specifically for analysing and visualizing the sample on the micro or nano-scale dimension to an extended version image over a fluorescent screen. Figure 3.3.10 represents the functional details of a standard TEM system. Either a thermionic electron gun or field emission gun is used to produce electron beam, which is accelerated at high energy, typically in the range of 100 – 300 kV. According to the de-Broglie wave-particle dualism, the wavelength of the accelerated electron at high energy limit can be expressed by taking relativistic effect into account as:

$$\lambda = \frac{h}{\sqrt{2m_0 eU\left(1 + \frac{eU}{2m_0 c^2}\right)}} \qquad 3.3.10$$

Where, *U* is the electric field strength, m_0 is the rest mass of electron, *e* is the electron's charge, *c* is the speed of light and *h* is the Planck's constant. The electron beam is then travelled to the condensed apertures and lenses to converted into to a parallel beam of light (TEM) or a focussed beam for scanning technique. They also help to get magnified image. The lens includes a coil of copper wire inside an iron cylinder and behaves as a magnetic lens. In the presence of electric current, the coil creates a magnetic field in the iron cylinder and experiences the Lorentz force given by:

$$\boldsymbol{F} = -e\,(\boldsymbol{U} + \boldsymbol{v} \times \boldsymbol{B}) \qquad 3.3.11$$

Where, *U* represents the electric field strength, *B* is the magnetic field strength and *v*, is the velocity of electron.

The electron beam then strikes the sample. Most of the microscopes include goniometers to insert the sample holder inside the high vacuum chamber. In most of the cases, double tilt holders are used which provide the additional advantage of tilting an arbitrary oriented sample into two perpendicular directions. The objective lens is situated just below the specimen to generate the image. The quality of the image formed by the objective lens represents the resolution of the whole microscope. The diffraction lens system positioned under the objective lens are used to change the mode from imaging as shown (a) or the diffraction (b) in Fig. 3.3.10. The projective lens magnifies the image or diffraction pattern depending on the mode of measurement. In order to confirm high quality image, the aperture is needed to be set in the in the optical axis of the microscope. In the case of high resolution TEM, a large aperture is used to provide a pathway for some additional diffracted beam to enhance the interference to occur in the imaging plane. The final image or the diffraction pattern is can be directly viewed in the screen positioned in the projection chamber or by a CCD camera mounted below the microscope column. High vacuum condition in the measurement chamber is very important to avoid any unwanted interaction of the electron beam. In our study, high resolution transmission electron microscope (TEM) observation of N-doped (Zn,Fe)Te thin films have been carried out with an accelerating voltage of 300 keV (JEM-3100FEF, JEOL), together with chemical analysis using energy-dispersive spectroscopy (EDS). Cross-sectional pieces with thickness ~ 100 nm were prepared by standard mechanical polishing followed by Ar^+ - ion milling at 7.0 kV for more than 2 hours.

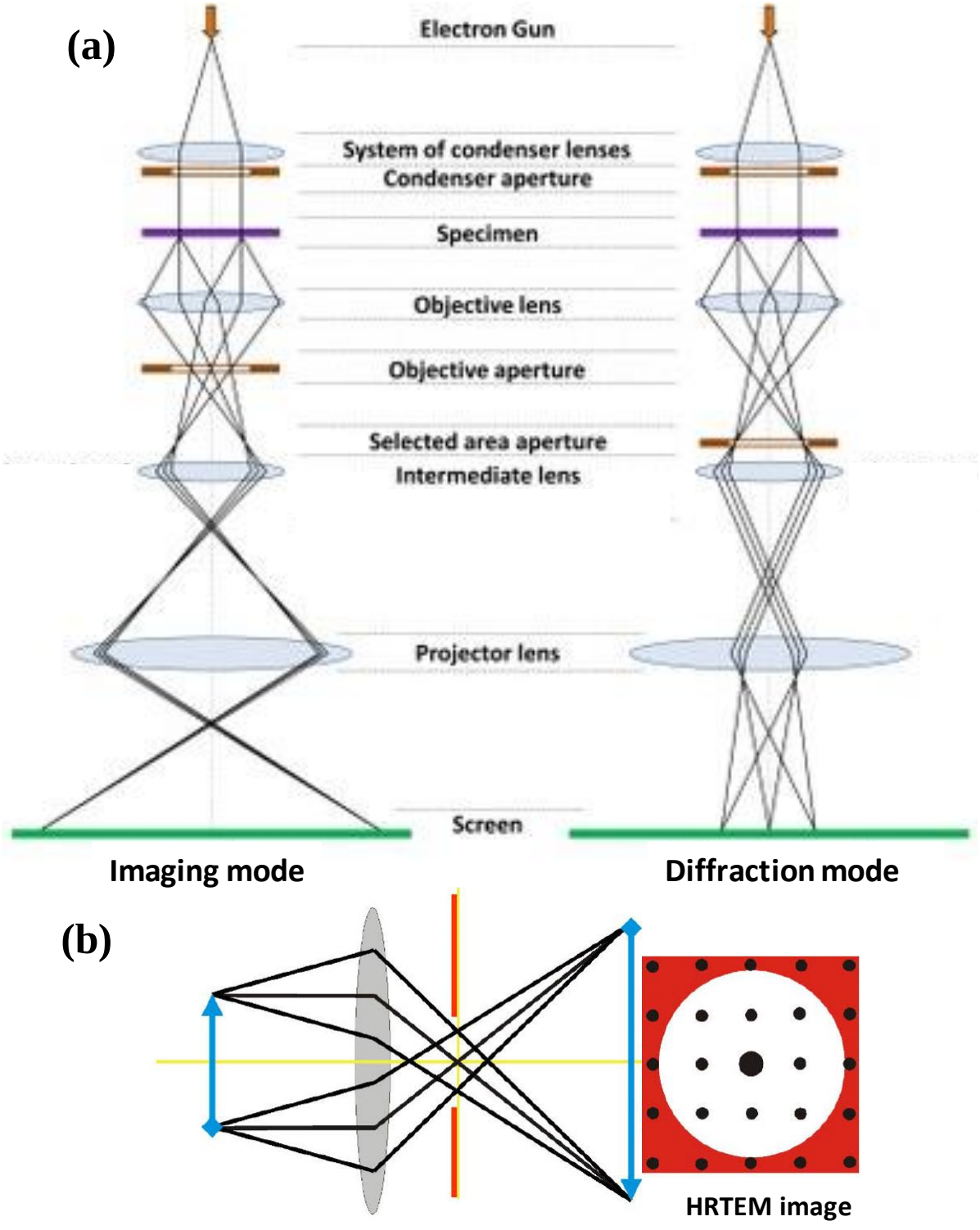

Figure 3.3.10: (a) Schematic representation of the pathway of electron beam in the imaging mode and the diffraction pattern mode **(b)** Imaging mode of high resolution TEM [82].

3.4 Magnetization measurement of samples:

3.4.1 Superconducting quantum interference device (SQUID) measurement

The SQUID (Superconducting quantum interference device) is used to measure the magnetization of samples precisely with the change of extremely small magnetic field. The device consists of a superconducting ring interrupted by resistive region, called Josephson junction. Depending on the number of Josephson junction, SQUID can be categorized as radiofrequency (rf) SQUID which contains only one Josephson junction and direct current (DC) SQUID which consists of two Josephson junctions. The junctions should be sufficiently thin for the superconducting Copper pairs to tunnel through the resistive layer (Josephson contact) which is referred to as weak link, without any voltage drop of the superconducting current.

The working principle of SQUID is based on the effect of flux quantization in the superconducting ring which in turns, provide an insight for the passage of superconducting current without any resistance. The reason behind this, is the long-ranged coherence of the superconducting wavefunction. In other words, the wavefunctions of electron at different points in a superconductor are related by a simple phase change. For a full rotation in the superconducting ring, the phase change will be 2π so that it will provide the wavefunction to a single value at a particular point. According to the electromagnetic theory, the application of magnetic field to a superconductor induces a change in the phase of the wavefunction. Since the phase change for a complete rotation is some multiple of 2π to maintain the single-valued wavefunction, the flux contained within the ring can only accept certain discrete values. Specifically, the superconducting ring usually possesses a magnetic flux whose amount is an integral multiple of the elementary flux quantum,

$$\varphi_0 = \frac{h}{2e} = 2.068 \times 10^{-15} \quad 3.4.1$$

Where, *h* represents the Planck's constant and *e* is the elementary charge of an electron. It is known that the same principle can be applied even if the superconducting material makes small junction by sandwiching very thin piece of resistive material.

Now, if a small magnetic field is applied to the SQUID, the superconducting loop opposes the applied magnetic field by generating a screening current that flows around the loop. This screening current generates a magnetic field with equal magnitude but opposite to the direction of applied magnetic field and thus, canceling out the net flux in the ring. The applied magnetic field has reduced the critical current of the SQUID or the amount of bias that we can pass without any voltage in the SQUID. As the total amount of current is the sum of the screening current and the bias current in the Josephson junction, so when it exceeds the critical current, the SQUID becomes resistive, so a voltmeter will register a voltage across it. With the increase of the applied magnetic flux, the screening current increases. But as soon as the flux reaches half of a flux quantum, the junction monotonically goes to the normal state. The continuity of the superconducting loop is destroyed for one quantum of magnetic flux to pop inside the loop and the superconductivity is then restored again. Thus, the junction behaves as the gate that allow magnetic flux to enter or leave. In order to construct a magnetometer or magnetic field detector, the SQUID is usually operated with the bias current slightly greater than the critical current so that the SQUID always stays in the resistive condition. It should be noted that foe a constant bias current, the voltage across the SQUID is maximum only when the critical current is minimum. In this study, we have used the radiofrequency (rf) SQUID element of the magnetic property measurement system (Quantum design, MPMS XL) shown in Fig. 3.4.1 to measure the magnetic properties of undoped and N-doped (Zn,Fe)Te thin films

Figure 3.4.1: MPMS system used in this study

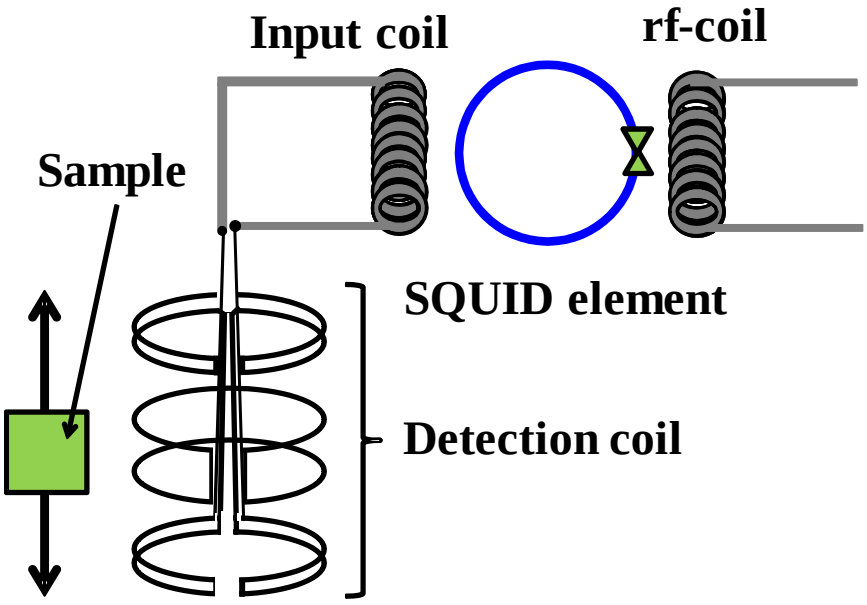

Figure 3.4.2: The functional details of a radiofrequency (rf) SQUID magnetometer

Figure 3.4.2 has demonstrated the structural components of the rf-SQUID measurement system. Here, magnetic flux is inductively coupled to the SQUID loop through an input coil that in turns, connected to the detection coils and a rf coil which is part of a high-*Q* resonant (tank) circuit. The tank circuit is tuned and controlled by a constant current radio-frequency oscillator which is weakly coupled to the SQUID loop. With the increase of amplitude of the oscillator, the detected output of the rf amplifier increases until a critical value. The rf drive is set so that the SQUID can operate at this optimal condition. But the detected output relies on the current flowing in the input coil. The magnetization of the sample is performed by moving through the superconducting detection coils. The detection coils are positioned outside the sample chamber and at the centre of the magnet. As the sample moves through the detection coils, the magnetic moment of the sample induces an electric current in the detection coils. The detecting coils, the connecting wires and the input coil construct a superconducting loop. As a result, any change of magnetic flux in the detection coils makes corresponding variations in the persistent current in the detection circuit which is proportional to the change in magnetic flux. As the SQUID works as a highly current-to-voltage converter, the variations in the current in the detection coils provide corresponding change in the output voltage of the SQUID which is proportional to the magnetic moment of the sample.

3.5 Transport properties of samples:

3.5.1 Physical property measurement system (PPMS): Hall measurement

In this study, we determine the carrier concentration and the type of carrier by using Hall measurements. At first, the principle of the Hall effect has been described. Figure 3.5.1 represents the schematic diagram for Hall effect. Here, the electric field is applied along the +x direction and the magnetic field is applied along the +z direction. We are considering the case of p-type semiconductor as shown in Fig. 3.5.1 (b). The Lorentz force due to the magnetic will act in the -y direction on the holes which are flowing along the +x direction in the p-type semiconductor. The magnitude of the Lorentz force is given by qv_xB_z, where q represents the elementary charge. An electric field, E_y will generate in the +y direction to oppose this force. In the steady sate, these two forces cancel each other and there will be no net flow of holes in the y direction. Thus, we can write:

$$qE_y = qv_xB_z \qquad 3.5.1$$

When E_y and v_xB_z become equal, the force acting on the holes in the y direction disappears and drifts towards the x direction. The generation of this electric field is known as the Hall effect and the equation (3.5.1) is known as the Hall electric field and the resulting voltage is called the Hall voltage.

In this study, a four-terminal method has been used to perform the Hall measurements. Figure 3.5.2 (a) shows the schematic diagram for the measurement by using the four-terminal method. The current, I_x (current density, J_x) is caused by the electric field, E_x along the length of the sample of width, b and thickness, d and the magnetic field of magnetic flux density, B_z is applied along the z-direction as shown in the Fig. 3.5.2 (a). An electric field, E_y (voltage, V_y) is generated in the y direction perpendicular to both electric field and the magnetic field. Lat us consider that the carrier group velocity is v, the magnetic flux density is B and the Hall electric field is E, the Lorentz force on the holes of charge $+q$ and the electrons of charge $-q$ is given by

$$F = \pm q[E + v \times B]\ (q > 0) \qquad 3.5.2$$

In the steady sate, a force in the y direction is not applied to the holes or electrons, so that, $F_y = 0$ is satisfied. This gives,

$$\begin{aligned} F_y &= \pm qE_y + q(v \times B)_y \\ &= \pm qE_y + q(v_z B_x - v_x B_z) = 0 \end{aligned} \qquad 3.5.3$$

Thus, $B_y = 0$ in equation (3.5.3) yields

$$\pm(E_y - v_x \times \mathrm{B_z}) = 0$$

$$E_y = v_x \mathrm{B_z} \qquad 3.5.4$$

Which represents the electric field generated in the y direction.

By assuming that the number of electrons is *n* and the number of holes, *p* and the current density, J_x,

$$J_x = -qnv_x\ (v_x < 0) \qquad 3.5.5$$

$$J_x = +qpv_x\ (v_x > 0) \qquad 3.5.6$$

Substituting equation (3.5.5) and (3.5.6) in equation (3.5.4), we get

$$E_y = -\frac{J_x}{qn} B_z = -\frac{1}{qn} J_x B_z\ (\text{Electron}) \qquad 3.5.7$$

$$E_y = +\frac{J_x}{qn} B_z = +\frac{1}{qn} J_x B_z\ (Hole) \qquad 3.5.8$$

E_y is in the +y direction when the carrier is hole and in the -y direction when the carrier is electron. The type of carrier can be determined by the direction of the electric field.

The magnitude of the x component of current, I_x and the y component of generated voltage, V_y are given by

$$V_y = b\, E_y \tag{3.5.9}$$

$$I_x = b\, dJ_x \tag{3.6.0}$$

After substituting in equations (3.5.7) and (3.5.8) gives,

$$V_y = -\frac{1}{qn}\frac{I_x B_z}{b} \quad \text{(Electron)} \tag{3.6.1}$$

$$V_y = +\frac{1}{qn}\frac{I_x B_z}{b} \quad \text{(Hole)} \tag{3.6.2}$$

Which gives,

$$-\frac{1}{qn} = R_H \quad \text{(Electron)} \tag{3.6.3}$$

$$+\frac{1}{qn} = R_H \quad \text{(Hole)} \tag{3.6.4}$$

Which gives,

$$R_H = \frac{V_y d}{I_x B_z} = \frac{V_y}{I_x\left(B_z/d\right)} \tag{3.6.5}$$

The sigh of the R_H follows the sign of the V_y. The R_H is called the Hall coefficient and the type of carrier can be determined from the sign of the Hall coefficient.

R_H can be experimentally measured, and the carrier concentration n and p can be calculated as,

$$n = -\frac{1}{qR_H} \quad (R_H < 0) \tag{3.6.6}$$

$$p = -\frac{1}{qR_H} \quad (R_H > 0) \tag{3.6.7}$$

In this study, we have also measured the temperature dependence of the N-doped samples by using the four terminal method shown in Fig. 3.5.2 (b). The current leads will create an electric field within the bar shaped sample. So, the voltage leads are arranged in such a way that they measure a potential drop across a region where the field line are relatively straight that is, in line with the current leads or separated by a distance that is small compared to their distance from the current leads. The voltage leads draw very little current or ideally no current. So, current though and potential drop across the sample can be measured with high degree of accuracy.

$$V = IR \tag{3.6.8}$$

$$\rho = \frac{RA}{L} = \frac{VA}{IL} \tag{3.6.9}$$

Where, V is the voltage, I is the current, R is the resistance, ρ is the resistivity, l is length and A is area of sample.

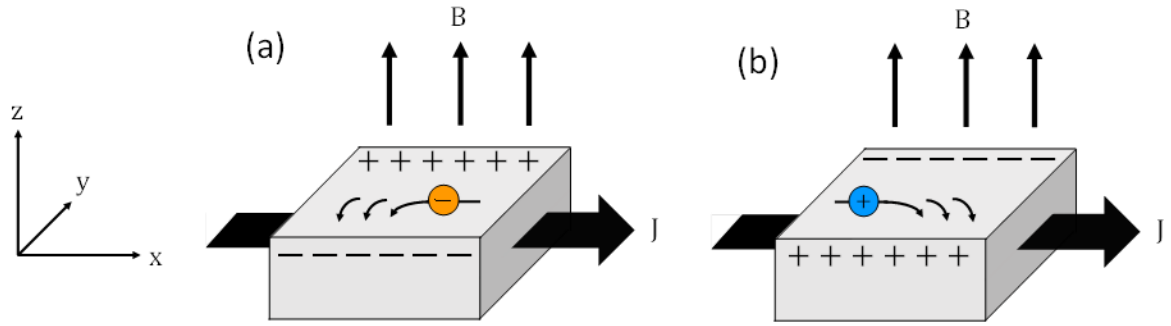

Figure 3.5.1: Schematic diagram of Hall effect

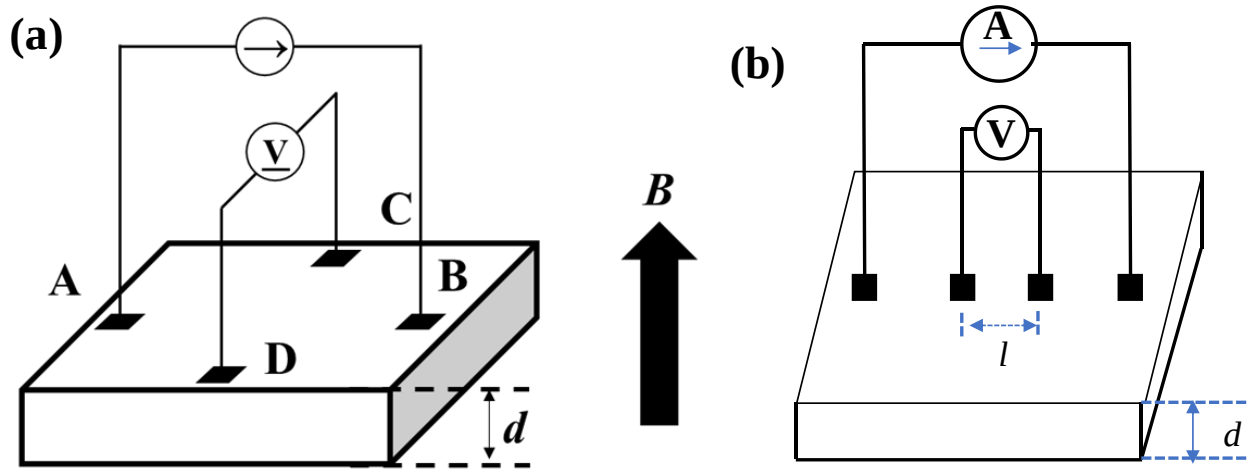

Figure 3.5.2: Four terminal method used for **(a)** carrier concentration measurement **(b)** temperature dependence resistance measurement.

3.6 Electric field control study

3.6.1 Formation of electric double layer transistor structure (EDLT) by using liquid electrolyte

In this study, the electric field has been applied by forming an electric double layer transistor (EDLT) structure using an ionic liquid between the magnetic layer and the gate electrode. An ionic liquid consists of cations and anions, which is also called molten salt at ambient temperature has been attracting attention in recent years.

We have introduced an example shown in Fig. 3.6.1 to explain the working principle of ionic liquid as electric double layer. We fabricate a structure in which an ionic liquid is sandwiched between a magnetic layer and a gate electrode, and copper wire is bonded to the magnetic layer and the electrode to apply external voltage. Then, when a voltage is applied with the magnetic layer side as the cathode and the electrode side as the anode, the ions move, and the cations densely accumulate on the surface of the magnetic layer. As a result, electrons are attracted to the surface of the magnetic layer, and EDL is formed by a layer in which ions are dense and a layer of electrons (Fig. 3.6.1). Since the thickness of EDL is about 1 nm or less, which is about the same as the ion radius, a huge electric field of about 10 MV/cm can be applied with an applied voltage of 1 V. In this study, to measure the magnetization inside the SQUID, a sample of several mm square is required for the convenience of measurement, but if an ionic liquid is dropped on the sample and introduced into the inside of the device, liquid may leak out. Therefore, by using an ionic gel in which the ionic liquid was mixed with the polymer, has been made so that it cannot leak from the sample surface.

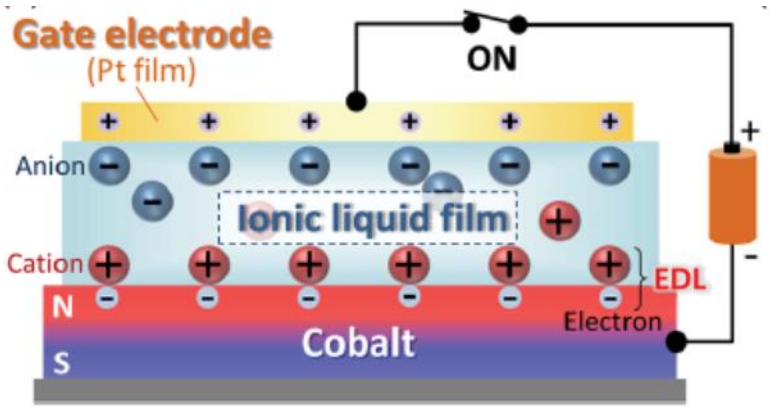

Figure 3.6.1: Example of sample structure using ionic gel as insulating layer [83]

Now, we have described the preparation technique of ionic gel. Ionic gel was prepared by mixing ionic liquid and polymer at a weight ratio of 10: 1. The ionic liquid in this study contains N, N-diethyl-N-methyl (2-methoxyethyl) ammonium [DEME] as cation and bis (trifluoromethylsulfonyl) imide [TFSI] as anion. The chemical structures of the cation and anion are shown in Fig. 3.6.2. Then, the formation of the device structure has been explained. Copper wire has been bonded to the backside of the sample with indium and adhesive glue to attach tightly. The adhesive used is a cyanoacrylate-based adhesive. Once the adhesive has dried, the ionic gel has poured onto the sample surface and after that a piece of Pt foil approximately of the sample size has been put on the ionic gel and wait some time for bonding. In some cases, the sample has gently heated on a hotplate for good bonding. By warming, the ionic gel becomes viscous and the Pt foil adheres well to the sample.

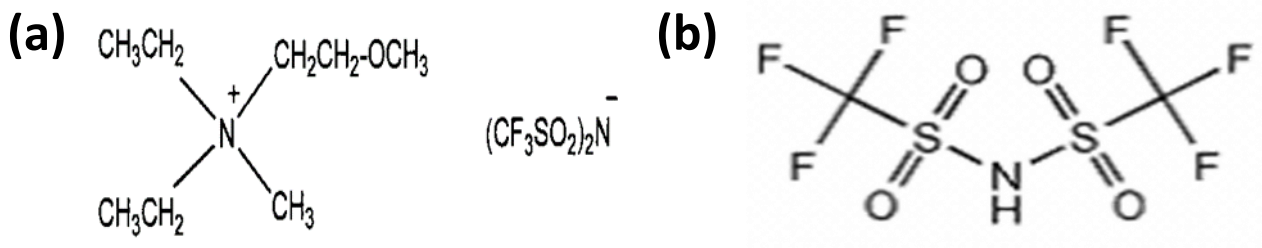

Figure 3.6.2: The chemical structure of **(a)** N, N-diethyl-N-methyl (2-methoxyethyl) ammonium **(b)** bis (trifluoromethylsulfonyl) imide [84].

Finally, copper (Cu) wire is bonded to the surface of the platinum (Pt) foil with indium, and the Pt foil and the Cu wire are fixed by attaching an adhesive similarly to the back surface. The Pt foil having thickness of 2.5 μm has been used as an electrode. In addition, it should be noted that indium (In) having a purity of 99.99% has been used.

3.6.2 Evaluation of magnetization of samples by SQUID

Magnetic modulation due to external electric field has been evaluated by using SQUID. The MPMS equipment manufactured by Quantum Design has been used in this study. However, in the existing system, there was no option to apply field externally to the sample. Therefore, in this study, we have evaluated the magnetization during the application of external electric field by using the parts manufactured in our laboratory so that the magnetization characteristics can be measured under the application of external gate voltage by using the existing MPMS system.

In order to apply an electric field to the sample, it is necessary to attach the newly constructed capping part having the facility of applying external voltage instead of the traditional cap as shown in Fig. 3.6.3. Since the sample vibrates during the highly sensitive magnetization measurement (RSO) to measure the small changes in the magnetization of $Zn_{1-x}Fe_xTe$ layer, sufficient place has been ensured inside the capping tube for smooth movement of the sample. The O-ring is attached between the exit terminal of the control box and the cylindrical part of the field control to maintain high vacuum condition.

In many cases, indium (In) is used for bonding to the sample. But In exhibits superconductivity at a temperature of about 3.4 K or less and produces a magnetic signal as shown in Fig. 3.6.4 [84]. Therefore, it is necessary to measure magnetization of the $Zn_{1-x}Fe_xTe$ layer at a temperature at which there is no impact of the magnetic properties of superconducting In. In addition, it is necessary to draw attention whether there are some contaminated substances adhere in the iron rod while attaching the molten In to the Cu wire for bonding with the sample. Therefore, when processing the sample in this experiment, the soldering iron rod is wrapped with aluminum foil to avoid the possibility of contamination of In with external impurities. We are not confirmed whether the response of magnetic signal from superconducting In have been reduced at the temperature 5 K or more. In this laboratory, experiments of magnetic modulation by the external electric field in the past have been performed at the temperature of 5 *K*. Therefore, in this study, the magnetization of the $Zn_{1-x}Fe_xTe$ layer under the application of external gate voltages, has been measured at 6 *K*.

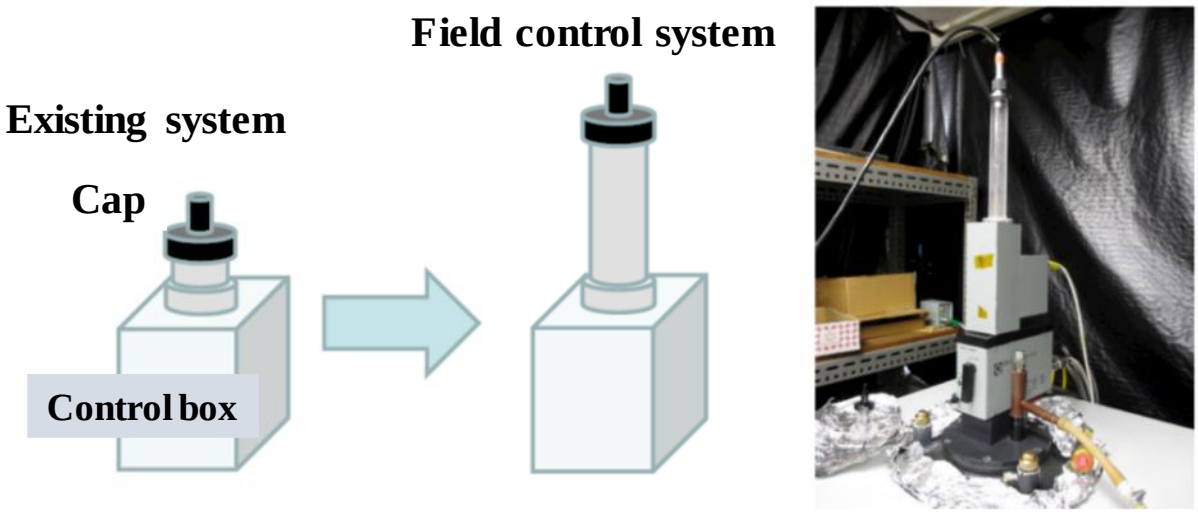

Figure 3.6.3 Schematic diagram for the cylindrical tube used for electric field control experiment [84]

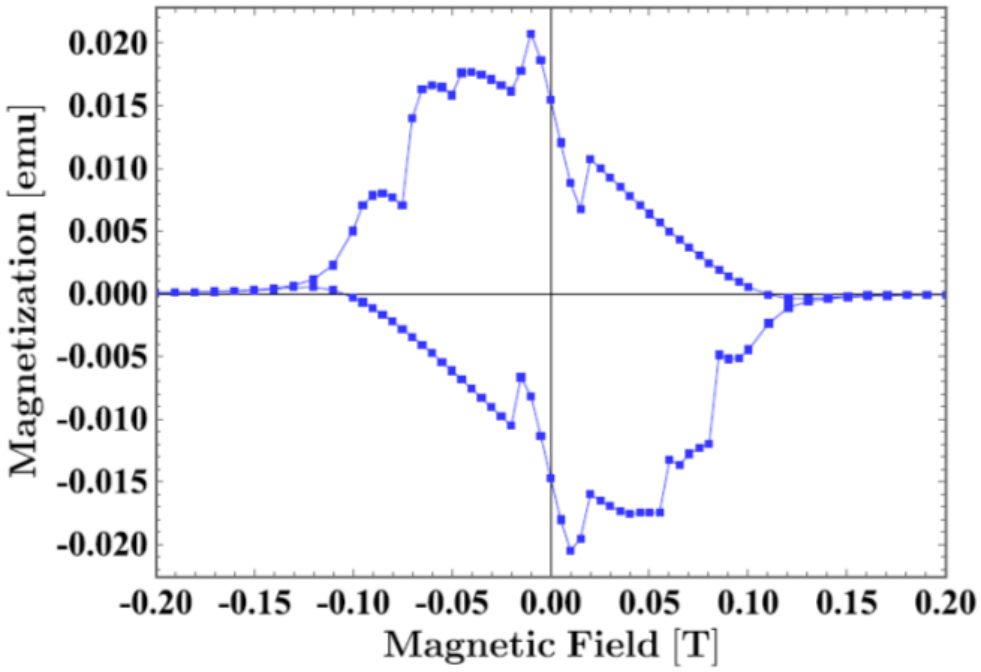

Figure 3.6.4: Magnetic field dependence of magnetization (*M-H* curve) at 2*K* explaining the superconductive behavior of indium [84].

3.6.3 Electric field control study by using Al_2O_3 as solid insulating layer

In this section, the method of modulation of magnetic properties by applying external gate through a device structure containing solid insulating film in between the magnetic layer and gate insulator has been discussed. The use of a solid insulation film as gate insulator will help to investigate the change in magnetism by applying external gate voltage quantitatively. In addition, according to the previous reports on electric field study in our laboratory, there is no such problem of staying charge polarization in the sequence of applying different values of gate voltage as it is observed in the case of ionic polymer – the charge polarization persists even after applying 0V [85, 86]. In this study, Al_2O_3 has been used as a gate insulating film to apply external electric field on $Zn_{1-x}Fe_xTe$ thin film sample. Since Al_2O_3 has relatively high dielectric constant of 8.5 and large capacitance, it is possible to charge more electric charges on the magnetic material surface. In order to charge the surface of the magnetic material with charges, it is necessary to minimize the leak current of the insulating film during the application of high electric field. In that case, Al_2O_3 is considered to be a suitable candidate as compared to other insulating materials. The leakage current has the following three major impacts:

- Electricity flows through the defects in the gate insulating film.
- When a high electric field is applied, bonds between atoms are broken.
- Zener effect occurs by application of high electric field.

The third cause depends on the combination of the semiconductor to be bonded to the gate insulating film. Generally, in a semiconductor device, a gate insulating film having band offset of 1.5 eV or more has been considered for bonding with semiconductor film. Figure 3.6.5 demonstrates the band offset for several oxide materials on Si substrate. Al_2O_3 form the valence band in the lowest energy position as shown in Fig. 3.6.5 and is suitable as an insulating film to be deposited on $Zn_{1-x}Fe_xTe$.

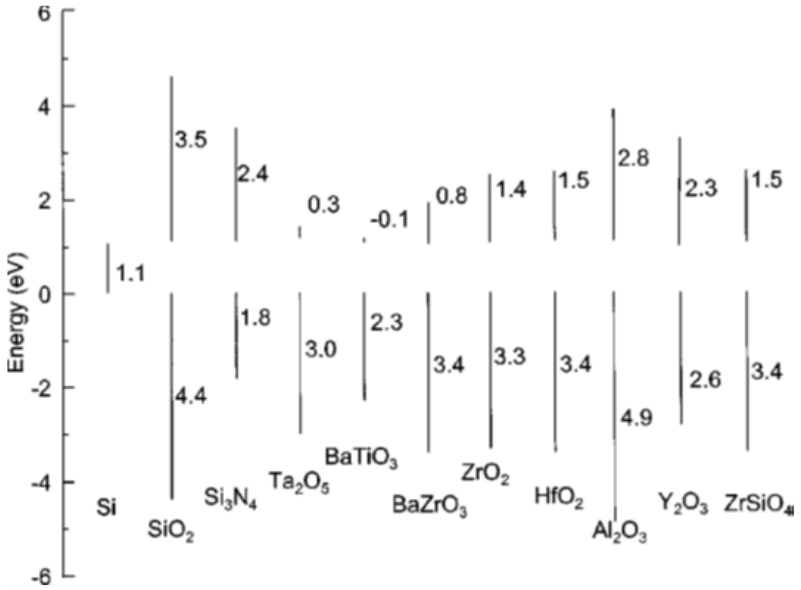

Figure 3.6.5: Band offset of gate insulating material for Si [87]

According to the previous reports, it is known that, a high electric field of 1 MV/cm or more is needed to be applied to the gate insulating film to observe modulation of the magnetic properties by external gate voltages. So, in the case of $Zn_{1-x}Fe_xTe$, such a high electric field is needed to be applied on the insulating film for significant magnetic modulation. Therefore, the most important thing is to prepare an Al_2O_3 insulating film with high insulating properties so that a high electric field can be applied. In this study, we have attempted to prepare an Al_2O_3 film showing high insulation properties so that an electric field of 1 MV/cm or more can be applied by using the atomic layer deposition (ALD) method as a preliminary step for the applying of electric field on $Zn_{1-x}Fe_xTe$ sample. The deposition of Al_2O_3 on $Zn_{1-x}Fe_xTe$ has been checked by measuring the value of resistance.

3.6.4 Atomic layer deposition process of Al_2O_3

The deposition of Al_2O_3 has been performed by Atomic Layer Deposition (ALD) method. Unlike the physical vapor deposition (PVD) method which adsorbs and grows vaporized raw materials such as MBE method on the substrate, the ALD method uses chemical gas which adsorbs and deposits by chemical reaction using chemical gas. It is a type of phase growth method (CVD: Chemical Vapor Deposition). The process in which Al_2O_3 has actually adsorbed and deposited by using the ALD method has been explained with reference to Fig. 3.6.6.

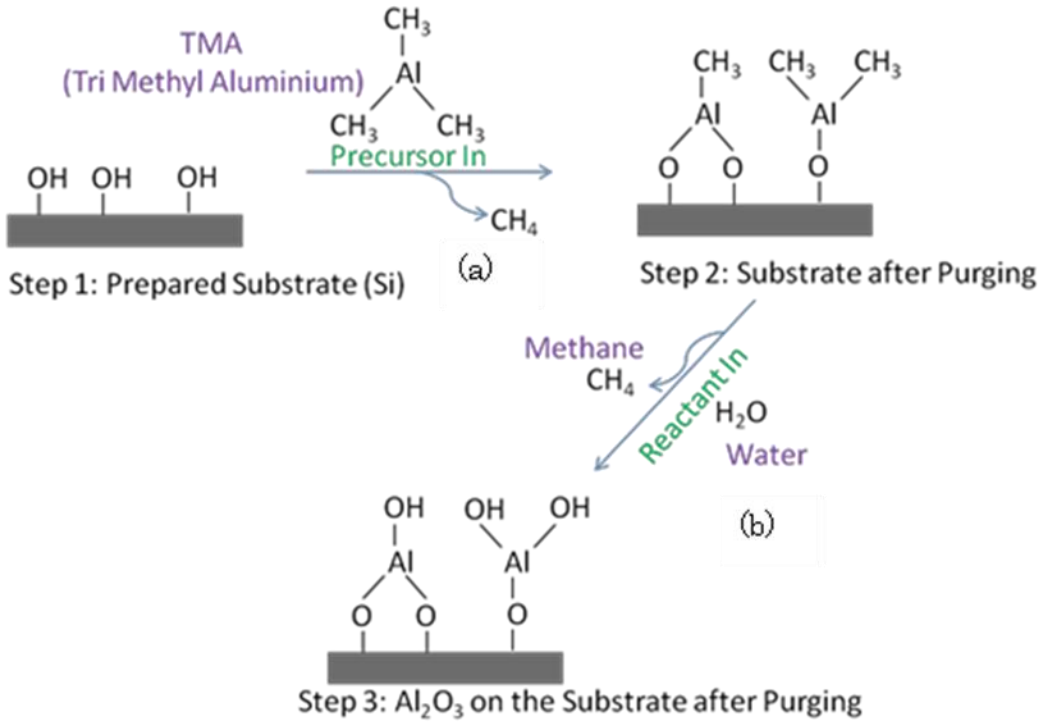

Figure 3.6.6: Schematic representation of the deposition of Al_2O_3 film by ALD method

First, trimethylaluminum [TMA: Al $(CH_3)_3$] gas is supplied and adsorbed on the surface of the Si substrate by a chemical reaction (a). At this time, the methane gas is generated by the chemical reaction and the remaining unreactive TMA gas is driven out of the chamber by a vacuum pump. Next, H_2O is supplied and reacted with

TMA adsorbed on the surface to adsorb Al_2O_3 (b). And as before, the generated methane gas and unreacted H_2O are pumped out. Through such a series of flows, one atomic layer of Al_2O_3 is generated (Step 3).

In the ALD method, since the surface is covered with adsorbed methyl group (CH_3 - group) or hydroxy group (- OH group), only one atomic layer is adsorbed in a series of steps. Therefore, if the film thickness per cycle (growth rate) is known, it is possible to accurately control the film thickness of the Al_2O_3 layer. Also, since the chemical gas is used as a feature of the ALD method, unlike the PVD method such as the MBE method, it is possible to form a film without depending on the shape of the underlayer. Due to these advantages, the ALD method is currently used as an important tool for fabricating semiconductor devices.

3.6.5 ALD device used in this study

Figure 3.6.7 represents the ALD system used in this study. The growth chamber and preparation chamber of the ALD system are separated by a gate valve like the MBE apparatus. The growth chamber is usually maintained a degree of vacuum of the order of $1o^{-4}$ Pa by using a rotary pump and a turbo molecular pump. The degree of vacuum is measured by an ion gauge. On the other hand, the preparatory chamber is evacuated with a rotary pump and the degree of vacuum is measured with a Pirani gauge. The chemical gas was supplied by controlling the on / off of the electromagnetic valve via the I/O communication board by the Lab view program. Also, a ribbon heater was wound around the growth chamber to heat the entire growth chamber. This was done to prevent H_2O from liquidizing in the chamber and to drive out the unreacted gas and methane during growth. In addition, a ribbon heater was wound around the tube supplying H_2O and in the region of the tube from the H_2O containing container to the growth chamber. During the growth, the substrate temperature has been fixed depending on the optimal machine condition. The film formation was performed on a hot substrate. In order to stabilize the supply amount of H_2O during growth, heating of the flask containing distilled water is kept slightly heating by using a hot plate. Trimethylaluminum (TMA) gas was supplied at normal temperature under atmospheric pressure. During the film formation, the degree of vacuum in the growth chamber was monitored by PC. Figure 3.6.8 shows a graph showing the change in degree of vacuum in actual film growing condition.

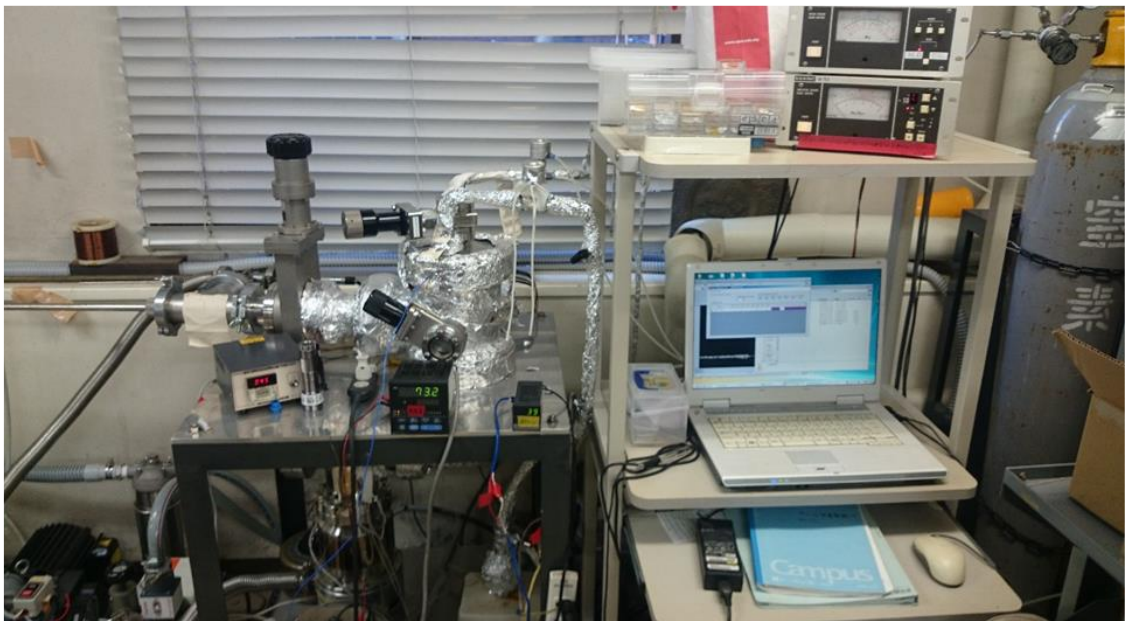

Figure 3.6.7: Schematic view of ALD system used in this study

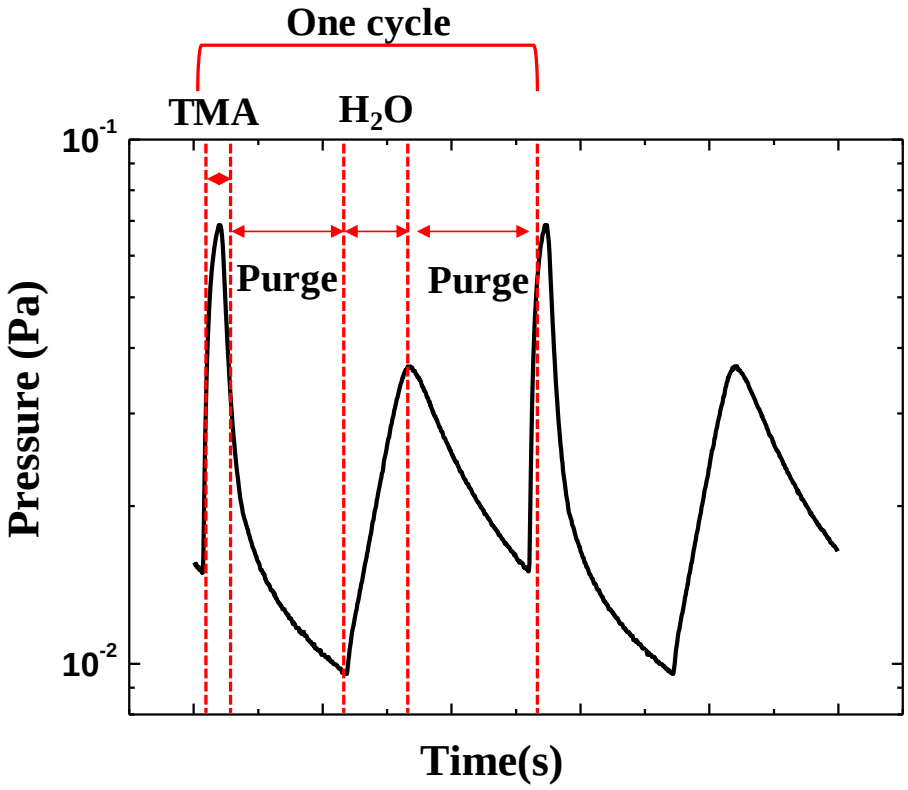

Figure 3.6.8: Graph of degree of vacuum during Al_2O_3 film deposition

Chapter 4: Experimental results and discussions - I

4.1 Structural and magnetic properties of $Zn_{1-x}Fe_xTe$: N thin films (Te-rich growth condition)

On the basis of the previous research on $Zn_{1-x}Fe_xTe$ thin films performed in our laboratory, the pure dilute phase of $Zn_{1-x}Fe_xTe$ thin films have been confirmed for Fe composition, $x \leq 0.02$ and the isoelectronic Fe^{2+} state on the substitutional site of II-VI compounds produced only field-induced magnetic moments which is typically known as van-Vleck paramagnetism [32, 33]. As the substitutional Fe forms the deep donor $Fe^{2+/3+}$ levels within the bandgap of the host ZnTe, the trap of carriers supplied by additional charge doping or by applying external gate voltages is expected to deviate the Fe charge state from Fe^{2+}, resulting in a possible modification of magnetic properties. In this section, we have provided the experimental results of the structural and magnetic properties of N-doped $Zn_{1-x}Fe_xTe$ thin films grown under Te-rich growth condition.

4.1.1 Sample preparation

Thin films of N-doped (Zn,Fe) Te were grown by molecular beam epitaxy (MBE) in excess of Te flux over Zn flux. The Te-rich growth condition of (Zn,Fe) Te was chosen for N-doped thin films in order to suppress the self-compensation by native defects. We have used elemental solid sources of Zn, Te and Fe and nitrogen plasma source with N_2 gas excited by rf-plasma. The power of the plasma source was fixed at 300W and the N_2 gas flow rate was maintained at 0.3 cc/min throughout the growth of $Zn_{1-x}Fe_xTe$: N layer. We first grew a thick layer of ZnTe buffer (~900 nm) on a GaAs (001) substrate in order to relax a large lattice mismatch and successively grew a $Zn_{1-x}Fe_xTe$: N layer (~700 nm) on it. The sample structure configuration is shown in Fig. 4.1.1. The substrate temperature during the growth was set to 260°C. During the growth of the N-doped $Zn_{1-x}Fe_xTe$ layer, the N concentration was controlled by changing the size of holes in the shutter of the plasma source. The Fe and N concentrations in the N-doped $Zn_{1-x}Fe_xTe$ layer were measured by electron probe microanalyzer (EPMA) and secondary ion mass spectroscopy (SIMS), respectively. We prepared a series of $Zn_{1-x}Fe_xTe$ thin films with a fixed Fe composition, $x = 0.015$ and varied N concentrations; one without N doping (A#1), referred to as undoped, and those with different N concentrations [N] = 8×10^{17} cm^{-3} (A#2), 7×10^{18} cm^{-3} (A#3), and 4×10^{19} cm^{-3} (A#4) as shown in Table 4.1.

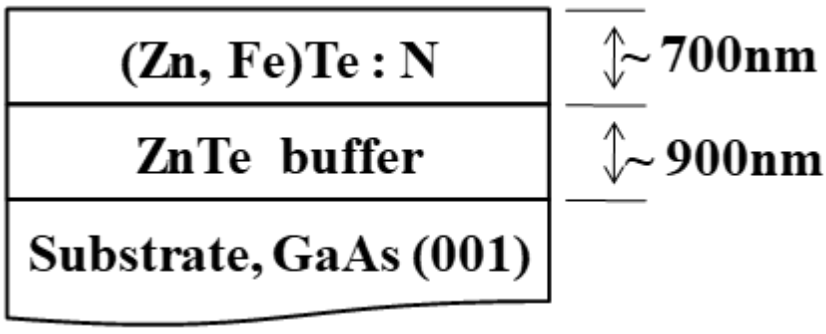

Figure 4.1.1: Sample structure for N-doped (Zn,Fe)Te thin films

Table 4.1: Sample list of $Zn_{1-x}Fe_xTe$: N thin films

Sample No.	Substrate T_S [°C]	Diameter of Hole	N concentration [cm^{-3}]	Fe Composition [%]
A#1	260	Closed	0	1.5
A#2	260	Small open	8.0×10^{17}	1.5
A#3	260	Large open	7.0×10^{18}	1.5
A#4	260	Fully Open	4.0×10^{19}	1.5

4.1.2 Evaluation of the sample surface by reflection high energy electron diffraction (RHEED)

During the growing, we have monitored the growth by using the reflection high energy electron diffraction (RHEED) system installed in the MBE system. Figure 4.1.2 represents the RHEED pattern of the samples after the growth of the magnetic layer. In the case of both undoped and N-doped films, spotty-streak pattern has been observed.

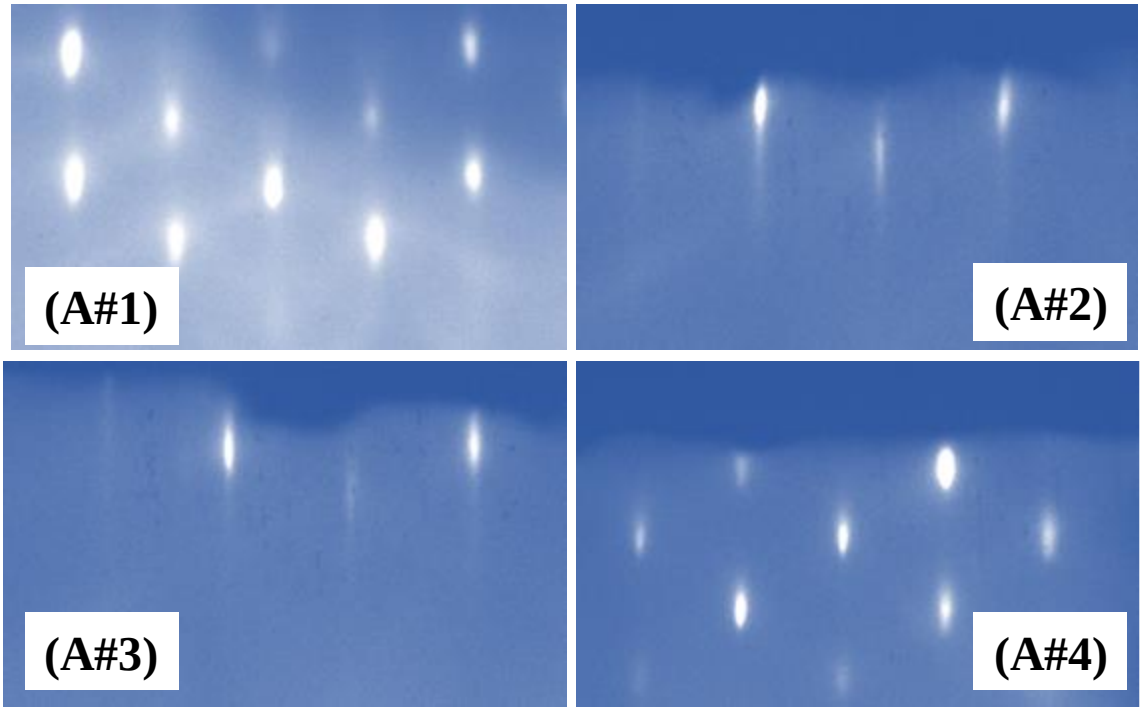

Figure 4.1.2: RHEED pattern of undoped (A#1) and N-doped (A#2 – A#4) $Zn_{1-x}Fe_xTe$: N thin films after the growth.

4.1.3 Structural analysis of $Zn_{1-x}Fe_xTe$: N thin films: X-ray diffraction analysis (XRD)

In this section, the result of structural characterization of the grown films has been demonstrated. Figure 4.1.3 shows the XRD θ-2θ scan profiles of the undoped (A#1) and N-doped (A#2 - A#4) films with a fixed Fe

composition, $x = 0.015$ and variable nitrogen concentrations. Diffraction peaks have been detected only from ZnTe buffer layer and GaAs substrate; but diffraction from any other phases has not been observed. This result indicates that either the amount of precipitates is very small, or they are embedded inside the host crystal in such a particular orientation that it is difficult to be detected by ordinary θ-2θ scan [88, 89]. Only broadening of the ZnTe diffraction peaks has been identified with the increase of N concentration. At the highest N concentration (A#4), we have seen separated peaks from the ZnTe buffer layer and the $Zn_{1-x}Fe_xTe$: N layer for the (400) and (600) diffractions.

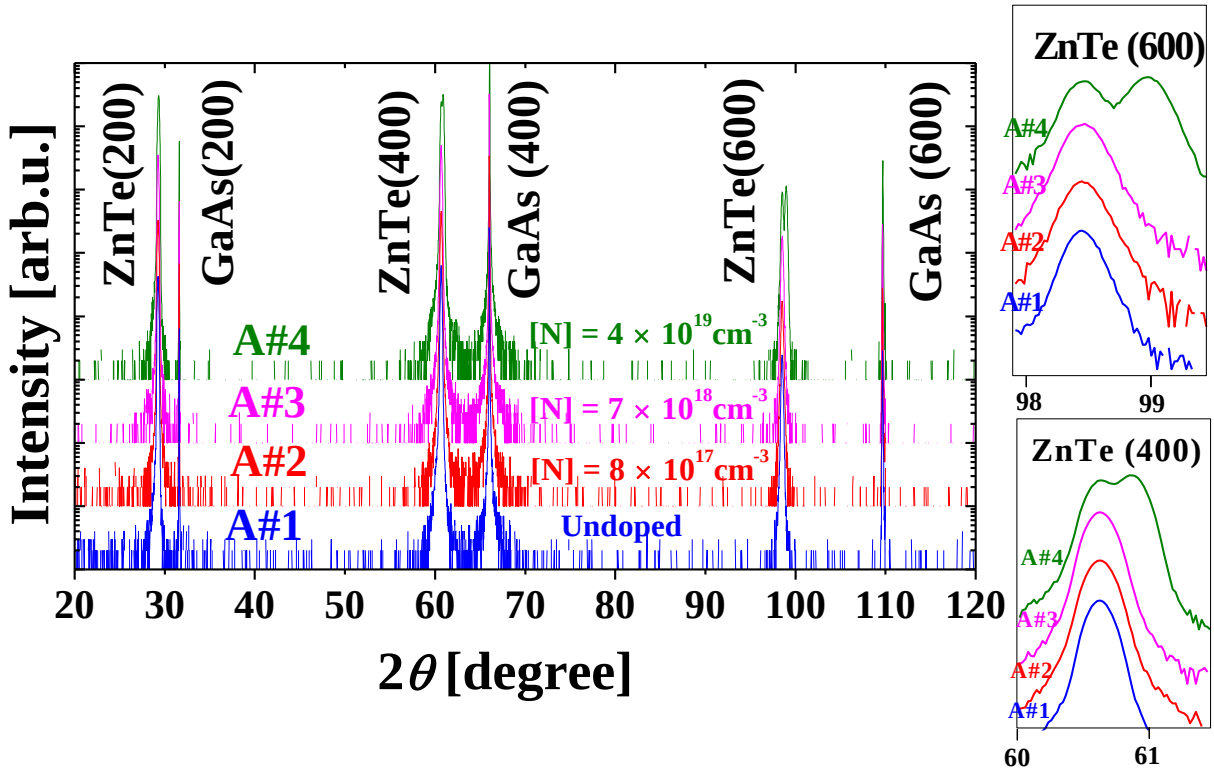

Figure 4.1.3: The XRD θ-2θ scan profiles of the undoped (A#1) and N-doped (A#2- A#4) $Zn_{1-x}Fe_xTe$ ($x = 0.015$) films with different N concentrations. The scan curves around the ZnTe (400) and (600) diffractions are also shown in an enlarged scale.

4.1.4 Structural analysis of $Zn_{1-x}Fe_xTe$: N films: X-ray absorption fine structure (XAFS) analysis

In order to investigate the local environment of Fe, X-ray absorption fine structure (XAFS) measurements have been performed at the beamline BL9A or BL12C of KEK-PF. The XAFS spectra at Fe K-edge have been measured in the fluorescence-detection mode at a low temperature around 20K. The intensity of the incident X-ray beam monochromated by a Si (111) double crystal monochromator was monitored by a nitrogen-filled ionization chamber and the fluorescence signal has been detected by an array of 19 elements of Ge detector. We have studied the radial distribution function (RDF) for $Zn_{1-x}Fe_xTe$: N thin films around the Fe atom, derived from Fourier transforms of extended x-ray absorption fine structure (EXAFS) oscillation, as shown in Fig. 4.1.4. The oscillatory parts $\chi(k)$ extracted from the observed EXAFS spectra at Fe K-edge have been multiplied by k^3 for weighting and transformed into real space. In the Fig. 4.1.4, the result of simulation for an Fe atom in the substitutional site in the zinc-blende (ZB) structure, and Fe-N compounds such as, γ-Fe_4N, ε-Fe_3N and ζ-Fe_2N have also been plotted

as reference. For the simulation of an Fe atom in the substitutional site, it is considered that a single Fe atom substitutes the Zn site in the host crystal of ZnTe without any change of the lattice constant and the outgoing photoelectron is scattered only once with the neighboring atoms (single scattering approximation). As we have observed from the Fig. 4.1.4, the experimental curve for the undoped film (A#1) resembles the result of simulation for the substitutional Fe, showing a main peak at around 2.5 Å corresponding to the bond with Te atoms at the first nearest neighbor (1st NN). On the other hand, the position of the 1st NN peak in the N-doping films with intermediate N concentrations (A#2, A#3), has been shifted from the position of 2.5 Å in the case of undoped film to a shorter distance with the increase of N concentration. In addition, in the film with a higher N concentration (A#3), an additional small peak has come into view at around 1.5 Å. The change of position of the 1st NN peak towards the shorter distance can be explained by assuming a portion of the four tetrahedrally-coordinated Te atoms around Fe has been replaced by N atoms, since the bond length of Zn- N_{Te} (2.2 Å) is smaller than that of Zn- Te (2.62 Å).

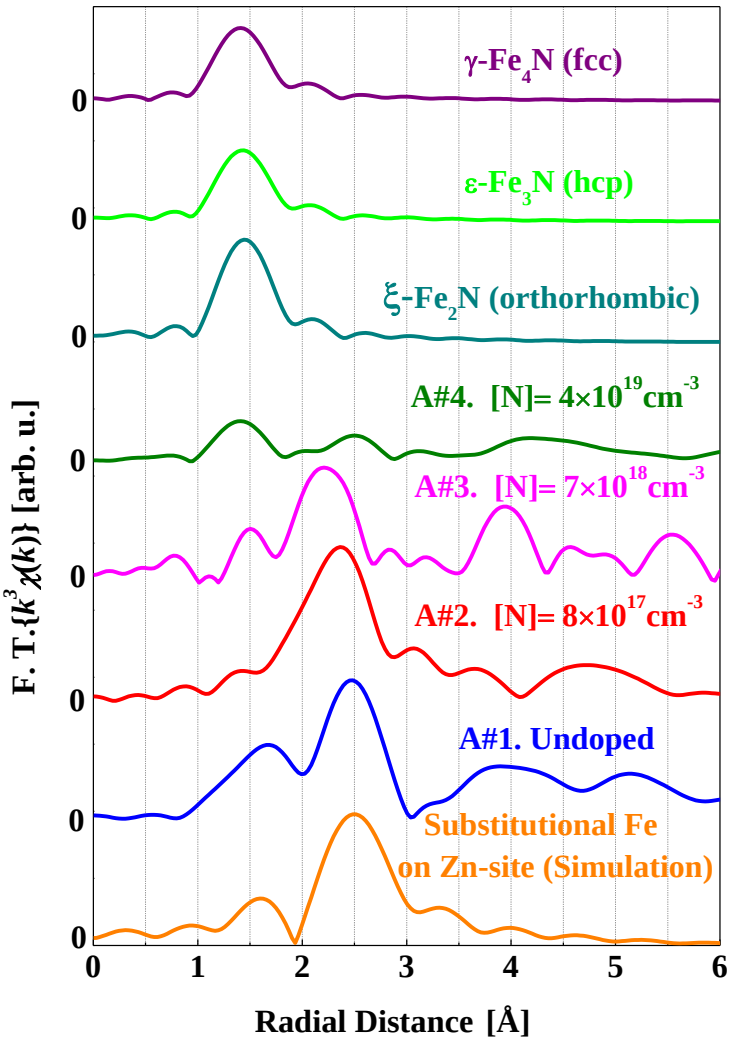

Figure 4.1.4: RDF spectra of the undoped (A#1) and N-doped (A#2 – A#4) $Zn_{1-x}Fe_xTe$ (x = 0.015) films. The results of simulation assuming an Fe atom in the substitutional site in the ZB structure and Fe-N compounds are presented as reference.

However, in the case of the highest N-doped film (A#4), the shape of the RDF curve is totally different; one can see only a small peak at around 1.3 Å, which almost coincides with the position of the 1st NN peak in the simulation curves of Fe-N compounds. This result has reflected the tendency of Fe in the forming of extrinsic precipitates of Fe-N compounds at the highest N concentration. Possible candidates of extrinsic precipitates are γ-Fe_4N, ε-Fe_3N and ζ-Fe_2N, having the crystal structure of fcc, hcp and orthorhombic, respectively.

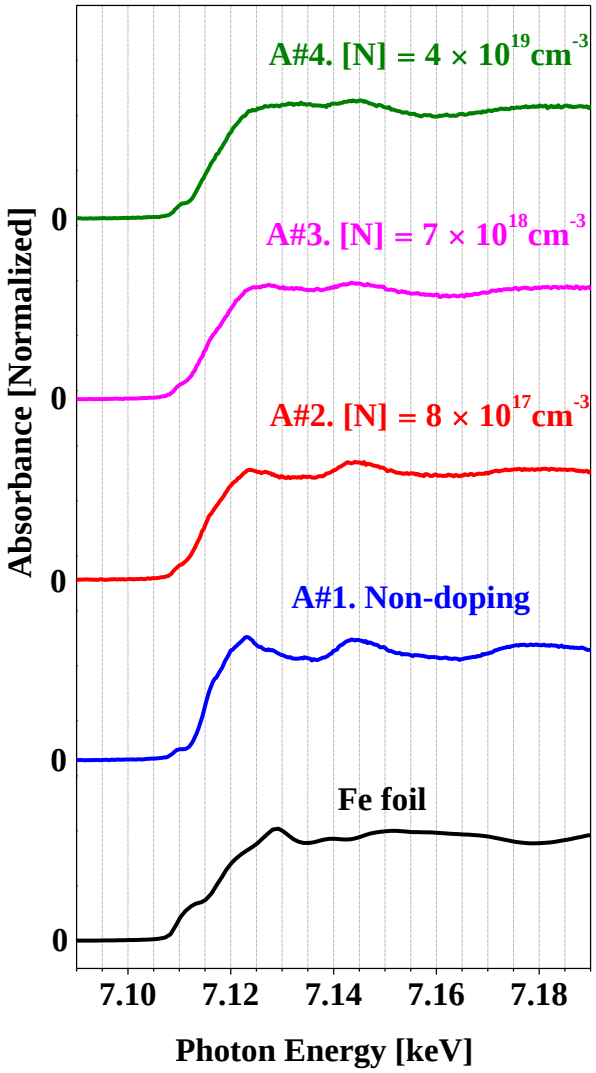

Figure 4.1.5 XANES spectra of the undoped (A#1) and N-doped (A#2 - A#4) $Zn_{1-x}Fe_xTe$ (x = 0.015) films, together with that of an elemental Fe foil for reference.

Figure 4.1.5 shows the X-ray absorption near edge structure (XANES) spectra of the undoped (A#1) and N-doped (A#2 - A #4) films, together with the spectrum of an elemental Fe foil as reference. In the undoped film (A#1), we observed three absorption peaks near the Fe K-edge; the pre-edge peak at 7.10967 keV, the shoulder peak at 7.1165 keV and the main peak at 7.1239 keV. The pre-edge peak is assigned as the transitions from the 1*s* state to the 3*d*-like state (quadrupolar), while the shoulder and main peaks both are associated to the transition

from the 1*s* state to the 4*p*-like state (dipolar) [68]. In the N- doped films (A#2 - A#4), we have identified a slight change in the shape of the pre-edge peak in terms of the energy position and integrated intensity, the most useful feature to discriminate the oxidation state and coordination number of Fe. According to previous studies on Fe-K pre-edge peak by several research groups [68, 90], the energy and intensity of the pre-edge peak gradually increase as the valence state of Fe changes from the pure Fe^{2+} state to the pure Fe^{3+} state. The separation between the average pre-edge energy positions for these two states is 1.4 ± 0.1 eV [90, 91]. This scenario has been observed in the energy position of the pre-edge peak for N-doped films when compared with that of the undoped film. In our study, we have made the baseline curve coinciding with the experimental curve for the region around the absorption edge for subtracting the background and hence, measured the pre-edge peak region of the undoped (A#1) and N-doped films (A#2 - A#4) as shown in Fig. 4.1.6 and 4.1.7. Then, we have fitted the pre-edge region with Gaussian function to find the exact position of the pre-edge peak as indicated by the straight line.

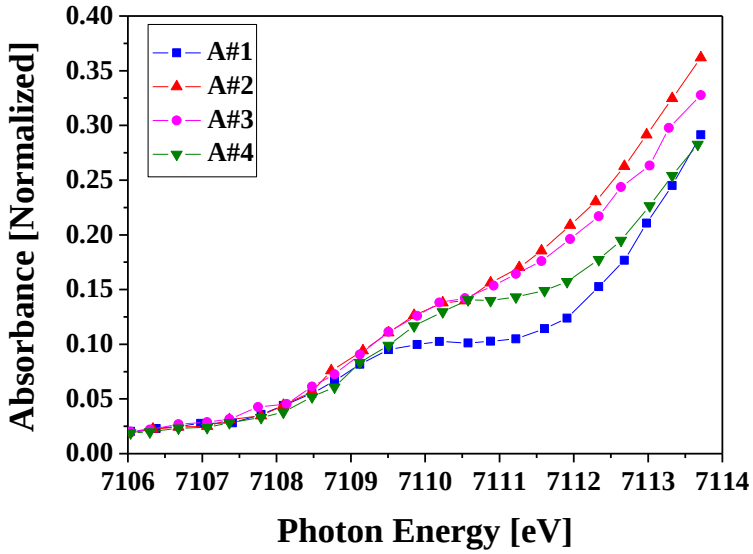

Figure 4.1.6: Fe-K pre-edge region for undoped (A#1) and N-doped (A#2-A#4) $Zn_{1-x}Fe_xTe$ (x = 0.015) films.

In the present study, we have detected the pre-edge peak at 7109.67 eV in the undoped film A#1, which is considered to be the pure diluted phase with Fe being incorporated in the substitutional site and in the isoelectronic state of Fe^{2+}. However, as seen clearly in Fig. 4.1.7, the pre-edge peak in the N-doped films is shifted to a higher energy as compared to that in the undoped sample A#1; the energy position of the N-doped the films A#2, A#3, and A#4 has been found at 7109.96, 7110.07 and 7110.12 eV respectively. Figure 4.1.8 demonstrates the shifting of pre-edge energy position towards higher energy with the increase of N-doping concentration. The result indicates the deviation of Fe valence state from Fe^{2+} to $Fe^{2+/3+}$ mixed states becomes higher with the increase of N-doping.

On the basis of the RDF and XANES spectra, it can be concluded that the shift of the pre-edge peak in the films with the intermediate N concentrations (A#2, A#3) reflects the valence state change of substitutional Fe from Fe^{2+} in the undoped film to the $Fe^{2+/3+}$ mixed state due to the incorporation of N. While Fe atoms staying at the substitutional site, their valence is considered to be changed because Te atoms bonded in the tetrahedral coordination are partially replaced by N atoms. On the other hand, in the film with the highest N concentration (A#4), the analysis of the RDF spectrum suggests that Fe atoms are dominantly incorporated in a Fe-N compound, in which Fe are in a different valence state and coordination [92, 93].

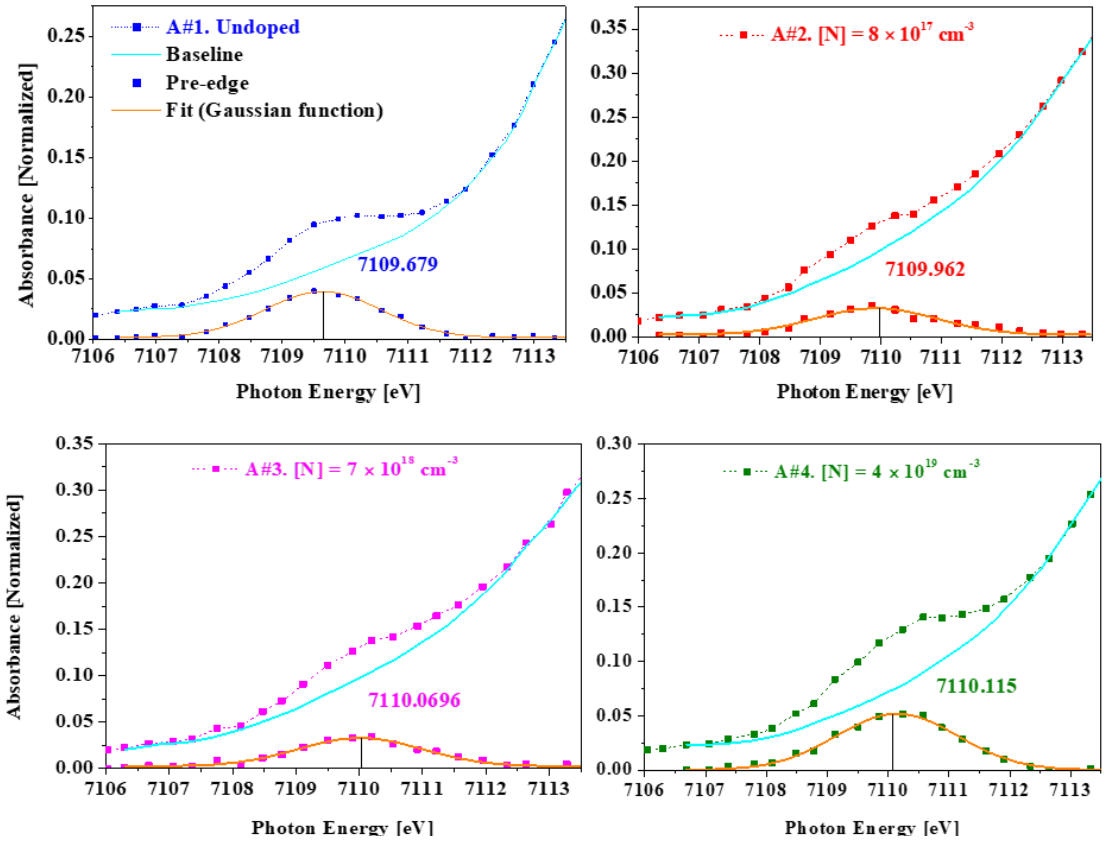

Figure 4.1.7: Fitting of Fe-K pre-edge region after baseline subtraction for undoped (A#1) and N-doped (A#2-A#4) $Zn_{1-x}Fe_xTe$ (x = 0.015) films using Gaussian function. The pre-edge peak position is indicated by the straight line.

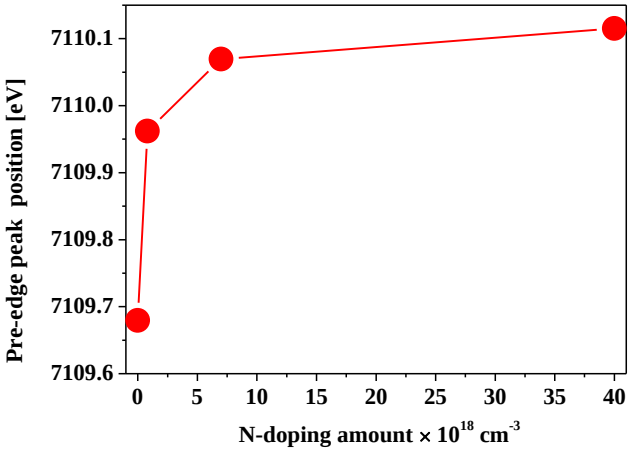

Figure 4.1.8: The pre-edge peak position vs N-doping concentration graph for undoped (A#1) and N-doped (A#2-A#4) $Zn_{1-x}Fe_xTe$ (x = 0.015) films grown under Te-rich condition.

4.1.5 Structural analysis of $Zn_{1-x}Fe_xTe$: N films: Transmission electron microscope (TEM) observation

High resolution transmission electron microscope (TEM) observation has been performed with an accelerating voltage of 300 keV (JEM-3100FEF, JEOL), together with chemical analysis using energy-dispersive spectroscopy (EDS) [94]. Cross-sectional pieces with thickness ~ 100 nm have been prepared by standard mechanical polishing followed by Ar^+ - ion milling at 7.0 kV for more than 2 hours. We have made an attempt to assess the crystal structure of the formed precipitates in the N-doped films with the two higher N concentrations (A#3, A#4) by TEM. Figure 4.1.9 shows typical cross-sectional TEM images and the corresponding FFT patterns of the N-doped films (A#3, A#4).

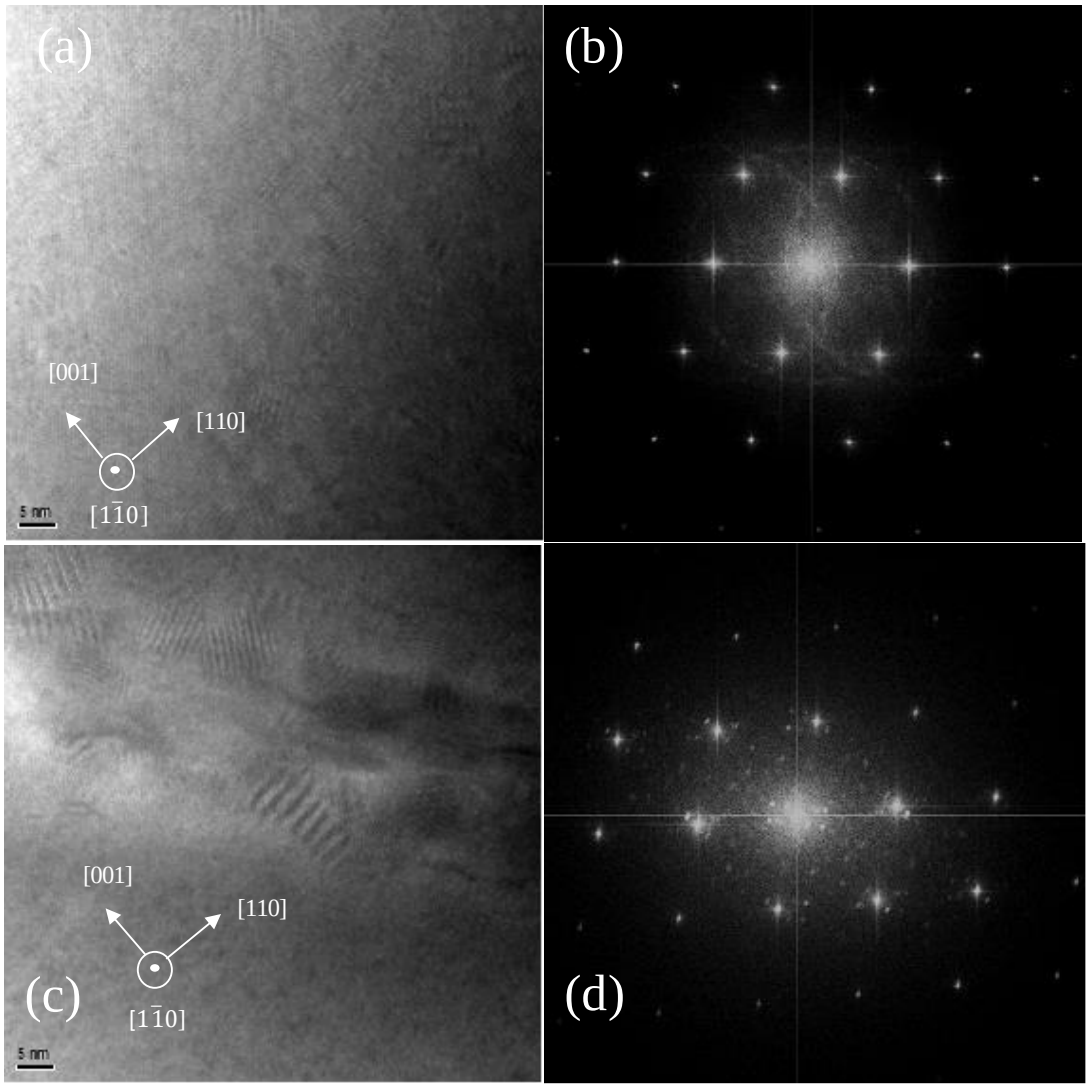

Figure 4.1.9: Transmission electron micrographs and corresponding fast Fourier-transform (FFT) patterns of the N-doped $Zn_{1-x}Fe_xTe$ films (A#3, A#4) having different N concentrations; (a) and (b) represent the results for [N] = 7×10^{18} cm^{-3} (A#3), (c) and (d) represent the results for [N] = 4×10^{19} cm^{-3} (A#4), respectively.

In the N-doped film (A#3) with N concentration, [N] = 7×10^{18} cm^{-3}, one can observe several small regions of translational Moiré fringes, but the crystal is mainly composed of the zinc-blende structure, as demonstrated by the set of fundamental diffraction spots in the fast Fourier transforms (FFT) pattern. On the other hand, in the N-doped film (A#4) with the highest N concentration, [N] = 4×10^{19} cm^{-3}, the cross-sectional TEM micrograph includes such translations Moiré regions with a larger size and as a consequence, several weak diffraction spots come into view in the FFT pattern, along with the fundamental spots of the ZB structure. These observations suggest that the increase of N concentration has raised the extrinsic precipitates formation tendency. However, it has been difficult to discern the crystal structure of the precipitates from the TEM image since these precipitates, with their sizes smaller than the thickness of the observed piece, were submerged in the host matrix. Figure 4.1.10 and 4.1.11 represent the Fe mapping image from the energy dispersive spectroscopy study for the N-doped films (A#3, A#4). Although there seem little fluctuations in the Fe distribution in the overall region of the studied small pieces, there is no significant evidence of Fe clustering in both the N-doped films (A#3, A#4).

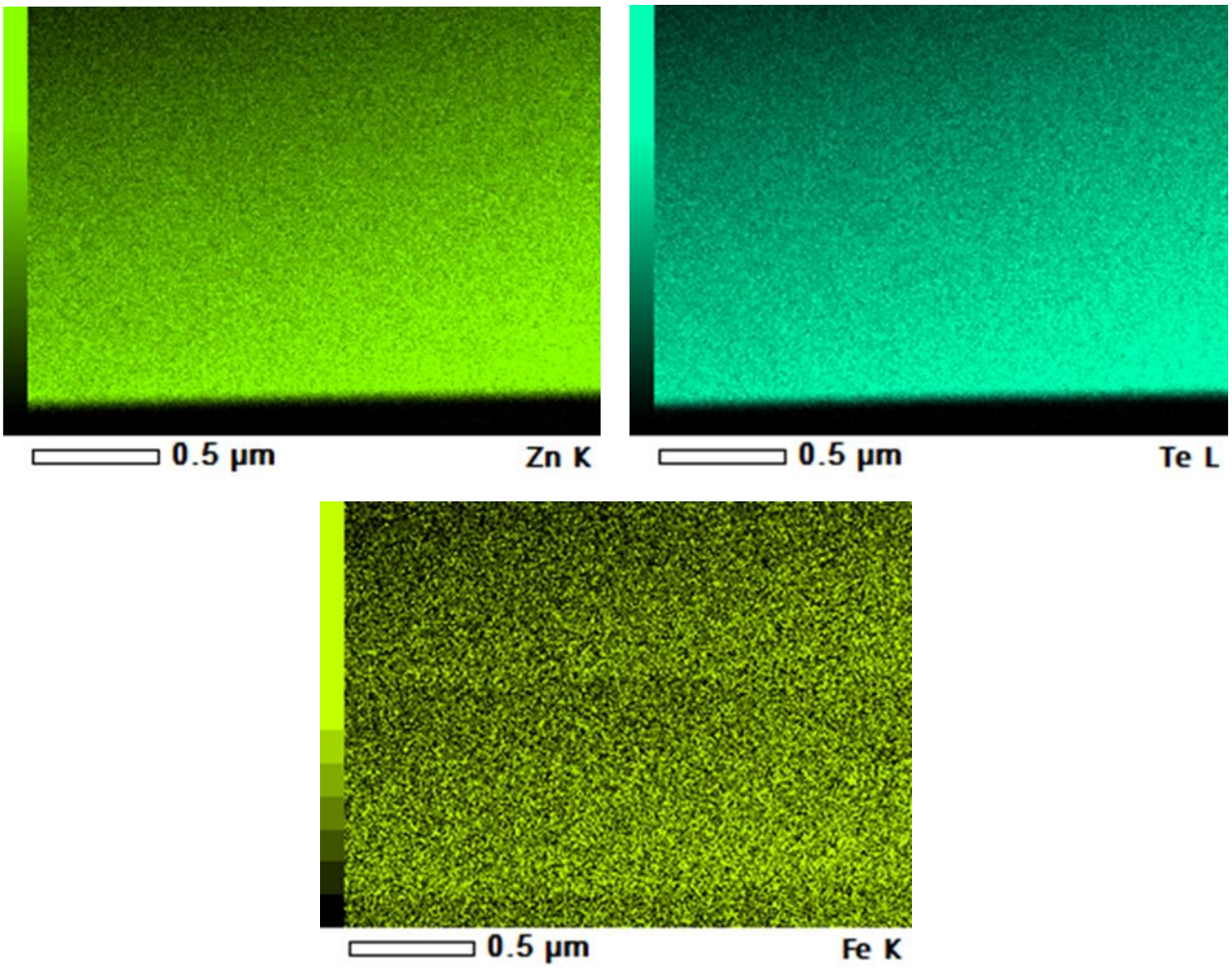

Figure 4.1.10: Energy-dispersive spectroscopy showing the mapping of the elements Zn, Te and Fe in the N-doped $Zn_{1-x}Fe_xTe$ film (A#3) with N concentration, [N] = 7×10^{18} cm^{-3}.

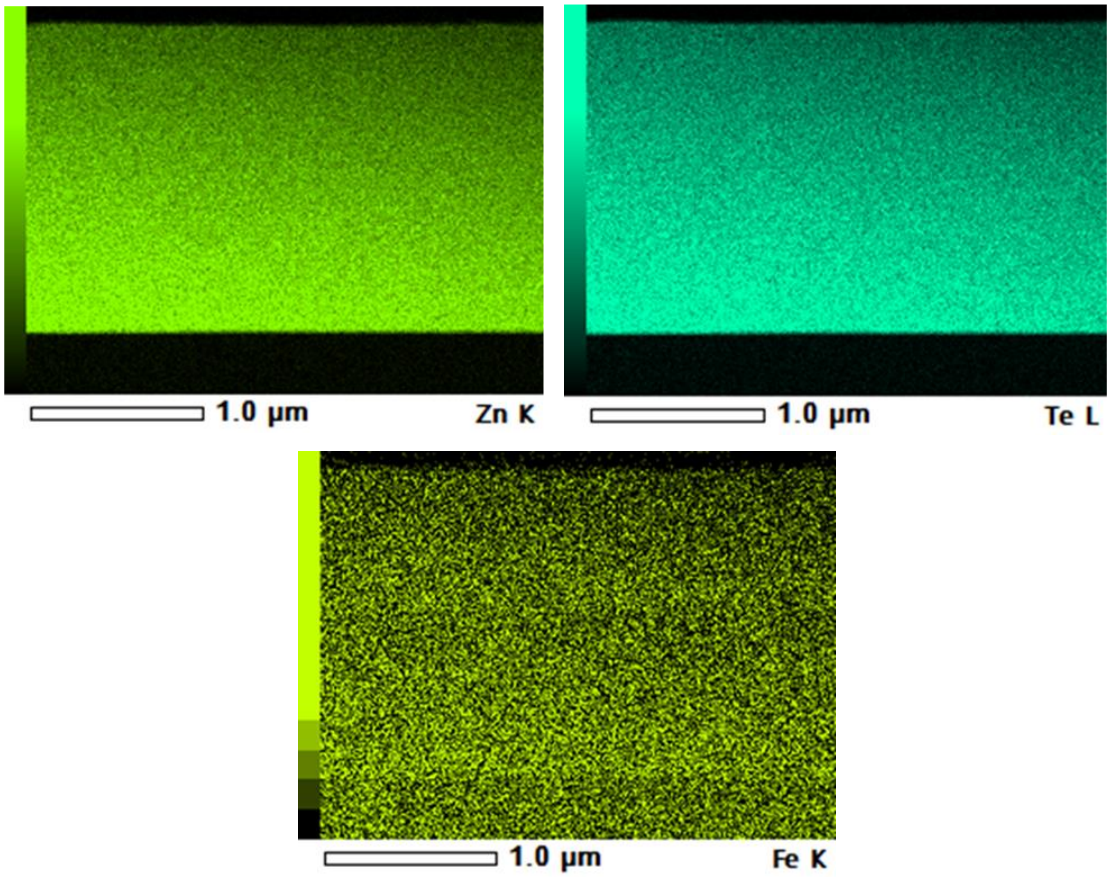

Figure 4.1.11: Energy-dispersive spectroscopy showing the mapping of the elements Zn, Te and Fe in the N-doped $Zn_{1-x}Fe_xTe$ film (A#4) with N concentration, [N] = 4×10^{19} cm^{-3}.

4.1.6 Magnetization measurements of $Zn_{1-x}Fe_xTe$: N films: Superconducting quantum interference device (SQUID)

The magnetization measurements have been performed by using superconducting quantum interference device (SQUID) magnetometer with the application of magnetic field perpendicular to the film plane. We have measured both the dependences of magnetization on magnetic field (*M-H*) and temperature (*M-T*) in order to analyze various aspects of the magnetic behaviors [9]. Figure 4.1.12 represents the *M-H* curves measured at 2K for the undoped (A#1) and N-doped (A#2 - A#4) films. The magnetization measurement has disclosed a drastic change of magnetic properties by N-doping as represented by the evolution of *M-H* curves shown in Fig. 4.1.12. In the undoped film (A#1), the magnetization increases almost linearly with magnetic field without being saturated and a very weak hysteresis is seen in the low field region. The linear dependence of magnetization with magnetic field is a typical behavior of the van-Vleck paramagnetism [95]; the localized magnetic moment which is quenched at zero field, has been induced by the application of an external magnetic field. The linear *M-H* curve in the undoped film (A#1) has been transformed into a ferromagnetic feature with hysteresis in the N-doped films with the intermediate N concentrations (A#2 - A#3). In the N-doped film (A#3) showing eminent ferromagnetic behavior, the coercivity has been measured to be 1100 Oe and the magnetization has become saturated at the magnetic field of 5T. Figure 4.1.13 represents the field dependence magnetization (*M-H* curves) measured at different temperatures.

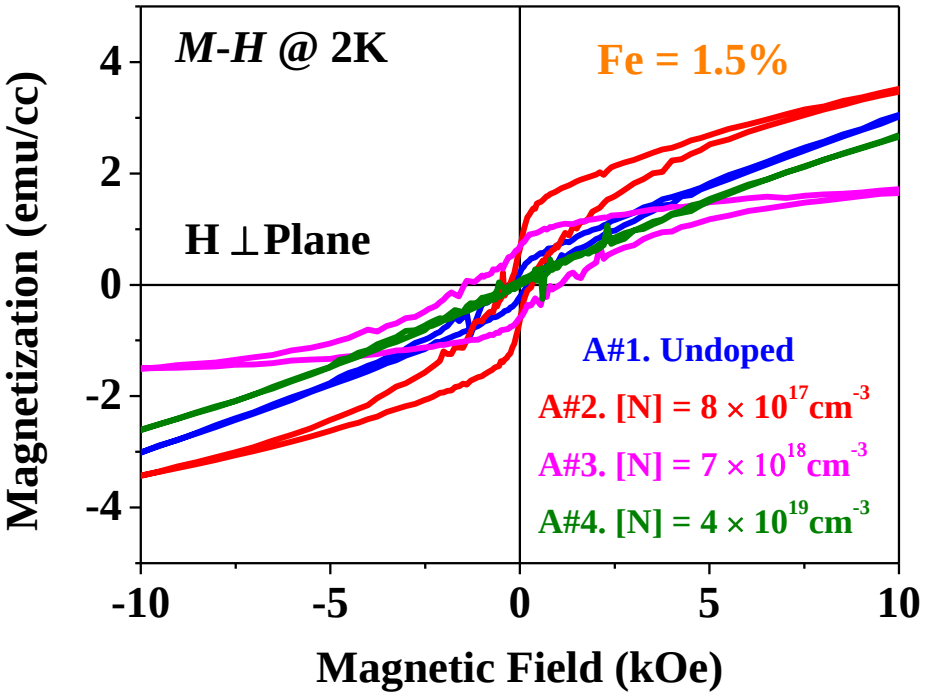

Figure 4.1.12: *M-H* curves of the undoped (A#1) and N-doped (A#2- A#4) $Zn_{1-x}Fe_xTe$ (x = 0.015) films. The measurement has been performed at 2K under magnetic field perpendicular to the film plane.

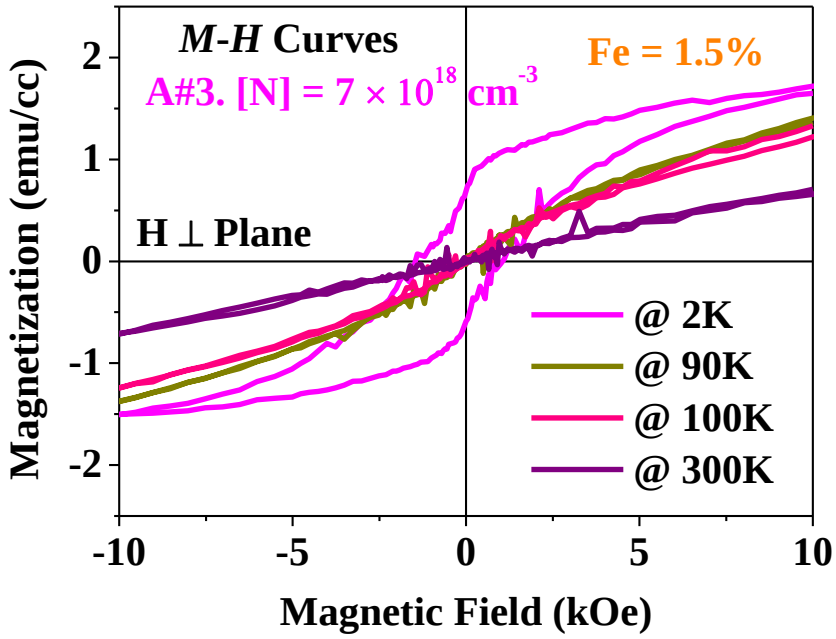

Figure 4.1.13: *M-H* curves of the N-doped $Zn_{1-x}Fe_xTe$ (x = 0.015) film (A#3). The measurement has been performed at different temperatures with magnetic field perpendicular to the film plane.

The observed ferromagnetic properties for the N-doped film (A#3) measured at 2K has changed into the ordinary paramagnetic (S-shape *M-H* curve) feature at 100K and van-Vleck type paramagnetic at room temperature. Based on the XAFS results which have suggested the incorporation of Fe atoms are predominantly in the substitutional site for these films, the observed ferromagnetic behavior observed at the intermediate N concentrations may not originate from the formation of extrinsic precipitates of ferromagnetic Fe-N compounds. The most possible origin is the deviation of the Fe valence state from Fe^{2+} due to the doping of nitrogen acceptor impurity which has been clearly observed from the shift of the Fe-K pre-edge peak towards higher energy in the XANES spectra. The deviation of Fe valence state can produce a finite magnetic moment even at zero external magnetic field and can also enhance the exchange interaction between these magnetic moments. This may alter the magnetic properties of (Zn,Fe)Te as observed here. On the other hand, the linear dependence that we have observed in the N-doped film with the highest nitrogen concentration (A#4) may come from extrinsic precipitates such as ζ-Fe_2N (orthorhombic) [23], which is known to be either antiferromagnetic [96] or slowly saturating weak ferromagnetism [97].

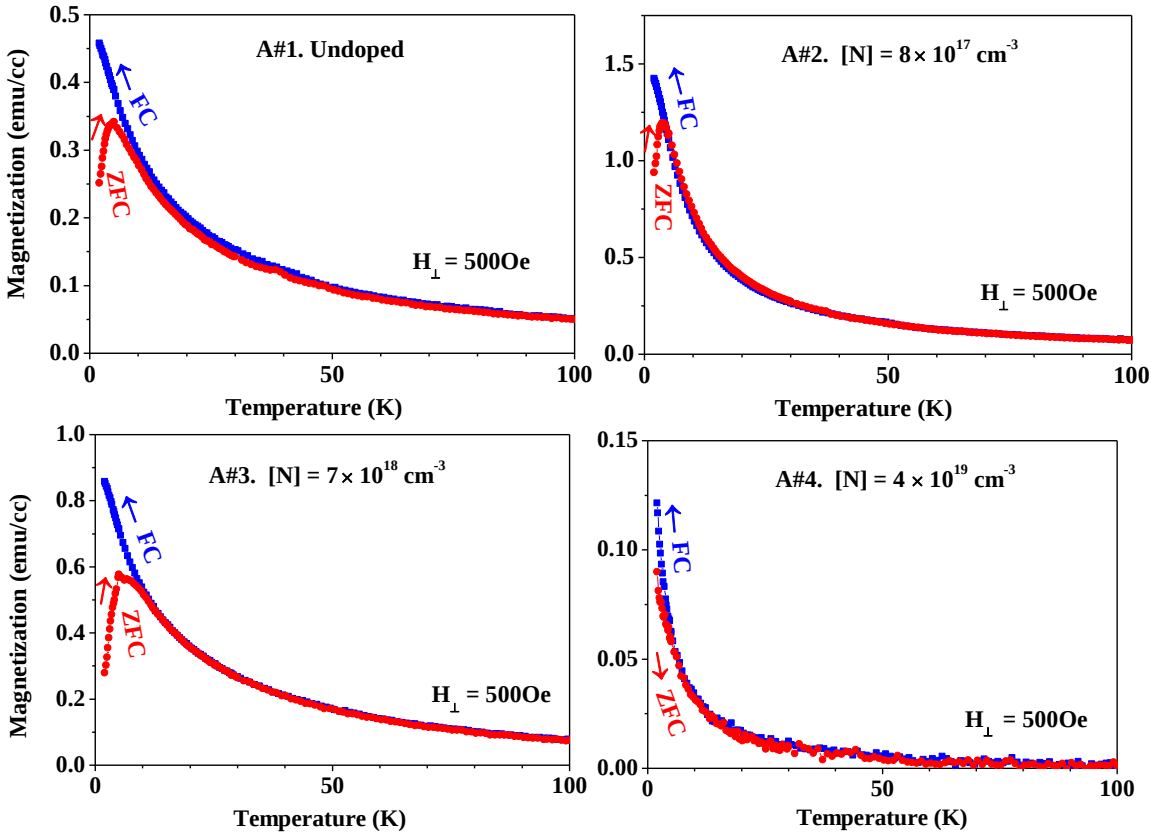

Figure 4.1.14 *M-T* curves of the undoped (A#1) and N-doped (A#2- A#4) $Zn_{1-x}Fe_xTe$ (x = 0.015) films. The magnetization has been measured both in the field-cooled (FC) and zero-field-cooled (ZFC) processes under a constant magnetic field of 500Oe applied perpendicular to the film plane.

We have also studied *M-T* curves of the undoped and N-doped films under a fixed magnetic field of 500 Oe as shown in Fig. 4.1.14. For the undoped (A#1) and N-doped (A#2, A#3) films with the intermediate N concentrations,

small blocking phenomenon has been seen at temperature around (T_B ~ 5K, while in the N-doped (A#4) film with the highest N concentration, monotonic increase of the field-cooled (FC) and zero- field-cooled (ZFC) curves with lowering temperature has been observed (no blocking phenomena). The blocking phenomena and the irreversibility between the FC and ZFC processes are typical behaviors of superparamagnetism. The superparamagnetic behaviors originate from a magnetic inhomogeneous system, in which ferromagnetic clusters are formed inside the crystal. In this case, either of extrinsic precipitates of a ferromagnetic compound or the aggregation of Fe incorporated in the substitutional site in the ZB structure could act as ferromagnetic clusters. According to the result of XAFS measurement, the formation of precipitates would not be believable in these films (A#2, A#3) with the intermediate N concentrations, then the Fe aggregation may possibly be the source of ferromagnetic clusters. Though the mapping of Fe distribution using EDS in the cross-sectional TEM observation revealed almost uniform distribution, small fluctuations of the local Fe composition, which have remained undetectable in the mapping image, may possibly be responsible for the observed superparamagnetic behaviors.

Figure 4.1.15 shows the Curie-Weiss plotting for the undoped (A#1) and N-doped (A#3) films. In the case of undoped film the Curie-Weiss temperature is, Θ_P = -20K, while the Curie-Weiss temperature for the N-doped film is,Θ_P = +180K. The discrepancy between Curie temperature, T_C and Θ_P is that the former represents ferromagnetic transition temperature of the whole system and the latter represents the ferromagnetic interaction between localized spins in a macroscopic scale.

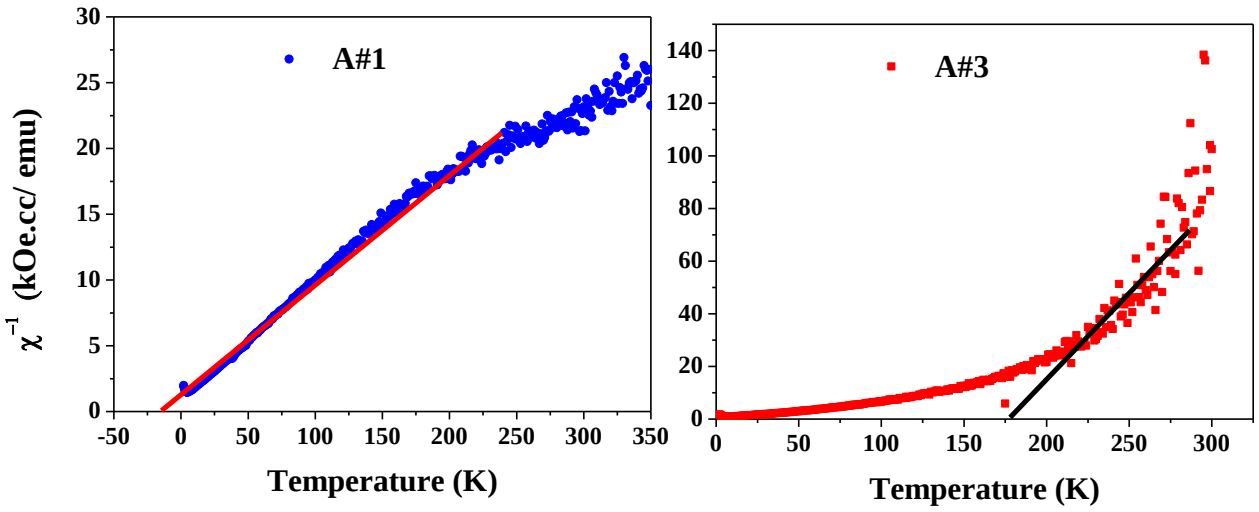

Figure 4.1.15 *M-T* curves of the undoped (A#1) and N-doped (A#2- A#4) $Zn_{1-x}Fe_xTe$ (x = 0.015) films.

4.1.7 Transport measurements of $Zn_{1-x}Fe_xTe$: N film: Physical property measurement system (PPMS)

We have measured the temperature dependence resistance of (*R-T*) and Hall resistance of the highest N-doped $Zn_{1-x}Fe_xTe$ thin film (A#4) with N concentration, [N] = 4×10^{19} cm^{-3} by using PPMS machine. We have used the four-terminal method (described in the experimental method section) to measure the temperature dependence resistivity of the N-doped film (A#4) as shown in Fig. 4.1.16.

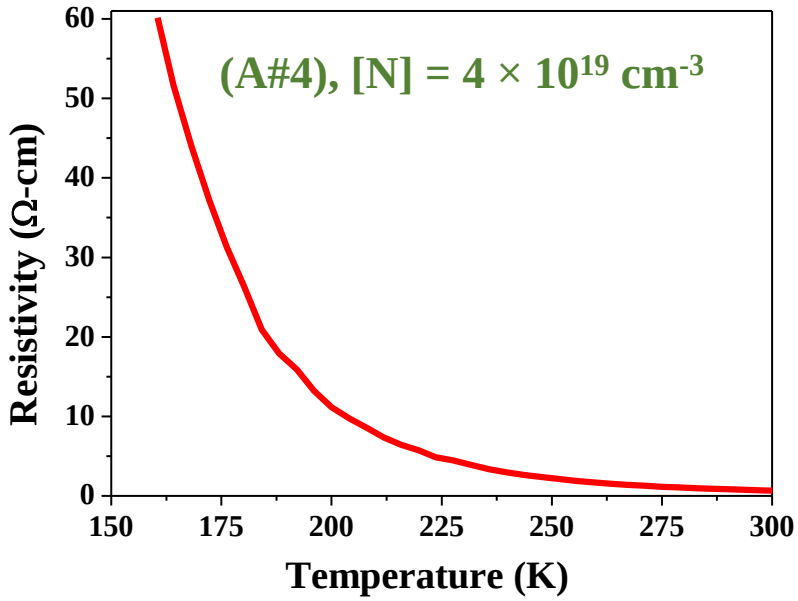

Figure 4.1.16: Temperature dependence resistivity for the $Zn_{1-x}Fe_xTe$: N film (A#4) with N concentration [N] = 4×10^{19} cm^{-3}.

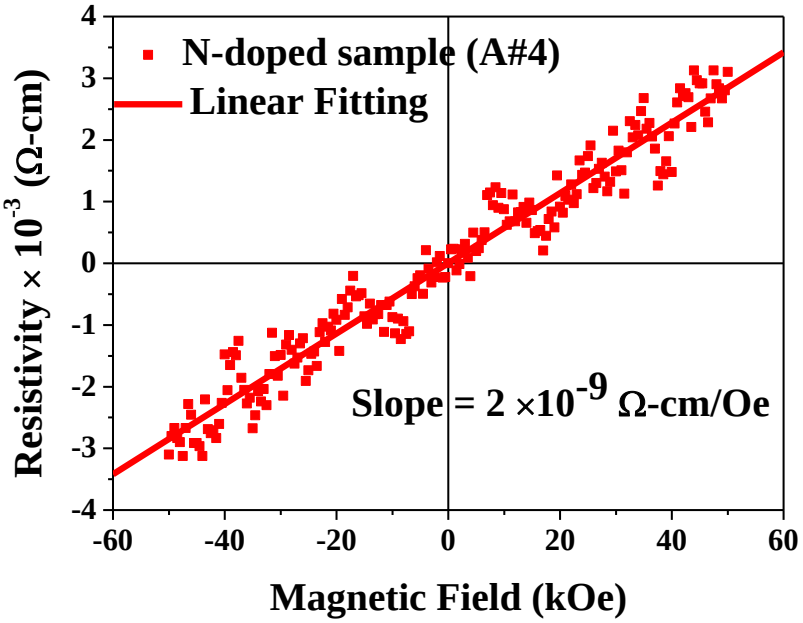

Figure 4.1.17: Magnetic field dependence of resistivity for the $Zn_{1-x}Fe_xTe$: N film (A#4) with N concentration [N] = 4×10^{19} cm^{-3}. The magnetic field is applied in the perpendicular direction of the film plane at 300K.

The temperature dependence of resistivity has shown the semiconductor behavior, with the increase of temperature, the resistivity decreases. The resistivity of the film at room temperature is measured as around 1 Ω-

cm. Figure 4.1.17 represents the Hall resistivity versus magnetic field graph. From the slope of the graph, we have measured the Hall coefficient. The current used in this measurement is 10μA.We have used the same four-terminal method, but this time the voltage leads are connected in the perpendicular direction of the current leads. The magnetic field in the range (-5T to +5T) has been applied perpendicular to the film plane.

$$\text{Hall coefficient, } R_H = \frac{E_H}{jB} = \frac{V_H}{IlB} = \frac{\rho}{B}$$

$$= 2 \times 10^{-9}\ \Omega\text{-cm/Oe}$$

$$= 2 \times 10^{-9} \times 10^{8}\ \text{cm}^3/\text{C}$$

$$= 0.2\ \text{cm}^3/\text{C}$$

$$\text{Carrier density, } n = \frac{1}{qR_H} = \frac{1}{0.2\times1.6\times10^{-19}}\ \text{cm}^{-3} = 3.13 \times 10^{19}\ \text{cm}^{-3}$$

4.1.8 Summary

We have investigated the structural and magnetic properties of $Zn_{1-x}Fe_xTe$:N thin films grown by MBE under Te-rich condition with constant Fe composition, $x = 0.015$ and variable N concentrations in the range of $8 \times 10^{17} - 4 \times 10^{19}$ cm^{-3}. According to the experimental results of XAFS and TEM observation, it can be concluded that the Fe atoms are predominantly incorporated in the substitutional site with the valence state of Fe deviated from Fe^{2+} due to the N-doping in the intermediate range of 10^{17}- 10^{18} cm^{-3}. However, Fe atoms are observed to form the extrinsic precipitates of Fe-N compounds at the highest N concentration of the order of 10^{19} cm^{-3}. These results are in agreement with the magnetic properties of the grown films; *M-H* curves have shown drastic changes from a linear dependence, typical of van-Vleck paramagnetism in the undoped film, to ferromagnetic behaviors with hysteresis at the intermediate N concentrations, which may originate from the deviation of the Fe valence state from Fe^{2+}. On the other hand, the linear dependence of the *M-H* curve at the highest N concentration may come from the formation of precipitates of Fe-N compounds.

4.2 Structural and magnetic properties of $Zn_{1-x}Fe_xTe$: N thin films (Zn-rich growth condition)

In this study, we have investigated the structural and magnetic properties of nitrogen (N) acceptor co-doped (Zn,Fe)Te thin films grown under Zn-rich condition. The key observation that inspired us to perform this study is the slightly different energy position of the Fe-K pre-edge peak position for undoped (Zn,Fe)Te thin films with nominally the same Fe composition grown between Te-rich and Zn-rich condition.

Before explaining the structural and magnetic properties of $Zn_{1-x}Fe_xTe$:N thin films grown under Zn-rich condition, a comparative study of the structural and magnetic properties of the undoped $Zn_{1-x}Fe_xTe$ thin film with Fe composition, $x \leq 1.5\%$ grown between Te-rich condition and Zn-rich condition has been demonstrated. Figure 4.2.1 representes the radial distribution function (RDF) derived from the Fourier transforms of the extended X-ray absorption fine structure (EXAFS) oscillations after weighted by k^3, for $Zn_{1-x}Fe_xTe$ thin films with Fe composition, $x = 1.5\%$ and 1.4% grown in the Te-rich and Zn-rich conditions respectively. As shown in Fig. 4.2.1, Fe atoms stay in the substitutional position on the Zn-site in both growth condition for the respective Fe composition of the $Zn_{1-x}Fe_xTe$ thin films. This is because the first nearest neighbor peak position (1st NN) which corresponds to the bond of Fe with Te (~ 2.5 Å) has been found same for both the simulation data and experimental curves.

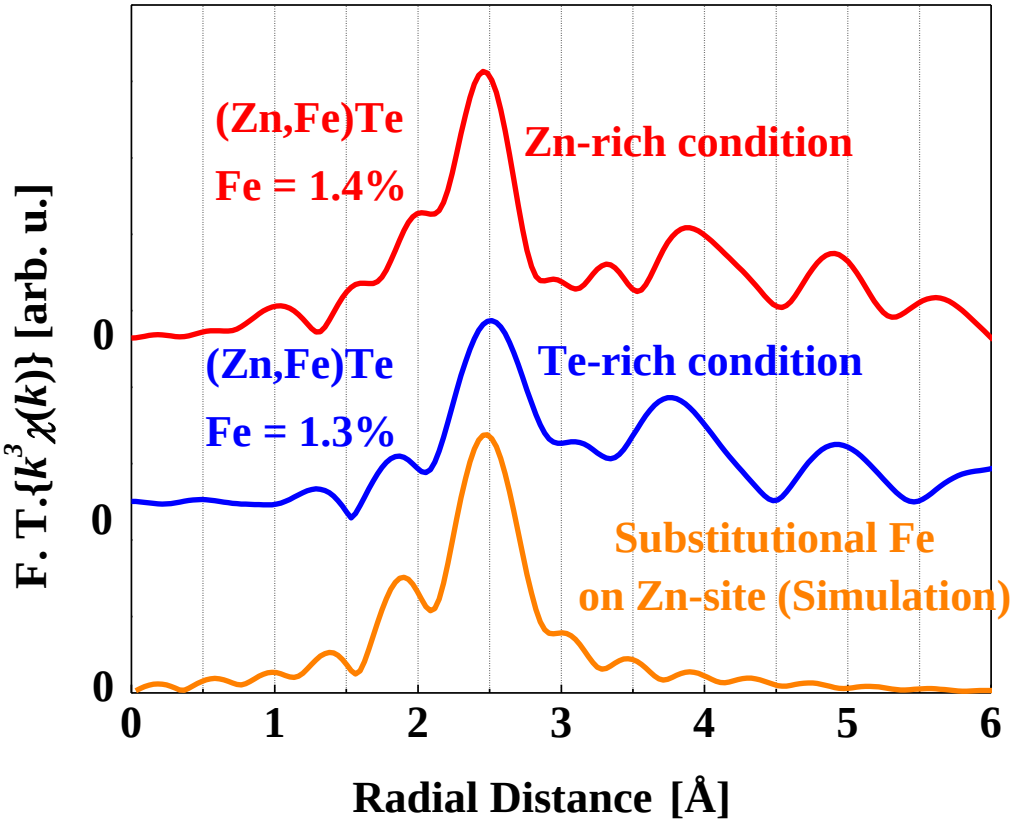

Figure 4.2.1: RDF spectra of the undoped $Zn_{1-x}Fe_xTe$ films with Fe composition, x = 1.5 % and 1.4% grown under Te-rich and Zn-rich condition respectively. The results of simulation assuming an Fe atom in the substitutional site in the ZB structure are also shown as reference.

Now, the XANES spectra for the respective samples has been demonstrated in Fig. 4.2.2. It has already been known that the pre-edge peak position of the XANES spectra possesses important information about the valence state of Fe. In order to determine the pre-peak energy position precisely, we have plotted baseline around the Fe absorption edge region in the XANES spectra of the $Zn_{1-x}Fe_xTe$ thin films as shown in Fig. 4.2.3. In this way, we have subtracted the background and found the pre-edge peak region precisely. Then we have fitted the pre-edge curve with Gaussian function to evaluate the peak position. The pre-edge peak energy position is slightly higher in the Zn-rich case.

According to the previous research on Fe-K pre-edge peak by several research groups, the pre-edge peak energy position of the XANES spectra is very sensitive to Fe redox states and shifts towards higher energy with increasing oxidation state. Based on this information, it seems to us that the Fe oxidation state is slightly different for undoped $Zn_{1-x}Fe_xTe$ thin film grown under Zn-rich condition than Te-rich condition for almost the same Fe composition. However, we have not identified any significant difference in the magnetic properties of the undoped $Zn_{1-x}Fe_xTe$ thin films for the Fe composition, $x \geq 1.5$ % grown between Te-rich and Zn-rich condition as shown in Fig. 4.2.4. The *M-H* curves show predominantly the liner dependence of magnetization on magnetic field, typical of van-Vleck paramagnetism and a small hysteresis has observed in the low field region for both the cases.

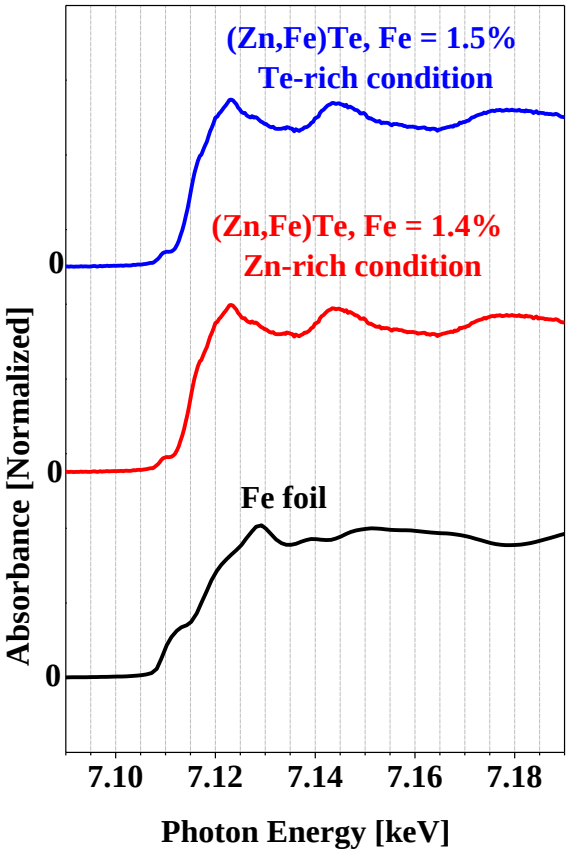

Figure 4.2.2: XANES spectra of the undoped $Zn_{1-x}Fe_xTe$ films with Fe composition, x = 1.5 % and 1.4% grown under Te-rich and Zn-rich condition respectively along with that of elemental Fe foil as reference.

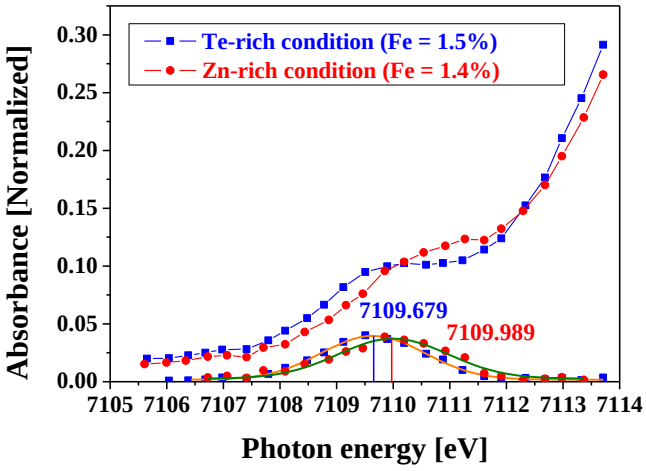

Figure 4.2.3: Fitting of Fe-K pre-edge region after baseline subtraction for undoped $Zn_{1-x}Fe_xTe$ films with Fe composition, x = 1.5 % and 1.4% grown under Te-rich and Zn-rich condition respectively using Gaussian function. The pre-edge peak position is indicated by straight line.

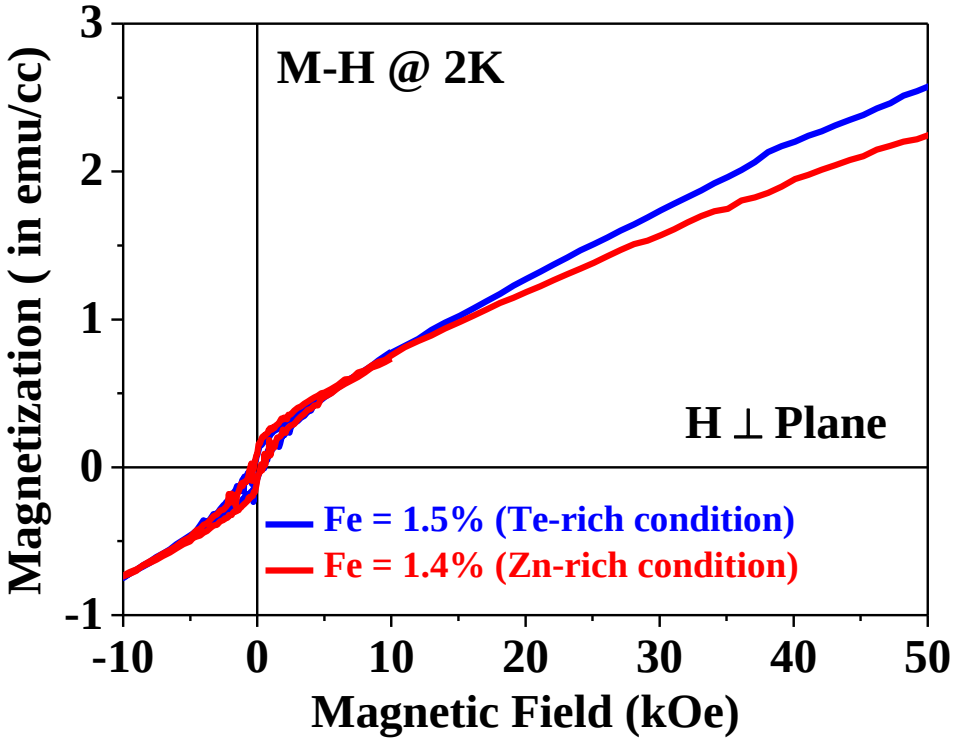

Figure 4.2.4: *M-H* curves of the undoped $Zn_{1-x}Fe_xTe$ films with Fe composition, x = 1.5 % and 1.4% grown under Te-rich and Zn-rich condition respectively. The measurement has been performed at 2K under magnetic field perpendicular to the film plane.

we have already learnt that the nitrogen acceptor co-doping has deviated the valence state of substitutional Fe from Fe^{2+} and produce significant impact on the magnetic properties of (Zn,Fe)Te thin films grown under Te-rich condition. From these points of view, it is expected that the amount of deviation of substitutional Fe valence state from Fe^{2+} due to N-doping might be different in (Zn,Fe)Te thin films grown under Zn-rich condition and might have different impact on its magnetic properties.

4.2.1 Sample preparation

Thin films of N-doped (Zn,Fe) Te have been grown in excess of Zn flux over Te flux by molecular beam epitaxy (MBE) using elemental solid sources of Zn, Te and Fe and nitrogen plasma source with N_2 gas excited by rf-plasma. The power of the plasma source was fixed at 300W and the N_2 gas flow rate has been maintained at 0.3 cc/min throughout the growth of $Zn_{1-x}Fe_xTe$: N layer. A thick layer of ZnTe buffer (~900 nm) is grown on a GaAs (001) substrate in order to relax the large lattice mismatch and then a $Zn_{1-x}Fe_xTe$: N layer (~700 nm) has been deposited on it. Figure 4.2.5 has demonstrated the sample structure used in this study. The substrate temperature is kept at 260°C during the growth. During the growth of the N-doped $Zn_{1-x}Fe_xTe$ layer, the N concentration is controlled by changing the size of holes in the shutter of the plasma source and the distance between the plasma source and the substrate. The concentrations of Fe and N in the N-doped $Zn_{1-x}Fe_xTe$ layer has been measured by electron probe microanalyzer (EPMA) and secondary ion mass spectroscopy (SIMS), respectively. In the SIMS measurement, we have used primary ion beam of $^{133}Cs^+$ accelerated at 3keV and quantified the N concentration by measuring a N-implanted ZnTe thin film as reference. We have confirmed an almost flat depth profile of N

concentration across the entire region of the N-doped film. We have prepared a series of $Zn_{1-x}Fe_xTe$ thin films with a fixed Fe composition $x = 0.014$ and varied N concentrations; one without N doping (B#1, referred to as undoped), and those with different N concentrations [N] = 1. 8×10^{18} cm^{-3} (B#2), 4.3×10^{18} cm^{-3} (B#3), 1.8×10^{19} cm^{-3} (B#4) and 5.1×10^{19} cm^{-3} (B#5).

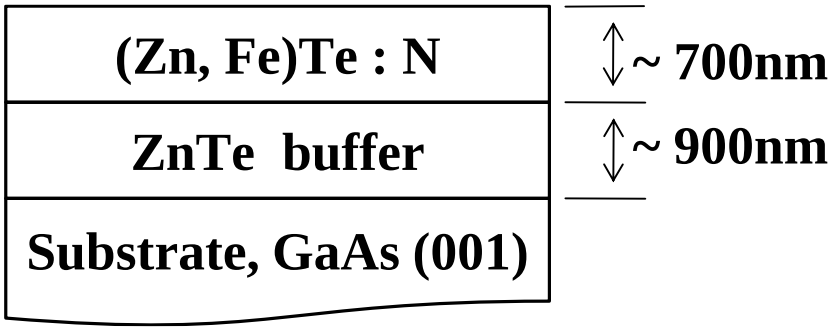

Figure 4.2.5: Sample structure for $Zn_{1-x}Fe_xTe$: N thin films

Table 4.2: Sample list of $Zn_{1-x}Fe_xTe$: N thin films

Sample No.	Substrate T_S°C	Diameter of Hole	Distance between plasma source and substrate (cm)	N doping Concentration (cm^{-3})	Fe Composition [%]
B#1	260	Closed	-	0	1.4
B#2	260	Small open	6	1.8×10^{18}	1.4
B#3	260	Small open	2	4.3×10^{18}	1.4
B#4	260	Large Open	6	1.8×10^{19}	1.4
B#5	260	Fully open	6	5.1×10^{19}	1.4

4.2.2 Evaluation of the sample surface by reflection high energy electron diffraction (RHEED)

During the growing of the thin film, we have observed in-*situ* of the growth using the reflection high energy electron diffraction (RHEED) system connected in the MBE system. Figure 4.2.6 shows the RHEED pattern of the samples after the growth of the magnetic layer. In the case of both undoped (B#1) and N-doped films (B#2-B#5), spotty-streak pattern has been observed. In addition, in the highest N-doped film (B#5) with N concentration, [N] = 5.1×10^{19} cm^{-3}, the intensity of the diffraction spots decreases dramatically.

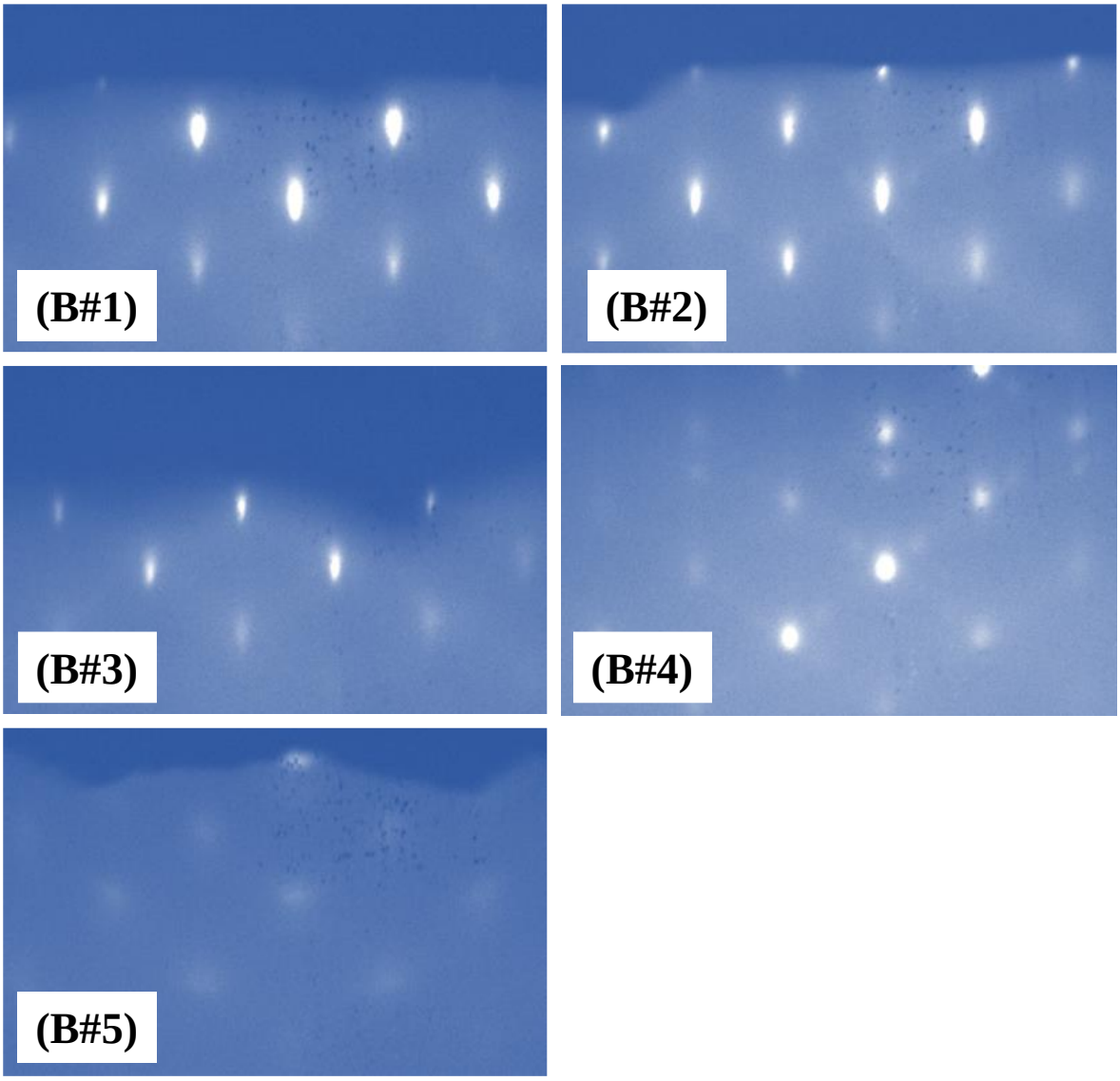

Figure 4.2.6: RHEED pattern of undoped (B#1) and N-doped (B#2 – B#5) $Zn_{1-x}Fe_xTe$: N thin films after the growth.

4.2.3 Structural characterization of $Zn_{1-x}Fe_xTe$: N thin films: X-ray diffraction analysis (XRD)

First, we have demonstrated the result of structural characterization of the grown films. Figure 4.2.7 shows the XRD θ-2θ scan profiles of the undoped (B#1) and N-doped (B#2 - B#5) films with a fixed Fe composition, x = 0.014 and variable nitrogen concentrations. In the undoped (B#1) and N-doped (B#2- B#4) films, other diffraction peaks than those from the ZnTe buffer layer and the GaAs substrate are not detected. However, in the case of the highest N-doped (B#5) film, other than diffraction peaks from the (n00) planes of the (Zn,Fe)Te layer, ZnTe buffer layer and GaAs substrate, two small additional diffraction peaks at 2θ = 23.97° and 49.63° are observed, which may possibly originate from some phase of Fe-N compounds. The most possible candidates for the diffraction peaks at the 2θ = 23.97° and 49.63° may be Fe_4N (100) of the fcc crystal structure and Fe_8N (301) of the tetragonal

crystal structure respectively [101, 102].These results suggest that the N-doped films (B#2- B#4) with lower N concentration are composed of the pure diluted phase in which Fe atoms substitute the Zn site in the zinc-blende (ZB) structure, while precipitates of Fe-N compounds were formed in the N-doped film (B#5) with the highest N concentration.

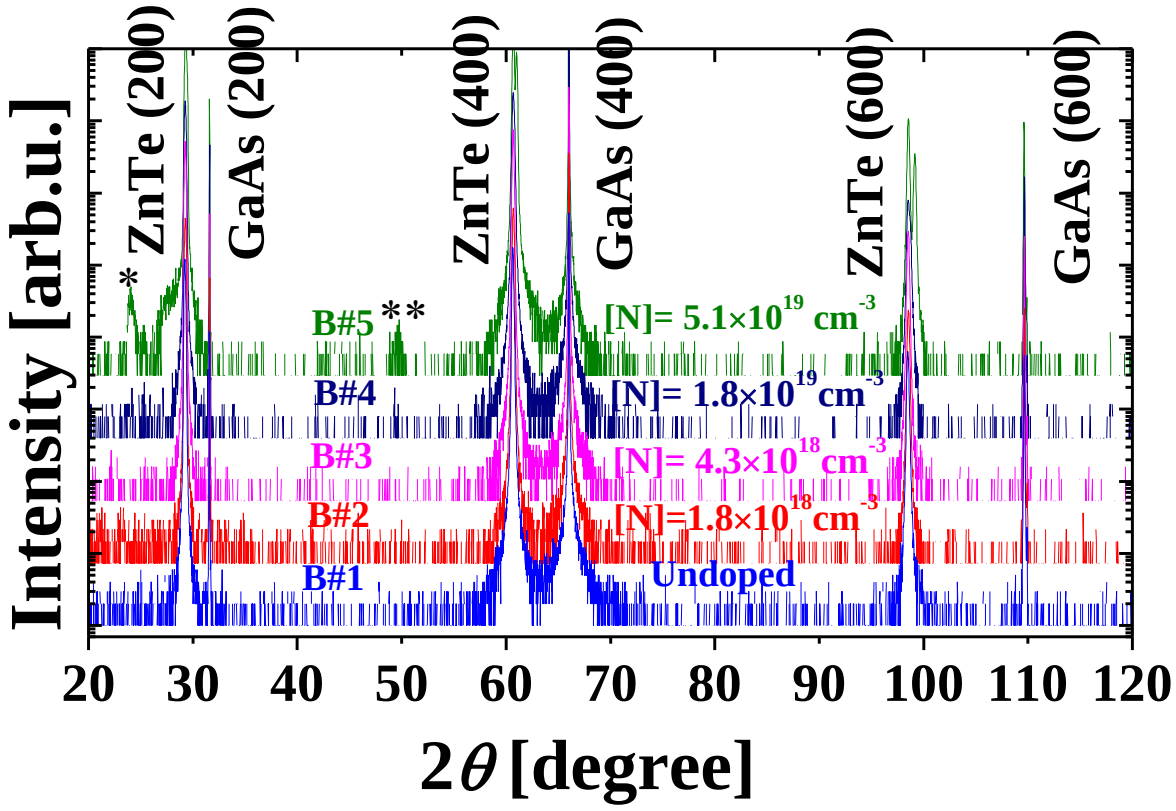

Figure 4.2.7 The XRD θ-2θ scan profiles of the undoped (B#1) and N-doped (B#2- B#5) $Zn_{1-x}Fe_xTe$ (x = 0.014) films with different N concentrations. The * marked in the highest N-doped film (B#5) are the positions of extrinsic precipitate phases.

4.2.4 Structural analysis of $Zn_{1-x}Fe_xTe$: N films: X-ray absorption fine structure (XAFS) analysis

In order to analyze structural properties in the atomic scale, we have performed XAFS measurement at Fe K-edge. We analyze the radial distribution function (RDF) around the Fe atom, derived from Fourier transforms of extended x-ray absorption fine structure (EXAFS) oscillation, as shown in Fig. 4.2.8. The oscillatory parts $\chi(k)$ extracted from the observed EXAFS spectra at Fe K-edge have been multiplied by k^3 for weighting and transformed into real space. In the figure, the result of simulation for an Fe atom in the substitutional site in the zinc-blende (ZB) structure is also plotted as reference. For the simulation of an Fe atom in the substitutional site, it is assumed that a single Fe atom substitutes the Zn site in the host crystal of ZnTe without any change of the lattice constant and only the single scattering path is taken into account. As we observe in the figure, the experimental curve for the undoped film (B#1) and the N-doped films with intermediate N concentrations (B#2,

B#3) are very similar to the result of simulation for the substitutional Fe, showing a main peak at around 2.5 Å corresponding to the bond with Te atoms at the first nearest neighbor (1st NN). On the other hand, in the N-doping films with higher N concentrations (B#4, B#5), the main peak is shifted to a shorter distance, which suggests that Fe atoms are incorporated in different sites or form some extrinsic phase other than the ZB structure. In fact, the result of XRD has confirmed the presence of diffraction peaks from extrinsic phases in the highest N-doped film (B#5).

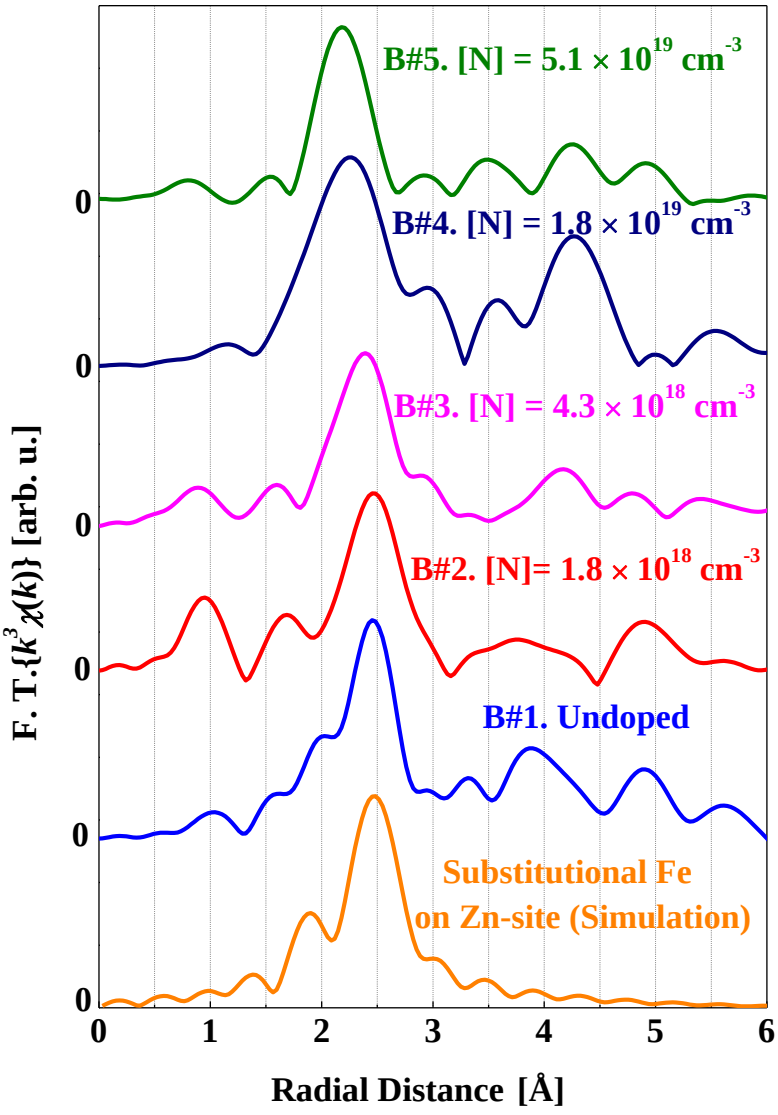

Figure 4.2.8: Radial distribution function (RDF) for the undoped (B#1) and N-doped (B#2- B#5) $Zn_{1-x}Fe_xTe$ (x = 0.014) films. The result of simulation considering Fe atom in the substitutional position on the Zn-site in the zinc-blende crystal structure is also plotted for reference.

Figure 4.2.9 has demonstrated the X-ray absorption near edge structure (XANES) spectra of the undoped (B#1) and N-doped (B#2 - B#5) films, together with the spectrum of an elemental Fe foil as reference. In the undoped film (B#1), we have observed three absorption peaks near the Fe K-edge; the pre-edge peak at 7.1099 keV, the shoulder peak at 7.1168 keV and the main peak at 7.1238 keV. The pre-edge peak is assigned as the transitions from the 1s state to the 3d-like state (quadrupolar), while the shoulder and main peaks are both related to the transition from the 1s state to the 4p-like state (dipolar) [68].

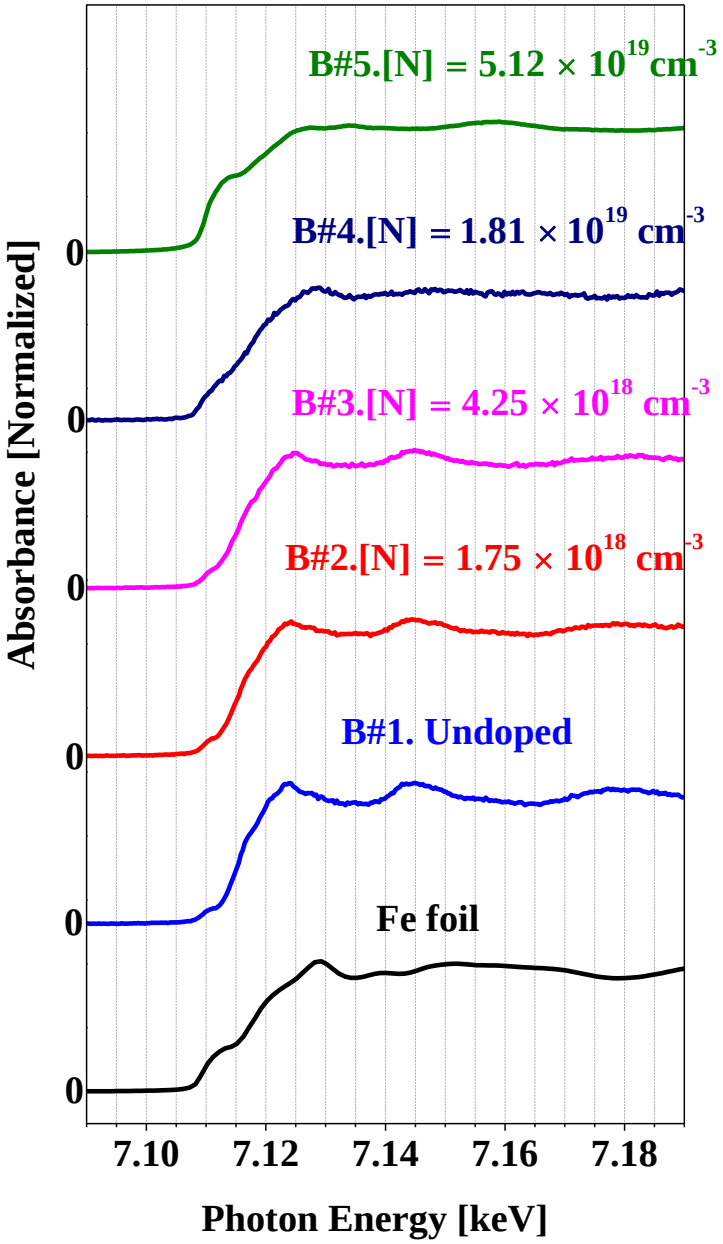

Figure 4.2.9: XANES spectra for the undoped (B#1) and N-doped (B#2- B#5) $Zn_{1-x}Fe_xTe$ (x = 0.014) films. The XANES spectra for an elemental Fe foil is also presented.

According to the previous studies on high energy resolution XANES spectra of the Fe-K edge by several research groups, it is known that the shape and position of the main absorption edge is sensitive to the co-ordination geometry, while the pre-edge region is less sensitive to changes in the local environment and solid state effects because 3d final states are more tightly bound than higher energy final states. In addition, it is mentioned that the pre-edge peak energy position is the most important feature for determining Fe valence state; the energy position and intensity of the pre-edge peak gradually increase in passing from the purely Fe^{2+} state to the purely Fe^{3+} state and the separation between the pre-edge energy positions for these two states is 1.4 ± 0.1 eV [90, 91]. In our study, we have plotted a baseline along the absorption edge region to subtract the background and found the pre-edge peak region of the XANES spectra in the studied undoped (B#1) and N-doped films (B#2 - B#5). Then, the experimentally observed pre-edge region (shown in Fig. 4.2.10) is fitted with the Gaussian function and the peak position of the pre-edge is determined precisely. Figure 4.2.11 has demonstrated the background subtracted pre-edge peak energy position for the studied (B#1-B#5) films.

In the undoped film B#1, the pre-edge peak is observed at 7.1099 keV, which is considered to be pure diluted phase with Fe being incorporated in the substitutional position on the Zn-site and in the isoelectronic state of Fe^{2+}. However, in the case of N- doped films (B#2 - B#5), the energy position of the pre-edge peak is located at 7.1103, 7.1106, 7.1108 and 7.1124 keV respectively. Figure 4.2.12 represents the shifting of pre-edge energy position with the increase of N-doping concentration. This shift of the pre-edge peak towards higher energy in the N-doped films (B#2 - B#5) reflects the change of valence state of Fe from Fe^{2+} in the undoped film to the $Fe^{2+/3+}$ mixed state or in other valence state due to the incorporation of N.

In addition, there exists significant difference in the shape and position of the main absorption peak among N-doped films with intermediate N concentrations (B#2, B#3) and higher N concentrations (B#4, B#5). In the case of intermediate N concentrations (B#2, B#3), the shape and position of the main absorption peak are almost same as the undoped film (B#1). On the other hand, at higher N concentrations (B#4, B#5), the position and shape of the main absorption peak are found to be different from those of the undoped film (B#1). For the N-doped film (B#4), the position of the main absorption peak is shifted towards higher energy at 7.128 keV, while it is located at 7.124 keV in the case of the undoped film (B#1). Accordingly, in the case of highest N-doped film (B#5), the shape of the main absorption peak changes and the shoulder peak disappears completely. This change in energy position in the N-doped film (B#4) and the shape in the N-doped film (B#5) of the main absorption peak suggest different co-ordination environment around Fe atom in those films.

Thus, both the RDF and XANES spectra show a clear difference in the local environment around Fe atom between intermediate N concentrations (B#2, B#3) and higher N concentrations (B#4, B#5) films. For N-doped films (B#2, B#3), Fe atoms are incorporated in the substitutional position on Zn-site with the valence state deviated from Fe^{2+} to $Fe^{2+/3+}$ mixed states due to N-doping; while Fe is dominantly incorporated in forming Fe-N compounds with Fe valence state $Fe^{2+/3+}$ or other valence state in N-doped films (B#4, B#5). In fact, the XRD result has already confirmed the presence of extrinsic precipitates in the highest N-doped film (B#5).

We have demonstrated a comparative study between the pre-edge energy position of the N-doped films grown under Te-rich and Zn-rich condition for nominally the same Fe composition as shown in Fig. 4.2.13. We have observed that the energy position of the pre-edge peak is higher in Zn-rich samples than in Te-rich samples even with the same N-doping concentration. This indicates that the change of valence state of Fe from Fe^{2+} to Fe^{3+} due to N-doping is significant in Zn-rich samples.

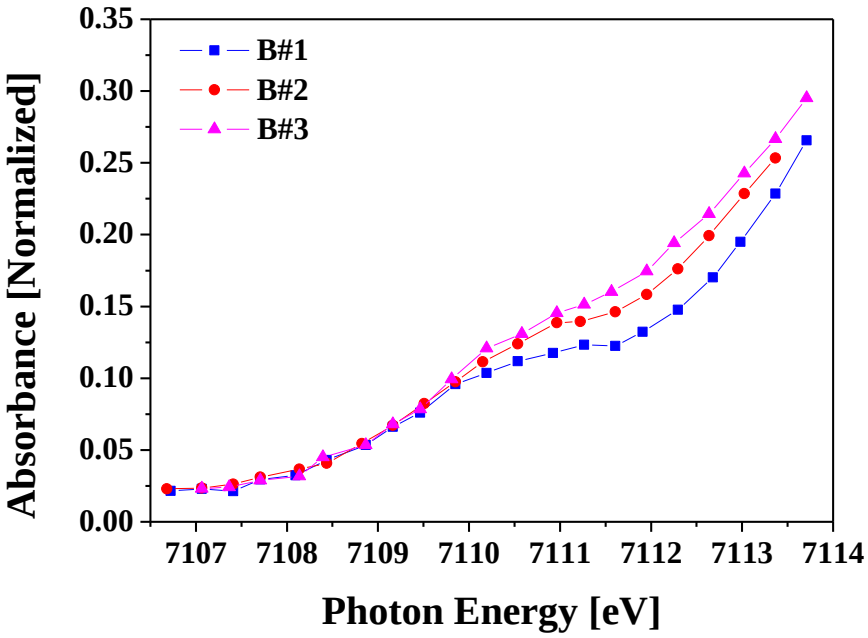

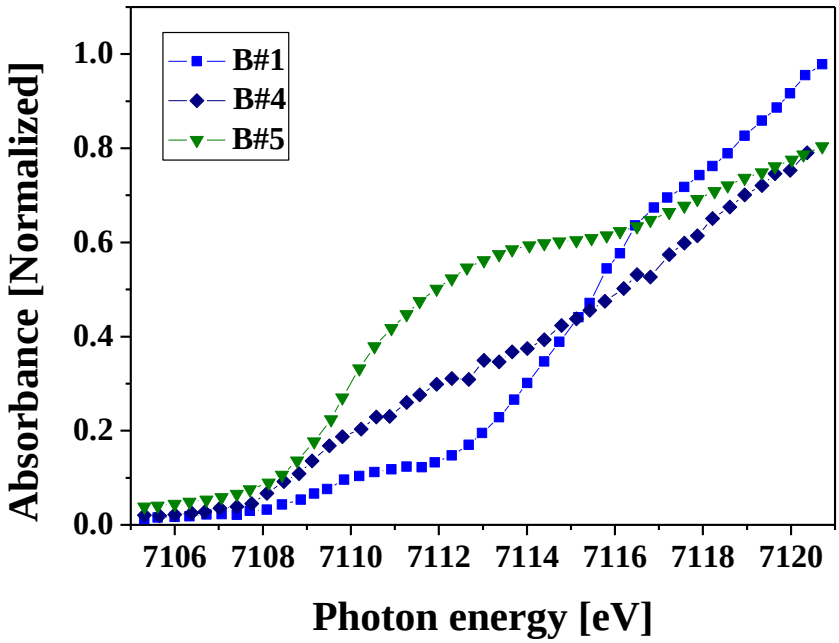

Figure 4.2.10: Fe-K pre-edge region for undoped (B#1) and N-doped (B#2-B#5) $Zn_{1-x}Fe_xTe$ (x = 0.014) films. In the upper panel shows the Fe-K pre-edge region for the undoped (B#1) and N-doped (B#2, B#3) films and the bottom panel shows the Fe-K pre-edge region for the undoped (B#1) and N-doped (B#4, B#5) films .

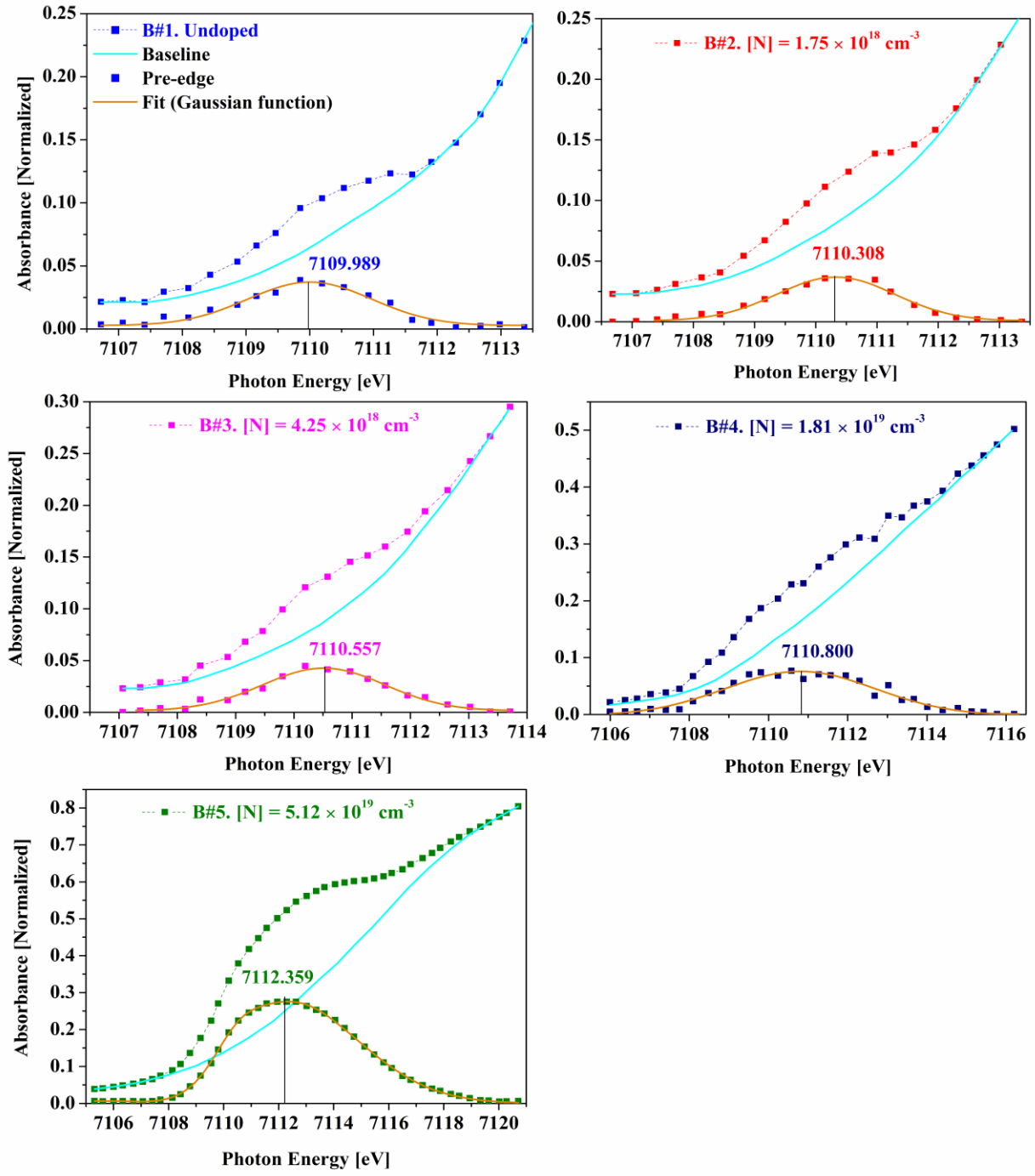

Figure 4.2.11: Fe-K pre-edge region for undoped (B#1) and N-doped (B#2-B#5) $Zn_{1-x}Fe_xTe$ (x = 0.014) films after baseline subtraction and fitted with Gaussian function. The pre-edge peak position is marked by the straight line.

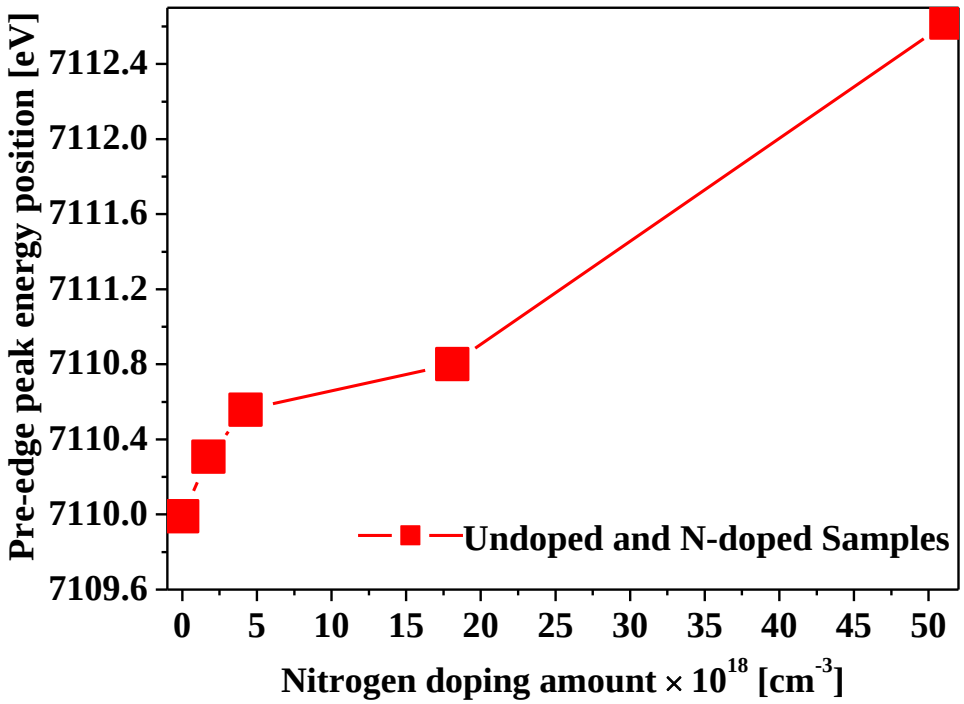

Figure 4.2.11: N-doping concentration dependence pre-edge peak position of the XANES spectra for undoped (B#1) and N-doped (B#2-B#5) $Zn_{1-x}Fe_xTe$ (x = 0.014) films grown under Zn-rich condition.

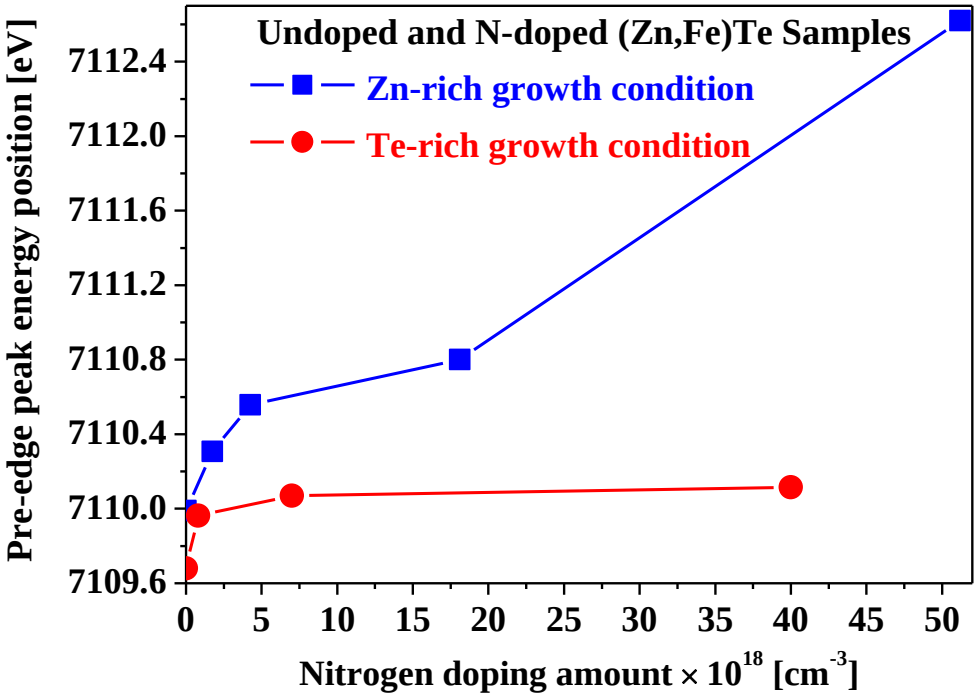

Figure 4.2.13: The pre-edge peak position vs N-doping concentration graph for undoped and N-doped $Zn_{1-x}Fe_xTe$ films grown under Te-rich and Zn-rich conditions for nominally the same composition of Fe.

4.2.5 Magnetization measurements of $Zn_{1-x}Fe_xTe$: N films: Superconducting quantum interference device (SQUID)

The magnetization measurements have been performed by using SQUID with the application of magnetic field perpendicular to the film plane. Figure 4.2.13 (a) and (b) have shown the *M-H* curves of the undoped (B#1) and N-doped (B#2 - B#5) films measured at 2K and 300K respectively. The magnetization measurement reveals a drastic change of magnetic properties by N-doping as represented by the evolution of *M-H* curves.

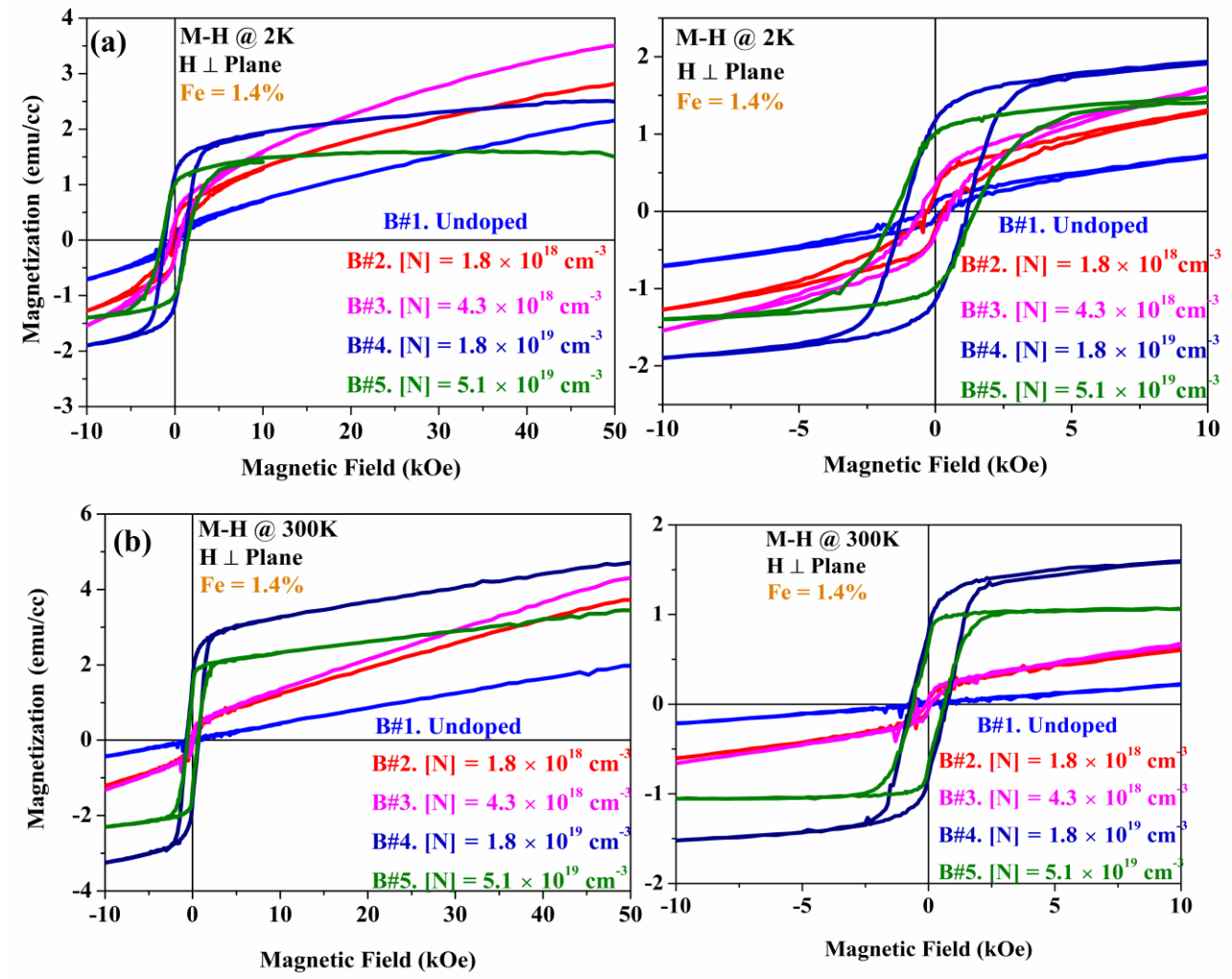

Figure 4.2.14: *M-H* curves of the undoped (B#1) and N-doped (B#2- B#5) $Zn_{1-x}Fe_xTe$ (x = 0.014) films. The measurement was performed at **(a)** 2*K* and **(b)** 300*K* under magnetic field perpendicular to the film plane. **(a)** Left panel (*M-H* curve at 2K, total field area), right panel (*M-H* curve at 2K, low field area).

In the case of undoped film (B#1), the magnetization increases almost linearly with magnetic field without being saturated and hysteresis is observed in the low field region. The linear dependence of magnetization on magnetic field is a typical behavior of van-Vleck paramagnetism; the localized magnetic moment which is quenched at zero field, is induced by the application of an external magnetic field. The linear *M-H* curve in the

undoped film changes into room temperature ferromagnetic feature with hysteresis in the N-doped films (B#2 - B#5).

However, different tendency in saturation magnetization and coercivity has been observed among N-doped films between intermediate N concentrations (B#2, B#3) and higher N concentrations (B#4, B#5). In the case of N-doped films (B#2, B#3) with N concentrations in the range [N] = $1.8 \times 10^{18} – 4.3 \times 10^{18}$ cm^{-3}, the magnetization remains unsaturated at 5T and the coercivity has increased gradually with the increase of the N-doping concentration as represented by the evolution of *M-H* curves measured at 2K [shown in Fig. 4.2.13(a)] and 300K [shown in Fig. 4.2.13(b)]. The coercivity is measured to be 300 Oe and 99.5 Oe for the N-doped film (B#2) and 500 Oe and 125 Oe for the N-doped film (B#3) at 2K and 300K respectively. The weak room temperature ferromagnetic behavior observed at the intermediate N concentrations could be attributed to the deviation in the valence state of substitutional Fe from Fe^{2+} to $Fe^{2+/3+}$ mixed states as indicated by the pre-edge peak shifting in the XANES spectra for the respective N-doped films. This deviation of the Fe valence state from Fe^{2+} due to the doping of an acceptor impurity would produce robust finite magnetic moment even at zero external magnetic field and may also modify the exchange interaction between these magnetic moments.

On the other hand, in the case of N-doped films with higher N concentrations (B#4, B#5), we have observed room temperature ferromagnetic behavior with robust hysteresis curve; the coercivity is measured to be 1203 Oe and 702.4 Oe for N-doped film (B#4) and 1404 Oe and 601.8 Oe for N-doped film (B#5) at 2K and 300K respectively. In addition, the magnetization value has found to be saturated at 5T for both films and the saturation magnetization value has started to decrease with the increase of N-doping concentration. This observed robust room temperature ferromagnetic behavior in the higher N concentrations may arise from extrinsic precipitates such as Fe_4N (fcc) and Fe_8N (tetragonal), as observed from the additional diffraction peaks in the X-ray diffraction analysis for the highest N-doped film (#5). These Fe-N compounds have room temperature ferromagnetic behavior in the bulk form and have large saturation magnetization value even higher than pure iron [98, 99].

We have also measured *M-T* curves of the undoped and N-doped films under a fixed magnetic field of 500 Oe. As seen in Fig. 4.2.15, small blocking phenomenon was observed at around 3.9K for the undoped (B#1) and N-doped (B#2, B#3) films with intermediate N concentrations. In addition, a small bifurcation between the field-cooled (FC) and zero-field-cooled (ZFC) curves with lowering temperature is observed for the N-doped film (B#3). These superparamagnetic features such as the irreversibility between magnetizations determined under FC and ZFC conditions and a cusp in the *M*(T) dependence taken in the ZFC process are more pronounced in magnetic inhomogeneous system, in which ferromagnetic clusters are formed inside the crystal [108-110].These ferromagnetic clusters may originate from either the extrinsic precipitates of a ferromagnetic compound or the aggregation of Fe incorporated in the substitutional site in the ZB structure. According to the result of XAFS measurement, the formation of precipitates would not be plausible in these films with the intermediate N concentrations, then the Fe aggregation may possibly be the origin of ferromagnetic clusters. However, markedly different behavior, namely the increasing FC-ZFC difference on lowering temperature was observed in the case of N-doped films with higher N concentrations (B#4, B#5). We further noticed that the FC and ZFC magnetizations are characterized by temperature gradients of the opposite signs without a maximum appearing in the ZFC curve. These behaviors exhibited by the *M-T* curves clearly suggest the formation of extrinsic precipitates of ferromagnetic compound in the N-doped films with higher N concentrations (B#4, B#5). The non-spherical shape of the precipitates may lead to an additional magnetic anisotropy that can elevate the blocking temperature [111]. In fact, the XRD result has already confirmed the formation of extrinsic precipitates such as Fe_4N (fcc) and Fe_8N (tetragonal) in the highest N-doped film (B#5). According to the previous research, it is known that the cubic ordered iron nitride compound, Fe_4N (fcc) exhibits magneto-crystalline anisotropy in the bulk form with the easy axis being the [100] direction [100].

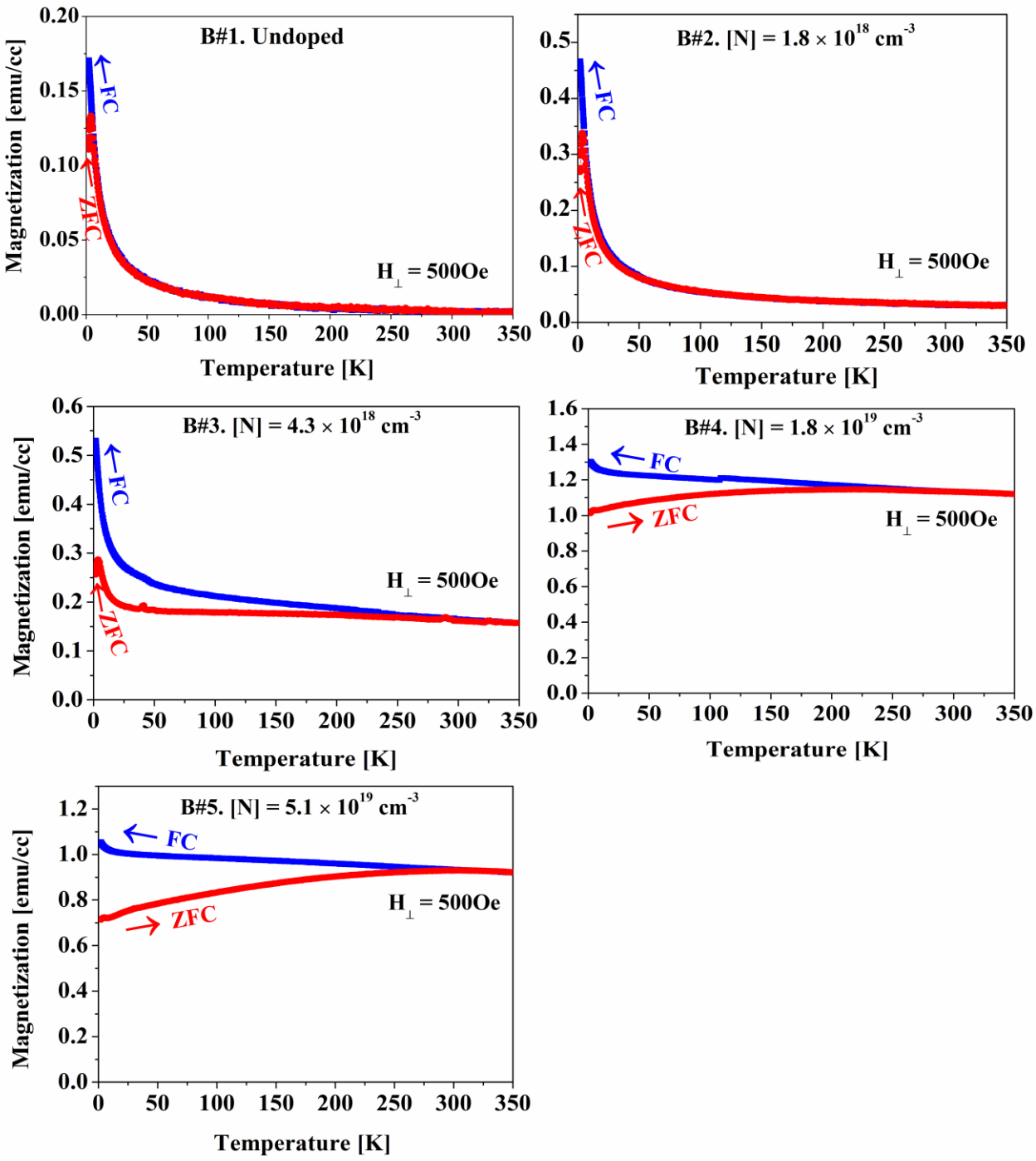

Figure 4.2.15: *M-T* curves of the undoped (B#1) and N-doped (B#2- B#5) $Zn_{1-x}Fe_xTe$ (x = 0.014) films. The magnetization has been measured both in the field-cooled (FC) and zero-field-cooled (ZFC) processes under a constant magnetic field of 500Oe applied perpendicular to the film plane.

The observed opposite temperature gradients of FC and ZFC magnetization for the N-doped films (B#4, B#5) has been reduced by increasing the external magnetic field. Figure 4.2.16 has demonstrated the *M-T* curves of the N-doped films (B#4, B#5) under different magnitudes of external magnetic field. With the increase of external magnetic field, the energy barriers that blocked the magnetic moments have been removed and hence, the difference in magnetization under FC and ZFC processes in the low temperature region has been reduced.

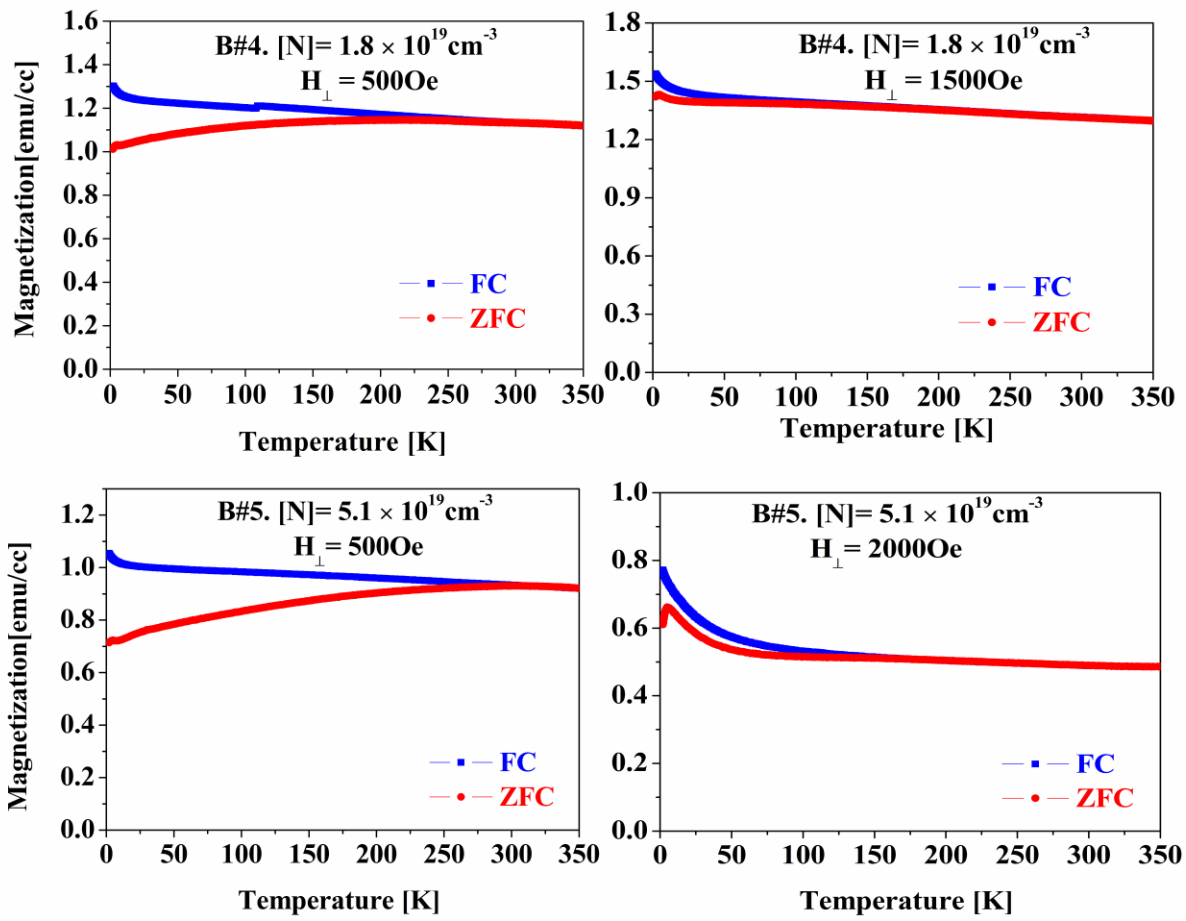

Figure 4.2.16: *M-T* curves of the N-doped $Zn_{1-x}Fe_xTe$ (x = 0.014) films (B#4, B#5) at different external magnetic field perpendicular to the film plane. The magnetization has been measured both in the field-cooled (FC) and zero-field-cooled (ZFC) processes.

We have also observed different behaviors between N-doped films with intermediate N concentrations (B#2, B#3) and higher N concentrations (B#4, B#5) on the basis of magnetic anisotropy. In the case of intermediate N concentrations films (B#2, B#3), we have noticed almost the same coercivity for the *M-H* curves with the applied field both parallel and perpendicular to the film plane. Similar magnetization values are found for FC and ZFC processes in the *M-T* curves with the applied field both parallel and perpendicular to the film plane. Figure 4.2.17 has shown (a) the *M-H* curves (*H* applied both parallel and perpendicular to the film plane), (b) *M-T* curves (*H* applied perpendicular to the film plane) and (c) *M-T* curves (*H* parallel to the film plane) for the N-doped film (B#2) with N concentration [N] = 1.8×10^{18} cm^{-3}.

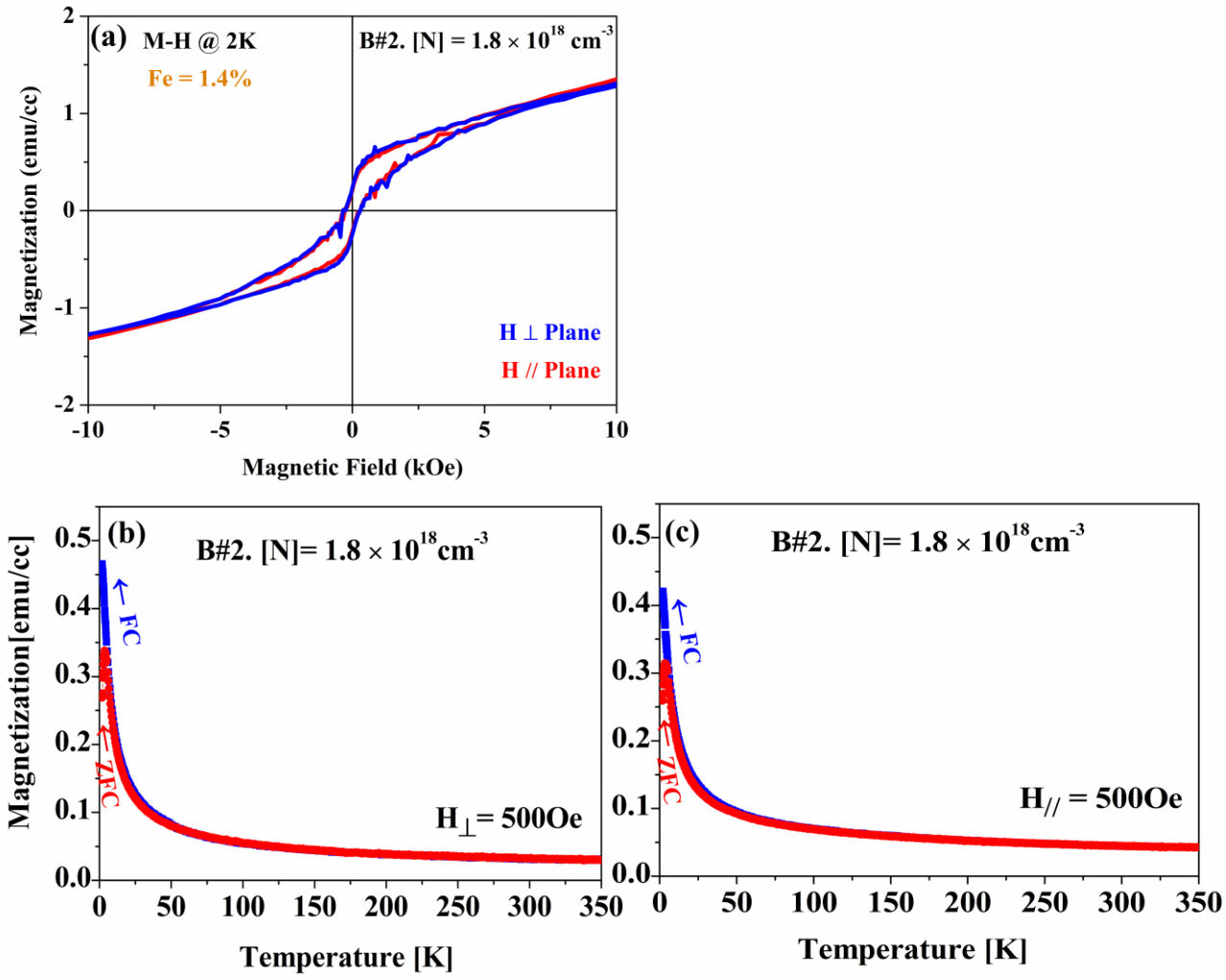

Figure 4.2.17: Magnetization measurements of N-doped film (B#2) with N concentration, [N] = 1.8×10^{18} cm^{-3} **(a)** *M-H* curves measured at 2K with applied field both perpendicular and parallel to the film plane **(b)** *M-T* curves with applied field of 500Oe perpendicular to the film plane **(c)** *M-T* curves with applied field of 500Oe parallel to the film plane.

However, in the N-doped films with higher N concentrations (B#4, B#5), we have observed difference in coercivity in the *M-H* curves measured with applied field parallel and perpendicular to the film plane; the coercivity is found to be larger in the case of applied field perpendicular to the film plane. In addition, the magnetization values under the FC and ZFC processes in the *M-T* curves are larger for applied field perpendicular to the film as compared to the values obtained for applied field parallel to the film plane. These anisotropic magnetic behaviors of the N-doped films (B#4) with N concentration [N] = 1.8×10^{19} cm^{-3} and (B#5) with N concentration [N] = 5.1×10^{19} cm^{-3} are shown in Fig. 4.2.18 and 4.2.19 respectively. The magnetic anisotropy is found to be largest in the highest N-doped film (B#5). So, the robust ferromagnetic behavior observed in the N-doped films with higher N concentrations (B#4, B#5) may predominantly originate from extrinsic precipitates of ferromagnetic compounds exhibiting magnetic anisotropy such as Fe_4N and Fe_8N compounds, as detected by the additional diffraction peaks in the XRD analysis for the highest N-doped film (B#5).

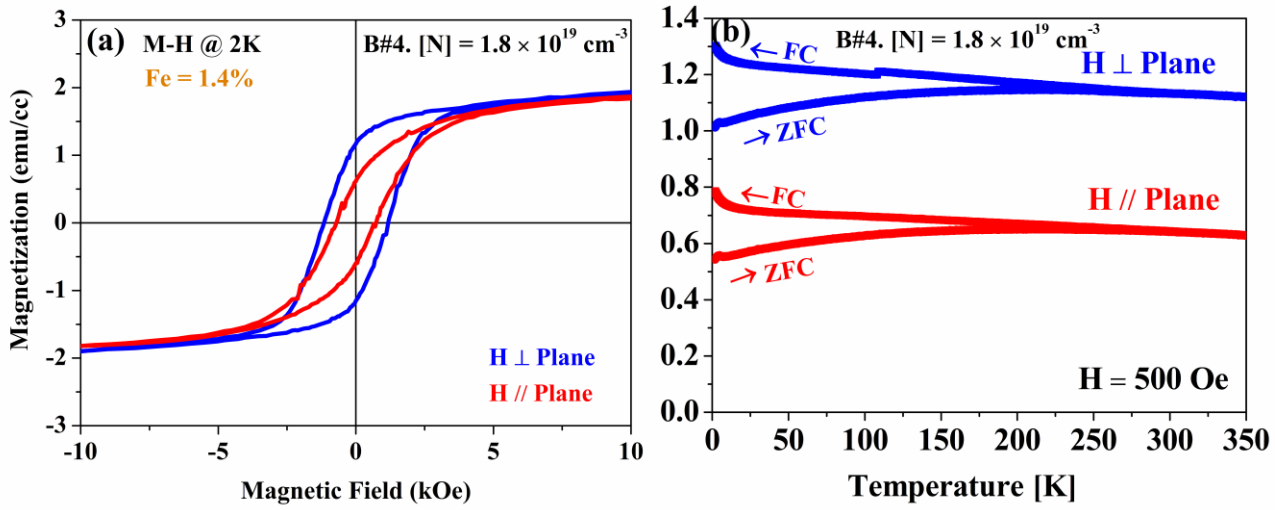

Figure 4.2.18: Magnetization measurements of N-doped film (B#4) with N concentration, [N] = 1.8×10^{19} cm^{-3} **(a)** *M-H* curves measured at 2K **(b)** *M-T* curves with applied field of 500Oe with applied field both perpendicular and parallel to the film plane.

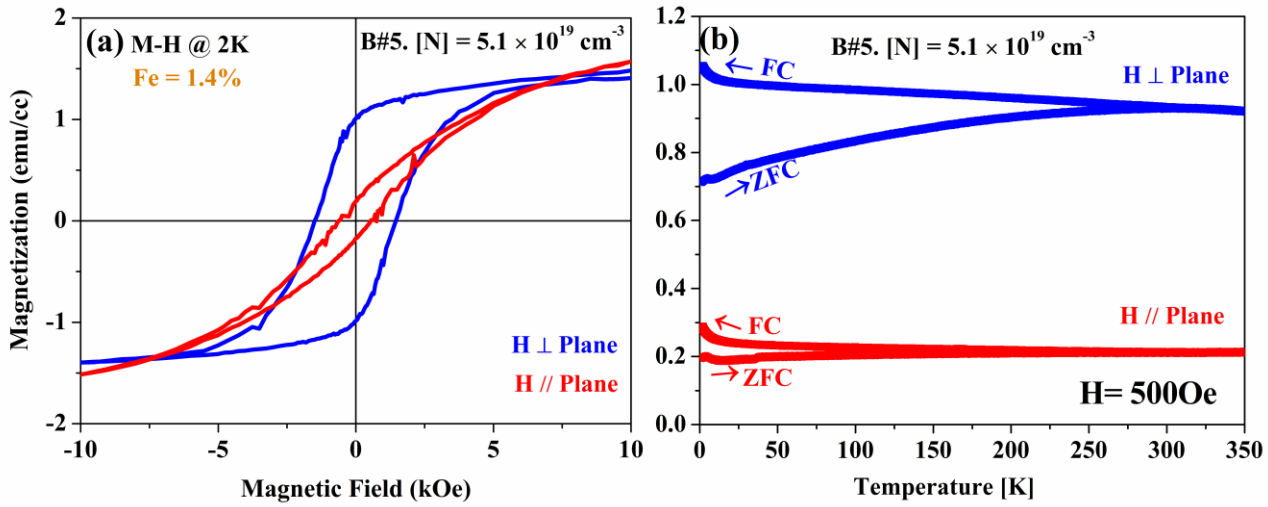

Figure 4.2.19: Magnetization measurements of N-doped film (B#5) with N concentration, [N] = 5.1×10^{19} cm^{-3} **(a)** *M-H* curves measured at 2K **(b)** *M-T* curves with applied field of 500Oe with applied field both perpendicular and parallel to the film plane.

4.2.6 Transport measurements of $Zn_{1-x}Fe_xTe$: N film: Physical property measurement system (PPMS)

We have determined the temperature dependence of resistivity (ρ-T) and Hall resistivity of the highest N-doped $Zn_{1-x}Fe_xTe$ thin film (B#5) with N concentration, [N] = 5.1×10^{19} cm^{-3} by using PPMS machine. We have utilized the four-terminal method (explained already in the experimental method section) to measure the temperature dependence of resistivity of the N-doped film (B#5) as shown in Fig. 4.2.20.

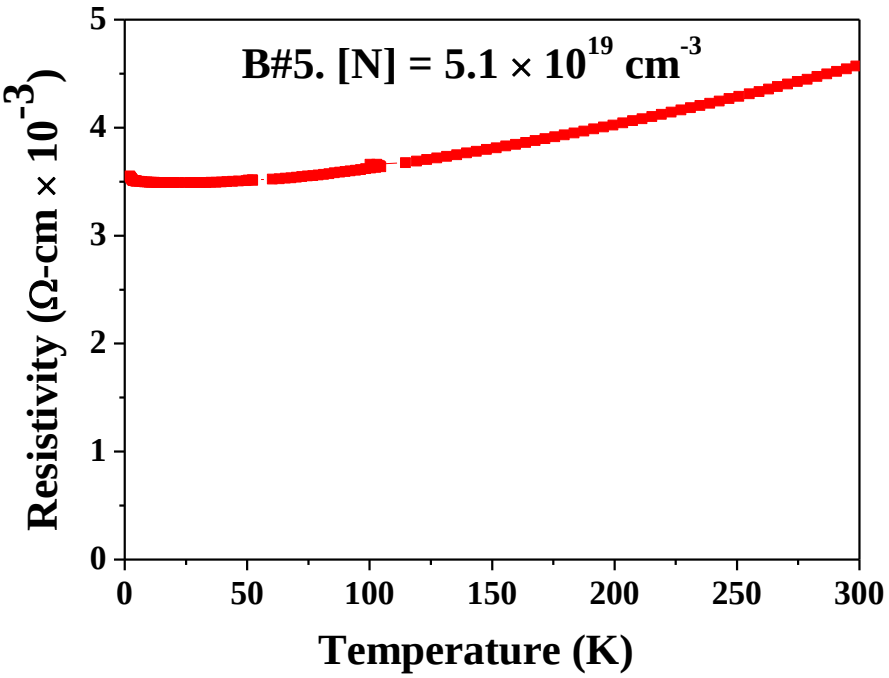

Figure 4.2.20: Temperature dependence of resistivity for the $Zn_{1-x}Fe_xTe$: N film (B#5) with N concentration [N] = 5.1×10^{19} cm^{-3}.

The temperature dependence of resistivity has exhibited the metallic behavior, with the increase of temperature, the resistivity also increases. The resistivity of the film at room temperature is measured as around 4.6×10^{-3} Ω-cm. Figure 4.2.21 has shown the Hall resistivity versus magnetic field graph. Using the slope of the graph, we have evaluated the Hall coefficient. The current used in this measurement is 50μA.We have connected the sample in the same four-terminal method, but this time the voltage leads are attached in the perpendicular direction of the current leads. The measurement was performed with a magnetic field in the range (-5T to +5T) perpendicular to the film plane.

$$\text{Hall coefficient, } R_H = \frac{E_H}{jB}$$

$$= \frac{V_H}{IlB}$$

$$= \frac{\rho}{B}$$

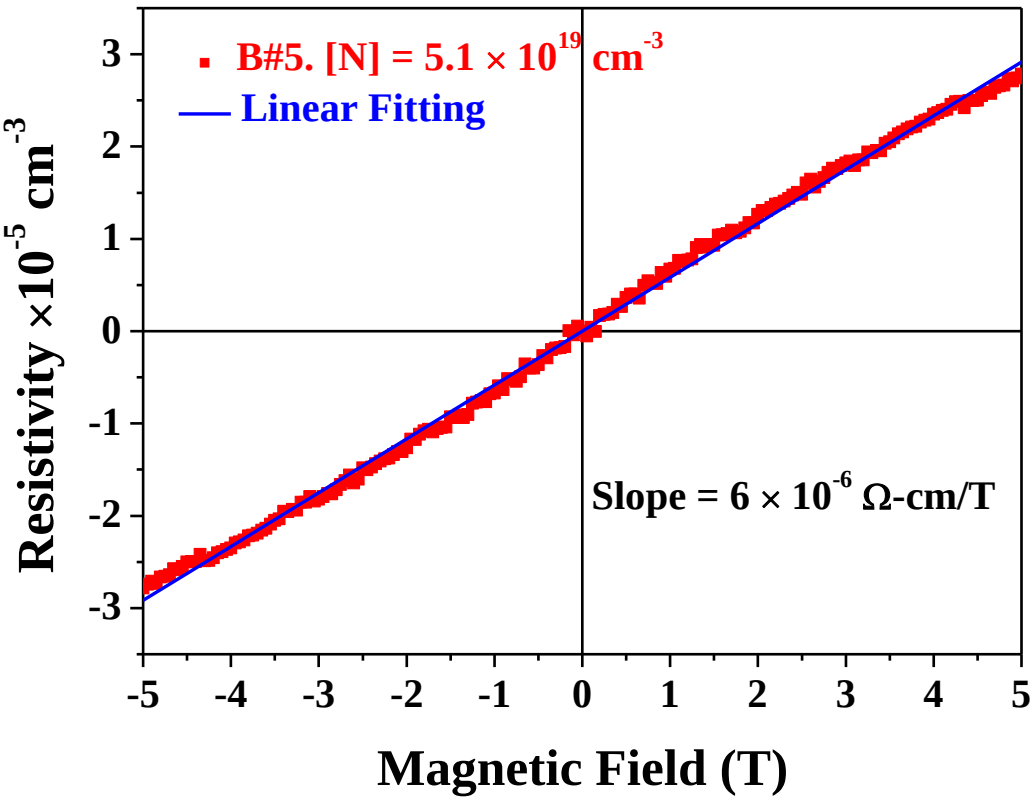

Figure 4.2.21: Magnetic field dependence of Hall resistivity for the $Zn_{1-x}Fe_xTe$: N film (B#5) with N concentration [N] = 5.1 × 10^{19} cm^{-3}. The magnetic field is applied in the perpendicular direction of the film plane.

$$= 6 \times 10^{-10}\ \Omega\text{-cm/Oe}$$

$$= 6 \times 10^{-10} \times 10^{8}\ cm^3/C$$

$$= 0.06\ cm^3/C$$

$$\text{Carrier density, } n = \frac{1}{qR_H} = \frac{1}{0.06 \times 1.6 \times 10^{-19}}\ cm^{-3} = 1.04 \times 10^{20}\ cm^{-3}$$

In this film (B#5), the N concentration is [N] = 5.1 × 10^{19} cm^{-3} and the Fe composition is of the order of 10^{20} cm^{-3}. At T = 0K, it is known that the holes provided by the N will first trapped by the Fe. But the N concentration measured by SIMS is lower than the Fe composition. So, the conductivity might be related to the precipitate that formed in the film at this n concentration.

4.2.7 Summary

We have investigated the structural and magnetic properties of nitrogen acceptor co-doped $Zn_{1-x}Fe_xTe$ thin films grown by MBE under Zn-rich condition with an Fe composition fixed at x = 0.014 and N concentrations varied in the range of $1.8 \times 10^{18} - 5.1 \times 10^{19}$ cm^{-3}. The XRD θ - 2θ scan profiles has detected the presence of extrinsic precipitates possibly of Fe-N compounds in the N-doped films with the highest N concentrations. Similarly, the structural analysis by XAFS revealed that, the Fe atoms were dominantly incorporated in the substitutional site with the valence state deviated significantly from Fe^{2+} to $Fe^{2+/3+}$ mixed states due to the N-doping of the range of $1.8 \times 10^{18} - 4.3 \times 10^{18}$ cm^{-3}, while at the higher N concentrations in the range of $1.8 \times 10^{19} - 5.1 \times 10^{19}$ cm^{-3}, the extrinsic precipitates of Fe-N compounds were formed in the crystal. These results are in accordance with the magnetic properties of the grown films; *M-H* curves exhibited drastic changes from a linear dependence, typical of van-Vleck paramagnetism in the undoped film, to weak room temperature ferromagnetic behaviors with hysteresis at the intermediate N concentrations of the order of 10^{18} cm^{-3}, which may reflect the deviation of the substitutional Fe valence state from Fe^{2+} to $Fe^{2+/3+}$ mixed states. On the other hand, at the higher N concentrations of the order of 10^{19} cm^{-3}, the *M-H* curves have shown robust room temperature ferromagnetic behavior, which may originate from the formation of extrinsic precipitates of Fe-N compounds.

In the case of N acceptor co-doped $Zn_{1-x}Fe_xTe$ thin films with x = 0.015 grown under Te-rich condition, we have also observed the change of magnetic behavior from van-Vleck paramagnetic in the film without N-doping to low-temperature ferromagnetic in the N-doped film with N concentrations of the order of 10^{18} cm^{-3}. The origin of this drastic change of magnetic properties is the change of valence state of substitutional Fe from Fe^{2+} to $Fe^{2+/3+}$ mixed states due to N-doping. However, in the N-doped films grown under Zn-rich condition, we have observed larger deviation of substitutional Fe valence state from Fe^{2+} to $Fe^{2+/3+}$ mixed states due to N-doping as compared to the previous Te-rich growth condition even for the same N-doping concentration. This significant change of valence state of substitutional Fe from Fe^{2+} to Fe^{3+} can induce robust magnetic moment even at zero external magnetic field and can also modify the exchange interactions between the magnetic moments. Thus, we get the room temperature ferromagnetic behavior in the N-doped films with N concentrations of the order of 10^{18} cm^{-3} in the case of Zn-rich growth condition. Figure 4.2.22 has schematically shown the difference in deviation of valence state of Fe from Fe^{2+} to $Fe^{2+/3+}$ mixed sates for N-doped films grown under Te-rich and Zn-rich condition and its impact on the magnetic properties of (Zn,Fe)Te.

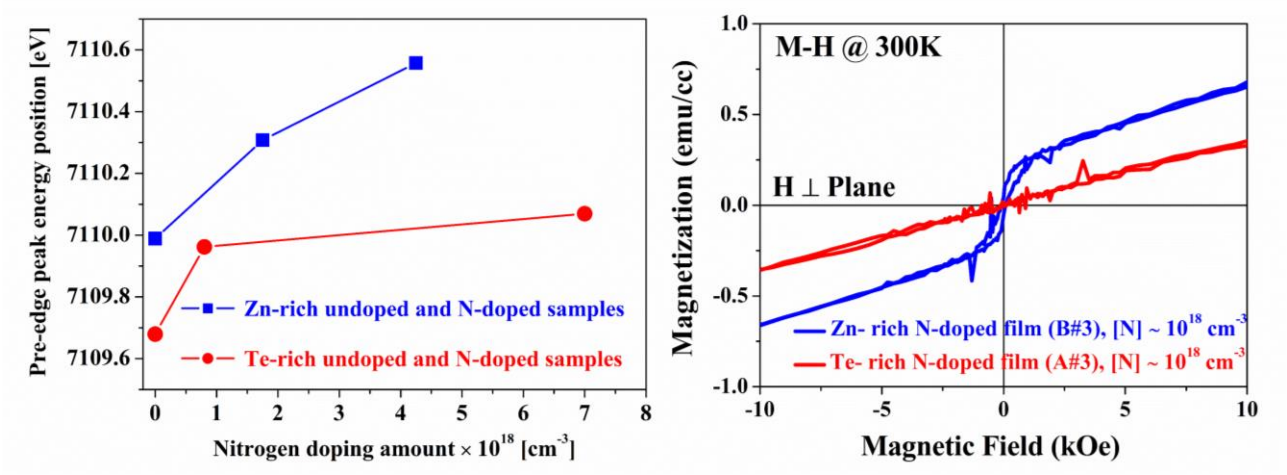

Figure 4.2.22: The pre-edge peak energy position difference of the N-doped films for N concentration of the order of 10^{18} cm^{-3} grown between Te-rich and Zn-rich growth condition and the effect on the magnetic properties of (Zn,Fe)Te.

Chapter 5: Experimental results and discussions - II

5.1 Structural and magnetic properties of modulation doped $Zn_{1-x}Fe_xTe$ thin films

In the previous chapter, we have discussed the impact of additional acceptor impurities doping in the valence state of Fe in $Zn_{1-x}Fe_xTe$ thin film and hence, on its magnetic properties. In those cases, we have grown $Zn_{1-x}Fe_xTe$ layer on undoped thick ZnTe buffer layer (~ 900nm) which in turns, was deposited on the GaAs (001) substrate. In this section, we have intended to grow $Zn_{1-x}Fe_xTe$ layer over N-doped ZnTe layer so that the additional hole provided by the N impurity at the interface can induce any exchange interaction between the Fe ions and hence, impact the magnetic properties of (Zn,Fe)Te. It has already been known that the activation energy of N in ZnTe (≈ 54meV) rapidly reduces with the increase of N-doping concentration and at the critical carrier density of the order of 10^{19} cm^{-3}, ZnTe exhibits metallic behavior [36].

5.1.1 Sample preparation

Thin films of (Zn,Fe) Te have been deposited in excess of Te flux over Zn flux by MBE using elemental solid sources of Zn, Te and Fe. In the case of growing conventional $Zn_{1-x}Fe_xTe$ layer (~300 nm) on GaAs (001) substrate, we usually grow a thick layer of ZnTe buffer (~600 nm) in between the magnetic layer and the GaAs substrate to reduce the lattice mismatch. Similarly, in the modulation doped sample structure, we have also grown a ZnTe buffer on the GaAs substrate, then the N-doped ZnTe layer (~300 nm) and finally, the $Zn_{1-x}Fe_xTe$ layer (~40 nm). Nitrogen plasma source with N_2 gas excited by rf-plasma has been operated at 300W and the N_2 gas flow rate has been kept at 0.3 cc/min throughout the growth of ZnTe: N layer. We have used the fully open shutter condition of the plasma source positioned at 2cm from the substrate. In both cases, we have deposited a thin ZnTe cap layer (~ 2nm) to avoid the surface oxidization when exposed to air. All the epitaxial layers are grown at the substrate temperature of 260°C. Figure 5.1.1 (a) and (b) show the schematic view of the conventional (C#1) and modulation doped (C#2) sample structures respectively. The concentration of Fe in the sample (C#1) has been measured as x = 1.3% by electron probe microanalyzer (EPMA) and the modulated doped sample (C#2) has been grown at the same Fe beam flux condition. Table 5.1 represents all the information relating the epitaxial growth.

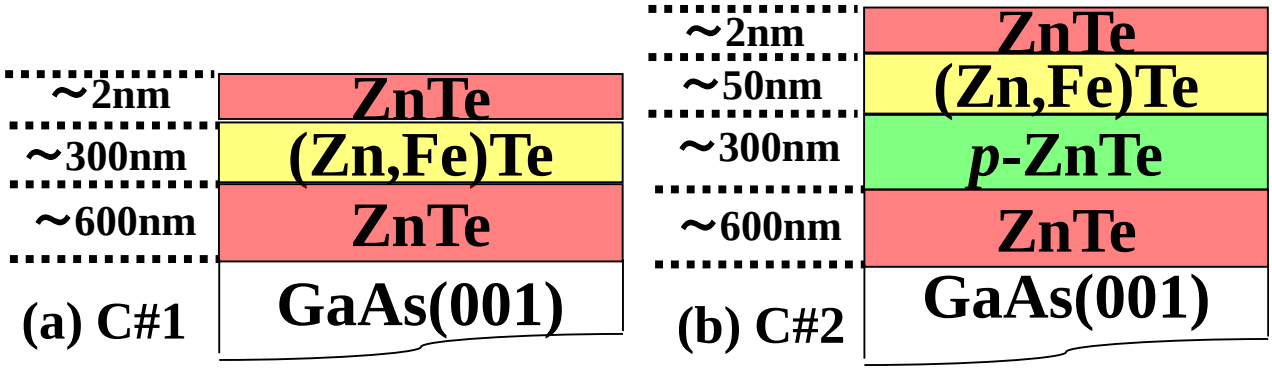

Figure 5.1.1: Schematic view of the sample structure **(a)** $Zn_{1-x}Fe_xTe$ layer grown on ZnTe buffer layer (C#1) **(b)** $Zn_{1-x}Fe_xTe$ layer grown on ZnTe:N buffer layer (C#2).

Table 5.1: Sample list of $Zn_{1-x}Fe_xTe$ thin films

Sample No.	Substrate Temperature (°C)	Te/Zn (Flux ratio)	Fe composition (%)	Thickness of $Zn_{1-x}Fe_xTe$ layer (nm)
C#1	260	2.18	1.30 (EPMA)	~ 300 nm
C#2	260	2.42	~ 1.30	~ 40nm

5.1.2 Evaluation of the sample surface by RHEED

The surface of the grown layer has been monitored *in-situ* by employing the RHEED system. Figure 5.1.2 (a) and (b) demonstrates the RHEED pattern for the samples C#1 and C#2 respectively. In the sample C#1 spotty-streak RHEED pattern has been identified after the growth of $Zn_{1-x}Fe_xTe$ layer, while in the case of $Zn_{1-x}Fe_xTe$ grown on N-doped ZnTe buffer (C#2) spotty pattern has been seen. We have observed similar spotty pattern in the case of the highest N-doped (Zn,Fe)Te film discussed in the previous chapter. This indicates that the introduction of nitrogen has made the surface of the magnetic layer rougher. According to the previous research on ZnTe doped with N, it can be estimated that the N concentration in this sample C#2 may be of the order of 10^{19} cm^{-3}.

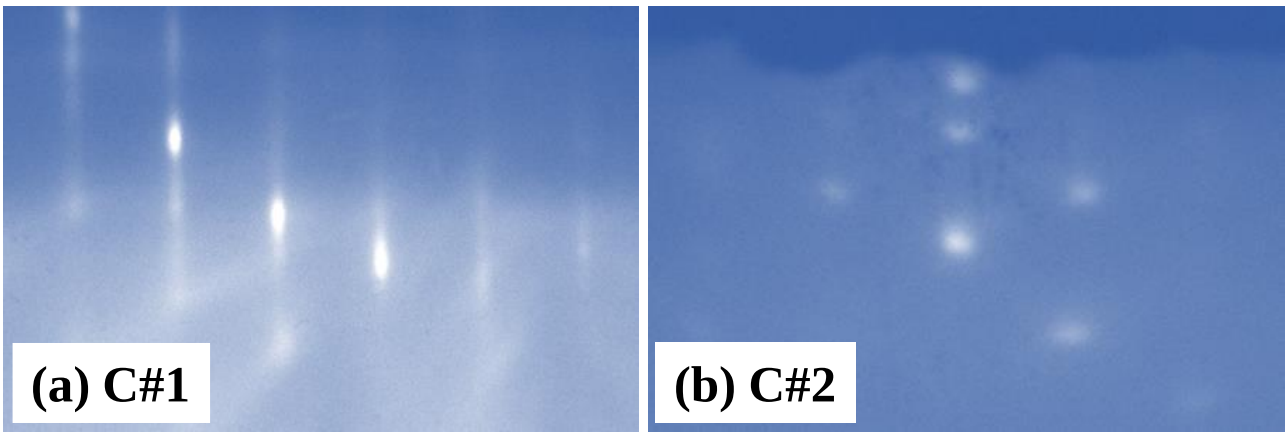

Figure 5.1.2: RHEED patterns of $Zn_{1-x}Fe_xTe$ thin films after the growth **(a)** C#1 **(b)** C#2

5.1.3 Structural characterization of $Zn_{1-x}Fe_xTe$ thin films: XRD

Figure 5.1.3 represents the XRD θ-2θ scan profiles of the $Zn_{1-x}Fe_xTe$ thin films C#1 and C#2 with Fe composition, x = 0.013. Diffraction peaks have been observed only from ZnTe buffer layer and GaAs substrate; but diffraction from any other phases has not been seen. However, in the case of C#2, the separated peaks are observed for the ZnTe (400) and ZnTe (600) diffractions. The reason of this separated peaks for N-doped ZnTe has already been explained in section 2.1.3. The doping of N induces small change in the lattice parameter of ZnTe, as we are

growing heavily N-doped layer on the undoped ZnTe layer, this will create small angular shift in the diffraction peak [45]. As a result, the separated peak has been appeared in the case of C#2 sample.

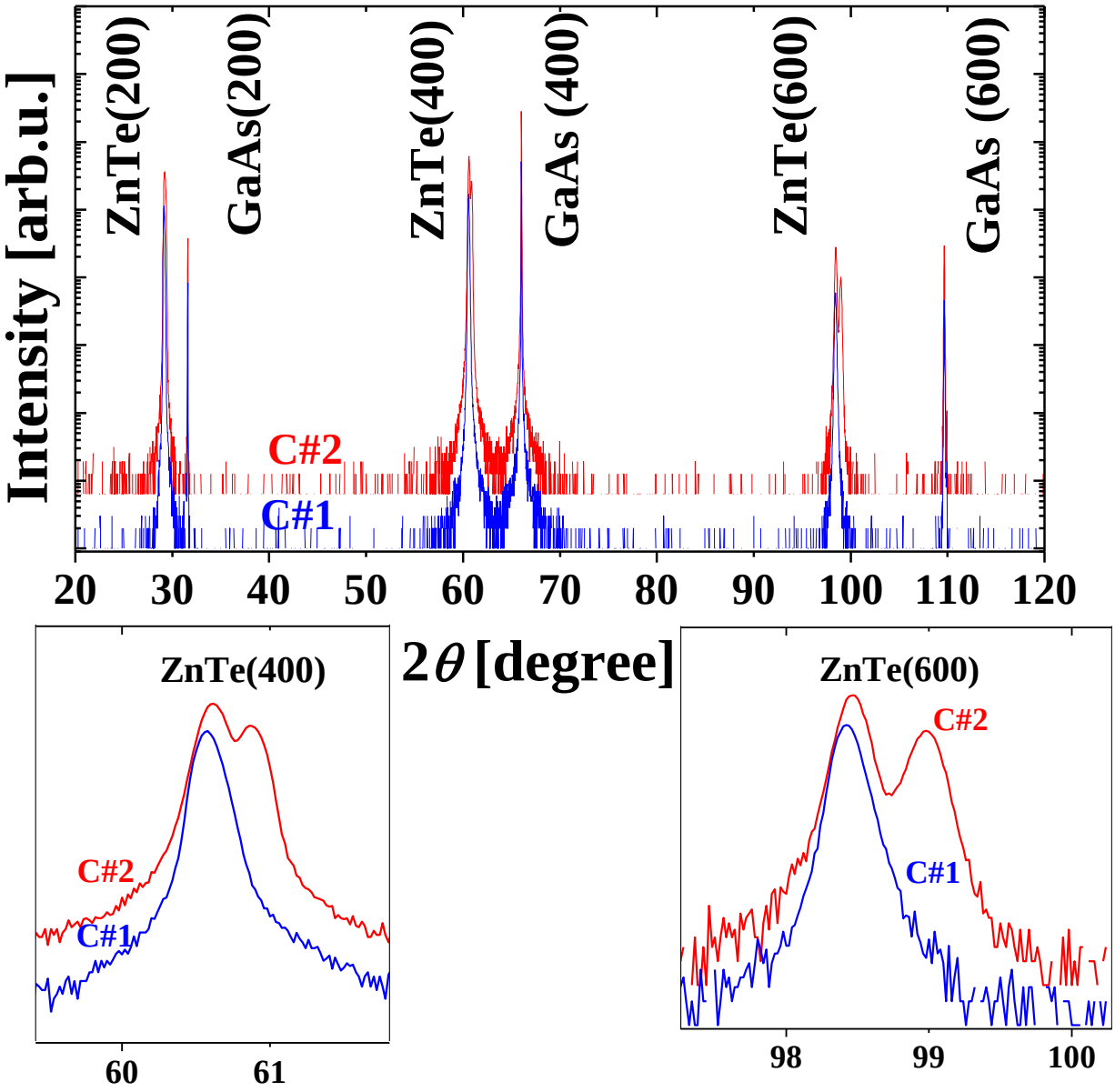

Figure 5.1.3: The XRD θ-2θ scan profiles of the $Zn_{1-x}Fe_xTe$ (x = 0.013) films grown on the ZnTe buffer layer (C#1) and ZnTe:N buffer layer (C#2). The bottom panels represent the separated peaks of sample C#2 for the (400) and (600) diffractions.

5.1.4 Magnetization measurements of $Zn_{1-x}Fe_xTe$ films: SQUID

Figure 5.1.4 represents the *M-H* curves for the $Zn_{1-x}Fe_xTe$ thin films C#1 and C#2 with Fe composition, x = 1.3%. We have noticed different magnetic properties of (Zn,Fe)Te thin films grown on undopd ZnTe and N-doped ZnTe buffer layers. The thin film C#1 which was grown on the undoped ZnTe buffer layer exhibits van-Vleck paramagnetic behavior, while the film C#2 grown on the N-doped ZnTe layer looks (ordinary) paramagnetic behavior with S-shape *M-H* curve.

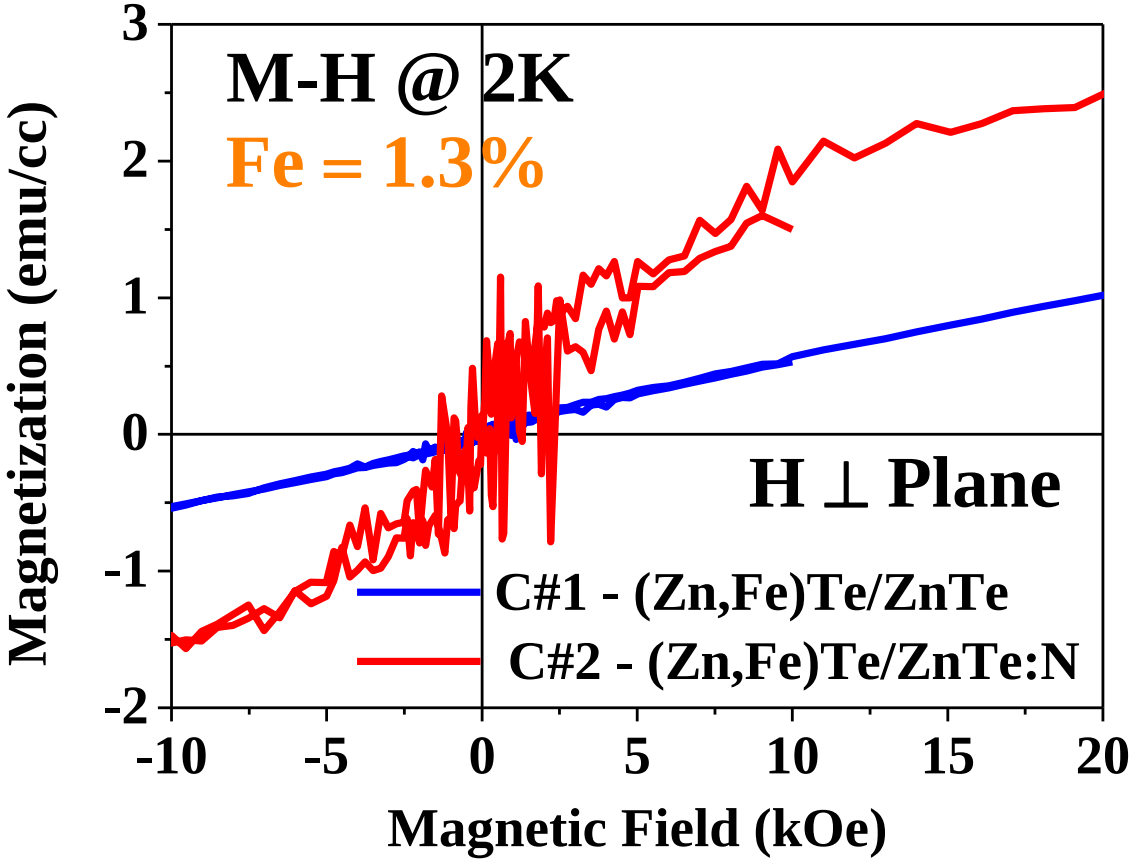

Figure 5.1.4: *M-H* curves for $Zn_{1-x}Fe_xTe$ thin films grown on undoped ZnTe (C#1) and N-doped ZnTe buffer layer (C#2).

According to the structural analysis by XAFS (shown in the previous chapter), it is known that for $Zn_{1-x}Fe_xTe$ thin films with Fe composition, $x \leq 2\%$, Fe atoms stay on the substitutional position on the Zn-site in the zinc-blende structure and exhibits the van-Vleck paramagnetic properties. The ordinary paramagnetic behavior exhibited by the $Zn_{1-x}Fe_xTe$ thin film (C#2) may originate from the impact of interfacial hole on the magnetic layer. The interfacial holes may deviate the valence sate of the Fe and hence impact on the magnetic properties of $Zn_{1-x}Fe_xTe$ thin films. Figure 5.1.5 (a) and (b) represents the energy band diagram of the conventional (C#1) and modulation doped sample structures (C#2).

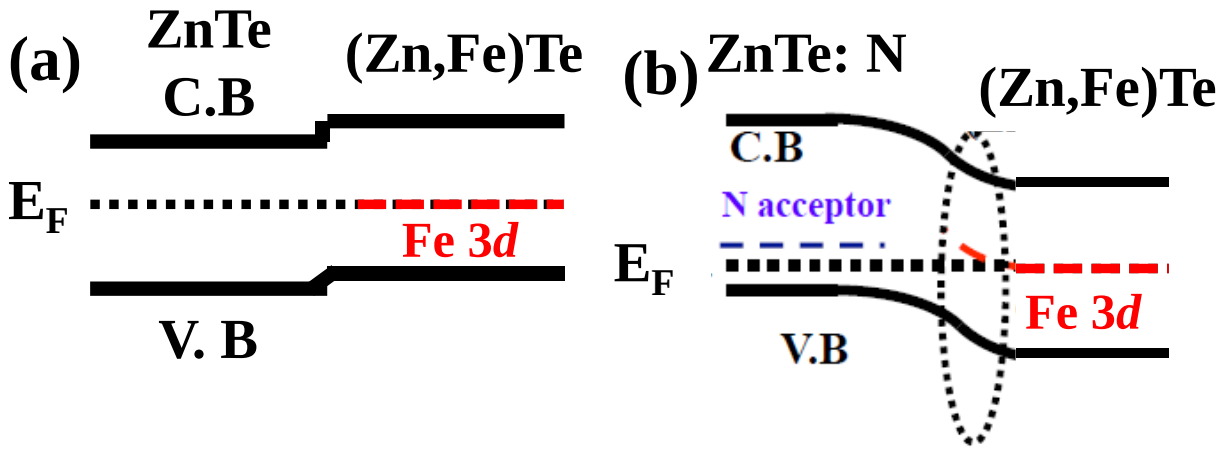

Figure 5.1.5: Schematic energy band diagram of the **(a)** conventional sample structure (C#1) and **(b)** modulation doped sample structure (C#2).

In the case of intrinsic ZnTe, at temperature, T = 0 K, the Fermi level is usually situated in the mid bandgap region. But for extrinsic semiconductors, in this case the N acceptor impurity doped ZnTe, the Fermi has to shift downwards in order to conserve the action law and to fulfill the electrical charge neutrality (shown in Fig. 5.15(b)). It is known that, the binding energy of N in ZnTe is about 54 meV and this activation rapidly decreases as the doping concentration increases. Highly N-doped ZnTe ([N] ≈ 10^{19} cm^{-3}) shows the metallic behavior. So, at the interface between the ZnTe:N and the (Zn,Fe)Te layer, the delocalized holes supplied by the heavily N-doped ZnTe buffer layer can be trapped by the Fe 3*d* levels positioned in the mid gap region in (Zn, Fe)Te. This trapping can change the valence state of the magnetic. This deviation in valence state can produce magnetic moment even in the absence of external magnetic field. Therefore, the ordinary paramagnetic behavior (S-shape *M-H* curve) observed in the film (C#2) might originate fron the impact of the interfacial holes.

5.2 Magnetic modulation by applying electric field study

5.2.1 Sample preparation

In order to investigate the modulation of magnetism by the application of electric field, Zn_{1-x} Fe_xTe thin films of different thickness has been prepared under Te-rich condition by MBE (Table 5.2). From the previous research in our laboratory, it is known that Zn_{1-x} Fe_xTe thin films grown under Te-rich condition with Fe composition, $x \leq 2\%$, the Fe atoms substitute the Zn site and the ZB structure is maintained [32]. Therefore, in this study, we have prepared sample series with Fe composition, $x \leq 2\%$ in which Fe is thought to be in the substitution position, to apply the electric field. The sample structure of prepared samples is shown in Fig. 5.2.1. A ZnTe/ZnTe: N buffer layer (~ 250 – 400 nm) was grown on a p-doped GaAs (001) substrate and $Zn_{1-x}Fe_xTe$ layer (~ 14 – 78 nm) was grown on the buffer layer. Finally, a ZnTe cap layer has been deposited on the layer Zn_{1-x} Fe_xTe to prevent the surface oxidation and adhesion of impurities to the magnetic layer. Depending on the available SIMS data of previously grown N-doped samples in the same doping condition, the N-doping concentration in this ZnTe: N buffer layer can be estimated to be of the order of 10^{19} cm^{-3}. At the time of sample preparation, the sample surface

is observed with RHEED. The RHEED image after the growth of Zn_{1-x} Fe_xTe layer shows a spotty-streak pattern as shown in Fig. 5.2.2. This suggests that the surface of the Zn_{1-x} Fe_xTe layer is not perfectly flat but slightly uneven. The film thickness of the Zn_{1-x} Fe_xTe layer has been measured by using the step difference between the region covered with the nail of the Mo holder and the film grown. For the Fe composition measurement, a thick sample (~ 1000 nm) was prepared separately under the same fabrication conditions and Fe composition was measured by using EPMA.

Table 5.2: Sample list of $Zn_{1-x}Fe_xTe$ thin films for electric field control study

Sample No.	Growth Temp. (°C)	Te/Zn (Flux ratio)	Fe Composition (%)	$Zn_{1-x}Fe_xTe$ layer thickness (nm)	Thickness of cap layer (nm)
D#1	260	2.30	~1.30 (EPMA)	13.96	~3 nm
D#2	260	2.45	1.34 (EPMA)	21.2	~ 3 nm
D#3	260	2.46	~1.30 (EPMA)	40.26	~ 3 nm
D#4	260	2.46	~1.30 (EPMA)	51.66	~ 3 nm
D#5	260	2.41	1.30 (EPMA)	78	~ 4 nm

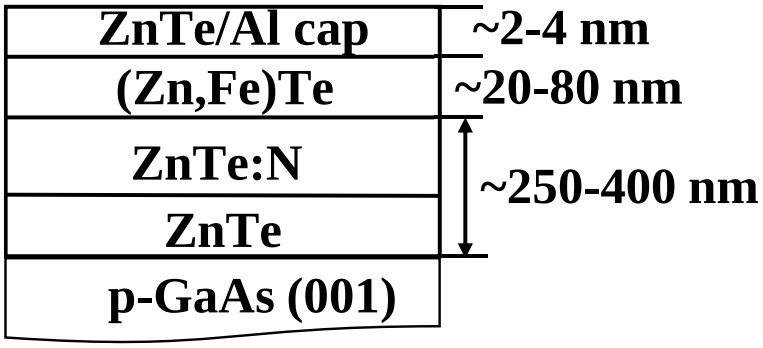

Figure 5.2.1: Schematic view of the sample structure of Zn_{1-x} Fe_xTe thin films for electric field control study

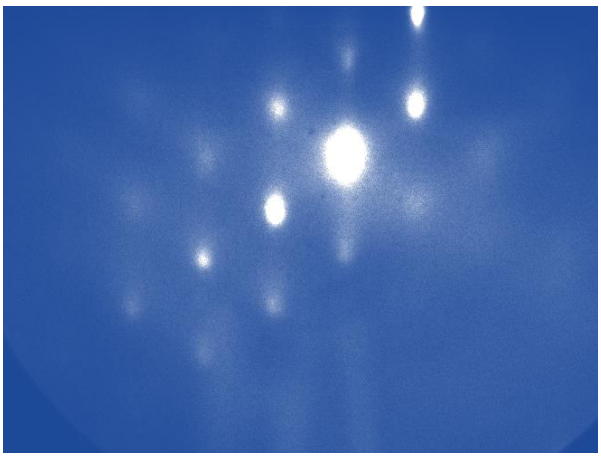

Figure 5.2.2: RHEED pattern after the growth of Zn_{1-x} Fe_xTe thin film (D#1)

5.2.2 Magnetization measurements of $Zn_{1-x}Fe_xTe$ films: SQUID

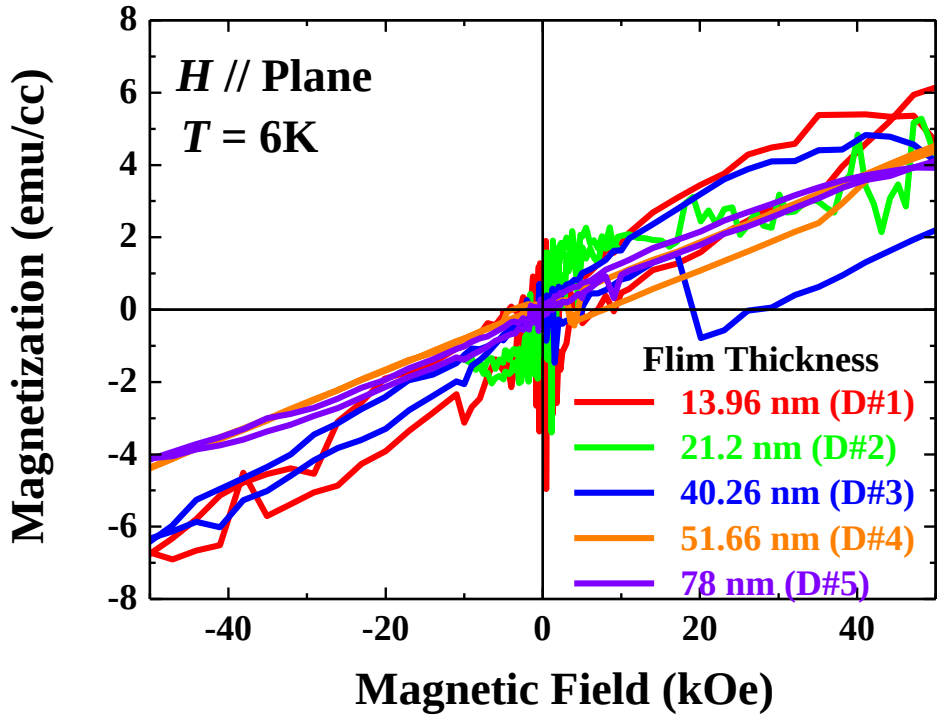

Figure 5.2.3: *M-H* curves of Zn_{1-x} Fe_xTe thin films having different thicknesses.

Before the electric field application, the magnetization characteristics of the fabricated samples have been measured by SQUID. Figure 5.2.3 shows the *M-H* curves of the films (D#1 – D#5) measured at 6 K with the external magnetic field applied parallel to the film plane. The *M-H* curves particularly in the thinner films (D#1, D#2) have exhibited different behavior than the previously observed van-Vleck paramagnetism. In these thinner films, the magnetization rises sharply in the low magnetic field region and behaves like the ordinary paramagnetic behavior (S-shape *M-H* curve). The following factors have been considered to be the origin of this discrepancy. The first reason can be the difference in film thickness of the $Zn_{1-x}Fe_xTe$ layer, as we have noticed in the case of present series (D#1 - D#5), the magnetization characteristics of thinner films (D#1, D#2) differ from the relatively thicker films (D#3 – D#5). The second possible origin may be the impact of interfacial holes on the films due to the doping N acceptor impurity that may cause the deviation of the Fe valence state and thus induce magnetic moment of Fe. In addition, the thinner buffer layer of the grown films as compared to the conventional thicker buffer layer (~ 900 nm) layer that we usually used for growing conventional (Zn,Fe)Te thin films on GaAs substrate, is another factor to be considered. It can be considered that the strain in the ZnTe buffer layer has not been fully relaxed and the crystallinity of the $Zn_{1-x}Fe_xTe$ layer deteriorated due to the thin buffer layer and this in turns, enhance the formation of ferromagnetic precipitates in the sample. We have grown these samples for field control study. In field control study, we usually measured the magnetization of the films at 6 K to avoid the impact of magnetic signal originated from superconducting indium at a temperature of 3.4 K or below [84].

5.3 Magnetic modulation of the device structure of (Zn,Fe)Te thin films by electric field

5.3.1 Magnetic modulation by applying electric field using ion polymer as gate insulator

In order to investigate the modulation of the magnetic properties of the film (D#2) by the applying of electric field, the device structure has been constructed by using ion-gel film as liquid insulator as shown in Fig. 5.3.1. The Pt foil has been utilized as the gate electrode and Cu wire has been connected through indium at the electrode and back side of the substrate for the application of external gate voltage.

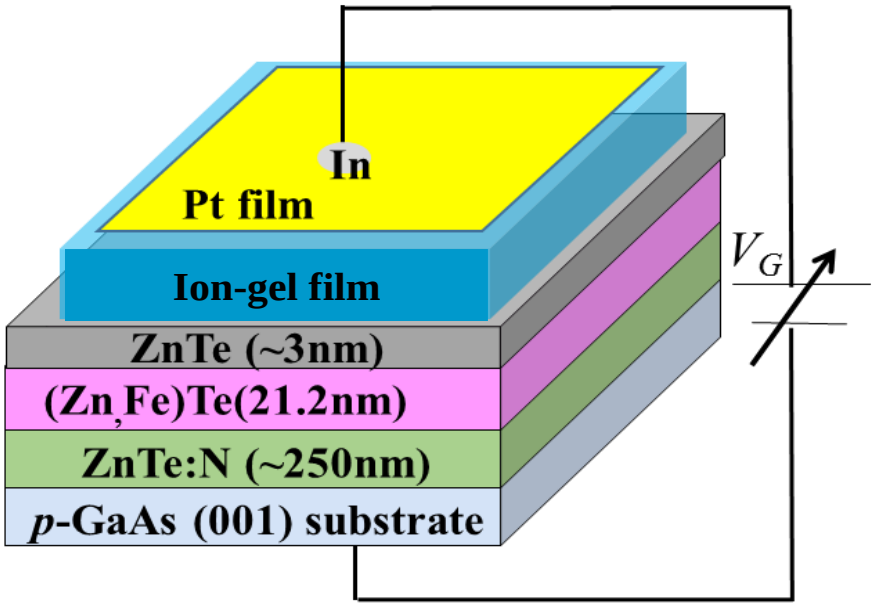

Figure 5.3.1: Electric double layer transistor (EDLT) structure of $Zn_{1-x}Fe_xTe$ thin film (D#2)

Figure 5.3.2 represents the *M-H* curves of D#2 measured at 6K under different applied voltages. Gate Voltage has been applied in the sequence 0 V → 1.5 V → -2.5 V → 0 V (Re). The notation V_G = 0 V, V_G = 0 V (Re) represents the condition before and after the application of positive and negative voltages respectively. As observed in Fig. 5.33, the change in the saturation magnetization due to the applied gate voltages is irreversible in nature. When the gate voltage, V_G = + 1.5V is applied, the saturation magnetization has decreased from around 57 emu/cc to 30 emu/cc. After that the magnetization has remained unchanged even if we changed the gate voltage to V_G = - 2.5V, Finally with the application of gate voltage, V_G = 0 V, the magnetization has not go back to the initial value and has decreased further to 23 emu/cc. As the change in magnetization is irreversible, so the observed change of magnetic properties due to external gate voltages cannot be regarded as the modulation of the intrinsic magnetism of (Zn,Fe)Te. One possible reason of this irreversible change may be that the ionic liquid has not worked properly. When the negative gate voltage is applied, the anion and the cation in the ionic liquid used for the insulating layer may not have moved. Therefore, even if the voltage is switched from positive to negative, the *M - H* curve hardly changes and does not return to the initial state after the application of 0 V again. Another reason for this irreversible change in magnetic properties due to the application of external gate voltages is that there might be any chemical interaction between the ionic liquid with the (Zn,Fe)Te layer at the interface.

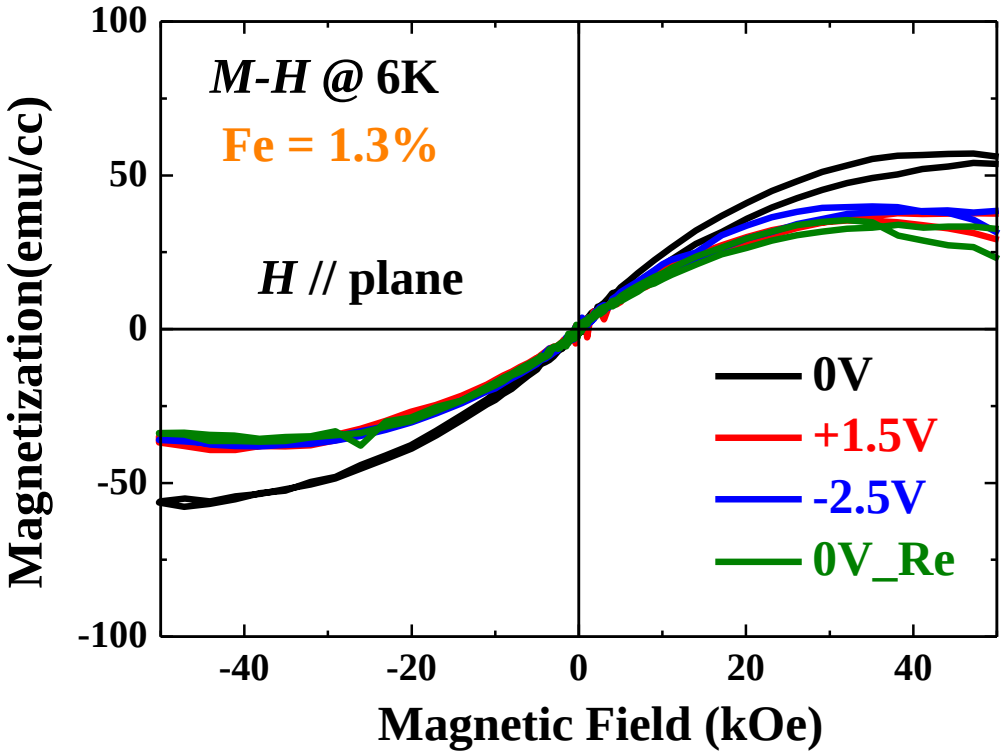

Figure 5.3.2 : *M-H* curves of D#2 thin film measured at 6 K under different applied gate voltages, V_G

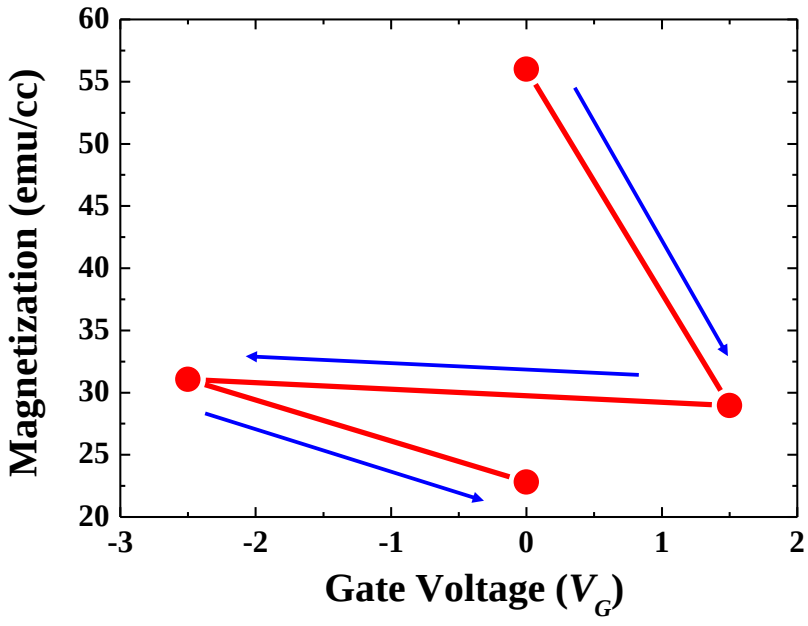

Figure 5.3.3: Changes in the value of saturation magnetization as obtained from the *M-H* curves at different applied gate voltages, V_G (Arrows indicate the sequence of applied gate voltages).

5.3.2 Possible reason of increase in magnetization during processing

Comparing the *M-H* curve of the film (D#2) before processing (shown in Fig. 5.2.3) and after processing for applying the electric field (shown in Fig. 5.3.2), it has been observed that the value of the magnetization in the latter case is about 10 times greater than that of the former case. In order to identify whether the increase in magnetization occurred due to the processing of the device or not, the magnetism of the material used for processing has been investigated.

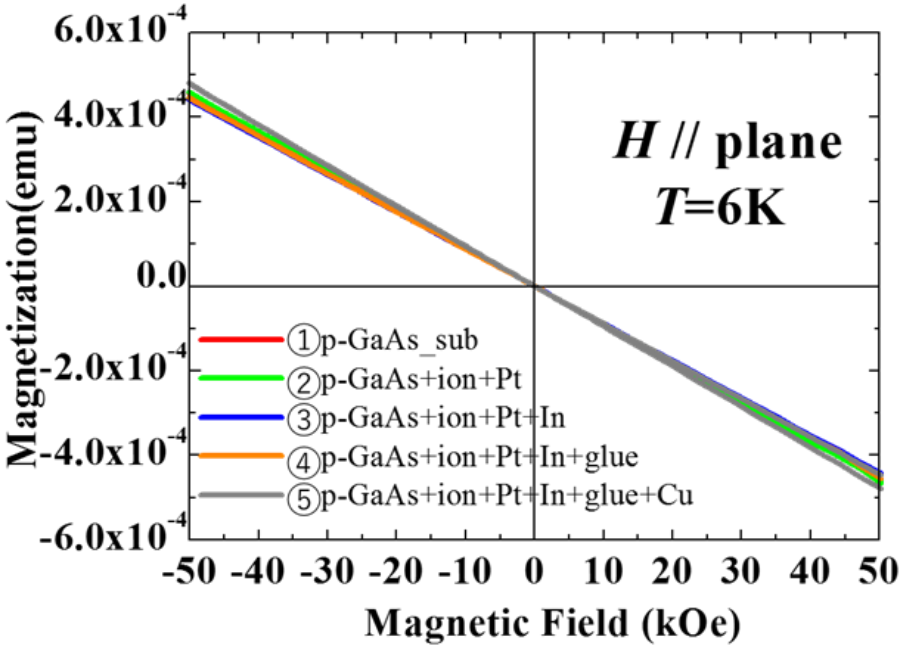

Figure 5.3.4: Changes in *M -H* curve measured at 6 K during attaching substances on p-GaAs (001) substrate during processing of field effect transistor (FET) device structure.

Figure 5.3.4 shows the *M -H* curves for the (1) p-GaAs substrate, (2) p-GaAs substrate + ionic polymer + Pt, (3) p-GaAs substrate + ionic polymer + Pt + In, (4) p-GaAs substrate + ionic polymer + Pt + In + glue, (5) p-GaAs substrate + Ionic polymer + Pt + In + glue + Cu wire. These are the substances used for constructing the device structure. From this figure, it is seen that the inclination of the straight line of *M-H* curve is slightly larger at the stage (5) after processing with the Cu wire. However, this change due to the diamagnetic component of the Cu wire is negligible at this measurement temperature. Therefore, it has been confirmed that processing substance has not contributed to the positive magnetization of $Zn_{1-x}Fe_xTe$ thin film. Solder which is used in the experiment and in the sample rod can be a source to explain this difference in magnetic properties before and after processing. This is because we usually use different rod for installing sample in the SQUID for field control study and the ordinary measurement.

5.3.3 Summary

The *M-H* curve of thin film D#2 before the application of electric field has not shown the linear relationship of increasing magnetization with applied external magnetic field, the typical van-Vleck paramagnetism as shown in

the previous study [32].The magnetization has increased abruptly in the low magnetic field region and shown a S-shape *M-H* curve. This may be caused by a change in magnetization characteristics due to the difference in film thickness of the Zn_{1-x} Fe_xTe layer or a change in crystallinity of the $Zn_{1-x}Fe_xTe$ layer due to the thinner buffer layer. The irreversible change in saturation magnetization in the device structure of the film D#2 after the application of gate voltages can be possibly explained on the basis of chemical interaction of the ionic liquid with the magnetic layer or improper of the ionic liquid. In the case of other films (D#3-D#5), the abrupt increase of the magnetization in the low field reduced with the increase of the film thickness. This may be explained in such a way that with the increase of film thickness the effect of interfacial holes on the magnetic layer become unclear.

5.3.4 Preparation of Al_2O_3 layer by ALD method and evaluation of insulation properties

Al_2O_3 solid insulating layer with good insulating property has been deposited on $Zn_{1-x}Fe_xTe$ thin film as an insulating film for electric field modulation experiment. Table 5.2 shows the film deposition conditions of Al_2O_3. In the Al_2O_3 insulating film deposition, the substrate temperature was set at 200°C and ALD growth was performed for 855 cycles. The film thickness has been estimated at approximately 100 nm based on the previously grown film on the same condition.

Table 5.2: Growth condition of Al_2O_3 deposited over $Zn_{1-x}Fe_xTe$ layer (D#5)

Sample No.	TMA (s)	Purge (s)	H_2O (s)	Purge (s)	Thickness (nm)
D#5	1	10	4	30	~ 100

In the previous study, using the same exposing time of TMA and H2O for 855 cycles, a good insulating layer has been deposited. From the result of spectroscopic ellipsometry measurement, the film formation rate has been found to be 1.17 Å / cycle and the film thickness is around 100nm. Therefore, for sample D#5 prepared in this study, we have adopted the same sequence and same number of deposition cycles. After the growth of the Al_2O_3 layer, we checked insulating property by using the ohmmeter in the laboratory insulating property.

5.3.5 Magnetic modulation by applying electric field using Al_2O_3 solid insulating layer

In order to observe the magnetic modulation of the film (D#5) by the applying of electric field, the device structure has been developed by growing Al_2O_3 insulator layer on the magnetic layer as shown in Fig. 5.3.5. As the gate electrode, the Pt foil has been used and external gate voltages have been applied through Cu wire connected at the electrode and back side of the substrate. Figure 5.3.6 demonstrates the *M-H* curves of D#5 measured at 6K under different applied voltages. Gate Voltage has been changed in the sequence 0 V → +20 V → - 20 V → 0 V (Re). The notation V_G = 0 V, V_G = 0 V (Re) represents the condition before and after the application of positive and negative gate voltages respectively. We have not seen any change in the magnetic properties of (Zn,Fe)Te due to the application of external gate voltages. The possible reason may be the thickness of the magnetic channel layer (≈ 78 nm) is large and hence cannot accumulate sufficient amount of charge carriers on the surface of the channel layer. According to the previous research on field-controlled study on magnetic properties of DMS, thicker layer will make the modulation of magnetic properties smaller [28].

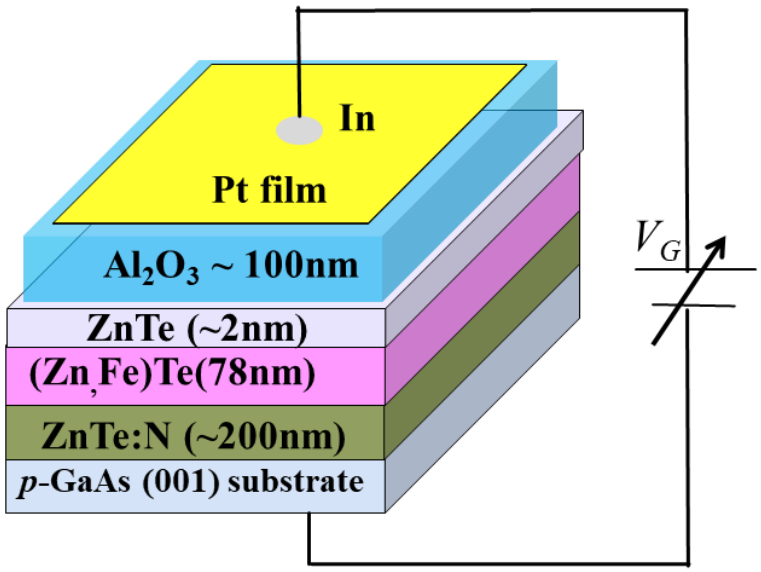

Fig. 5.3.5 : Field effect transistor (FET) structure of $Zn_{1-x}Fe_xTe$ thin film (D#5).

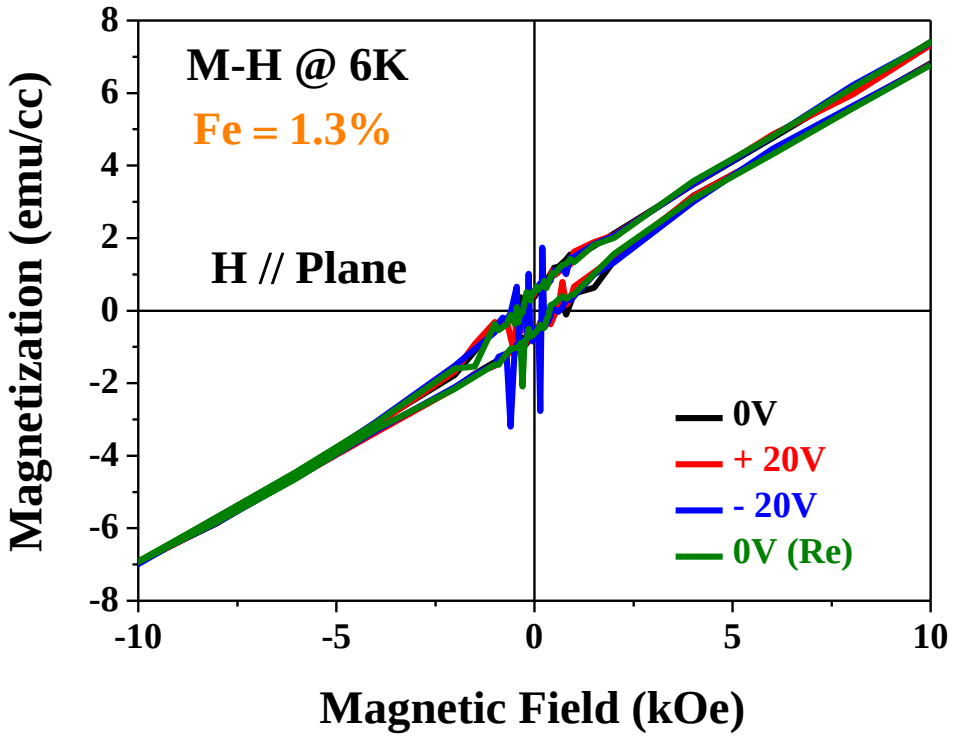

Figure 5.3.6: *M-H* curves of D#5 film measured at 6 K with different applied gate voltages, V_G

5.3.6 Future tasks

In future electrical manipulation of the magnetic studies of Zn_{1-x} Fe_xTe thin film, the following steps can be considered. Firstly, it is necessary to investigate the reason of different behavior of magnetization in the Zn_{1-x} Fe_xTe thin films like this sample D#2, as compared to the previous study [32]. If the change in magnetization property is caused by deterioration of crystallinity, it is possible to prepare a thin film of Zn_{1-x} Fe_xTe with good crystallinity. Then, it is necessary to pay attention as much as possible so that impurities do not adhere during the processing of the device structure to apply electric field. In addition, the thin (Zn,Fe)Te layer with the thick diamagnetic GaAs substrate may make it difficult to measure the electrical manipulation of magnetization of the (Zn,Fe)Te layer. The magnetization dependent Hall effect may be helpful to extract a small change in the electrical field controlled magnetic properties of the (Zn,Fe)Te layer.

Chapter 6: Conclusion

The ability to externally control the properties of magnetic materials would be highly desirable from fundamental and technological viewpoints, particularly in view of recent developments in magneto-electronics and spintronics. In this study, we have doped nitrogen (N) acceptor impurity in (Zn,Fe)Te thin films grown under Te-rich and Zn-rich growth condition in order to alter the valence state of Fe and hence to modulate the magnetic properties of (Zn,Fe)Te. At the same time, we have also performed several trials to control the magnetic properties by applying external gate voltages using device structures consisting of both ion-gel (liquid electrolyte) and ALD deposited Al_2O_3 layer as gate insulator.

At first, we want to conclude the study of N acceptor co-doped (Zn,Fe)Te.

We have explored the impact of nitrogen acceptor impurity doping on the structural and magnetic properties of $Zn_{1-x}Fe_xTe$ thin films grown by MBE under Te-rich condition. We have prepared $Zn_{1-x}Fe_xTe$ thin films by keeping the Fe composition fixed at $x = 0.015$ and changing N concentrations in the range of $8 \times 10^{17} – 4 \times 10^{19}$ cm^{-3}. The structural characterization by XAFS and TEM observation leads us to the conclusion that, Fe atoms are mainly incorporated in the substitutional position on the Zn-site with the Fe valence state deviated from Fe^{2+} due to the N-doping in the intermediate range of 10^{17}- 10^{18} cm^{-3}, while the N-doping has enhanced the formation of extrinsic precipitates of Fe-N compounds at the highest N concentration of the order of 10^{19} cm^{-3}. These structural analyses of the N-doped films are strongly correlated to their corresponding magnetic properties; *M-H* curves have shown remarkable changes from a linear dependence, typical of van-Vleck paramagnetism in the undoped film, to ferromagnetic behaviors with hysteresis due to the deviation of the Fe valence state from Fe^{2+} at the intermediate N concentrations. On the other hand, at the highest N concentration, the *M-H* curve has shown again a linear dependence, which may originate from the formation of precipitates of Fe-N compounds such as ξ-Fe_2N that exhibits antiferromagnetic or slowly saturating weak ferromagnetic behavior.

We have also identified small difference in the pre-edge peak energy position of the XANES spectra for $Zn_{1-x}Fe_xTe$ thin films for nominally the same Fe composition grown between Te-rich and Zn-rich condition. According to the previous studies on Fe-K edge, the pre-edge energy position is known to be very crucial in determining the valence state of Fe. The observed little difference in the pre-edge energy position has inspired us to investigate the structural and magnetic properties of nitrogen acceptor co-doped $Zn_{1-x}Fe_xTe$ thin films grown by MBE under Zn-rich condition. In this study we have deposited $Zn_{1-x}Fe_xTe$ thin films with a fixed Fe composition at $x = 0.014$ and variable N concentrations in the range of $1.8 \times 10^{18} – 5.1 \times 10^{19}$ cm^{-3}. The XRD θ - 2θ scan profiles has detected the presence of extrinsic precipitates possibly of Fe-N compounds in the N-doped films with the highest N concentration. Similarly, the structural analysis by XAFS has revealed that, the Fe atoms are dominantly incorporated in the substitutional site with the valence state deviated significantly from Fe^{2+} to $Fe^{2+/3+}$ mixed states due to the N-doping in the range of $1.8 \times 10^{18} – 4.3 \times 10^{18}$ cm^{-3}, while at the higher N concentrations of the order of $1.8 \times 10^{19} – 5.1 \times 10^{19}$ cm^{-3}, the extrinsic precipitates of Fe-N compounds have been formed in the crystal. These results are in strong accordance with the magnetic properties of the grown films; *M-H* curves exhibited drastic changes from a linear dependence, typical of van-Vleck paramagnetism in the undoped film, to weak room temperature ferromagnetic behaviors with hysteresis at the intermediate N concentrations of the order of 10^{18} cm^{-3}, reflecting the deviation of the valence state of substitutional Fe valence state from Fe^{2+} to $Fe^{2+/3+}$ mixed states. On the other hand, at the higher N concentrations of the order of 10^{19} cm^{-3}, the *M-H* curve has showed robust room temperature ferromagnetic behavior, which may originate from the formation of extrinsic precipitates of Fe-N compounds.

Though we have observed the impact of N acceptor co-doping in the magnetic properties of $Zn_{1-x}Fe_xTe$ thin films in both growth condition, the room temperature ferromagnetic properties exhibited by substitutional Fe

deviated from the valence state of Fe^{2+} is only detected in the case of Zn-rich samples with N concentrations of the order of 10^{18} cm^{-3}. As an origin we have observed larger deviation of substitutional Fe valence state from Fe^{2+} to $Fe^{2+/3+}$ mixed states due to N-doping in the Zn-rich samples as compared to the previous Te-rich growth condition even for the same N-doping concentration. This significant change of valence state of substitutional Fe from Fe^{2+} to Fe^{3+} can induce robust magnetic moment even at zero external magnetic field and can also modify the exchange interactions between the magnetic moments. Thus, we get the room temperature ferromagnetic behavior in the N-doped films with N concentrations of the order of 10^{18} cm^{-3} in the case of Zn-rich growth condition.

Now, we will summarize the experimental observations on the electric field control study on (Zn,Fe)Te.

In the electric field control study, our intention is also to change the valence state of Fe in (Zn,Fe)Te and hence to observe the impact on its magnetic properties. We have used field effect transistor (FET) by using both ionic liquid and Al_2O_3 solid insulating layer. In both cases, we have used the Pt foil as gate electrode and applied the external gate voltages through the Cu wire terminals attached to the opposite sides of the sample by using In.

In the case of the structure containing ionic polymer, the saturation magnetization has changed by the application of external gate voltages, but in an irreversible way. This suggests that the modulation does not originate from the intrinsic magnetic properties of (Zn,Fe)Te. It may come from any chemical interaction of the ionic liquid with the magnetic layer at the interface. In addition, we have not observed change in the magnetic properties by applying external voltages across the device containing Al_2O_3 layer as gate insulator. In this case, the possible reason is the large thickness of the magnetic channel layer which reduces the possibility of magnetic modulation. So, applying gate voltages across a relatively thin (Zn,Fe)Te layer may reflect better modulation of magnetic properties. In this study, we have measured the magnetic modulation by using the SQUID machine across the thick diamagnetic GaAs substrate, so the small variation in the magnetic properties of the magnetic channel layer may not be identified. In that case, the magnetization dependent Hall effect can directly provide us information about the minor changes in the magnetic properties of the (Zn,Fe)Te channel layer directly under the application of external gate voltages.

References

1. R. M. Park, M. B. Troffer, C. M. Rouleau, J. M. Depuydt and M. A. Haase, *Appl. Phys. Lett.* **57**, 2127 (1990).

2. K Ohkawa, T. Karasawa, and T. Mitsuyu, *Jpn. J. Appl. Phys*. **30**, L152 (1991).

3. T. Dietl and H. Ohno, *MRS Bulletin,* October 2003, pp. 714 – 719.

4. H. Ohno, H. Munekata, T. Penney, S. von Molnar and L. L. Chang, *Phys. Rev. Lett.* **68**, 2664 (1992).

5. H. Ohno, A. Shen, F. Matsukura, A. Oiwa, A. Endo, S. Katsumoto, and Y. Iye, *Appl. Phys. Lett.* **69**, 363 (1996).

6. T. Dietl, *Semimagnetic semiconductors in high magnetic fields, in Physics in High Magnetic Fields,* edited by S. Chikazumi and N. Miura (*Springer,* Berlin), 1981, p. 344.

7. S. V. Vonsovskii, *Magnetism* (*John Wiley and sons,* New York), 1974.

8. H. Akai, *Phys. Rev. Lett.* **81**, 3002 (1998).

9. S. Kuroda, N. Nishizawa, K. Takita, M. Mitome, Y. Bando, K. Osuch, and T. Dietl, *Nat. Mater.* **6**, 440 (2007).

10. K. Sato, T. Fukushima, M. Toyoda, H. Kizaki, V. A. Dinh, H. Fujii, L. Bergqvist, P. H. Dederichs, H. Katayama-Yoshida, *Physica B* **404**, 5237 (2009).

11. H. Katayama-Yoshida, K. Sato, T. Fukushima, M. Toyoda, H. Kizaki, V. A. Dinh, and P. H. Dederichs, *Phys. Status Solidi A* **204**, 15 (2007a).

12. A. Wolos, and M. Kamińska, *Magnetic impurities in semiconductors, in Spintronics,* edited by T. Dietl, D. D. Awschalom, M. Kamińska, and H. Ohno (*Elsevier,* Amsterdam), 2008, p. 325.

13. K. Sato, L. Bergqvist, J. Kudrnovsky, P. H. Dederichs, O. Eriksson, I. Turek, B. Sanyal, G. Bouzerar, H. Katayama-Yoshida, V. A. Dinh, T. Fukushima, H. Kizaki, R. Zeller, *Rev. Mod. Phys.* **82**, 1633 (2010).

14. J. B. Goodenough, *Phys. Rev.* **100**, 564 (1955).

15. J. Kanamori, *J. Phys. Chem. Solids* **10**, 87 (1959).

16. T. Dietl, H. Ohno, F. Matsukura, J. Cibert, and D. Ferrand, *Science* **287**, 1019 (2000).

17. S. J. Pearton, C. R. Abernathy, M. E. Overberg, G. T. Thaler, D. P. Norton, N. Theodoropoulou, A. F. Hebard, Y. D. Park, F. Ren, J. Kim, L. A. Boatner, *J. Appl. Phys.* **93**, 1 (2003).

18. T. Dietl, *Nat. Mater.* **2**, 646 (2003).

19. H. Ohno, *Science* **281**, 951 (1998).

20. D. Ferrand, J. Cibert, A. Wasiela, C. Bourgognon, S. Tatarenko, G. Fishman, S. Kolesnik, J. Jaroszynski, T. Dietl, B. Barbara and D. Dufeu, *J. Appl. Phys.* **87**, 6451 (2000).

21. T. Dietl, *Nat. Mater.* **5**, 673 (2006).

22. T. Dietl, *Nat. Mater*. **2**, 646 (2003).

23. A. Navarro-Quezada, W. Stefanowicz, Tian Li, B. Faina, M. Rovezzi, R. T. Lechner, T. Devillers, F. d'Acapito, G. Bauer, M. Sawicki, T. Dietl, A. Bonanni, *Phys. Rev.* B **81**, 205206 (2010).

24. A. Bonanni, A. Navarro-Quezada, Tian Li, M. Wegscheider, Z. Matej, V. Holy, R. T. Lechner, G. Bauer, M. Rovezzi, F. D'Acapito, M. Kiecana, M. Sawicki, T. Dietl, *Phys. Rev. Lett.* **101** 135502 (2008).

25. S. Ikeda, K. Miura, H. Yamamoto, K. Mizunuma, H. D. Gan, M. Endo, S. Kanai, J. Hayakawa, F. Matsukura and H. Ohno, *Nature Mater*. **9**, 721 (2010).

26. H. Sato, T. Yamamoto, M. Yamanouchi, S. Ikeda, S. Fukami, K. Kinoshita, F. Matsukura, N. Kasai, H. Ohno, *Tech. Dig. Int. Electron Devices Meeting* 60–63 (2013).

27. H. Ohno, D. Chiba, F. Matsukura, T. Omiya, E. Abe, T. Dietl, Y. Ohno and K. Ohtani, *Nature* **408**, 944 (2000).

28. D. Chiba, F. Matsukura and H. Ohno, *Appl. Phys. Lett.* **89**, 162505 (2006).

29. M. Weisheit, S. Fahler, A. Marty, Y. Souche, C. Poinsignon, D. Givord, *Science* **315**, 349 (2007).

30. A. Twardowski, *J. Appl. Phys.* **67**, 5108 (1990).

31. E. Malguth, A. Hoffmann, M. R. Philips, *Phys. Stat. Sol. (b)* **245**, 1 (2008).

32. S. Ishitsuka, T. Domon, R. Akiyama, K. Kanazawa, S. Kuroda, H. Ofuchi, *Phys. Stat. Sol.(c)* **11**, 1312 (2014).

33. T. Nakamura, Y. Sugimura, T. Domon, S. Ishitsuka, K. Kanazawa, H. Ofuchi, S. Kuroda, *J. Cryst. Growth*, **477**, 123 (2017).

34. W. Jantsch, G. Hendorfer, *J. Cryst. Growth*, **101**, 404 (1990).

35. A. J. Szadkowski, *J. Phys.: Cond. Matter*, **2**, 9853 (1990).

36. M. Grun, A. Haury, J. Cibert, A. Wasiela, *J. Appl. Phys.* **79**, 7386 (1996).

37. E. Malguth, A. Hoffmann, and M. R. Phillips, *Phys. Status Solidi (b)* **245**, 455 (2008).

38. A. Ibrahim, N. El-Sayed, M. Kaid, A. Ashour, *Vacuum* **75**, 189 (2004).

39. C. X. Shan, X. W. Fan, J. Y. Zhang, Z. Z. Zhang, X. H. Wang, J. G. Ma, Y. M. Lu, Y. C. Liu, D. Z. X. Shen, G. Kong, G. Z. Zhong, *J. Vac. Sci. Technol. A Vac. Surf. Films* **20**, 1886 (2002).

40. R. K. M. Raghupathy, T. D. Kuhne, C. Felser and H. Mirhosseini, *J. Mater. Chem. C* **6**, 541 (2018).

41. M. L. Cohen, and T. K. Bergstresser, *Phys. Rev. B* **141**, 789 (1966).

42. T. Yamamoto, *Jpn. J. Appl. Phys.* **42**, L514 (2003).

43. 46. J. Han, T. S. Stavrinides, M. Kobayashi, R. L. Gunshor, M. M. Hageroot and A. V. Nurmikko, *Appl. Phys. Lett.* **62**, 840 (1993).

44. T. Baron, K. Saminadayar and N. Magnea, *Appl. Phys. Lett.* **67**, 20 (1995).

45. T. Baron, K. Saminadayar and N. Magnea, *Appl. Phys. Lett.* **83**, 3 (1998).

46. J. Han, T. S. Stavrinides, M. Kobayashi, R. L. Gunshor, M. M. Hageroot and A. V. Nurmikko, *Appl. Phys. Lett.* **62**, 840 (1993).

47. J. K. Furdyna and J. Kossut, *Diluted Magnetic Semiconductors*, R. K. Willardson and A. C. Beer, J. K. Furdyna, *J. Appl. Phys*. **64**, R29 (1988).

48. M. Villeret, S. Rodriguez, and E. Kartheuser, *Phys. Rev. B* **41**, 10028 (1990).

49. E. Kartheuser, S. Rodriguez, and M. Villeret, *Phys. Rev. B* **48**, 14127 (1993).

50. S. Tsoi, I. Miotkowski, S. Rodriguez, A. K. Ramdas, H. Alawadhi and T. M. Pekarek, *Phys. Rev. B* **72**, 155207 (2005).
51. R. Singh, *J. Magn. Mag. Mater.* **322**, 290 (2010).

52. A. Twardowski, M. V. Ortenberg, and M. Demianiuk, *J. Cryst. Growth* **72**, 401 (1985).

53. W. Mac, M. Herbich, Nguyen The Khoi, A. Twardowski, Y. Shapira, and M. Demianiuk, *Phys. Rev. B* **53**, 9532 (1996).

54. A. Zunger, *Solid State Physics*, edited by F. Zeits, H. Ehrenreich, and D. Turnbull, Academic, New York, **39**, (1986) p. 275.

55. H. Katayama-Yoshida, *Int. J. Mod. Phys. B* **1**, 1207 (1987).

56. K. Sato, and H. Katayama-Yoshida, *Jpn. J. Appl. Phys.,* Part 2 **40**, L651 (2001c).

57. T. Fukushima, K. Sato, H. Katayama-Yoshida, and P. H. Dederichs, *Jpn. J. Appl. Phys*. **43**, L1416 (2004).

58. M. Kobayashi, Y. Ishida, J. I. Hwang, G. S. Song, A. Fujimori, C. S. Yang, L. Lee, H. J. Lin, D. J. Huang, C. T. Chen, Y. Takeda, K. Terai, S. I. Fujimori, T. Okane, Y. Saitoh, H. Yamagami, K. Kobayashi, A. Tanaka, H. Saito and K. Ando, *New J. Phy.* **10**, 055011 (2018).

59. M. Godlewski and M. Kaminska, *J. Phys. C* **13**, 6537 (1980).

60. T. Baron, K. Saminadayar, and N. Magnea, *J. Appl. Phys.* **83**, 1354 (1998).

61. N. Ozaki, N. Nishizawa, S. Marcet, S. Kuroda, O. Eryu, and K. Takita, *Phys. Rev. Lett.* **97**, 037201 (2006).

62. N. Ozaki, J. Okabayashi, T. Kumekawa, N. Nishizawa, S. Marcet, S. Kuroda, and K. Takita, *Appl. Phys. Lett*. **87**, 192116 (2005).

63. S. Kuroda, N. Ozaki, N. Nishizawa, T. Kumekawa, S. Marcet, K. Takita, *Sci. Tech. Adv. Mater*. **6**, 558 (2005).

64. M. Godlewski, and M. Kamińska, *J. Phys. C* **13**, 6537 (1980).

65. A. Bonanni, M. Kiecana, C. Simbrunner, T. Li, M. Sawicki, M. Wegscheider, M. Quast, H. Przybylinska, A. Navarro- Quezada, R. Jakiela, A. Wolos, W. Jantsch, and T. Dietl, *Phys. Rev. B* **75**, 125210 (2007).

66. G. M. Dalpian, L. F. Juarez Da Silva, and Su-Huai Wei, *Phys. Rev. B* **79**, 241201(R) (2009).

67. L. Galoisy, G. Calas and M. A. Arrio, *Chem. Geol.* **174**, 307 (2001).

68. T. E. Westre, P. Kennepohl, J. G. DeWitt, B. Hedman, K. O. Hodgson, E. I. Solomon, *J. Am. Chem. Soc.* **119**, 6297 (1997).

69. T. Dietl, *Phys. Rev. B* **77**, 085208 (2008a).

70. H. Munekata, H. Ohno, S. V. Molnar, A. Segmuller, L. L. Chang and L. Esaki, *Phys. Rev. Lett*. **63**, 1849 (1989).

71. Y. L. Soo, S. W. Huang, Z. H. Ming, Y. H. Kao and H. Munekata, *Phys. Rev. B* **53**, 4905 (1996).

72. T. Dietl, H. Ohno, F. Matsukura, J. Cibert and D. Ferrand, *Science* **287**, 1019 (2000).

73. Y. Yamada, K. Ueno, T. Fukumura, H. T. Yuan, H. Shimitani, Y. Iwasa, L. Gu, S. Tsukimoto, Y. Ikuhara, M. Kawasaki, *Science* **332**, 1065 (2011).

74. M. J. Calderon, S. D. Sarma, *Ann. Phys*. **332**, 2618 (2007).

75. K. A. Griffin, A. B. Pakhomov, C. M. Wang, S. M. Heald, K. M. Krishnan, *Phys. Rev. Lett*. **94**, 157204 (2005).

76. P. E. Luscher, and D. M. Collins, *Cryst. Growth. Charact.* **2**, 15 (1979).

77. L. Morresi, *Silicon based thin film solar cells*, 2013, p. 81 – 107.

78. J. Goodge, *Geochemical Instrumentation and analysis*.

79. J. Vervoort, *Geochemical Instrumentation and analysis*.

80. A. K. Chatterjee, *Handbook of Analytical Techniques in concrete Science and Technology*, 2001.

81. S. D. Conradson, *XAFS: A Technique to Probe Local structure, Los Alamos Science Number* **26** (2000).

82. F. Krumeich, *Introduction into Transmission and Scanning Transmission Electron Microscopy, 1st version,* May 2018.

83. K. Shimamura, D. chiba, S. Ono, S. Kukami, N. Ishiwata, M. Kawaguchi, K. Kobayashi, and T. Ono, *Appl. Phys. Lett.* **100**, 122402 (2012).

84. H. Oikawa, *Ph.D thesis dissertation: Modulation of magnetic properties of II-VI diluted magnetic semiconductors by the application of electric field*, University of Tsukuba, 2014.

85. S. Momose, *Master thesis: Modulation of magnetic properties of (Zn,Cr)Te thin film by the application of electric field using ionic liquid as gate insulating layer*, University of Tsukuba, 2016.

86. Y. Wada, Master thesis: *Effect of external electric field on the magnetism of Al donor co-doped (Zn,Cr)Te*, University of Tsukuba, 2016.

87. G.D.Wilk, R.M.Wallace, and J.M.Anthony, *J. Appl. Phys*. **89**, 5243 (2001).

88. T. Dietl, K. Sato, T. Fukushima, A. Bonanni, M. Jamet, A. Barki, S. Kuroda, M. Tanaka, P. N. Hai, H. Katayama-Yoshida, *Rev. Mod. Phys*. **87**, 1311 (2015).

89. H. Kobayashi, Y. Nishio, K. Kanazawa, S. Kuroda, M. Mitome, Y. Bando, *Physica B: Cond. Matter*, **407**, 2947 (2012).

90. G. Calas, J. Petiau, *Solid State Commun.* **48**, 625 (1983).

91. M. Wilke, F. Farges, P. E. Petit, G. E. Brown, F. Martin, *Am. Mineral., J. Ear. Plan. Mater*. **86**, 714 (2001)**.**

92. H. Okudera, A. Yoshiasa, K.Murai, M. Okube, T. Takeda, S. Kikkawa, *J. Mineral. Petrol. Sci.* **107**, 127 (2012).

93. X. P. Feng, W. B. Mi, H. L. Bai, *Appl. Surf. Sci*. **257**, 7320 (2011).

94. M. Mitome, Y. Bando, D. Golberg, K. Kurashima, Y. Okura, T. Kaneyama, H. Naruse, Y. Honda, Microsc. *Res. Tech.* **63**, 140 (2004).

95. A. Twardowski, A. Lewicki, M. Arciszewska, W. J. M. de Jouge, H. J. M. Swagten, M. Demianiuk, *Phys. Rev. B* **38**, 10749 (1988).

96. T. Hinomura and S. Nasu, *Nuoro. Cimento., D* **18**, 253 (1996).

97. H. Naganuma, Y. Endo, R. Nakatani, Y. Kawamura, M. Yamamoto, *Sci. Technol. Adv. Mater*. **5**, 83 (2004).

98. B. Kubaschewski, *Iron-Binary phase Diagrams* (Springer, New York, 1982) p. 67.

99. N. Terada, Y. Hoshi, M. Naoe and S. Yamanaka, *IEEE Trans. Magn.* 20, 1451 (1984).

100. K. R. Nikolaev, I. N. Krivorotov, E. D. Dahlberg, V. A. Vas'ko, S. Urazhdin, R. Loloee and W. P. Pratt, Jr., *Appl. Phys. Lett.* 82, 4534 (2003).

Acknowledgement

All the admiration to God, the merciful and beneficial who has enables me to submit this humble work leading to the Doctoral degree in Engineering.

First and foremost, I would like to express my deepest sense of gratitude and thanks to my esteemed teacher and supervisor Prof. Shinji Kuroda , Department of Nano-Science and Nano-Technology, University of Tsukuba, Japan for his constant encouragement, co-operation, inspirations, affectionate and indispensable guidance, and brilliant suggestions in my thesis work and introducing me to the exciting field of Semiconductor Spintronics.

I would like to reserve the first words for conveying my sincere gratefulness to the committee members of my PhD. degree evaluation board, Prof. Yuzo Ohno, Prof. Takashi Suemasu and Prof. Hideto Yanagihara, University of Tsukuba, Japan for their brilliant suggestions and inspirations.

I convey my heartfelt thanks and gratitude to Dr. Ken Kanazawa, Assistant Professor, University of Tsukuba, Japan for his generous support in doing measurements and giving constant inspiration in pursuing the whole investigation of the present research

I express sincere thanks to Prof. Hiroaki Nitani, High energy accelerator research organization (KEK), Japan for XAFS measurement, Prof. Tamostu Koyano, University of Japan for PPMS measurement, Prof. Masanori Mitome and Dr. Nakayama Yoshiko, NIMS microstructural characterization platform, Tsukuba, Japan for TEM observation and sample preparation, Dr Teruhisa Osuki, AIST Nano-processing facility, Japan for the nitrogen concentration measurements. Officer of material Science Division, Atomic Energy Centre, Dhaka, AECD, for his generous support in doing measurements.

I would like to express my gratitude to the Ministry of Education, Culture, Sports, Science and Technology (MEXT), Japan for the scholarship. I am also grateful to Mr. Takuma Nakamura, Mr. Kenji Makita, Mr. Yuta Tomohiro, Mr. Shojiro Kato for their company and support in the laboratory.

Finally, I extend my thanks to my parents, my family members, my friends, well-wishers for giving me all kinds of support. Without their enthusiastic inspiration, it was impossible for me to stay in this stage.

Appendix

$Zn_{1-x}Fe_xTe$: N thin films (Te-rich growth condition)

$Zn_{1-x}Fe_xTe$: N thin films Te-rich growth condition	
Sample No.	**Serial No.**
ZFT#122	A#1
p-ZFT#52	A#2
p-ZFT#50	A#3
p-ZFT#51	A#4

$Zn_{1-x}Fe_xTe$: N thin films (Zn-rich growth condition)

$Zn_{1-x}Fe_xTe$: N thin films Zn-rich growth condition	
Sample No.	**Serial No.**
ZFT#129	B#1
p-ZFT#29	B#2
p-ZFT#62	B#3
p-ZFT#28	B#4
p-ZFT#27	B#5

$Zn_{1-x}Fe_xTe$ thin films (Modulation doped structure)

$Zn_{1-x}Fe_xTe$ thin films Te-rich growth condition	
Sample No.	**Serial No.**
ZFT#135	C#1
ZFT#136	C#2

$Zn_{1-x}Fe_xTe$ thin films (Field control study)

$Zn_{1-x}Fe_xTe$ thin films Te-rich growth condition	
Sample No.	**Serial No.**
ZFT-FC#04	D#1
ZFT-FC#03	D#2
ZFT-FC#05	D#3
ZFT-FC#06	D#4
ZFT-FC#07	D#5